UNIVERSITÄT PADERBORN

Theoretical Investigations of Spatially Multimode High-Gain SU(1,1) Interferometers

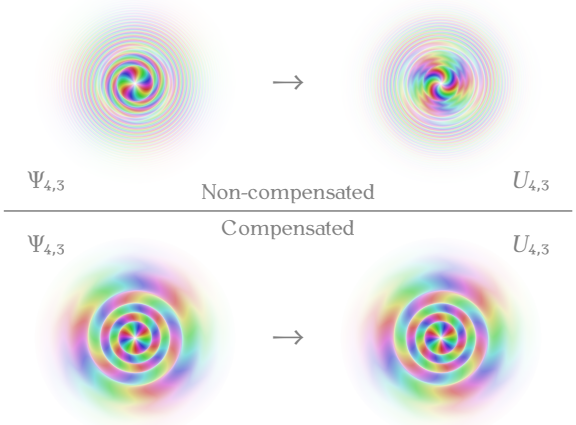

Eine der Fakultät für Naturwissenschaften
der Universität Paderborn vorgelegte

Dissertation

zur Erlangung des akademischen Grades

Doctor Rerum Naturalium (Dr. rer. nat.)

von

Dennis Scharwald

Tag der Abgabe: 14.11.2025
Tag der Disputation: 17.12.2025

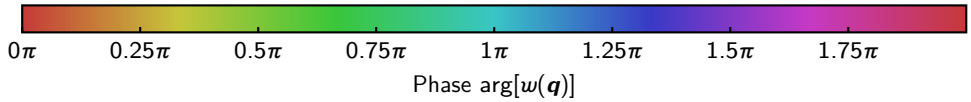

The title figure on the front page illustrates the phase profile and modulus of the input and output modes Ψ_{mn} and U_{mn} with $m = 4$ (radial index) and $n = 3$ (OAM index) for the full three-dimensional SU(1,1) interferometer consisting of two crystals with length $L_1 = 3\,\mathrm{mm}$ and pumped at high gain with a Gaussian pump with a $1/e^2$-radius of the intensity distribution of $70\,\mu\mathrm{m}$. Unlike in Chapter 5, the shown modes were obtained by integrating the integro-differential equations for the full three-dimensional model as described in Sec. A.4.2.2, including the simplifications for $l_p = 0$ and the case where the function r is even in the signal-idler angle difference. No fit to determine the fitting constant A was performed and instead the qualitative behaviors of the intensity profile (it has a Gaussian shape instead of a sinc^2-shape) and of the Schmidt modes (see below) were used as an indicator that the selected value of $\Gamma = 1.3$ corresponds to the high-gain regime. The modes are obtained by first applying the algorithm for the joint Schmidt decomposition developed for Refs. [3, 4] to the functions $\sqrt{qq'}\,\beta_3(q,q')$ and $\sqrt{qq'}\,\tilde{\eta}_3(q,q')$ as inferred from Eqs. (A.85). This is equivalent to how the Schmidt modes are obtained in the context of the Schmidt mode theory based description of the full three-dimensional model, see Sec. 5.2.2 and Ref. [2]. Finally, the modes $\Psi_{4,3}$ and $U_{4,3}$ result from the decomposition as written in Eqs. (A.75).

In the plots, the color indicates the phase of the mode at a certain wave-vector $\boldsymbol{q}$, while the visibility of the color encodes the modulus. More precisely, in the *HLS color space*, the *color coordinates* for the mode function $\Upsilon = U_{4,3}, \Psi_{4,3}$ are given by

$$H = \frac{\arg[\Upsilon(\boldsymbol{q})]}{2\pi}, \tag{i.1a}$$

$$L = 1 - \frac{1}{2}\left(\frac{|\Upsilon(\boldsymbol{q})|}{\max_{\boldsymbol{q}}|\Upsilon(\boldsymbol{q})|}\right)^{\frac{2}{3}}, \tag{i.1b}$$

$$S = 57\,\%, \tag{i.1c}$$

where $\arg : \mathbb{C} \mapsto [0, 2\pi[$ and the hue H is taken to be over the interval $[0, 1[$. Note that the choice for L also assumes that $\min_{\boldsymbol{q}}|\Upsilon(\boldsymbol{q})| \approx 0$, so that $|\Upsilon(\boldsymbol{q})| = 0$ corresponds to plain white, while $\max_{\boldsymbol{q}}|\Upsilon(\boldsymbol{q})|$ corresponds to the range of colors that are maximally distinct from the white background. The colorbar for the values $\max_{\boldsymbol{q}}|\Upsilon(\boldsymbol{q})|$ (meaning $L = 1/2$) is shown above. Similar coloring techniques are for example used in the context of *domain coloring* [D. S. Alexander *et al.*, *Early days in complex dynamics: A history of complex dynamics in one variable during 1906–1942* (American Mathematical Society, 2012); E. Wegert, *Visual Complex Functions: An Introduction with Phase Portraits* (Birkhäuser, 2012)].

The upper row presents the modes for a non-compensated interferometer with a distance of $d = 1\,\mathrm{cm}$ between the two crystals, while the lower row shows the corresponding modes for a fully compensated SU(1,1) interferometer with $\phi = 0$. For the compensated case, both crystals were integrated separately and no symmetry relation of the transfer functions analogous to Eqs. (3.43) was used. The behavior of the modes follows the behavior presented in Sec. 4.2 for the system where one transverse dimension is neglected: For the non-compensated interferometer, while the moduli of the input and output mode are to a good approximation the same, the phase profile of the input mode when following a radial direction away from the center is much flatter than that of the output mode, leading to a more pronounced swirl-like pattern than for the input mode. This result is essentially the same as shown in Sec. 4.2.1 for a single crystal in the system with only a single transverse dimension. Furthermore, for transverse wave-vectors further away from the collinear direction, a ripple-pattern can be observed. This is due to the fact that for the non-compensated setup, the destructive interference is imperfect because of the wave-vector dependent phase acquired by the light in the air gap. See also Sec. 5.3.2 and Sharapova *et al.* [5]. For the compensated setup, the input and output mode are identical, essentially illustrating the result for the analytical Schmidt decomposition for the system with a single transverse dimension presented in Sec. 4.2.2.1 and in particular in Eqs. (4.47). In both cases, the azimuthal dependence of the modes on the angle ϕ is given by a term $e^{-3i\phi}$, compare Eqs. (A.75). This leads to the threefold discrete rotational symmetry of the modes. The visible angular diameter of the shown modes in terms of the external angles is around $110\,\mathrm{mrad}$ (corresponding to $6.3°$).

Promotionskommission

Vorsitzender:	Prof. Dr. Thomas Zentgraf Ultraschnelle Nanophotonik Universität Paderborn
Erstgutachter:	Prof. Dr. Torsten Meier Computational Optoelectronics and Photonics Universität Paderborn
Zweitgutachter:	Prof. Dr. Jan Sperling Theoretische Quantensysteme Universität Paderborn
Vertreterin des Mittelbaus:	Dr. Polina Sharapova Theoretical Quantum Optics Universität Paderborn

Erklärung

Hiermit erkläre ich, dass ich die vorliegende Dissertation ohne fremde Hilfe und ohne Benutzung anderer als der angegebenen Quellen angefertigt habe und, dass ich diese in gleicher oder ähnlicher Form noch keiner anderen Prüfungsbehörde vorgelegt habe. Alle Ausführungen, die wörtlich oder sinngemäß übernommen worden sind, sind als solche gekennzeichnet.

Paderborn, 13.11.2025 **Dennis Scharwald**

Abstract

In this thesis, several aspects of high-gain multimode SU(1,1) interferometers are theoretically investigated, with the focus being on metrological applications. The parametric down-conversion (PDC) process utilized in these interferometers is theoretically described via integro-differential equations describing spatial evolution of the plane-wave operators.

It is shown that for the phase sensitivity of these interferometers, supersensitivity can be reached provided that proper diffraction compensation is applied. The phase sensitivity improves if the gain is increased or if the number of effective modes is decreased. This comes at the cost of the phase-region width over which supersensitivity can be reached.

Based on the Schmidt mode structure of SU(1,1) interferometers, a processing method is constructed which allows for the experimental retrieval of the levels of squeezing and anti-squeezing of the multimode state generated by the first PDC section of an SU(1,1) interferometer. It is then applied experimentally by collaborators and is found to be in good agreement with the theoretical predictions.

Finally, SU(1,1) interferometers pumped with Laguerre-Gaussian beams are analyzed in the context of angular displacement measurements. As either the gain, the OAM index or the radial index of the pump are increased, the measurement uncertainty is decreased, ultimately allowing for supersensitive measurements. Generally, the behavior is the same as for the phase sensitivity.

Zusammenfassung

In dieser Dissertation werden Aspekte von *high-gain multimode* SU(1,1) Interferometer theoretisch untersucht. Dabei wird der Prozess der parametrischen Fluoreszenz (PDC) mithilfe von Integro-Differentialgleichungen modelliert, welche die räumliche Entwicklung der Ebene-Wellen-Operatoren beschreiben.

Es wurde gezeigt, dass Supersensitivität für die Phasenempfindlichkeit dieser Interferometer erreicht werden kann, sofern die Beugung der PDC Strahlung kompensiert wird. Weiterhin führt eine Erhöhung der parametrische Verstärkung und eine Reduktion der Schmidt-Zahl zu einer Verbesserung der Phasenempfindlichkeit und einer Verkleinerung des Phasenbereiches, über den die Supersensitivität erreicht werden kann.

Basierend auf der Struktur der Schmidt-Moden von SU(1,1) Interferometern wurde ein numerisches Aufbereitungsverfahren konstruiert, welches die Messung der Stärke des *Squeezing* und *Anti-Squeezing* des Zustandes ermöglicht, der durch den ersten Kristall des Interferometers erzeugt wird. Das Verfahren wurde experimentell von Kooperationspartnern angewandt, wobei eine gute Übereinstimmung mit der Theorie festgestellt wurde.

Zuletzt wurden SU(1,1) Interferometer mit Laguerre-Gauß-Moden als *Pump*-Strahlung für die Messung von Winkelverschiebungen untersucht. Es zeigte sich, dass sich die quantenmechanisch bedingte Messunsicherheit verbessert, wenn die parametrische Verstärkung oder die Indizes der Pump-Mode erhöht werden. Das generelle Verhalten gleicht dem der Phasensensitivität.

Table of Contents

1

Introduction

Over the last nearly 40 years, SU(1,1) interferometers have become an important tool in quantum optics and quantum optical metrology [1–15], ever since they were proposed by Yurke *et al.* [16] in 1986 for supersensitive phase-shift measurements. These types of interferometers utilize quantum states of light, more precisely squeezed states generated via parametric down-conversion (PDC), in order to beat the shot-noise level for the phase sensitivity, which is the reference level that can be achieved using classical laser light [1, 9, 17]. Additionally, they are generally easier to construct than classical interferometers using quantum light since they require fewer optical elements [16].

In general, the PDC process generates a strongly multimode squeezed state, unless special filtering is applied [3, 4, 18–20]. While this multimode squeezed light finds many applications in quantum information processing [21–23] and quantum communication [24], previous theoretical descriptions of SU(1,1) interferometers in the context of phase sensitive measurements mainly focused on single or two-mode radiation [9, 25–27]. As such, in this work, the full multimode structure of the PDC light is accounted for at arbitrary parametric gain by describing the PDC process using the systems of coupled integro-differential equations derived in Sharapova *et al.* [5].

The state generated in the PDC process is generally a (multimode) squeezed state [4, 28, 29]. This means that there exists a certain set of modes [20, 30, 31] in which the quantum uncertainty of the electric field is reduced in one quadrature and increased in the quadrature orthogonal to the squeezed one [32–34]. Squeezing and squeezed states have many applications, such as in quantum imaging [35, 36] and quantum interferometry, most notably in gravitational wave detection [37, 38]. Measuring the strength (level) of the squeezing experimentally is normally done via homodyne detection [38–40]. However, for multimode squeezed states, this method becomes increasingly cumbersome due to the fact that it requires a local oscillator matching each mode to be measured and is additionally vulnerable to detection losses [3, 4, 18, 41]. As such, it is advisable to extend the method for Wigner function tomography suggested in Kalash and Chekhova [29] to multimode

squeezing measurements.

The eigenmodes of the PDC process in rotationally symmetric systems carry phase terms $e^{il\varphi}$, where $l \in \mathbb{Z}$ and φ denotes the azimuthal angle of the system [2, 11, 42–44]. This phase distribution implies that these modes carry orbital angular momentum (OAM) about the longitudinal axis [2, 45–47]. One interesting property of beams carrying OAM is that they can transfer the angular momentum onto objects, causing them to rotate. This property was originally described for Laguerre-Gaussian modes by Allen *et al.* [46], with the suggestion that this property may be used for the detection of OAM. Other methods for generating beams with OAM are spatial light modulators, optical gratings [48–50] and q-plates [51–53]. One of the most prominent applications of light beams carrying OAM is in angular displacement measurements, where they allow for supersensitive measurements below the standard quantum limit [48, 51, 54, 55]. As such, it stands to reason that SU(1,1) interferometers may also be used for supersensitive angular displacement measurements. Furthermore, if the pump beam carries OAM, it is naturally expected that modal structure of the PDC process can be influenced by varying the OAM of the pump.

The rest of this thesis is organized as follows: In Chapter 2, the fundamentals of nonlinear optics and quantum optics as they pertain to this thesis will be introduced, with the main focus being on the PDC process. Based on the fundamentals, in Chapter 3, SU(1,1) will be formally introduced and their phase sensitivity in dependence on the gain and the modal structure of the PDC process is analyzed. For the analysis, the integro-differential equation approach of Sharapova *et al.* [5] is used and along the way, several additional concepts, such as the joint Schmidt decomposition (Bloch-Messiah reduction), which is used to characterize the multimode nature of the PDC light, are introduced. In Chapter 4, the description of SU(1,1) interferometers is extended towards multimode squeezing measurements. Here, the first crystal is understood as a squeezer, which generates a multimode squeezed state, while the second crystal serves as the analyzer. From these investigations, a processing method is developed. This method has been applied experimentally in Barakat *et al.* [3] and the results will be sketched out. In Chapter 5, the focus will be on PDC systems pumped with Laguerre-Gaussian beams carrying OAM. For this, OAM will be first formally introduced. Then, the modal structure of PDC systems pumped with Laguerre-Gaussian pump beams will be analyzed, and it will be investigated how the occupations of the modes can be manipulated by varying the radial and OAM mode indices of the pump. Additionally, it will be assessed how SU(1,1) interferometers pumped with Laguerre-Gaussian beams can be used for angular displacement measurements. Finally, in Chapter 6, the results of this thesis are again summarized, along with suggestions for future research. Several auxiliary results, calculations and proofs used throughout this work are provided in Appendix A. Additionally, in Appendix B, the concept of diffraction compensation inside SU(1,1) interferometers, which is central to several parts of this work, is explained in detail.

2

Fundamentals

This chapter will introduce several fundamental concepts which form the basis of this work and are essential for the understanding of parametric down-conversion (PDC). Since PDC is a nonlinear quantum optical effect, Sec. 2.1 starts with a brief review of classical nonlinear optics and introduces uniaxial crystals, which are commonly used for PDC. Following that, Sec. 2.2 introduces the field operators for the quantized electromagnetic field which enable the mathematical description of the PDC process in quantum optics. By combining the concepts of Secs. 2.1 and 2.2, Sec. 2.3 will then provide an overview over the parametric down-conversion process and mathematical formalisms used for its theoretical description, which will be the main focus of the rest of this work.

2.1. Classical Nonlinear Optics

In nonlinear optics, the polarization response of a material is characterized by nonlinear behavior, as implied by the name of this field of study. Formally, the jth component of the polarization field $\boldsymbol{P}$ is connected to the electric field components E_k by [32, 56, 57]

$$P_j(\boldsymbol{r},t) = \varepsilon_0 \left[\sum_k \chi^{(1)}_{jk} E_k(\boldsymbol{r},t) + \sum_{k,l} \chi^{(2)}_{jkl} E_k(\boldsymbol{r},t)\, E_l(\boldsymbol{r},t) + \cdots \right], \tag{2.1}$$

where ε_0 is the vacuum permittivity, $\chi^{(1)}_{jk}$ is the *first-order (linear) susceptibility tensor* of the dielectric as known from linear optics and $\chi^{(2)}_{jkl}$ is the *second-order (nonlinear)* susceptibility tensor. Higher-order contributions beyond the second order are not explicitly written out here, since they are not relevant in the context of this work.

For simplicity, it is common to make several additional assumptions regarding the susceptibilities:

- It is usually assumed that the susceptibilities do not depend on the frequencies of the electric fields appearing in Eq. (2.1), meaning that the dielectric is dispersionless.

Generally, dispersion can be neglected when the appearing fields are narrowband and far away from absorption lines of the material [58].

- Furthermore, the susceptibilities are commonly assumed to not depend on the spatial coordinate $\boldsymbol{r} = [x \;\; y \;\; z]^\mathrm{T}$, meaning that the material is *homogeneous*[1]. This assumption is usually fulfilled if the spatial regions in which the dielectric is present are sufficiently large compared to the characteristic length scales over which the electric field is of relevant strength and when boundary effects are negligible.

- In the model used in the context of this work, the susceptibilities are additionally assumed to be real-valued. As a consequence, the described material is lossless [56, 59, 60]. This is justified if the material described by the model is transparent to the relevant frequencies [61, 62].

Ultimately, these assumptions mean that the polarization $\boldsymbol{P}$ depends only on the local (same-place) and current[2] (same-time) electric field $\boldsymbol{E}$.

The polarization $\boldsymbol{P}$, the electric field $\boldsymbol{E}$ and the displacement field $\boldsymbol{D}$ are connected via [32, 56, 57]:

$$\boldsymbol{D}(\boldsymbol{r}, t) = \varepsilon_0 \boldsymbol{E}(\boldsymbol{r}, t) + \boldsymbol{P}(\boldsymbol{r}, t). \tag{2.2}$$

Using Eq. (2.1), this expression may be rewritten as:

$$D_j = \sum_{n \geq 1} \sum_{k_1, \ldots, k_n} \varepsilon^{(n)}_{j k_1 \ldots k_n} E_{k_1} \cdots E_{k_n}, \tag{2.3}$$

where the permittivity tensors are $\underline{\varepsilon}^{(1)} = \varepsilon_0 \left(I_3 + \underline{\chi}^{(1)}\right)$, with I_3 being the 3×3 identity matrix, and $\underline{\varepsilon}^{(n)} = \varepsilon_0 \underline{\chi}^{(n)}$ for $n \geq 2$.

In general, for nonlinear, nonmagnetic media, the electromagnetic energy H contained in the spatial region occupied by the dielectric can be written in the form [57, 58, 63–65]:

$$H = \int \mathrm{d}^3 r \left(\frac{|\boldsymbol{B}|^2}{2\mu_0} + \int_0^{\boldsymbol{D}} \boldsymbol{E}(\boldsymbol{D}') \cdot \mathrm{d}\boldsymbol{D}' \right), \tag{2.4}$$

where $\boldsymbol{B}$ is the magnetic field, the spatial integral is over the region occupied by the dielectric and where the electric field has been written as a function of the displacement field. Generally, the value of the line integral over $\boldsymbol{D}'$ depends on the exact path taken from $\boldsymbol{D}' = 0$ to $\boldsymbol{D}' = \boldsymbol{D}$, which can lead to hysteresis effects [65]. However, if the susceptibility tensors $\underline{\chi}^{(n)}$ and therefore also the permittivity tensors $\underline{\varepsilon}^{(n)}$ have full permutation symmetry,

[1] This must not be confused with *isotropic* materials in which the nonlinear response is independent of the direction of the polarization of the electric field.

[2] More generally, $P_i(\boldsymbol{r}, t)$ may depend on $\boldsymbol{E}$ at all previous times $t' < t$ (*temporal* or *frequency dispersion*) and on all other spatial coordinates $\boldsymbol{r}'$ (*spatial dispersion*) [56, 60]. This is however beyond the scope of this work.

the line integral is path-independent and evaluating it using Eq. (2.3) results in[3] [57, 63]:

$$H = \int \mathrm{d}^3 r \left(\frac{|\boldsymbol{B}|^2}{2\mu_0} + \sum_{n\geq 1} \frac{n}{n+1} \sum_{j,k_1,\ldots,k_n} \varepsilon^{(n)}_{jk_1\ldots k_n} E_j E_{k_1} \cdots E_{k_n} \right). \tag{2.5}$$

The first-order term ($n = 1$), as it also appears in linear optics, reads

$$H^{(1)} = \frac{1}{2} \int \mathrm{d}^3 r \left(\frac{|\boldsymbol{B}|^2}{\mu_0} + \boldsymbol{E} \cdot \underline{\varepsilon}^{(1)} \cdot \boldsymbol{E} \right). \tag{2.6}$$

If the dielectric additionally is isotropic, meaning that the polarization response does not depend on the spatial direction of the electric field, the permittivity can be treated as a scalar $\varepsilon^{(1)}$. Then, Eq. (2.6) further simplifies to the well-known expression for the electromagnetic energy in vacuum or in linear isotropic media [32, 33, 56–58, 64, 65]:

$$H^{(1)}_{\mathrm{iso}} = \int \mathrm{d}^3 r \left(\frac{|\boldsymbol{B}|^2}{2\mu_0} + \varepsilon^{(1)} \frac{|\boldsymbol{E}|^2}{2} \right). \tag{2.7}$$

The second-order energy contribution [$n = 2$ in Eq. (2.5)] will form the interaction Hamiltonian for parametric down-conversion, as will be explained in Sec. 2.3. The contribution is given by

$$H^{(2)} = \frac{2}{3} \varepsilon_0 \int \mathrm{d}^3 r \sum_{j,k,l} \chi^{(2)}_{jkl} E_j E_k E_l \,. \tag{2.8}$$

As noted earlier, higher-order nonlinear contributions above the second order will be neglected in this work, since the interactions that they describe will be neglected.

An important requirement for a material to have a nonzero $\underline{\chi}^{(2)}$ susceptibility is that it is non-centrosymmetric, or in other words, it must not be inversion-symmetric [56]. For a material with inversion symmetry, both the second-order polarization components $P^{(2)}_j = \varepsilon_0 \sum_{k,l} \chi^{(2)}_{jkl} E_k(\boldsymbol{r}, t)\, E_l(\boldsymbol{r}, t)$ from Eq. (2.1) and the electric field components E_j change their sign when the coordinate system is inverted ($\boldsymbol{r} \to -\boldsymbol{r}$). However, since the electric field enters $P^{(2)}_i$ twice, this can clearly only hold when $P^{(2)}_i = 0$. Since this must hold for any P_j and E_j, it follows that $\underline{\chi}^{(2)} = \underline{0}$ for centrosymmetric materials [66].

Accordingly, the second order susceptibility also vanishes for isotropic dielectrics [62] since they are necessarily inversion-symmetric and therefore, bulk dielectrics used for PDC are necessarily anisotropic. Generally, in anisotropic dielectrics, the polarization response depends on the direction of the electric field and as a consequence, their refractive indices also have a directional dependence. One particular example for anisotropic materials are *uniaxial* crystals which are crystals that have a special symmetry axis called the *optic axis*

[3] This can be seen by first integrating by parts, so that $\int_0^{\boldsymbol{D}} \boldsymbol{E} \cdot \mathrm{d}\boldsymbol{D}' = \boldsymbol{E} \cdot \boldsymbol{D} - \int_0^{\boldsymbol{E}} \boldsymbol{D} \cdot \mathrm{d}\boldsymbol{E}'$, see Drummond and Hillery [57]. Then, the function $\mathcal{G}(\boldsymbol{E}') = \sum_n \frac{1}{n+1} \sum_{j,k_1,\ldots,k_n} \varepsilon^{(n)}_{jk_1\ldots k_n} E'_j E'_{k_1} \cdots E'_{k_n}$ is a potential function for the line integral $\int_0^{\boldsymbol{E}} \boldsymbol{D} \cdot \mathrm{d}\boldsymbol{E}'$. This can be seen by forming the total differential $\mathrm{d}\mathcal{G}(\boldsymbol{E}') = \sum_l \left[\partial \mathcal{G}(\boldsymbol{E}') / \partial E'_l\right] \mathrm{d}E'_l$ and using the full permutation symmetry, which implies that all resulting terms from the product rule are equal. Thus, $\int_0^{\boldsymbol{E}} \boldsymbol{D} \cdot \mathrm{d}\boldsymbol{E}' = \mathcal{G}(\boldsymbol{E})$ since $\mathcal{G}(\boldsymbol{0}) = 0$.

along which the refractive index differs from the directions perpendicular to it. For each wave vector $\boldsymbol{k}$ corresponding to the direction of travel of a plane wave, these crystals allow for the propagation of two fundamentally different orthogonally polarized plane waves[4]: Waves polarized in the *ordinary* polarization direction experience the ordinary refractive index n_o, while those waves polarized in any other *extraordinary* direction experience a refractive index n_x which depends on the angle θ between the wave vector $\boldsymbol{k}$ and the optic axis [56, 60, 67]:

$$n_x(\theta) = \left(\frac{\sin^2(\theta)}{n_e^2} + \frac{\cos^2(\theta)}{n_o^2} \right)^{-\frac{1}{2}}, \tag{2.9}$$

where n_e is the *extraordinary refractive index*[5] [67]. For plane waves propagating along the optic axis, both polarization directions experience the ordinary refractive index. Uniaxial crystals are further divided into *positive uniaxial* crystals, where $n_e > n_o$ and *negative uniaxial* crystals, where $n_e < n_o$ [56, 67].

2.2. The Quantized Electric Field

When transitioning from classical optics to quantum optics, the mathematical description of the electric field changes from it being described by continuous scalar-valued variables to field operators which act on field states. For a cuboidal cavity with side lengths L_x, L_y and L_z and periodic boundary conditions, the electric field operator takes the form [32, 58, 61, 64, 68]:

$$\hat{\boldsymbol{E}}(\boldsymbol{r}, t) = \mathrm{i} \sum_{\boldsymbol{k},\nu} \sqrt{\Delta k}\, \mathcal{E}_\nu(\boldsymbol{k}) \left[\hat{a}_{\boldsymbol{k}\nu} \boldsymbol{e}_{\boldsymbol{k}\nu} \mathrm{e}^{\mathrm{i}[\boldsymbol{k}\cdot\boldsymbol{r} - \omega_\nu(\boldsymbol{k})t]} - \hat{a}^\dagger_{\boldsymbol{k}\nu} \boldsymbol{e}^*_{\boldsymbol{k}\nu} \mathrm{e}^{-\mathrm{i}[\boldsymbol{k}\cdot\boldsymbol{r} - \omega_\nu(\boldsymbol{k})t]} \right], \tag{2.10}$$

where [32, 64]

$$\mathcal{E}_\nu(\boldsymbol{k}) = \frac{1}{\sqrt{(2\pi)^3}} \sqrt{\frac{\hbar \omega_\nu(\boldsymbol{k})}{2\varepsilon_0}} \tag{2.11}$$

is a constant which depends on the wave vector

$$\boldsymbol{k} = 2\pi \begin{bmatrix} \frac{m_x}{L_x} \\ \frac{m_y}{L_y} \\ \frac{m_z}{L_z} \end{bmatrix}, \qquad \text{for } m_x, m_y, m_z \in \mathbb{Z}, \tag{2.12}$$

of the plane-wave mode and ν labels the two polarization directions for each $\boldsymbol{k}$. With the volume $V = L_x L_y L_z$ of the cavity, the volume of the cells of the $\boldsymbol{k}$-grid spanned by $\boldsymbol{k}$ as

[4] Generally, the directions of the electric field vector for the two orthogonal polarization directions depends on the wave vector $\boldsymbol{k}$.

[5] Depending on the literature, n_e may also be more formally called the *principal value of the extraordinary refractive index* [56]. For brevity, it is just referred to as the *extraordinary refractive index* in this work, but must not be confused with $n_x(\theta)$ as given in Eq. (2.9).

defined in Eq. (2.12) is given by[6]

$$\Delta k = \frac{(2\pi)^3}{V}. \tag{2.13}$$

Furthermore, in Eq. (2.10), $\boldsymbol{e}_{\boldsymbol{k}\nu}$ denotes the (in general complex-valued) polarization unit vector for the plane wave with wave vector $\boldsymbol{k}$ and polarization direction ν and $\boldsymbol{e}^*_{\boldsymbol{k}\nu}$ denotes its element-wise complex conjugate. Generally, complex-valued polarization unit-vectors can for example be used to describe circularly polarized waves, while real-valued polarization unit vectors describe linearly polarized waves [64]. The plane-wave annihilation (creation) operators $\hat{a}^{(\dagger)}_{\boldsymbol{k}\nu}$ fulfill the commutation relations

$$[\hat{a}_{\boldsymbol{k}\nu}, \hat{a}_{\boldsymbol{k}'\nu'}] = 0, \tag{2.14a}$$
$$[\hat{a}^\dagger_{\boldsymbol{k}\nu}, \hat{a}^\dagger_{\boldsymbol{k}'\nu'}] = 0, \tag{2.14b}$$
$$[\hat{a}_{\boldsymbol{k}\nu}, \hat{a}^\dagger_{\boldsymbol{k}'\nu'}] = \delta_{\nu\nu'}\delta_{\boldsymbol{k}\boldsymbol{k}'}. \tag{2.14c}$$

The dispersion relation connecting the frequency and the modulus of the wave vector is given by [60]:

$$\omega_\nu(\boldsymbol{k}) = \frac{c_0}{n_\nu(\boldsymbol{k})}|\boldsymbol{k}|, \tag{2.15}$$

where c_0 is the speed of light (phase velocity of light) in vacuum and $n_\nu(\boldsymbol{k})$ is the refractive index associated with the polarization direction ν and wave vector $\boldsymbol{k}$. The wave-vector modulus is connected to the vacuum wavelength via $\lambda^{\text{vac}} = 2\pi/|\boldsymbol{k}|$. Furthermore, in the case of the vacuum, $\omega^{\text{vac}} = c_0|\boldsymbol{k}|$.

The expression for the electric field operators in Eq. (2.10) is obtained by starting at Maxwell's equations and performing a plane-wave expansion of either the vector potential [32, 61, 64] or directly of the electric field [33]. Afterwards, the expression for the energy of the electromagnetic field given in Eq. (2.7) is used to identify each field mode with a harmonic oscillator. The canonical momentum and position variables of each oscillator are then replaced by operators in the canonical quantization procedure, leading to the electric field operator as given in Eq. (2.10) above and a Hamiltonian of the form [32]:

$$\hat{H}_0 = \sum_{\boldsymbol{k},\nu} \hbar\omega_\nu(\boldsymbol{k}) \left(\hat{N}_{\boldsymbol{k}\nu} + \frac{1}{2}\right), \tag{2.16}$$

where

$$\hat{N}_{\boldsymbol{k}\nu} = \hat{a}^\dagger_{\boldsymbol{k}\nu}\hat{a}_{\boldsymbol{k}\nu} \tag{2.17}$$

is the photon number operator for the mode $(\boldsymbol{k}, \nu)$. For each field mode $(\boldsymbol{k}, \nu)$, the Hamiltonian corresponds to a quantum harmonic oscillator and, overall, all modes are uncoupled (the Hamiltonian is diagonal in terms of the plane wave modes). This is why in the following, this Hamiltonian and the corresponding field operators in Eq. (2.10) will

[6] This cell volume Δk should not be confused with the vectorial and scalar phase mismatches $\Delta\boldsymbol{k}$ and Δk introduced in Sec. 2.3.1 below. For better distinction, the Delta is italicized for the cell volume.

be referred to as the *free-field Hamiltonian* and the *free-field* operators, respectively, even though the presence of the refractive index in the dispersion relation in Eq. (2.15) implies coupling of the electric field to matter. This is justified by the fact that the field operators and the Hamiltonian have the same structure as in the case of the quantization in vacuum.

In many cases, it is useful to take the continuous limit[7] $V \to \infty$, which implies that the quantization box is extended over all space. This is usually useful if the regions over which the field is quantized are large. Then, the sum over the wave vectors in the expression for the electric field operator [Eq. (2.10)] is replaced with an integral according to the rule [33]

$$\Delta k \sum_{\boldsymbol{k}} \xrightarrow{V\to\infty} \int \mathrm{d}^3 k, \tag{2.18a}$$

while also replacing the plane-wave operators for the discrete wave-vector spacing with their continuous forms according to

$$\frac{1}{\sqrt{\Delta k}} \hat{a}_{\boldsymbol{k}\nu} \xrightarrow{V\to\infty} \hat{a}_\nu(\boldsymbol{k}), \tag{2.18b}$$

so that they fulfill the commutation relations [1, 32]

$$[\hat{a}_\nu(\boldsymbol{k}), \hat{a}_{\nu'}(\boldsymbol{k}')] = 0, \tag{2.19a}$$
$$[\hat{a}^\dagger_\nu(\boldsymbol{k}), \hat{a}^\dagger_{\nu'}(\boldsymbol{k}')] = 0, \tag{2.19b}$$
$$[\hat{a}_\nu(\boldsymbol{k}), \hat{a}^\dagger_{\nu'}(\boldsymbol{k}')] = \delta_{\nu\nu'}\delta(\boldsymbol{k}-\boldsymbol{k}'), \tag{2.19c}$$

which are the continuous-case versions of Eqs. (2.14a)–(2.14c), respectively. Then, in the continuous limit, the electric field operator from Eq. (2.10) becomes [5, 32, 69]:

$$\hat{\boldsymbol{E}}(\boldsymbol{r},t) = \mathrm{i}\sum_\nu \int \mathrm{d}^3 k\, \mathcal{E}_\nu(\boldsymbol{k}) \left[\hat{a}_\nu(\boldsymbol{k})\, \boldsymbol{e}_{\boldsymbol{k}\nu} \mathrm{e}^{\mathrm{i}[\boldsymbol{k}\cdot\boldsymbol{r}-\omega_\nu(\boldsymbol{k})t]} - \hat{a}^\dagger_\nu(\boldsymbol{k})\, \boldsymbol{e}^*_{\boldsymbol{k}\nu} \mathrm{e}^{-\mathrm{i}[\boldsymbol{k}\cdot\boldsymbol{r}-\omega_\nu(\boldsymbol{k})t]}\right]. \tag{2.20}$$

This expression can be split into the positive and negative frequency parts [32]:

$$\hat{\boldsymbol{E}}(\boldsymbol{r},t) = \hat{\boldsymbol{E}}^{(+)}(\boldsymbol{r},t) + \hat{\boldsymbol{E}}^{(-)}(\boldsymbol{r},t), \tag{2.21a}$$

where the negative part is given by

$$\hat{\boldsymbol{E}}^{(-)}(\boldsymbol{r},t) = -\mathrm{i}\sum_\nu \int \mathrm{d}^3 k\, \mathcal{E}_\nu(\boldsymbol{k})\, \boldsymbol{e}_{\boldsymbol{k}\nu} \mathrm{e}^{-\mathrm{i}[\boldsymbol{k}\cdot\boldsymbol{r}-\omega_\nu(\boldsymbol{k})t]} \hat{a}^\dagger_\nu(\boldsymbol{k}) \tag{2.21b}$$

and the positive part, evolving in time as[8] $\mathrm{e}^{-\mathrm{i}\omega_\nu(\boldsymbol{k})t}$, is its hermitian conjugate[9]:

$$\hat{\boldsymbol{E}}^{(+)}(\boldsymbol{r},t) = \left[\hat{\boldsymbol{E}}^{(-)}(\boldsymbol{r},t)\right]^\dagger. \tag{2.21c}$$

[7] This limit is to be understood in the sense that $L_j \to \infty$, for $j = x, y, z$.

[8] The convention that the *positive* frequency part oscillates with a *negative* sign in the exponent originates from the sign convention of the Fourier transform, where the integral transforming a function from the frequency domain to the temporal domain has a negative sign in the exponent, see Glauber [70].

[9] The hermitian conjugation † is here understood to act on the unit polarization vector only as element-wise complex conjugation: $\boldsymbol{e}^\dagger_{\boldsymbol{k}\nu} = \boldsymbol{e}^*_{\boldsymbol{k}\nu}$.

Splitting the field operator this way is convenient because $\hat{\boldsymbol{E}}^{(+)}(\boldsymbol{r},t)$ and $\hat{\boldsymbol{E}}^{(-)}(\boldsymbol{r},t)$ only contain plane-wave annihilation and creation operators, respectively. This will become useful in Sec. 2.3.2 to analyze the structure of the PDC interaction Hamiltonian.

2.3. Parametric Down-Conversion

2.3.1. General Introduction and Phase-Matching Considerations

Parametric down-conversion (PDC) is a nonlinear optical process induced by the $\underline{\chi}^{(2)}$-nonlinearity of a material in which a photon of a strong light beam (the *pump*) splits into two photons of lower energy called the *signal* and *idler* photons [61, 64, 71–73]. Regarding the convention of which of the generated photons is called signal and which one idler, Boyd [56] suggests that the photon at the "wanted" frequency which is the main focus of the experiment is called the signal, while Loudon [61] suggests that the higher frequency photon is called the signal by convention. The effect can be loosely divided into two regimes, depending on the *parametric gain*, which is a measure for the strength of the nonlinear interaction and the amount of signal-idler radiation that is generated: In the *low-gain regime*, only a few signal and idler photons are generated, and their field amplitudes grow proportionally to the pump amplitude. In contrast, in the *high-gain regime*, this growth becomes exponential [71]. For very low gain, the decay of pump photons into signal-idler pairs occurs spontaneously, which is why in this regime, the process is also referred to as *spontaneous parametric down-conversion* (SPDC) [74].

One way of understanding PDC is as *stimulated emission* induced by the random fluctuations of the quantum vacuum [75]. This observation directly leads to *bright squeezed vacuum* states of light: The light state generated by PDC is essentially quantum vacuum amplified in a parametric process [75] and for high parametric gain, this state becomes macroscopic (that is, it contains many photons), while still showing quantum properties such as entanglement [5, 76]. Similarly, Kulkarni *et al.* [71] have successfully modelled SPDC as a classical difference-frequency generation process, where the vacuum fluctuations are included via a (classical) stochastic seed field.

The PDC process requires that the total linear momentum is conserved, meaning that the wave vectors of the three photons are connected via [77]

$$\boldsymbol{k}_p = \boldsymbol{k}_s + \boldsymbol{k}_i\,, \tag{2.22}$$

where p, s and i label the pump, signal and idler wave-vector, respectively. This labeling of the three subsystems will continue throughout this work. The ideal condition described by Eq. (2.22) is called *perfect phase matching* and is generally difficult to achieve, if not impossible. However, signal and idler photons will still be generated even if this relation does not hold exactly due to a momentum-uncertainty introduced by the finite size of the interaction region along the $\boldsymbol{k}_p$ direction (the *longitudinal* or *collinear* direction), leading

to the definition of the wave-vector mismatch [32, 56, 74, 77, 78]:

$$\Delta \boldsymbol{k} = \boldsymbol{k}_p - \boldsymbol{k}_s - \boldsymbol{k}_i \,. \tag{2.23}$$

For $\Delta \boldsymbol{k} \neq \boldsymbol{0}$, the efficiency of the nonlinear process is generally strongly reduced, as will be seen below for a special case. A common assumption is that the system has infinite transverse size perpendicular to $\boldsymbol{k}_p$, based on the fact that the pump beam area is small compared to the system size [5, 11, 72]. In this case, the transverse wave-vector components[10] $\boldsymbol{q}$ perpendicular to $\boldsymbol{k}_p$ are conserved exactly [74], so that $\boldsymbol{q}_p = \boldsymbol{q}_s + \boldsymbol{q}_i$.

Analogously to the conservation of momentum, the PDC process must also conserve the photon energy, meaning that for *perfect frequency matching*, the frequencies of the three photons partaking in the process are connected via

$$\omega_p = \omega_s + \omega_i \,. \tag{2.24}$$

In the special case of $\omega_s = \omega_i$, the PDC process is said to be *frequency-degenerate* [14, 42]. Similar to the wave-vector mismatch as defined in Eq. (2.23), a finite interaction time leads to the definition of the *frequency mismatch* [5, 79]

$$\Delta\omega = \omega_p - \omega_s - \omega_i \,. \tag{2.25}$$

It should be noted that for the electric field operators as written in Eq. (2.20), the frequency mismatch would be a function of the pump, signal and idler wave-vectors.

In general, as mentioned above, it is virtually impossible to achieve perfect phase matching $\Delta \boldsymbol{k} = \boldsymbol{0}$ for all spatial directions. Therefore, the focus is generally on achieving optimal phase matching for particular emission directions. One such example is perfectly *collinear phase matching*, where, as the name implies, the three wave vectors of the pump, signal and idler waves lie parallel[11] ($\boldsymbol{k}_p \uparrow\!\uparrow \boldsymbol{k}_s \uparrow\!\uparrow \boldsymbol{k}_i$) and the signal and idler photons travel along the pump direction [72]. Since all three wave vectors lie in parallel, Eq. (2.23) may be reduced to a scalar expression, since only the moduli of the three wave vectors are relevant for the phase mismatch:

$$\Delta k = |\boldsymbol{k}_p| - |\boldsymbol{k}_s| - |\boldsymbol{k}_i| \,. \tag{2.26}$$

The importance of minimizing Δk can be seen from the fact that the intensity I of the signal and idler radiation usually scales as [72]

$$I \propto \operatorname{sinc}^2\!\left(\frac{L\Delta k}{2}\right), \tag{2.27}$$

where the sinc-function is defined as

$$\operatorname{sinc}(x) = \frac{\sin(x)}{x} \,, \tag{2.28}$$

[10] More precisely, the momenta associated with the transverse wave-vector components are conserved exactly.
[11] The symbol $\uparrow\!\uparrow$ denotes parallel vectors, while $\uparrow\!\downarrow$ denotes antiparallel vectors.

meaning that for $\Delta k > 0$, the PDC process becomes less efficient. This behavior can also be recovered analytically for the quantum optical description of low-gain PDC as for example shown by Sharapova *et al.* [11] and Christ *et al.* [80]. Analogously, as argued by Christ [79], a nonzero frequency mismatch $\Delta\omega \neq 0$ will also lead to a reduction in the efficiency of the process. It is worth noting that generally, in the context of collinear phase matching, the relevant wave vectors not only include those triplets fulfilling $\boldsymbol{k}_p \uparrow\uparrow \boldsymbol{k}_s \uparrow\uparrow \boldsymbol{k}_i$ precisely, but also those that slightly deviate from the $\boldsymbol{k}_p$-direction, due to the fact that, as mentioned above, PDC radiation will still be generated with a nonzero phase-mismatch. This leads to more involved mathematical descriptions, where the angles between the emitted photons must be considered or the wave-vector components $\boldsymbol{q}$ must be considered to be nonzero. This will be the case throughout the rest of this work. Ultimately, perfect phase matching with $\delta k = 0$ will then generally only hold for the collinear direction.

The expression for the collinear phase mismatch given in Eq. (2.26) can be further rewritten using the dispersion relation for linear media as written in Eq. (2.15) [81]. Then, assuming perfect frequency matching as in Eq. (2.24), the expression for the collinear phase mismatch takes the form

$$\Delta k = \frac{1}{c_0}\left[\left(n_p - n_s\right)\omega_s + \left(n_p - n_i\right)\omega_i\right]. \tag{2.29}$$

Here and in the following, the dependence of the refractive index on the frequency is implied by the subscript and will not be written out explicitly as a frequency argument for readability. Following the argument of Boyd [56], it is easy to see that $\Delta k = 0$ is difficult to achieve in isotropic media due to dispersion: If the refractive index $n(\omega)$ is an increasing function of the frequency, and $\omega_p > \omega_s$ and $\omega_p > \omega_i$, then $n_p - n_s > 0$ and $n_p - n_i > 0$, meaning $\Delta k > 0$. However, for anisotropic uniaxial crystals as described in Sec. 2.1, there are several possible configurations available to achieve $\Delta k = 0$, since the refractive index of the extraordinary waves can be tuned by cutting and rotating the crystal appropriately [see Eq. (2.9)] to achieve the refractive index required for the phase-matching condition [56, 72]. This phase-matching method is called *angle tuning* [56] and will be adopted for the rest of this work.

Correspondingly, the nonlinear material assumed for the theoretical descriptions in the rest of this work is β-Barium borate (BBO, β-BaB_2O_4), which is a negative uniaxial crystal [32, 82]. To achieve phase matching, the polarization direction of the pump beam is aligned with the extraordinary polarization direction, while the polarization directions of the signal and idler radiation can be so that they are either both ordinary (*type-I phase matching*) or ordinary and extraordinary (*type-II phase matching*) [56, 72].

Following Eq. (2.9), the refractive index experienced by the pump can then be tuned by changing θ, so that[12] $n_{pe} \leq n_p(\theta) \leq n_{po}$. Combining Eqs. (2.9) and (2.29) yields a formula

[12] In general, this alone does not guarantee that there exists a value of θ so that $\Delta k = 0$. More precisely, Eqs. (2.30)–(2.32), may give a purely imaginary value for θ. Whether a real-valued solution for the phase-matching angle exists depends on the concrete values of the ordinary and extraordinary refractive index at the pump, signal and idler frequencies. [56]

for the phase-matching angle θ:

$$\theta = \arcsin\left(\sqrt{\frac{\left(\frac{\omega_s+\omega_i}{n_s\omega_s+n_i\omega_i}\right)^2 - \frac{1}{n_{po}^2}}{\frac{1}{n_{pe}^2} - \frac{1}{n_{po}^2}}}\right). \tag{2.30}$$

For the frequency-degenerate case ($\omega_s = \omega_i$), this simplifies to

$$\theta = \arcsin\left(\sqrt{\frac{\frac{4}{(n_s+n_i)^2} - \frac{1}{n_{po}^2}}{\frac{1}{n_{pe}^2} - \frac{1}{n_{po}^2}}}\right), \tag{2.31}$$

which, for type-I phase matching with $n_s = n_i = n_{sio}$, can again be further simplified to

$$\theta = \arcsin\left(\sqrt{\frac{\frac{1}{n_{sio}^2} - \frac{1}{n_{po}^2}}{\frac{1}{n_{pe}^2} - \frac{1}{n_{po}^2}}}\right). \tag{2.32}$$

Unsurprisingly, Eq. (2.32) has a similar structure to the expressions for the phase-matching angle for *second-harmonic generation* (SHG) found in Boyd [56]. In principle, SHG is the opposite nonlinear process of degenerate PDC: Two signal (idler) photons at frequency ω_s combine to form a pump photon at frequency $\omega_p = 2\omega_s$ (the second harmonic). The reason for this similarity is that the phase-matching conditions for both processes are the same. Furthermore, as will be seen in Sec. 2.3.2, the Hamiltonian describing the PDC process is the hermitian conjugate of the Hamiltonian describing SHG.

The wavelength of the pump laser used in the theoretical investigations and experiments connected to this work is 354.6 nm (third harmonic of an Nd:YAG laser) [1–3]. Plugging this into the *Sellmeier equations* found for BBO in Eimerl *et al.* [82] yields $n_{po} = 1.7056$ and $n_{pe} = 1.5776$ and, for frequency degenerate PDC, $n_{sio} = 1.6645$ and $n_{sie} = 1.5482$. Hence, for $\omega_s = \omega_i$, the phase-matching angle is $\theta = 32.955°$ for type-I phase matching, which coincides with the value found by Kulkarni *et al.* [71], and $\theta = 60.257°$ for type-II phase matching. Equation (2.29) also implies that for perfect frequency-degenerate type-I phase matching, where $\Delta k = 0$ (near the collinear direction) and the photons are completely indistinguishable, the three refractive indices coincide: $n_p(\theta) = n_{so} = n_{io}$.

2.3.2. The PDC Hamiltonian

Parametric down-conversion is commonly described by introducing an interaction Hamiltonian derived from the second-order energy contribution of the electric field as given in Eq. (2.8), as already mentioned in Sec. 2.1 [68, 83]. To this end, the electric field vectors entering the Hamiltonian in Eq. (2.8) in the tensor product with the second-order susceptibility are replaced with the electric field operators discussed in Sec. 2.2. Hence, the initial expression for the resulting PDC interaction Hamiltonian $\hat{H}_I$ is then given by [58]

$$\hat{H}_I = \frac{2}{3}\varepsilon_0 \int \mathrm{d}^3 r \sum_{j,k,l} \chi^{(2)}_{jkl} \hat{E}_j \hat{E}_k \hat{E}_l \,. \tag{2.33}$$

It should be noted that in the model described in the following, the electric field operators in Eq. (2.33) above are the free-field electric field operators. Thus, this description of PDC assumes that the nonlinearity and the PDC interaction are sufficiently small to not influence the quantization procedure leading to the free-field electric field operator expressions written in Eq. (2.10) [61, 64].

Following Harder [58], the electric field in PDC is the superposition of the pump, signal and idler field:

$$\hat{\boldsymbol{E}}(\boldsymbol{r},t) = \hat{\boldsymbol{E}}_p(\boldsymbol{r},t) + \hat{\boldsymbol{E}}_s(\boldsymbol{r},t) + \hat{\boldsymbol{E}}_i(\boldsymbol{r},t). \tag{2.34}$$

For readability, the spatial and temporal dependence is not explicitly written out in the following. Furthermore, it is assumed that the field operators $\hat{\boldsymbol{E}}_p$, $\hat{\boldsymbol{E}}_s$ and $\hat{\boldsymbol{E}}_i$ commute.

Plugging the expression for the electric field operator given in Eq. (2.34) into the Hamiltonian in Eq. (2.33) and expanding out the parentheses leads to $3^3 = 27$ summands, some of which are equal due to the full permutation symmetry of $\chi^{(2)}_{jkl}$, as described in Sec. 2.1:

1. There are three terms of the form $\hat{E}_{j,m}\hat{E}_{k,m}\hat{E}_{l,m}$, where $m = p, s, i$.

2. There are six terms of the form $\hat{E}_{j,m}\hat{E}_{k,m}\hat{E}_{l,m'}$, $m \neq m'$, each of which has three equivalent permutations for j, k and l, which means there are $3 \times 6 = 18$ terms overall where one field enters twice.

3. Finally, there are six terms $\hat{E}_{j,m}\hat{E}_{k,m'}\hat{E}_{l,m''}$, where m, m' and m'' are distinct.

For *degenerate PDC*, where the signal and idler photons are fully indistinguishable [61] (meaning $\hat{\boldsymbol{E}}_s = \hat{\boldsymbol{E}}_i$), some contributions mentioned above will coincide. One particular example are the terms of the form $\hat{E}_{j,p}\hat{E}_{k,m}\hat{E}_{l,m'}$, for $m, m' = s, i$, listed in both Items 2 and 3 above, which will then be identical since the labels s and i are equivalent. This leads to the definition of the constant

$$\mathcal{D}_{si} \overset{\text{def.}}{=} \begin{cases} 1, & \text{for non-degenerate PDC} \\ 2, & \text{for degenerate PDC} \end{cases} \tag{2.35}$$

to account for the different prefactors in both cases, which will be used below two write both cases in a single expression.

By splitting the electric field operators of these terms into their positive and negative frequency parts, as seen in Eq. (2.21a), it is possible to exclude numerous contributions from the Hamiltonian. The resulting expressions are of the form $\hat{E}^{(\pm)}_{j,m_1}\hat{E}^{(\pm)}_{k,m_2}\hat{E}^{(\pm)}_{l,m_3}$, which describe certain interactions, depending on whether they contain the positive or negative frequency parts or, more precisely, annihilation or creation operators. They contain exponential terms of the form $\mathrm{e}^{\mathrm{i}\Delta\omega(\boldsymbol{k})t}$, where the form of the frequency mismatch $\Delta\omega(\boldsymbol{k})$ depends on the specific interaction. Since the evaluation of the system dynamics involves the integration of this exponential over the interaction time, the interaction is inefficient

for $\Delta\omega(\boldsymbol{k}) \neq 0$ due to the oscillations of the exponential term, as argued by Christ [79]. This can be easily seen for an infinitely long interaction time ranging from the asymptotic past $t \searrow -\infty$ to the asymptotic future $t \nearrow \infty$: The time integral over the exponential is then $\int_{-\infty}^{\infty} \mathrm{d}t\, \mathrm{e}^{\mathrm{i}\Delta\omega(\boldsymbol{k})t} = 2\pi\delta(\Delta\omega(\boldsymbol{k}))$, meaning that the interaction only takes place for $\Delta\omega(\boldsymbol{k}) = 0$, which is the condition for the conservation of the photon energy. Similarly, this has been found in Sharapova *et al.* [5] when evaluating the Heisenberg equations for the PDC process and in Karan *et al.* [72] and Christ [79] for the perturbation expansion of the PDC state. This observation justifies that terms of the form $\hat{E}^{(-)}_{j,m}\hat{E}^{(-)}_{k,m'}\hat{E}^{(-)}_{l,m''}$ and $\hat{E}^{(+)}_{j,m}\hat{E}^{(+)}_{k,m'}\hat{E}^{(+)}_{l,m''}$ can be neglected, since they describe[13] the energy-nonconserving creation and annihilation of photon-triplets without the annihilation or creation (respectively) of other particles (photons) [68]: Clearly, the frequency mismatch $\Delta\omega$ can never vanish in these cases since the frequencies must be positive and the temporal exponential functions of the three fields all have the same sign. Neglecting these terms corresponds to the *rotating-wave approximation* (RWA) [79].

All other terms contain both photon creation and annihilation operators and therefore describe different mixing processes of the three fields. Without further restrictions, all of these processes may occur. In experimental setups it is then possible to filter out certain frequencies of interest from the generated radiation. If done correctly, this allows for the selection of radiation that can only have been efficiently generated by certain interactions. For example, by filtering out frequencies close to $\omega_p/2$, the obtained radiation originates from frequency-degenerate PDC. It should be noted that this line of reasoning also requires the pump field and the band-pass filters are sufficiently narrowband. Furthermore, the phase-matching condition restricts which interactions can occur efficiently and therefore acts as another filtering mechanism.

Ultimately, after removing all terms as discussed above and accounting for the full permutation symmetry with the help of the constant defined in Eq. (2.35), only one term and its hermitian conjugate remain for the PDC Hamiltonian:

$$\hat{H}_{\mathrm{PDC}} = 4\mathcal{D}_{si}\varepsilon_0 \int \mathrm{d}^3 r \sum_{j,k,l} \chi^{(2)}_{jkl} \hat{E}^{(+)}_{j,p} \hat{E}^{(-)}_{k,s} \hat{E}^{(-)}_{l,i} + \mathrm{h.c.} \tag{2.36}$$

This Hamiltonian describes two processes: The term written out explicitly in the equation above describes the *actual* PDC process, where one pump photon is annihilated and a signal-idler photon pair is created. The hermitian conjugate term describes *sum-frequency generation* (SFG) or second-harmonic generation in the frequency-degenerate case, where a signal-idler photon pair is annihilated, and a pump photon is created. However, as also noted in Christ [79], both terms are required for the Hamiltonian to be hermitian and therefore, $\hat{H}_{\mathrm{PDC}}$ as written in Eq. (2.36) is usually used for the description of PDC.

[13] These processes can be seen as *virtual interactions*. On short time scales, these contributions appear due to the energy-time uncertainty and can serve as short-lived intermediate steps for more complex interactions, as for example described in Butcher and Cotter [84] for nonlinear optical processes and Peng and Li [85] for the rotating wave approximation in the context of atom-field coupling. However, as discussed in the text, the contributions from these terms disappear for long interaction times.

In experiments, the geometry of the setup can usually be assumed to be fixed. For example, only wave vectors of the three fields with certain directions may be of interest, while additionally, as described in Sec. 2.3.1, the polarization directions are determined by the phase-matching condition. This allows for further simplifications of the PDC Hamiltonian in Eq. (2.36), which still accounts for the full vectorial character of the electric field operators. More precisely, for certain geometries, the susceptibility tensor $\underline{\chi}^{(2)}$ can effectively be approximated by a scalar susceptibility $\chi^{(2)}_{\mathrm{eff}}$. As a consequence, the electric field operators can be treated as scalar-valued operators, see for example Sharapova *et al.* [5], Boyd [56], and Karan *et al.* [72]. With this simplification applied, the Hamiltonian now reads

$$\hat{H}_{\mathrm{PDC}} = 4\mathcal{D}_{si}\varepsilon_0\chi^{(2)}_{\mathrm{eff}} \int \mathrm{d}^3 r\, \hat{E}_p^{(+)} \hat{E}_s^{(-)} \hat{E}_i^{(-)} + \mathrm{h.c.}\,, \tag{2.37}$$

where the negative frequency parts of the field operators are of the form

$$\hat{E}_\nu^{(-)}(\boldsymbol{r}, t) = -\mathrm{i} \int \mathrm{d}^3 k\, \boldsymbol{\mathcal{E}}_\nu(\boldsymbol{k})\, \mathrm{e}^{-\mathrm{i}[\boldsymbol{k}\cdot\boldsymbol{r} - \omega_\nu(\boldsymbol{k})t]} \hat{a}_\nu^\dagger(\boldsymbol{k}), \qquad \text{for } \nu = p, s, i\,, \tag{2.38}$$

and the positive frequency parts are their hermitian conjugates, see Eq. (2.21c).

A rigorous expression for the scalar-valued effective susceptibility can be written as

$$\chi^{(2)}_{\mathrm{eff}} = \sum_{j,k,l} \chi^{(2)}_{jkl} \left(\boldsymbol{e}_{\boldsymbol{k}_p p}\right)_j \left(\boldsymbol{e}_{\boldsymbol{k}_s s}\right)_k \left(\boldsymbol{e}_{\boldsymbol{k}_i i}\right)_l, \tag{2.39}$$

where $\left(\boldsymbol{e}_{\boldsymbol{k}_\nu \nu}\right)_j$ denotes the jth component of the (here real-valued) unit polarization vector for the field ν. This expression can only be pulled out of the integrals over the wave vectors appearing in the electric field operators in Eq. (2.36), if only those plane-wave modes $(\boldsymbol{k}_\nu, \nu)$ have significant contributions to the Hamiltonian that have polarization vectors $\boldsymbol{e}_{\boldsymbol{k}_\nu \nu}$ compatible with the chosen $\chi^{(2)}_{\mathrm{eff}}$, so that the wave-vector dependence of the unit polarization vectors may be safely ignored. This is what the geometry of the experiment and the cut of the crystal have to ensure.

It is also important to note that the precise prefactor of the Hamiltonian, which for Eq. (2.37) would be $4\mathcal{D}_{si}\varepsilon_0\chi^{(2)}_{\mathrm{eff}}$ multiplied with potential additional prefactors resulting from the expressions for the pump, signal and idler fields, may differ, depending on the literature. This can be seen by comparing the prefactors of the initial expression for the second-order electromagnetic energy contribution [Eq. (2.8)] and the Hamiltonian derived from it [Eq. (2.33)] with the corresponding expressions used for example in Sharapova *et al.* [5], Boyd [56], Drummond and Hillery [57] and Quesada and Sipe [63]. The convention used in this work coincides with the one suggested in the latter two works. However, as described in Ref. [2], the choice of the value of this prefactor does not affect the results presented here and in the associated works (Refs. [1–4]) since they are based on the definition of the *experimental gain*, which will be elaborated on in Sec. 3.4.

Since the propagation axis of the pump beam usually defines a special axis in the system, it is useful to split the wave vectors into their longitudinal and transverse components, as

already described in Sec. 2.3.1. If the pump vector $\boldsymbol{k}_p$ is oriented along the z-axis, then the transverse wave-vector components of some wave vector $\boldsymbol{k}$ are $\boldsymbol{q} = \begin{bmatrix} k_x & k_y \end{bmatrix}^\mathsf{T} \overset{\text{def.}}{=} \begin{bmatrix} q_x & q_y \end{bmatrix}^\mathsf{T}$. The z-component k_z of the wave vector may then be expressed in terms of the transverse part $\boldsymbol{q}$ and the frequency ω_ν [2, 72]:

$$k_z(\boldsymbol{q}, \omega_\nu) = s \sqrt{\left(\frac{\omega_\nu n_\nu(\omega_\nu)}{c_0} \right)^2 - |\boldsymbol{q}|^2}\,, \tag{2.40}$$

where the dispersion relation as written in Eq. (2.15) has been used to express $|\boldsymbol{k}|^2$ in terms of the frequency ω_ν and where $s = \pm 1$ has been introduced to account for the sign of k_z which is otherwise lost. With this, the negative parts of the field operators can be expressed as [2, 72]:

$$\hat{E}_\nu^{(-)}(\boldsymbol{r}, t) = -\mathrm{i} \sum_{s=\pm 1} \iint \mathrm{d}^2 q \, \mathrm{d}\omega_\nu \, \mathcal{E}_\nu(\boldsymbol{q}, \omega_\nu) \, \mathrm{e}^{-\mathrm{i}[\boldsymbol{q}\cdot\boldsymbol{r}_\perp + s k_z(\boldsymbol{q}, \omega_\nu) z - \omega_\nu t]} \hat{a}_\nu^\dagger(\boldsymbol{q}, \omega_\nu), \tag{2.41}$$

where $\mathrm{d}^2 q = \mathrm{d}q_x \mathrm{d}q_y$, $\boldsymbol{r}_\perp = [x \;\; y]^\mathsf{T}$ and the integrals are over the entire two-dimensional transverse wave-vector plane and all $\omega_\nu \geq 0$. If only plane waves traveling in certain directions are of relevance, for example along the positive z-axis direction ($k_z > 0$), it may also be sufficient to only account for one of the signs (here $s = +1$). Additionally, it should be noted that the form of $\mathcal{E}_\nu$ appearing in Eq. (2.41) is not the same as in Eq. (2.21b) since $\mathrm{d}^3 k = |\partial\omega_\nu / \partial k_z| \mathrm{d}q_x \, \mathrm{d}q_y \mathrm{d}\omega_\nu$. For simplicity, the prefactor $\mathcal{E}_\nu$ is also usually assumed to be constant [2, 5, 72].

The PDC interaction Hamiltonian as given in Eq. (2.37) is commonly used in the literature in combination with the *undepleted pump approximation* (or *parametric approximation* [32]) where the pump field is assumed to be a strong and classical coherent field [1, 2, 5, 11, 69, 72, 79, 80, 86]. This is justified since the pump beam is usually very strong, meaning that it remains approximately unchanged if pump photons are down-converted to pairs of signal and idler photons. The field operator for the pump field can then be replaced by a scalar-valued function of the form [2, 5, 87]

$$E_p^{(+)}(\boldsymbol{r}, t) = \mathrm{i} \mathcal{E}_p \tilde{\alpha}_p(\boldsymbol{r}, t) \, \mathrm{e}^{\mathrm{i}(\boldsymbol{k}_p \cdot \boldsymbol{r} - \omega_p t)}\,, \tag{2.42}$$

where $\tilde{\alpha}_p(\boldsymbol{r}, t)$ is the (possibly complex-valued) spatio-temporal envelope function of the pump field and $\mathcal{E}_p$ is the pump amplitude. The imaginary unit i has been added as a prefactor to keep consistency with the expression for the operator $\hat{\boldsymbol{E}}^{(+)}$, see Eqs. (2.21b) and (2.21c).

Starting from the PDC Hamiltonian in Eq. (2.37) and the electric field operators as written in Eqs. (2.38) and (2.41), there are two main options for the theoretical description of PDC, which will be used in this work and discussed in more detail in the respective chapters:

1. By carefully manipulating the Heisenberg equations for the signal and idler plane-wave operators $\hat{a}_{\boldsymbol{k},s/i}$, Sharapova *et al.* [5] have arrived at sets of coupled *integro-differential*

equations that describe their evolution through the PDC section. This approach is rigorous and includes *time-ordering effects*, but the equations can generally be only integrated numerically for a finite-width pump. For a plane-wave pump, an analytical solution is possible [1, 88]. The approach leads to accurate results at both low and high gain. The details of this method will be explored further in Chapters 3 and 4.

2. A simpler approach, which allows for a more analytical treatment, is *Schmidt-mode theory*. In the context of this work, the focus will be on the description of this approach provided in Sharapova *et al.* [11]. Here, the dependence of the frequency mismatch as defined for PDC in Eq. (2.25) on the wave-vectors of the three fields is neglected, and as a result, the interaction Hamiltonian becomes time-independent [5]. For low parametric gain, the integro-differential equation approach and Schmidt-mode theory coincide, but at high gain they show discrepancies and Schmidt-mode theory agrees less well with experimental results. While in Sharapova *et al.* [11] only Gaussian pump beams are considered, the approach was later extended in Ref. [2] to *Laguerre-Gaussian* envelopes. This will be the main focus of Chapter 5.

For completeness, it should be mentioned that in the above-mentioned references, both approaches were described in the spatial domain, meaning that all relevant quantities are written in dependence on the wave vectors. However, it is also possible to apply these approaches in the frequency domain, see for example Christ *et al.* [80], Quesada *et al.* [86], and Sharapova *et al.* [87].

Furthermore, it should be noted that several recent studies have focused on relaxing certain simplifications contained in the model as presented in this section: When constructing the PDC interaction Hamiltonian in Eq. (2.33), the free-field expressions for the electric field operators in Eq. (2.20) are substituted for the electric field. As mentioned above, this makes sense if the interaction is sufficiently small. However, more rigorously, it is possible to perform the quantization directly for a nonlinear dielectric, see Drummond and Hillery [57]. Then, in order to obtain the correct equations of motion for the fields (Maxwell's equations) while preserving their transversality, it is necessary to choose the displacement field $\boldsymbol{D}$ (instead of the electric field $\boldsymbol{E}$) and the magnetic field (*magnetic flux density*) $\boldsymbol{B}$ as the canonical variables [57, 63]. This formalism has then for example been applied in Schneeloch *et al.* [89], for the description of the absolute brightness and number statistics of SPDC and, as already hinted at above, in Quesada *et al.* [86] for the derivation of integro-differential equations describing PDC in the frequency domain, which similar to those of Sharapova *et al.* [5] for the spatial domain (described above in Item 1).

3

Phase Sensitivity of High-Gain SU(1,1) Interferometers

This chapter will present the main results of Ref. [1], which is an investigation of the phase sensitivity of spatially multimode high-gain SU(1,1) interferometers. To this end, Sec. 3.1 will introduce SU(1,1) interferometers, which are central to the remainder of this work. Furthermore, in Sec. 3.2, the description of parametric down-conversion via integro-differential equations in the spatial domain developed in Sharapova *et al.* [5] will be extended to allow for an analytical description of certain aspects of the interferometers which are relevant for analyzing their phase sensitivity. Several additional important concepts will be introduced throughout Secs. 3.2–3.4, such as the joint Schmidt decomposition, which will be an important tool in the analysis of multimode squeezing in Chapter 4, and the concept of diffraction compensation, which is essential for the construction of high performance multimode SU(1,1) interferometers operating at high parametric gain.

3.1. SU(1,1) Interferometers and the Phase Sensitivity

SU(1,1) interferometers, as first described by Yurke *et al.* [16], are *nonlinear interferometers* utilizing parametric down-conversion to achieve better performance than *classical interferometers*, which are interferometers constructed from beam splitters and using *classical states* of light, most prominently coherent states [1, 9, 13]. In principle, there are several configurations possible for an SU(1,1) interferometer, as discussed in Chekhova and Ou [13]: In the simplest case, the mirrors of a classical Mach-Zehnder interferometer which split the laser beam into the two interferometer arms can be replaced by nonlinear crystals. A simplified sketch of such a setup for collinear PDC is shown in Fig. 3.1. The propagation of the light fields between the two crystals is described mathematically by an abstract *phase object* which applies phases ϕ_ν to the pump ($\nu = p$), signal ($\nu = s$) and idler ($\nu = i$) fields [1]. Generally, this phase may have some spatial dependence or, equivalently,

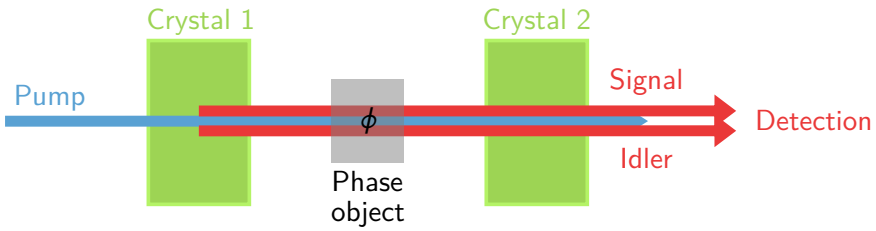

Figure 3.1: Simplified sketch of a Mach-Zehnder type [13] SU(1,1) interferometer for collinear PDC. The PDC radiation (signal and idler, marked with red arrows) generated in the first crystal acquires some phase (which possibly has some spatial or angular dependence) and is amplified and deamplified in the second crystal depending on the relative phase difference $\phi = \phi_p - \phi_s - \phi_i$ of the pump, signal and idler radiation. After the second crystal, the radiation, usually only the signal and idler fields, are sent to the detector and the pump beam is filtered out. More generally, it is also possible to have only some combination of the pump, signal and idler fields interact with the phase object, so that the phase is applied only to a subset of the three fields. Adapted from Ref. [1].

depend on the transverse wave-vector components $\boldsymbol{q}_\nu$, as introduced in Sec. 2.3.1. In the simplest case, this phase object is just given by the air gap between the two crystals. More concrete examples will be given in Sec. 3.3 when the concept of *diffraction compensation* is introduced. After the phase object, all three fields recombine in the second crystal and depending on the relative phase difference $\phi = \phi_p - \phi_s - \phi_i$, the signal and idler radiation will be amplified or deamplified (*nonlinear interference* [8]) in dependence on the transverse wave-vector components. After the second crystal, the PDC radiation is sent to the detector.

In quantum metrology, one central challenge is improving the sensitivity of measurements and determining fundamental bounds for parameter estimation [90, 91]. More precisely, the goal here is to determine with which accuracy the relative phase shift ϕ which the pump, signal and idler fields experience can be determined. This leads to the definition of the *phase sensitivity* $\Delta\phi$, which here is defined in terms of the total[1] output intensity $\langle \hat{N}_{\mathrm{tot}} \rangle$ via the error propagation relation as [6, 9, 10, 12, 32]:

$$\Delta\phi = \frac{\Delta N_{\mathrm{tot}}}{\left| \frac{\mathrm{d}\langle \hat{N}_{\mathrm{tot}} \rangle}{\mathrm{d}\phi} \right|}, \tag{3.1}$$

Here, $\hat{N}_{\mathrm{tot}}$ is the total (or *integral*) photon-number operator for the output radiation and

$$\Delta N_{\mathrm{tot}} = \sqrt{\langle \hat{N}_{\mathrm{tot}}^2 \rangle - \langle \hat{N}_{\mathrm{tot}} \rangle^2} \tag{3.2}$$

is the corresponding standard deviation. It should be emphasized that the quantity $\Delta\phi$ defined in Eq. (3.1) is the *standard deviation* (square root of the variance) or *error* associated with the phase measurement, as described around Eq. (3.1) [32]. This means that the

[1] In principle, it is not necessary to use the total output intensity for the phase sensitivity and instead filter certain (plane-wave) modes associated with certain spatial directions. However, for simplicity, the total output intensity is used in this work and Ref. [1].

central goal is to minimize $\Delta\phi$. However, in the literature, this quantity is called phase *sensitivity*, see for example Xin *et al.* [10] or Yurke *et al.* [16], which may lead to confusion since the term "sensitivity" implies that the numerical value of $\Delta\phi$ should instead be maximized. [6]

For a classical interferometer operating with coherent light, the phase sensitivity is fundamentally bound by the *shot-noise limit* (SNL) $\Delta\phi_{\mathrm{SNL}}$, which is sometimes also referred to as the *shot-noise level*, *standard quantum limit* (SQL) or *coherent state limit* [1, 6, 8–10, 12, 13, 16, 92–95]:

$$\Delta\phi_{\mathrm{SNL}} = \frac{1}{\sqrt{\langle \hat{N}_{\mathrm{tot}}^{(1)} \rangle}}, \tag{3.3}$$

where $\hat{N}_{\mathrm{tot}}^{(1)}$ is the integral photon-number operator for the radiation that interacts with the phase object. The superscript $^{(1)}$ has been added in an analogy to the SU(1,1) interferometer, where the radiation interacting with the phase object is the radiation generated by the *first* crystal. More generally, in the rest of this work, the notation introduced in Ref. [1] will be used where the superscripts $^{(1)}$ and $^{(2)}$ refer to quantities related to the first and second crystal, respectively.

The shot-noise level serves as a reference point for the sensitivity of the interferometer, which leads to the definition of the *normalized phase sensitivity* [1, 94]:

$$f = \frac{\Delta\phi}{\Delta\phi_{\mathrm{SNL}}}. \tag{3.4}$$

The importance of this quantity lies in the fact that for $f < 1$, the sensitivity beats the shot-noise level and the interferometer is said to be *supersensitive* [9]. Evidently, the interferometer then shows better performance than a classical interferometer operating with a coherent light beam that has the same integral intensity as the signal and idler radiation interacting with the phase object. Achieving supersensitivity one of the central goals of quantum interferometry [96].

A more fundamental bound for the phase sensitivity is the *Heisenberg limit* (HL) [6, 8, 12, 16, 27, 93–96]

$$\Delta\phi_{\mathrm{HL}} \propto \frac{1}{\langle \hat{N}_{\mathrm{tot}}^{(1)} \rangle}, \tag{3.5}$$

which is derived from the phase-intensity uncertainty relation and is the asymptotic limit for large photon numbers [9, 95]. It should be noted that the Heisenberg limit can also be reached using classical interferometer setups by feeding squeezed states of light into the normally unused input port, as first proposed by Caves [92]. However, as suggested by Yurke *et al.* [16], one advantage of SU(1,1) interferometers is that they can reach the HL with fewer optical elements than classical interferometer setups.

Clearly, both the HL and SNL decrease as the number of photons increases, see Eqs. (3.3) and (3.5), suggesting that at higher intensities the phase sensitivity is usually improved

compared to low intensities. Furthermore, as mentioned above, the HL is only the limit at large photon numbers and for low photon numbers the SNL is the lower bound for the phase sensitivity: $\Delta\phi_{\mathrm{SNL}} > \Delta\phi_{\mathrm{HL}}$ for sufficiently small N; the exact value for N here depends on the proportionality factor of Eq. (3.5). Generally, large photon numbers in the PDC process correspond to high parametric gain and as described in Sec. 2.3.2, an accurate description of high-gain PDC is possible using sets of coupled integro-differential equations. Accordingly, this approach will be discussed in more detail in the following.

3.2. Describing PDC in Cascaded Systems with Integro-Differential Equations

The approach for the description of PDC using coupled sets of integro-differential equations used in this work (and Ref. [1]) was developed in Sharapova *et al.* [5], as already mentioned in Sec. 2.3.2. It focuses on the description in the spatial domain and, for simplicity, only considers one transverse dimension which is labelled by the scalar-valued wave-vector component q and the corresponding real-space coordinate x. This approximation is justified by the radial symmetry of the system [2, 5]. Furthermore, it is assumed that the pump is monochromatic at ω_p, that it fulfills the undepleted pump approximation (see Sec. 2.3.2) and that it has a Gaussian transverse spatial envelope of the form [compare Eq. (2.42)]:

$$\tilde{\alpha}_p(x) = \mathrm{e}^{-\frac{x^2}{2\sigma^2}}. \tag{3.6}$$

Here, σ is the pump width parameter so that the full width at half maximum (FWHM) of the pump intensity distribution is given by $2\sqrt{\ln(2)}\,\sigma$ [5].

The approach utilizes the Heisenberg picture and describes the evolution of the plane-wave operators through the PDC section using sets of coupled integro-differential equations of the form [5]

$$\frac{\mathrm{d}\hat{a}_s(q_s, L)}{\mathrm{d}L} = \Gamma \int \mathrm{d}q_i\, \mathrm{e}^{-\frac{(q_s+q_i)^2\sigma^2}{2}} h(q_s, q_i, L)\, \hat{a}_i^\dagger(q_i, L), \tag{3.7a}$$

$$\frac{\mathrm{d}\hat{a}_i^\dagger(q_i, L)}{\mathrm{d}L} = \Gamma \int \mathrm{d}q_s\, \mathrm{e}^{-\frac{(q_s+q_i)^2\sigma^2}{2}} h^*(q_s, q_i, L)\, \hat{a}_s(q_s, L), \tag{3.7b}$$

where $h(q_s, q_i, L)$ is a complex-valued function describing the phase-matching and depending on the geometry of the system. For readability, the frequency dependence of $\hat{a}_s$ on ω_s and $\hat{a}_i^\dagger$ on $\omega_i = \omega_p - \omega_s$ has not been written out explicitly. The coordinate L over which the system must be integrated will coincide with the propagation axis of the pump and the z-coordinate axis in the following. The variable Γ introduced in the integro-differential equations (3.7) is the *theoretical gain parameter* which, among other parameters, collects the prefactors from the PDC Hamiltonian as described in Sec. 2.3.2, including the amplitude $\mathcal{E}_p$ of the (undepleted) pump field and the (identical) group velocities of the signal and idler photons. The precise expression for this prefactor is not important, since it will ultimately be expressed via the *experimental gain* G_{exp}, see Sec. 3.4 below.

The commutation relations for the plane-wave operators at fixed values of L are given by [1]

$$[\hat{a}_s(q_s, L), \hat{a}_s^\dagger(q_s', L)] = \delta(q_s - q_s'), \tag{3.8a}$$
$$[\hat{a}_i(q_i, L), \hat{a}_i^\dagger(q_i', L)] = \delta(q_i - q_i'), \tag{3.8b}$$
$$[\hat{a}_s(q_s, L), \hat{a}_i^\dagger(q_i', L)] = 0. \tag{3.8c}$$

Here, the last commutation relation in Eq. (3.8c) implies that the signal and idler plane-wave operators describe photons which are distinguishable in some degree of freedom, for example the polarization directions or the frequencies ω_s and ω_i. In the case of indistinguishable photons, the commutation relation instead reads

$$[\hat{a}_s(q_s, L), \hat{a}_i^\dagger(q_i', L)] = \delta(q_s - q_i') \tag{3.9}$$

and the plane-wave operators can be set equal: $\hat{a}_s(q_s, L) = \hat{a}_i(q_s, L)$. It should be noted that regardless of whether the commutation relation between the signal and idler operators is of the form as written in Eq. (3.8c) or Eq. (3.9), the integro-differential take the form as written in Eqs. (3.7), assuming that the group velocities of the signal and idler photons are (approximately) identical, see the derivation in Sharapova *et al.* [5]. This is because changing the commutation relation only leads to a rescaling of the theoretical gain parameter Γ.

In the undepleted pump approximation, the PDC Hamiltonian in Eq. (2.37) is at most quadratic in the plane-wave operators. As shown by Ekert and Knight [97], for such systems, the plane-wave operators before and after the interaction are connected via linear transformations, which here are of the form [1, 5]:

$$\hat{a}_s(q_s, L) = \hat{a}_s(q_s) + \int \mathrm{d}q_s'\, \eta(q_s, q_s', L)\, \hat{a}_s(q_s') + \int \mathrm{d}q_i'\, \beta(q_s, q_i', L)\, \hat{a}_i^\dagger(q_i'), \tag{3.10a}$$
$$\hat{a}_i^\dagger(q_i, L) = \hat{a}_i^\dagger(q_i) + \int \mathrm{d}q_i'\, \eta^*(q_i, q_i', L)\, \hat{a}_i^\dagger(q_i') + \int \mathrm{d}q_s'\, \beta^*(q_i, q_s', L)\, \hat{a}_s(q_s'), \tag{3.10b}$$

where $\hat{a}_s(q_s, L)$ and $\hat{a}_i^\dagger(q_i, L)$ are the operators at the end of the interaction at the coordinate L (*output* plane-wave operators) and $\hat{a}_i^\dagger(q_i')$ and $\hat{a}_s(q_s')$ are the plane-wave operators at the beginning of the interaction (*input* plane-wave operators). The complex-valued *transfer functions* [1, 86, 98] $\eta(q, q', L)$ and $\beta(q, q', L)$ connect the input and output plane-wave operators and may, in general, couple any input plane-wave mode (the mode before the interaction) to all output plane-wave modes (the modes after the interaction).

As described in more detail in Sec. A.1, by plugging the form of the solutions for the plane-wave operators given in Eqs. (3.10) into the integro-differential equations (3.7), it is possible to obtain a coupled set of integro-differential equations for the transfer functions [1]:

$$\frac{\mathrm{d}\beta(q_s, q_i', L)}{\mathrm{d}L} = \Gamma \int \mathrm{d}q_i\, \mathrm{e}^{-\frac{(q_s+q_i)^2\sigma^2}{2}} h(q_s, q_i, L)\, \tilde{\eta}^*(q_i, q_i', L), \tag{3.11a}$$
$$\frac{\mathrm{d}\tilde{\eta}^*(q_i, q_i', L)}{\mathrm{d}L} = \Gamma \int \mathrm{d}q_s\, \mathrm{e}^{-\frac{(q_s+q_i)^2\sigma^2}{2}} h^*(q_s, q_i, L)\, \beta(q_s, q_i', L), \tag{3.11b}$$

where

$$\tilde{\eta}^*(q_i, q_i', L) \overset{\text{def.}}{=} \eta^*(q_i, q_i', L) + \delta(q_i - q_i'). \tag{3.12}$$

These coupled integro-differential equations are no longer operator-valued [1] and can be easily solved using numerical approaches such as the Runge-Kutta methods.

It should be emphasized that the form of the solution of the integro-differential equations as given in Eqs. (3.10) requires that the pump term $\mathrm{e}^{-(q_s+q_i)^2\sigma^2/2}$ and the phase-matching function $h(q_s, q_i, L)$ are symmetric under the exchange $q_s \leftrightarrow q_i$ for any L, as also shown in Sec. A.1. This symmetry requires that the refractive indices of the signal and idler photons are identical. This is most easily achieved in the degenerate regime, where the signal and idler photons are indistinguishable. Alternatively, as has been described in Ref. [1], this condition can also be approximately achieved by spectrally filtering the PDC radiation at a small offset from the degenerate frequency. In doing so, the generated signal-idler pairs are still well described by assuming equal refractive indices for both photons, while only one photon of each pair is actually detected. The commutation relation for this case is given by Eq. (3.8c) since the photon frequencies are slightly different. This is the case that was considered in Ref. [1] and will be explored in the rest of this section.

For a system that consists of a single PDC section, the initial value conditions for the plane-wave operators are given by

$$\hat{a}_s^{(\mathrm{in})}(q_s) = \hat{a}_s(q_s), \tag{3.13a}$$

$$\left[\hat{a}_i^{(\mathrm{in})}(q_i)\right]^\dagger = \hat{a}_i^\dagger(q_i), \tag{3.13b}$$

where instead of a concrete value for the coordinate L at the beginning of the PDC section, the superscript $^{(\mathrm{in})}$ has been used to identify the input operators. This initial value condition follows from the fact that before the PDC interaction, the plane-wave operators are given by the vacuum plane-wave operators $\hat{a}_s(q_s)$ and $\hat{a}_i^\dagger(q_i)$.

In *cascaded systems* consisting of multiple consecutive PDC sections, the connection between these sections can be achieved by requiring that the output plane-wave operators of one section labeled with the index m are the input operators of the following section with index $m+1$:

$$\hat{a}_s^{(m+1,\mathrm{in})}(q_s) = \hat{a}_s^{(m,\mathrm{out})}(q_s), \tag{3.14a}$$

$$\left[\hat{a}_i^{(m+1,\mathrm{in})}(q_i)\right]^\dagger = \left[\hat{a}_i^{(m,\mathrm{out})}(q_i)\right]^\dagger, \tag{3.14b}$$

where analogous to above, the superscript $^{(\mathrm{out})}$ has been introduced as to label the output plane-wave operators, replacing the concrete value of the coordinate L at the output of the PDC section. Note that the indexing with $m \in \mathbb{N}_1$ in the superscript to label the PDC sections was previously also used in Eq. (3.3) above. This notation has been introduced in Ref. [1] to describe the connection of the two crystals of the SU(1,1) interferometer. When transitioning between different PDC sections with different optical properties, for

example width different refractive indices, it is not immediately obvious that the connection between the sections can be made using Eqs. (3.15) since they assume that the transverse wave-vectors components q_s and q_i remain the same after transitioning between the PDC sections. However, as discussed in Sec. A.2, when transitioning between media with different refractive indices, the transverse wave-vector components are conserved.

For a system consisting of several cascaded PDC sections, such as an SU(1,1) interferometer, there are two main options for obtaining the transfer functions connecting the input plane-wave operators at the beginning of the system to the output plane-wave operators at the end of the system:

Integrating the System Section-by-Section. By expressing both sides of Eqs. (3.14) in terms of the linear input-output transformations as written in Eqs. (3.10) and comparing both sides, it is clear that the initial value conditions for the $(m+1)$th PDC section when integrating the system of integro-differential equations for the transfer functions as given in Eqs. (3.11) are simply

$$\beta^{(m+1,\mathrm{in})}(q,q') = \beta^{(m,\mathrm{out})}(q,q'), \tag{3.15a}$$

$$\tilde{\eta}^{(m+1,\mathrm{in})}(q,q') = \tilde{\eta}^{(m,\mathrm{out})}(q,q'), \tag{3.15b}$$

where the same notation using the superscripts instead of concrete values for L as introduced above has been used. Assuming that the first crystal ($m = 1$) has no prior PDC sections, its input plane-wave operators are the vacuum operators and by comparing Eqs. (3.13) with Eqs. (3.10) it is then clear that

$$\beta^{(1,\mathrm{in})}(q,q') = 0, \tag{3.15c}$$

$$\tilde{\eta}^{(1,\mathrm{in})}(q,q') = \delta(q-q') \tag{3.15d}$$

are the initial value conditions for the transfer functions of the first PDC section. Equations (3.15a)–(3.15d) combined fully describe the initial value condition for each PDC section. If there are N PDC sections in total, so that $m = 1,\dots,N$, and given the phase matching functions $h^{(m)}$, for $m = 1,\dots,N$, which describe these sections, it is possible to obtain the output transfer functions $\beta^{(N,\mathrm{in})}$ and $\tilde{\eta}^{(N,\mathrm{in})}$ for the last PDC section by starting at the first PDC section with $h^{(1)}$ and its initial value conditions as written in Eqs. (3.15c) and (3.15d) and then consecutively integrating the PDC sections using the initial value conditions as written in Eqs. (3.15a) and (3.15b). This approach is easy to implement and is generally the simpler approach if only the transfer functions for the entire system are needed. However, after the integration of the entire system is completed, only the transfer functions connecting the input plane-wave operators of the first section to the output operators of the last section (or any intermediate section) are obtained and not the transfer functions connecting the plane-wave operators of any input section (other than the first) to its output operators. For this reason, this method does not allow for an in-depth analysis of the evolution of the plane-wave operators in-between the PDC sections. This is addressed with the alternative method presented in the following.

Integrating PDC Sections Separately. More generally, the linear transformation equations (3.10) for the mth PDC section can be written in the following form, after taking the definition of $\tilde{\eta}$ in Eq. (3.12) into account:

$$\begin{aligned}\hat{a}_s^{(m,\mathrm{out})}(q_s) &= \int \mathrm{d}q_s'\, \tilde{\eta}^{(m)}(q_s, q_s')\, \hat{a}_s^{(m,\mathrm{in})}(q_s') \\ &\quad + \int \mathrm{d}q_i'\, \beta^{(m)}(q_s, q_i') \left[\hat{a}_i^{(m,\mathrm{in})}(q_i')\right]^\dagger,\end{aligned} \tag{3.16a}$$

$$\begin{aligned}\left[\hat{a}_i^{(m,\mathrm{out})}(q_i)\right]^\dagger &= \int \mathrm{d}q_i'\, \left[\tilde{\eta}^{(m)}(q_i, q_i')\right]^* \left[\hat{a}_i^{(m,\mathrm{in})}(q_i')\right]^\dagger \\ &\quad + \int \mathrm{d}q_s'\, \left[\beta^{(m)}(q_i, q_s')\right]^* \hat{a}_s^{(m,\mathrm{in})}(q_s').\end{aligned} \tag{3.16b}$$

Here, $\tilde{\eta}^{(m)}$ and $\beta^{(m)}$ are the transfer functions connecting the input operators $\hat{a}_s^{(m,\mathrm{in})}$ and $\hat{a}_i^{(m,\mathrm{in})}$ of the mth PDC section to its output operators $\hat{a}_s^{(m,\mathrm{out})}$ and $\hat{a}_i^{(m,\mathrm{out})}$. Clearly, plugging these expressions for the transfer functions into the integro-differential equations (3.7) and following Sec. A.1 yields again integro-differential equations of the form as in Eqs. (3.11), just with additional superscripts $^{(m)}$ for the transfer functions. For each PDC section m, integrating the resulting set of integro-differential equations leads to solutions in terms of the transfer functions which describe the evolution of *some* input operators $\hat{a}_s^{(m,\mathrm{in})}$ and $\hat{a}_i^{(m,\mathrm{in})}$ through the PDC section m via Eqs. (3.16). The initial value conditions read, *regardless of the index* m,

$$\beta^{(m,\mathrm{in})}(q, q') = 0, \tag{3.17a}$$

$$\tilde{\eta}^{(m,\mathrm{in})}(q, q') = \delta(q - q'). \tag{3.17b}$$

Importantly, note that here the Dirac delta on the right-hand side of Eq. (3.17b) does not imply that the system for the PDC section m initially starts at the vacuum state, as was the case with Eq. (3.15d). Instead, the precise meaning is as follows: For both Eqs. (3.15d) and (3.17b), this Dirac delta originates from the plane-wave operators written outside the integrals in Eqs. (3.10). For the step-by-step integration approach, the system starts in the vacuum state at the first PDC section ($m = 1$) meaning these operators refer to the vacuum operators. Contrary to that, when each subsystem is integrated separately, these operators are the *output operators of the preceding PDC section*. In other words, Eqs. (3.16) and the integro-differential equations that would be obtained by plugging them into Eqs. (3.7) as described above, are independent of the prior history of the system before PDC section m, which is only described by *some* input operators $\hat{a}_s^{(m,\mathrm{in})}$ and $\hat{a}_i^{(m,\mathrm{in})}$. As a consequence, once the solutions $\tilde{\eta}^{(m)}$ and $\beta^{(m)}$ for each m have been obtained, they need to be connected to each other in order to obtain the transfer functions describing the entire system. To this end, Eqs. (3.16) as written above can be recursively applied to themselves and each other as prescribed by Eqs. (3.14) by shifting the index $m \to m + 1$ once. After bringing the result back to the same form as the solutions of the integro-differential equations [Eqs. (3.16)], it is possible to identify new transfer functions $\tilde{\eta}^{(m+1,m)}$ and $\beta^{(m+1,m)}$ which connect the

input operators of section m to the output operators of section $m+1$:

$$\begin{aligned}\hat{a}_s^{(m+1,\mathrm{out})}(q_s) = &\int \mathrm{d}q_s'\, \tilde{\eta}^{(m+1,m)}(q_s, q_s')\, \hat{a}_s^{(m,\mathrm{in})}(q_s') \\ &+ \int \mathrm{d}q_i'\, \beta^{(m+1,m)}(q_s, q_i') \left[\hat{a}_i^{(m,\mathrm{in})}(q_i')\right]^\dagger,\end{aligned} \tag{3.18a}$$

$$\begin{aligned}\left[\hat{a}_i^{(m+1,\mathrm{out})}(q_i)\right]^\dagger = &\int \mathrm{d}q_i'\, \left[\tilde{\eta}^{(m+1,m)}(q_i, q_i')\right]^* \left[\hat{a}_i^{(m,\mathrm{in})}(q_i')\right]^\dagger \\ &+ \int \mathrm{d}q_s'\, \left[\beta^{(m+1,m)}(q_i, q_s')\right]^* \hat{a}_s^{(m,\mathrm{in})}(q_s').\end{aligned} \tag{3.18b}$$

The *connection relations* that give the expressions for the new transfer functions $\tilde{\eta}^{(m+1,m)}$ and $\beta^{(m+1,m)}$ read

$$\tilde{\eta}^{(m+1,m)}(q, q') = \int \mathrm{d}\bar{q}\, \tilde{\eta}^{(m+1)}(q, \bar{q})\, \tilde{\eta}^{(m)}(\bar{q}, q') + \int \mathrm{d}\bar{q}\, \beta^{(m+1)}(q, \bar{q}) \left[\beta^{(m)}(\bar{q}, q')\right]^*, \tag{3.19a}$$

$$\beta^{(m+1,m)}(q, q') = \int \mathrm{d}\bar{q}\, \tilde{\eta}^{(m+1)}(q, \bar{q})\, \beta^{(m)}(\bar{q}, q') + \int \mathrm{d}\bar{q}\, \beta^{(m+1)}(q, \bar{q}) \left[\tilde{\eta}^{(m)}(\bar{q}, q')\right]^*. \tag{3.19b}$$

By repeatedly recursively applying these connection relations, it is possible to obtain the generalized transfer functions $\tilde{\eta}^{(m,l)}$ and $\beta^{(m,l)}$, for $l < m$, connecting the input plane-wave operators of the lth PDC section with the output plane-wave operators of the mth PDC section. In the special case of $l = 1$ and $m = N$, where N is the index of the last PDC section (and the number of PDC sections), these transfer functions connect the input operators of the entire system to its output operators. Equations (3.15a)–(3.19b) are generalizations of the results presented in Ref. [1] for the two PDC sections forming the SU(1,1) interferometer ($N = 2$). The approach described by these equations has the advantage that each PDC section is first treated separately and therefore allows for a more detailed analysis based on the transfer functions that describe each section, while integrating the PDC sections sequentially as described above only results in the transfer functions connecting the input plane-wave operators of the entire system to the output operators of any section. The rest of this chapter and Chapters 4 and 5 will extensively utilize the approach described by Eqs. (3.15a)–(3.19b).

An important connection between the two transfer functions $\tilde{\eta}$ and β, regardless of whether they describe a subsystem or the full system, is that they admit a *joint Schmidt-decomposition*. The existence of this decomposition has for example been shown by Christ *et al.* [80] and Quesada *et al.* [86] for the frequency domain and the basic steps for the proof can be applied here. In the context of this work, the decomposition reads [1]

$$\beta(q, q') = \sum_n \sqrt{\Lambda_n}\, u_n(q)\, \psi_n(q'), \tag{3.20a}$$

$$\tilde{\eta}(q, q') = \sum_n \sqrt{\tilde{\Lambda}_n}\, u_n(q)\, \psi_n^*(q'), \tag{3.20b}$$

where $\sqrt{\Lambda_n}$ and $\sqrt{\tilde{\Lambda}_n}$ are the *singular values* of β and $\tilde{\eta}$, respectively and their squares Λ_n and $\tilde{\Lambda}_n$, respectively, are the *(Schmidt) eigenvalues*. The name "singular values" for the square roots of the Schmidt eigenvalues originates from the fact that in numerical applica-

tions, both Eqs. (3.20a) and (3.20b) have the structure of a singular value decomposition (SVD), see also Secs. A.6 and 5.2.2. The Schmidt eigenvalues are connected via

$$\tilde{\Lambda}_n = \Lambda_n + 1. \tag{3.21}$$

The mode functions u_n and ψ_n fulfill the orthonormality conditions

$$\int \mathrm{d}q\, u_n(q)\, u^*_{n'}(q) = \delta_{nn'}, \tag{3.22a}$$

$$\int \mathrm{d}q\, \psi_n(q)\, \psi^*_{n'}(q) = \delta_{nn'}, \tag{3.22b}$$

and in general, they will be different *even* for the same index n: $u_n(q) \neq \psi_{n'}(q)$ for *any* pair (n, n'), compare Sec. 4.2. See also Eqs. (4.20) and the text surrounding below, which describe this decomposition in the context of discrete variables. The physical meaning of these mode functions can be seen by plugging Eqs. (3.20) into the form of the solutions of the integro-differential equations, Eqs. (3.10), and bringing the result to the form[2]

$$\hat{A}^{(\mathrm{out})}_n = \sqrt{\tilde{\Lambda}_n}\, \hat{A}^{(\mathrm{in})}_n + \sqrt{\Lambda_n}\, \left[\hat{B}^{(\mathrm{in})}_n\right]^\dagger, \tag{3.23a}$$

$$\hat{B}^{(\mathrm{out})}_n = \sqrt{\tilde{\Lambda}_n}\, \hat{B}^{(\mathrm{in})}_n + \sqrt{\Lambda_n}\, \left[\hat{A}^{(\mathrm{in})}_n\right]^\dagger, \tag{3.23b}$$

where

$$\hat{A}^{(\mathrm{in})}_n = \int \mathrm{d}q\, \psi^*_n(q)\, \hat{a}^{(\mathrm{in})}_s(q), \tag{3.24a}$$

$$\hat{A}^{(\mathrm{out})}_n = \int \mathrm{d}q\, u^*_n(q)\, \hat{a}^{(\mathrm{out})}_s(q), \tag{3.24b}$$

$$\hat{B}^{(\mathrm{in})}_n = \int \mathrm{d}q\, \psi^*_n(q)\, \hat{a}^{(\mathrm{in})}_i(q), \tag{3.24c}$$

$$\hat{B}^{(\mathrm{out})}_n = \int \mathrm{d}q\, u^*_n(q)\, \hat{a}^{(\mathrm{out})}_i(q) \tag{3.24d}$$

are the input and output Schmidt operators for the signal ($\hat{A}$-operators) and idler photons ($\hat{B}$-operators). Equations (3.23) are the well-known Bogoliubov transformations for the Schmidt operators [11, 80]. From Eqs. (3.24) it is clear that the ψ_n functions are associated with the input Schmidt operators, while the u_n are associated with the output Schmidt operators. Thus, in the following, ψ_n and u_n will be called *input Schmidt modes* and *output Schmidt modes*, respectively. The newly introduced Schmidt modes are spatially broadband (multimode) [1, 2] and generally reach over all transverse plane-wave modes q. However, their advantage is that in terms of the Schmidt mode operators, the input output relation is diagonalized, compare Eqs. (3.10) and (3.23). For the rest of this chapter, only the existence of the Schmidt decomposition and the orthonormality of the Schmidt modes as written in Eqs. (3.22) is of relevance. A more detailed discussion regarding the Schmidt modes is presented in Sec. 4.2, including concrete plots of the modes.

[2] To see this, Eqs. (3.20) can be plugged into Eqs. (3.10) after applying Eq. (3.12). Then, both sides should be multiplied with $u^*_{n'}(q_s)$ for Eq. (3.10a) and $u_{n'}(q_i)$ for Eq. (3.10b). Integrating both sides over q_s for Eq. (3.10a) and q_i for Eq. (3.10b) then results in Eqs. (3.23) and (3.24).

Ultimately, from either approach for obtaining the solutions of the integro-differential equations of the interferometer as described above, it is necessary to compute quantities such as the output intensity in order to obtain the phase sensitivity, see Eq. (3.1). Depending on the detection scheme and whether the PDC process is degenerate, there may be several possibilities for the choice of the relevant output photon-number operator $\hat{N}(q)$:

$$\hat{N}(q) \overset{\text{def.}}{=} \begin{cases} \hat{N}_s(q),\ \hat{N}_i(q) \text{ or } \hat{N}_s(q) + \hat{N}_i(q), & \text{for non-degenerate PDC} \\ \hat{N}_s(q) + \hat{N}_i(q) = 2\hat{N}_s(q) = 2\hat{N}_i(q), & \text{for degenerate PDC} \end{cases} \tag{3.25}$$

This definition can be summarized as follows: In the case of non-degenerate PDC, it is possible to consider the signal and idler beams separately or consider the photons as indistinguishable and take the sum of their intensities. For degenerate PDC however, it is not possible to separate the signal and idler photons and therefore the relevant operator is the sum of the signal and idler intensity operators, which due to the indistinguishability is the same as twice the signal or idler operator. For the rest of this chapter,

$$\hat{N}(q) = \hat{N}_s(q), \tag{3.26}$$

unless stated otherwise, since the focus is on the case where the signal and idler photons are distinguishable and only the signal photons are assumed to be detected.

Generally, in order to evaluate expectation values of the output plane-wave operators, it is advisable to express them in terms of the vacuum plane-wave operators and bring the resulting operator chains into normal order, since the action of the vacuum annihilation operators quantum vacuum state $|0\rangle$ is known: $\hat{a}(q)|0\rangle = 0$. As a simple example, the intensity distribution $\langle \hat{N}_s(q_s) \rangle$ for the signal photon-number operator $\hat{N}_s(q_s) = \left[\hat{a}_s^{(\text{out})}(q_s)\right]^\dagger \hat{a}_s^{(\text{out})}(q_s)$ is given by [5]:

$$\langle \hat{N}_s(q_s) \rangle = \int \mathrm{d}q_i' \ |\beta(q_s, q_i', L)|^2, \tag{3.27}$$

where β is the transfer function describing the system. This result follows by expressing $\hat{a}_s^{(\text{out})}(q_s)$ via the vacuum plane-wave operators $\hat{a}_i^\dagger(q_i')$ and $\hat{a}_s(q_s)$ using Eqs. (3.10).

The second important *statistical moment* is the photon-number covariance $\mathrm{cov}(q, q')$, which is defined in terms of the intensity operator as written in Eq. (3.25) as

$$\mathrm{cov}(q, q') = \langle \hat{N}(q)\hat{N}(q') \rangle - \langle \hat{N}(q) \rangle \langle \hat{N}(q') \rangle . \tag{3.28}$$

For the signal photon-number operator as written in Eq. (3.26) above, this expectation value can be evaluated as described in more detail in Ref. [1] and the resulting expression in terms of the β transfer function reads [1]:

$$\mathrm{cov}(q_s, q_s') = \left| \int \mathrm{d}\bar{q}_i \, \beta(q_s, \bar{q}_i, L) \, \beta^*(q_s', \bar{q}_i, L) \right|^2 + \delta(q_s - q_s') \, \langle \hat{N}_s(q_s) \rangle . \tag{3.29}$$

Comparing Eqs. (3.28) and (3.29) with Eq. (6) of Averchenko *et al.* [99], the argument

of the modulus squared can be identified as the field amplitude (first-order) correlation function $G^{(1)}(q_s, q_s')$, while the second summand can be identified as the *shot-noise term*, which results from the Dirac-delta commutation relations of the plane-wave operators. It should be emphasized that here, it is assumed that the signal and idler plane-wave operators commute, as written in Eq. (3.8c). If instead their commutation relation is given by a Dirac delta distribution, as written in Eq. (3.9), an additional term appears in the covariance functions which describes the signal-idler cross-correlations, as discussed in Ref. [1].

3.3. Diffraction-Compensated SU(1,1) Interferometers

The sketch of the SU(1,1) interferometer shown in Fig. 3.1 above is simplified in the sense that it does not account for the diffraction of the generated signal and idler radiation. For a more realistic characterization, it must be taken into account that the signal and idler beams broaden as the radiation travels inside the crystals and between them [1], as for example depicted in Fig. 3.2(a).

As suggested in Frascella *et al.* [7], the divergence of the PDC light can be *compensated* using a focusing element, such as a lens placed between the two crystals, with the idea being that the radiation gets imaged onto the second crystal. Experimentally, this focusing can also be realized by using a spherical mirror which reflects the PDC light back through the crystal it was generated from [7, 100], as shown in Fig. 3.2(b). This kind of setup has been called *wide-field SU(1,1) interferometer* in Frascella *et al.* [7] but will be simply called *compensated (interferometer) setup* based on Ref. [1] in the following. The center of the crystal should be placed at the $2f$ position, where f is the focal length of the mirror, since $2f$ is then the radius of the mirror [101], meaning that all light rays starting from the $2f$ position are perpendicular to the mirror surface and are reflected back on the same path, as indicated by four red arrows at the top right in Fig. 3.2(b).

Alternatively, it is possible to use two lenses with focal length f forming a *4f-lens system* to compensate for the diffraction, as for example suggested by Marino *et al.* [6] and Roux [102]. Figure 3.2(c) shows how the lenses should be aligned with respect to the crystals. The first one should be placed so that its focal point lies at the effective point where the PDC radiation is generated inside the first crystal. The second lens should be placed at a distance of $2f$ from the first one and the second crystal should be placed after it so that the distance between the output face of the first crystal to the first lens and the distance from the second lens to the input face of the second crystal are the same. This way, the PDC light generated from the first crystal gets first collimated by the first lens and then focused into the second crystal by the second lens.

In general, the function h describing the phase matching and appearing in the integro-differential equations (3.11) will depend on the geometry of the setup and the properties of the phase object. This is why in the following, several important cases relevant for the SU(1,1) interferometers discussed in this work will be presented.

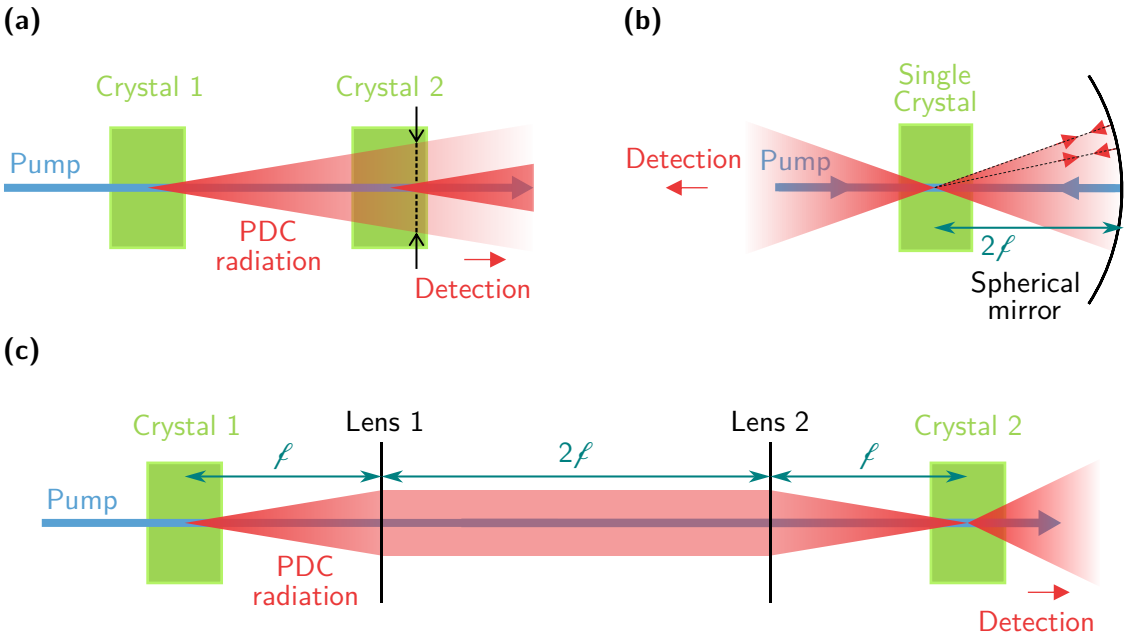

Figure 3.2: **(a)** Non-compensated (Mach-Zehnder type) and compensated SU(1,1) interferometers in **(b)** reflection (*Michelson-type* [13]) and **(c)** transmission (*4f-setup* [6, 102]) geometry. Due to diffraction, the radiation diverges inside and between the crystals in the non-compensated case which leads to bad spatial overlap with the radiation generated in the second crystal as indicated by the black arrows. It should be noted that for collinear PDC, the broadening is shown exaggerated compared to the crystal dimensions. As seen later in this chapter, for example in Fig. 3.4, the light cone emitted of the second crystal only has an opening angle of about 40 to 50 mrad (2.3 to 2.87°). Both compensated setups use focusing elements to focus the PDC radiation before it is amplified/deamplified in the second pass through the PDC section. For the reflected geometry, only a single crystal is used and the focusing is achieved using a spherical mirror placed at a distance of about $2f$ from the crystal, where f is the focal length of the mirror and $2f$ corresponds to its radius. For the transmission geometry two lenses with focal length f are used to focus the radiation onto a second crystal as indicated. It should be noted that these figures, for simplicity, neglect the refraction of the signal and idler radiation at the crystal-air boundaries. This is discussed in more detail in Sec. A.2. Note that an all three cases, the phase object (apart from the air gap) is not explicitly shown. Figures **(a)** and **(b)** were adapted from Ref. [1] and Fig. **(c)** is based on Ref. [2].

First/Single Crystal. For a single crystal of length L_1, or equivalently, the first crystal of the SU(1,1) interferometer of the same length, the integro-differential equations (3.11) can be integrated over the interval $[0, L_1]$. The function $h^{(1)}$ appearing in the integro-differential equations for the first crystal is of the form [1]

$$h^{(1)}(q_s, q_i, L) = \mathrm{e}^{\mathrm{i}\Delta k(q_s,q_i)L}, \tag{3.30}$$

where

$$\Delta k(q_s, q_i) = k_{pz}(q_s, q_i) - k_{sz}(q_s) - k_{iz}(q_i) \tag{3.31a}$$

$$= \sqrt{k_p^2 - (q_s + q_i)^2} - \sqrt{k_s^2 - q_s^2} - \sqrt{k_i^2 - q_i^2} \tag{3.31b}$$

is the longitudinal wave-vector mismatch inside the PDC section and $k_\nu = |\boldsymbol{k}_\nu|$, for $\nu = p, s, i$, labels the modulus of the pump, signal and idler wave-vector in the material section, respectively. As discussed in Sec. 2.3.2, the z-components k_{pz}, k_{sz} and k_{iz} have been rewritten in terms of the respective wave-vector modulus and the transverse wave-vector components q_s and q_i, see Eq. (2.40). Note that $q_p = q_s + q_i$, compare Sec. 2.3.1.

Non-Compensated Configuration. In the non-compensated configuration, the expression for the phase-matching function $h^{(2)}$ for the second crystal is the same as for the first crystal but with an additional phase $\phi(q_s, q_i)$ which describes the relative phase added to the pump, signal and idler radiation by the phase object [1]:

$$h^{(2)}_{\mathrm{ncom}}(q_s, q_i, L) = \mathrm{e}^{\mathrm{i}\Delta k(q_s,q_i)L}\mathrm{e}^{\mathrm{i}\phi(q_s,q_i)}\,. \tag{3.32}$$

Here, the integration of the integro-differential equations (3.11) is performed over the interval $[L_1, L_1 + L_2]$, where L_2 is the length of the second crystal which for the rest of this work will coincide with the length of the first crystal, meaning $L_1 = L_2$. Equivalently, if the pump function does not depend on L, as is the case in Eqs. (3.11) for the Gaussian pump, the integration can instead be performed over the interval $[0, L_2]$, so that instead of Eq. (3.32), the phase-matching function is given by

$$h^{(2)}_{\mathrm{ncom}}(q_s, q_i, L) = \mathrm{e}^{\mathrm{i}\Delta k(q_s,q_i)[L+L_1]}\mathrm{e}^{\mathrm{i}\phi(q_s,q_i)}\,, \tag{3.33}$$

which is the form of $h^{(2)}$ as written in Ref. [1]. If the pump function depends on L, a more careful substitution $L' = L - L_1$ with the new integration variable L' has to performed directly in the integro-differential equations to enable the integration over the interval $[0, L_2]$.

If the phase object is just given by the air gap between the two crystals, the phase $\phi(q_s, q_i)$ can be written as [5]

$$\phi(q_s, q_i) = \Delta k^{\mathrm{air}}(q_s, q_i)\, d\,, \tag{3.34}$$

where d is the length of the air gap and $\Delta k^{\mathrm{air}}(q_s, q_i)$ is the longitudinal wave-vector mismatch in air, analogous to Eq. (3.31b):

$$\Delta k^{\mathrm{air}}(q_s, q_i) = \sqrt{\left(k_p^{\mathrm{air}}\right)^2 - (q_s + q_i)^2} - \sqrt{\left(k_s^{\mathrm{air}}\right)^2 - q_s^2} - \sqrt{\left(k_i^{\mathrm{air}}\right)^2 - q_i^2}\,, \tag{3.35}$$

where $k_\nu^{\mathrm{air}} = \left|\boldsymbol{k}_\nu^{\mathrm{air}}\right|$, for $\nu = p, s, i$, labels the modulus of the pump, signal and idler wave-vector in air, so that $k_\nu^{\mathrm{air}} = \omega_\nu n^{\mathrm{air}}(\omega_\nu)/c_0$, see Eq. (2.15). To reduce the numerical complexity, it can be assumed that the air gap is sufficiently small so that ϕ can be treated as effectively constant with respect to the transverse wave-vectors [1]. In this case, the function $h^{(2)}$ is of the form

$$h^{(2)}_{\mathrm{ncom,flat}}(q_s, q_i, L) = \mathrm{e}^{\mathrm{i}\Delta k(q_s,q_i)L}\mathrm{e}^{\mathrm{i}\phi}\,, \tag{3.36}$$

where now the q-dependence of $h^{(2)}_{\mathrm{ncom,flat}}$ is only induced by the phase mismatch $\Delta k(q_s, q_i)$.

Such a phase profile, which has no spatial dependence, is referred to in the following as a *flat phase (profile)*.

Diffraction-Compensated Configuration. For the diffraction-compensated configuration, the phase-matching function is given by [1]:

$$h^{(2)}_{\mathrm{comp}}(q_s, q_i, L) = \mathrm{e}^{-\mathrm{i}\Delta k(q_s,q_i)[L-2L_1]}\mathrm{e}^{\mathrm{i}\phi}. \tag{3.37}$$

The change in the sign in the exponent comes from the fact that the focusing element (for example the 4f-system or the spherical mirror) causes a change in the sign of the curvature of the wavefront of the signal-idler radiation. This is illustrated in more detail in Appendix B. For the phase-matching function as written in Eq. (3.37), the integration of the integro-differential equations for the second crystal is over the interval $[L_1, 2L_1]$, meaning that the second crystal has the same length as the first crystal. In principle, it is also possible to integrate over other intervals $[L_1, L_1 + L_2]$ with $L_1 \neq L_2$, however, then it is not possible to reach perfect compensation.

3.4. Definition of the Experimental Gain

In order to connect the theoretical gain parameter Γ, which first appears in the integro-differential equations Eq. (3.7a), with the physically relevant *experimental gain*[3] G_{exp}, the collinear output intensity $\langle \hat{N}(q=0)\rangle\, \mathrm{d}q$ of a *single* crystal in dependence on Γ is usually fitted with a function of the form $y(\Gamma) = B\sinh^2(A\Gamma)$, with parameters A and B, analogous to the experimental procedure. The experimental gain is then defined as $G_{\mathrm{exp}} = A\Gamma$. The range for the experimental gain is usually loosely divided into the low-gain regime, where $G_{\mathrm{exp}} \ll 1$ and the high-gain regime, for large G_{exp}. [1, 3, 5, 104]

As was noted in Ref. [1], since the PDC light is generally strongly multimode, the fitting procedure described above usually leads to a fit that does not properly describe both the low- and high-gain regime. To remedy this, it is possible to perform several fits of the form

$$y(\Gamma) = B\sinh^2\left(A_{\Gamma_c}\Gamma\right), \tag{3.38}$$

where Γ now ranges over a small interval around a central value Γ_c so that the fit locally approximates the intensity curve. Then, the A_{Γ_c} form a curve over Γ_c and the fit constants effectively become gain-dependent themselves. The experimental gain is then defined via $G_{\mathrm{exp}} = A_{\Gamma_c}\Gamma_c$. Given a targeted value for G_{exp}, the corresponding parameter value Γ_c can be computed numerically using root-finding algorithms to determine the solution[4] for Γ_c of $A_{\Gamma_c}\Gamma_c - G_{\mathrm{exp}} = 0$. Essentially, this root-finding performs an inversion of the functional

[3] The name originates from the fact that in experimental setups, the gain is defined similarly, which is, via a fit of the collinear or integral intensity output of a single crystal in dependence on the square root of the pump power, see for example Sharapova *et al.* [5] or Chekhova *et al.* [103].

[4] For this, it can be helpful to use interpolation to predict the target value of A_{Γ_c} if the grid used to compute the curve of the A_{Γ_c} has insufficient density. Afterwards, a more precise value of A_{Γ_c} can be computed by repeating the fit.

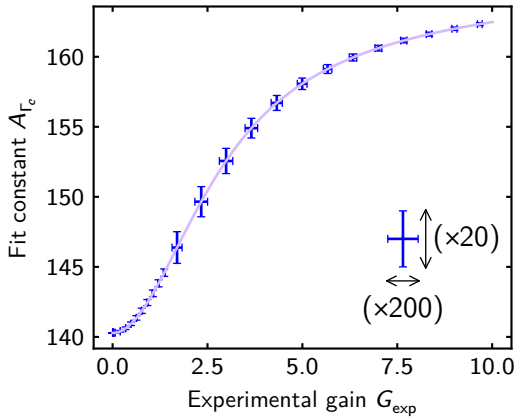

Figure 3.3: Fit constant A_{Γ_c} in dependence on the experimental gain G_{exp} obtained for the collinear intensity of a 2 mm BBO crystal with a Gaussian pump with a FWHM of the intensity profile of 50 µm. Concrete values are given in Table 3.1. The error bars indicate the error resulting from the fitting procedure of the collinear intensity, as described in the text and the error bars have been scaled up as shown in the figure. The point density of the Γ values for the fits of the collinear intensities decreases around $G_{\mathrm{exp}} = 1.9$, which leads to a jump in the error. Adapted from Ref. [1].

Table 3.1: Fit constant A_{Γ_c} for the selected experimental gain values G_{exp}. The error values originate from the fit error of the collinear intensities over A_{Γ_c}, see the text. See also Fig. 3.3. Adapted from Ref. [1].

Gain G_{exp}	Fit constant A_{Γ_c}
$0.01 \pm 5 \times 10^{-11}$	$140.285 \pm 6 \times 10^{-7}$
$1.25 \pm 1.2 \times 10^{-4}$	144.029 ± 0.013
$2.5 \pm 9 \times 10^{-4}$	150.44 ± 0.06
$3.75 \pm 9 \times 10^{-4}$	155.19 ± 0.04
$5.0 \pm 7 \times 10^{-4}$	158.080 ± 0.021
$10.0 \pm 4 \times 10^{-4}$	162.475 ± 0.005

dependence from $G_{\mathrm{exp}} = G_{\mathrm{exp}}(\Gamma_c)$ to $\Gamma_c = \Gamma_c(G_{\mathrm{exp}})$, so that Γ_c can be determined, given the targeted value of G_{exp}. It should be noted that any constant prefactor that might re-scale the collinear intensity $\langle \hat{N}(q=0) \rangle \, \mathrm{d}q$ is absorbed in the fit constant B [see Eq. (3.38)] and therefore does not influence the definition of the experimental gain [1].

Applying the latter relation to the definition of the parametric gain via A_{Γ_c} and Γ_c leads to a curve $A_{\Gamma_c}(G_{\mathrm{exp}})$, which is shown in Fig. 3.3 for a 2 mm BBO crystal pumped with a beam with transverse Gaussian envelope whose intensity distribution has an FWHM of 50 µm, which are the parameters used in Ref. [1]. Furthermore, Table 3.1 shows selected values from this curve. Clearly, the fit constant differs by about 16 % when comparing the low- and high-gain regime ($G_{\mathrm{exp}} = 0.01$ and $G_{\mathrm{exp}} = 10.0$, respectively). It should be noted that experimentally, values up to $G_{\mathrm{exp}} \approx 15$ have been achieved, see for example Pérez *et al.* [105] and Iskhakov *et al.* [106]. However, the more common range for the experimental gain is $G_{\mathrm{exp}} \leq 7$, compare Refs. [3, 5, 7, 11, 99].

For experimental applications, the procedure described above is usually impractical since it requires a large amount of data points for the collinear intensity. Hence, for experimental applications, a single fit encompassing both the low- and high-gain regime is usually performed, leading to a single fit constant A defining the gain, as was done for example in Ref. [3]. This approximation can also be applied in theoretical calculations if the experimental measurement error in the definition of the gain exceeds the error introduced by assuming that the difference in the fitting constants can be neglected [2].

3.5. Results

3.5.1. Analytical Groundwork for a Finite-Width Pump

The formalism for the description of the evolution of the plane-wave operators through the PDC section given in Sec. 3.2 yields output intensities in terms of the transverse wave-vector component q. A suitable expression for the integral output intensity operator to compute the phase sensitivity via Eq. (3.1) can be obtained by integrating the photon-number operator over all a transverse wave vectors:

$$\hat{N}_{\mathrm{tot}} = \int \mathrm{d}q\, \hat{N}(q). \tag{3.39}$$

Additionally, the standard deviation ΔN_{tot} for the integral photon number operator is required to compute the phase sensitivity. Plugging the expression for the integral photon-number operator in Eq. (3.39) into the definition of ΔN_{tot} in Eq. (3.2), it becomes evident that ΔN_{tot} can be written as [1]

$$\Delta N_{\mathrm{tot}} = \sqrt{\iint \mathrm{d}q\, \mathrm{d}q'\ \mathrm{cov}(q, q')}\,, \tag{3.40}$$

with the photon-number covariance function cov as written in Eq. (3.28).

In order to compute the normalized phase sensitivity f as given in Eq. (3.4), it is necessary to obtain both the intensity of the entire SU(1,1) interferometer and the intensity of the first crystal alone, since the latter determines the shot-noise level, as can be seen from Eq. (3.3). Therefore, it is advisable to obtain the transfer functions of the entire interferometer by first integrating the integro-differential equations (3.11) for each of the two sections separately and then combine them using the connection relations as described in Sec. 3.2.

For the non-compensated setup, a flat-phase profile is assumed for simplicity, as mentioned in Sec. 3.3. This means that for both the compensated and non-compensated interferometer, described via Eqs. (3.37) and (3.36), respectively, the phase ϕ does not depend on the transverse wave-vector components q_s and q_i. This allows for a significant reduction of the numerical complexity since the dependence of the transfer functions $\beta^{(2)}$ and $\tilde{\eta}^{(2)}$ describing the second crystal on the phase ϕ can be written analytically in terms of the transfer functions obtained when integrating the integro-differential equations (3.11) with $h^{(2)}$ without the phase term $\mathrm{e}^{\mathrm{i}\phi}$ or, equivalently, with Eqs. (3.36) and (3.37) and for $\phi = 0$. The transfer functions including the phase information, $\beta^{(2)}$ and $\tilde{\eta}^{(2)}$, are then connected to those that are obtained from the integration of the integro-differential equations without the phase factor, $\breve{\beta}^{(2)}$ and $\breve{\tilde{\eta}}^{(2)}$, via [1]

$$\beta^{(2)}(q, q') = \breve{\beta}^{(2)}(q, q')\, \mathrm{e}^{\mathrm{i}\phi}, \tag{3.41a}$$

$$\tilde{\eta}^{(2)}(q, q') = \breve{\tilde{\eta}}^{(2)}(q, q'). \tag{3.41b}$$

Here and in the following, the notation [4]

$$\check{x} \tag{3.42}$$

will be used for a quantity x (such as a transfer function or a Schmidt mode) that has been obtained by integrating the integro-differential equations without the phase term $\mathrm{e}^{\mathrm{i}\phi}$. By using Eqs. (3.41), it is no longer necessary to repeat the integration of the integro-differential equations for the second crystal for each value of the phase ϕ: If the transfer functions are obtained without accounting for the phase ϕ, it can be added by simply multiplying $\check{\beta}^{(2)}$ with $\mathrm{e}^{\mathrm{i}\phi}$, as indicated by Eq. (3.41a). Furthermore, this connection between the transfer functions allows for an analytical computation of the derivative of the integral intensity as required by Eq. (3.1).

For the compensated interferometer, it is possible to obtain further analytical insights. These are based on the fact that the diffraction compensation (more precisely, the focusing element) introduces a special symmetry in the system, due to which the transfer functions of both crystals are connected via [1]

$$\check{\beta}^{(2)}(q,q') = \beta^{(1)}(q',q), \tag{3.43a}$$

$$\check{\tilde{\eta}}^{(2)}(q,q') = \left[\tilde{\eta}^{(1)}(q',q)\right]^*, \tag{3.43b}$$

with $\check{\beta}^{(2)}$ and $\check{\tilde{\eta}}^{(2)}$ as defined above via Eqs. (3.41a) and (3.41b), respectively. The proof is provided in Ref. [1]. Using these relationships, it is possible to express all quantities related to the entire interferometer just in terms of the transfer functions of the first crystal. However, it should be emphasized that this requires that all properties such as the refractive indices, the parametric gain and the crystal lengths of both crystals are identical, see Sec. B.2.

Using Eqs. (3.41) and (3.43), the expressions for the expectation values of the signal intensity operator $\langle \hat{N}_s(q_s)\rangle$ and the corresponding covariance function $\mathrm{cov}(q_s,q_s')$ of the entire interferometer as written in Eqs. (3.27) and (3.29), respectively, can be expressed in the form [1]

$$\langle \hat{N}_s(q_s)\rangle = 4\cos^2\left(\frac{\phi}{2}\right)\int \mathrm{d}q'\ |\xi(q_s,q')|^2, \tag{3.44a}$$

$$\mathrm{cov}(q_s,q_s') = 16\cos^4\left(\frac{\phi}{2}\right)\left[\int \mathrm{d}\bar{q}\ |\xi(q_s,\bar{q})\,\xi^*(q_s',\bar{q})|^2\right] + \delta(q_s-q_s')\,\langle \hat{N}_s(q_s)\rangle\,, \tag{3.44b}$$

respectively, and with the newly defined function

$$\xi(q_s,q') = \int \mathrm{d}\bar{q}\,\beta^{(1)}(\bar{q},q_s)\left[\tilde{\eta}^{(1)}(\bar{q},q')\right]^*. \tag{3.44c}$$

Importantly, this function ξ no longer depends on ϕ and the full phase dependence is written out in Eqs. (3.44a) and (3.44b). Equations (3.44) reveal an additional advantage of the analytical treatment enabled by Eqs. (3.41): For $\phi \to \pi$, both the integral covariance and the derivative of the integral intensity with respect to ϕ will vanish. Both of these

quantities are required for the computation of the phase sensitivity, with the former being divided by the latter, see Eqs. (3.1) and (3.40). As ϕ approaches π, the expression for the phase sensitivity assumes the indeterminate form "0/0", leading to numerical instabilities which are difficult to resolve. With Eqs. (3.44), this division can be performed analytically since the limit as $\phi \to \pi$ can be evaluated without numerical methods.

Further simplifications for the integral intensity and covariance are possible by making use of the internal structure of the transfer functions that is described by their joint Schmidt decomposition, see Eqs. (3.20). Applying the decomposition to Eqs. (3.44) and evaluating the integrals over the transverse wave-vector components yields the following expressions for the integral intensity according to Eq. (3.39) and the integral covariance, as it appears under the square-root in Eq. (3.40) [1]:

$$\langle \hat{N}_{s,\mathrm{tot}} \rangle = 4\mathcal{A} \cos^2\left(\frac{\phi}{2}\right), \tag{3.45a}$$

$$\iint \mathrm{d}q_s \, \mathrm{d}q_s' \; \mathrm{cov}(q_s, q_s') = 4 \cos^2\left(\frac{\phi}{2}\right) \left[\mathcal{A} + 4\mathcal{B} \cos^2\left(\frac{\phi}{2}\right)\right], \tag{3.45b}$$

where $\hat{N}_{s,\mathrm{tot}} = \int \mathrm{d}q \, \hat{N}_s(q)$, see Eqs. (3.25) and (3.39), and with the two positive constants

$$\mathcal{A} = \sum_n \Lambda_n^{(1)} \left(1 + \Lambda_n^{(1)}\right), \tag{3.45c}$$

$$\mathcal{B} = \sum_n \left[\Lambda_n^{(1)} \left(1 + \Lambda_n^{(1)}\right)\right]^2. \tag{3.45d}$$

Hence, for the compensated SU(1,1) interferometer setup, the integral intensity and covariance of the SU(1,1) interferometer are fully defined by the phase ϕ and the Schmidt eigenvalues of the first crystal $\Lambda_n^{(1)}$. Note that $\mathcal{A} = 0$ and/or $\mathcal{B} = 0$ can only hold in the trivial case of $\Lambda_n^{(1)} = 0$ for all n, meaning that for this case, no PDC radiation is generated. This is generally not true for any nonzero value for the experimental gain and thus, it can normally be assumed that $\mathcal{A}, \mathcal{B} > 0$.

With Eqs. (3.45), the phase sensitivity can be analytically expressed in terms of these constants using Eqs. (3.1) and (3.40) [1]:

$$\Delta\phi = \frac{\sqrt{\mathcal{A} + 4\mathcal{B} \cos^2\left(\frac{\phi}{2}\right)}}{2\mathcal{A} \left|\sin\left(\frac{\phi}{2}\right)\right|}, \tag{3.46}$$

meaning that only $\mathcal{A}$ and $\mathcal{B}$ need to be computed numerically in order to determine the phase sensitivity. For the normalization with respect to the shot-noise level as in Eq. (3.4), the integral intensity of the first crystal can simply be calculated as

$$\langle \hat{N}_{s,\mathrm{tot}}^{(1)} \rangle = \sum_n \Lambda_n^{(1)}, \tag{3.47}$$

see Eqs. (3.20a), (3.27) and (3.39), meaning that the normalized phase sensitivity f can also be written purely in terms of ϕ and the $\Lambda_n^{(1)}$.

In order to develop a better understanding of the behavior of the phase sensitivity, the

constant $\mathcal{A}$ defined in Eq. (3.45c), said equation may be rewritten using Eq. (3.47) as [1]

$$\mathcal{A} = \left(1 + \frac{\langle \hat{N}^{(1)}_{s,\mathrm{tot}} \rangle}{K^{(1)}}\right) \langle \hat{N}^{(1)}_{s,\mathrm{tot}} \rangle, \tag{3.48}$$

where

$$K^{(1)} = \left[\sum_n \left(\bar{\Lambda}^{(1)}_n\right)^2\right]^{-1} \tag{3.49}$$

is the *Schmidt number* (*effective mode number*) of the first crystal, and where

$$\bar{\Lambda}^{(1)}_n = \frac{\Lambda^{(1)}_n}{\sum_k \Lambda^{(1)}_k} \tag{3.50}$$

are the normalized Schmidt eigenvalues of the first crystal.

Clearly, since the output intensity $\langle \hat{N}^{(1)}_{s,\mathrm{tot}} \rangle$ of the first crystal does not depend on the interferometer phase ϕ, the normalized phase sensitivity f is minimized for $\phi = \pi$, see Eq. (3.46). Hence, the minimal (optimal) phase sensitivity $f_{\min}$ can be written in terms of the integral intensity and the Schmidt number of the first crystal as [1]

$$f_{\min} = \frac{1}{2\sqrt{1 + \frac{\langle \hat{N}^{(1)}_{s,\mathrm{tot}} \rangle}{K^{(1)}}}}. \tag{3.51}$$

Therefore, in order to obtain an optimal phase sensitivity, the intensity output of the first crystal should be maximized, while the effective mode number should be reduced [1]. Furthermore, $f_{\min} < 1$ can be rearranged to $\langle \hat{N}^{(1)}_{s,\mathrm{tot}} \rangle / K^{(1)} > -3/4$, and thus, for compensated SU(1,1) interferometers, the optimal phase sensitivity always beats the shot-noise level since $\langle \hat{N}^{(1)}_{s,\mathrm{tot}} \rangle$ and $K^{(1)}$ are always positive.

For experimental purposes, it is important that the *supersensitivity region*, which is the phase range over which the phase sensitivity beats the shot-noise level ($f < 1$), is sufficiently broad to allow for stable measurements [2]. An analytical expression for the *supersensitivity region width* Δ was derived in Ref. [2] for a similar system and these results can be adapted to the interferometer as it is discussed in this chapter. The expression for Δ reads

$$\Delta = 2\pi - 4 \arctan\left(\sqrt{\frac{1 + 4\frac{\mathcal{B}}{\mathcal{A}}}{3 + 4\frac{\langle \hat{N}^{(1)}_{s,\mathrm{tot}} \rangle}{K^{(1)}}}}\right). \tag{3.52}$$

Details on how this expression was obtained are given in Sec. A.3.

3.5.2. Analytical Expressions for a Plane-Wave Pump

While the main focus of the results presented in this section will be on the phase sensitivity for a finite-width Gaussian pump, it should be noted that analogous results were also

presented in Ref. [1] for the case of a plane-wave pump. Since the intensity profiles for a plane-wave pump are very similar to the finite-width pump case and the covariance profiles basically follow the diagonal of the 2D covariance functions in the finite-width pump case, these will not be presented here. Instead, this detailed discussion can be found in Ref. [1] and, in this section, it will only be briefly demonstrated how these results were obtained.

Starting from the integro-differential equations (3.7), it is easy to see that the Gaussian transverse envelope approaches a Dirac delta for $\sigma \to \infty$ [1]:

$$\underbrace{\Gamma_0 \frac{\sigma}{\sqrt{2\pi}}}_{=\Gamma} \mathrm{e}^{-\frac{(q_s+q_i)^2\sigma^2}{2}} \xrightarrow{\sigma\to\infty} \Gamma_0 \delta(q_s + q_i), \tag{3.53}$$

where a factor $\sigma/\sqrt{2\pi}$ has to be split off from Γ and Γ_0 is the remaining theoretical gain parameter for the plane-wave case. The Dirac delta on the right-hand side in Eq. (3.53) removes the integrals in the integro-differential equations (3.7) in the limit $\sigma \to \infty$ and the resulting coupled differential equations can be solved analytically for a single crystal and both the compensated and non-compensated SU(1,1) interferometer setup. The appearing Dirac delta also implies strong correlations between the generated PDC photons: The wave vectors of the signal and idler photons are connected via $q_s = -q_i$.

A more rigorous derivation leading to the same expressions is possible by following Sharapova *et al.* [5] and initially assuming a plane-wave pump. The resulting set of first-order coupled *ordinary* (operator-valued) differential equations describing the evolution of the plane-wave operators is of the form [1]:

$$\frac{\mathrm{d}\hat{a}_s(q_s, L)}{\mathrm{d}L} = \Gamma_0 h_{\mathrm{pw}}(q_s, L)\, \hat{a}_i^\dagger(-q_s, L), \tag{3.54a}$$

$$\frac{\mathrm{d}\hat{a}_i^\dagger(-q_s, L)}{\mathrm{d}L} = \Gamma_0 h_{\mathrm{pw}}^*(q_s, L)\, \hat{a}_s(q_s, L), \tag{3.54b}$$

where

$$h_{\mathrm{pw}}(q_s, L) \overset{\mathrm{def.}}{=} h(q_s, -q_s, L) \tag{3.55}$$

and h on the right-hand side refers to the phase-matching function for the finite-width pump case as introduced in Sec. 3.3. Similar differential equations for the description of PDC have also been found by Klyshko [88]. Due to the strong correlations between the signal and idler photon wave-vectors, the system can be written purely in terms of the signal wave-vectors q_s since each signal photon with transverse wave-vector component q_s is connected to exactly one transverse idler wave-vector component $-q_i$. Analogous to Eqs. (3.10), the solutions are now of the form [1, 107–110]:

$$\hat{a}_s(q_s, L) = \tilde{\eta}_{\mathrm{pw}}(q_s, L)\, \hat{a}_s(q_s) + \beta_{\mathrm{pw}}(q_s, L)\, \hat{a}_i^\dagger(-q_s), \tag{3.56a}$$

$$\hat{a}_i^\dagger(-q_s, L) = \tilde{\eta}_{\mathrm{pw}}^*(-q_s, L)\, \hat{a}_i^\dagger(-q_s) + \beta_{\mathrm{pw}}^*(-q_s, L)\, \hat{a}_s(q_s). \tag{3.56b}$$

Similarly to the finite-width case, it is possible to arrive at a system of first-order coupled ordinary differential equations which is no longer operator-value by plugging Eqs. (3.56)

into Eqs. (3.54) [1]:

$$\frac{\mathrm{d}\beta_{\mathrm{pw}}(q_s,L)}{\mathrm{d}L} = \Gamma_0 h_{\mathrm{pw}}(q_s,L)\,\tilde{\eta}^*_{\mathrm{pw}}(-q_s,L), \tag{3.57a}$$

$$\frac{\mathrm{d}\tilde{\eta}^*_{\mathrm{pw}}(-q_s,L)}{\mathrm{d}L} = \Gamma_0 h^*_{\mathrm{pw}}(q_s,L)\,\beta_{\mathrm{pw}}(q_s,L). \tag{3.57b}$$

Similar to the finite-width case, writing the solutions as in Eqs. (3.56) requires that $h(q_s) = h(-q_s)$, see Sec. A.1.

Naively evaluating the expectation value of the photon-number operator $\hat{N}_s(q_s) = \hat{a}^\dagger_s(q_s)\,\hat{a}_s(q_s)$, where $\hat{a}_s$ is the solution of Eqs. (3.54) for the system under consideration, yields a divergent expression of the form [1]

$$\langle \hat{N}_s(q_s)\rangle = \left|\beta_{\mathrm{pw}}(q_s,L)\right|^2 \delta(0) \tag{3.58}$$

due to the Dirac-delta commutation relations of the plane-wave operators in the continuous limit, see Eq. (3.8a) and Eqs. (2.18). This issue has for example also been described by Gatti *et al.* [109], where it was also suggested to replace the divergent factor $\delta(0)$ with the reciprocal of the temporal and spatial bandwidth product of the pump. In Ref. [1] this issue was circumvented by considering photon number densities with respect to the transverse size of the system. As a consequence, in order to compute quantities such as the phase sensitivity via Eq. (3.1), it is necessary to provide a length L_x that when multiplied with the photon number densities yields a dimensionless quantity, the photon number. This length L_x can be understood in the sense that it filters out a certain length of the system's overall infinite number of emitted photons without modifying the photon statistics. The idea behind introducing this length L_x is similar to the introduction of a finite-size pupil over the output face of the crystal or interferometer, as suggested by Brambilla *et al.* [110]. Ultimately, the *finite* photon number density is given by [1]

$$\mathcal{N}_s(q_s) = |\beta_{\mathrm{pw}}(q_s,L)|^2. \tag{3.59}$$

Note that similar considerations are necessary in order to properly define the covariance function. Details regarding this can be found in Ref. [1].

Starting with a single crystal of length L_1, Eqs. (3.57) can be easily solved using h_{pw} defined via Eqs. (3.30) and (3.55). The solutions for the functions β_{pw} and $\tilde{\eta}_{\mathrm{pw}}$ are given by [1, 88]

$$\beta^{(1)}_{\mathrm{pw}}(q_s,L) = \frac{2\Gamma_0}{g(q_s)} \sinh\!\left(\frac{L_1 g(q_s)}{2}\right) \mathrm{e}^{\mathrm{i}\frac{\Delta k_{\mathrm{pw}}(q_s)L_1}{2}}, \tag{3.60a}$$

$$\tilde{\eta}^{(1)}_{\mathrm{pw}}(q_s,L) = \left[\cosh\!\left(\frac{L_1 g(q_s)}{2}\right) - \frac{\mathrm{i}\Delta k_{\mathrm{pw}}(q_s)}{g(q_s)} \sinh\!\left(\frac{L_1 g(q_s)}{2}\right)\right] \mathrm{e}^{\mathrm{i}\frac{\Delta k_{\mathrm{pw}}(q_s)L_1}{2}}, \tag{3.60b}$$

where

$$g(q_s) = \sqrt{4\Gamma_0^2 - \Delta k^2_{\mathrm{pw}}(q_s)} \tag{3.61}$$

and

$$\Delta k_{\mathrm{pw}}(q_s) \overset{\mathrm{def.}}{=} \Delta k(q_s, -q_s), \tag{3.62}$$

with $\Delta k(q_s, -q_s)$ being the phase mismatch for the finite-width pump case as given in Eqs. (3.31). From Eqs. (3.59) and (3.60a), it is then possible to obtain the well-known result for the photon number density of a single PDC section pumped with a plane-wave pump[5] [1, 88, 107, 108, 110]:

$$\mathcal{N}_s^{(1)}(q_s) = \left[\frac{2\Gamma_0}{g(q_s)} \sinh\left(\frac{L_1 g(q_s)}{2}\right)\right]^2. \tag{3.63}$$

In an analogous manner, the functions β_{pw} and $\tilde{\eta}_{\mathrm{pw}}$, as well as the photon number densities, the corresponding covariance functions and, ultimately, the phase sensitivities for the compensated and non-compensated SU(1,1) interferometer configurations were derived in Ref. [1]. Since, as mentioned above, the main focus in this work is on the finite-width case, only the phase sensitivities for a plane-wave pump will be presented and compared to the finite-width case in Sec. 3.5.4 below. The remaining details and results can be found in Ref. [1].

3.5.3. Intensity Profiles and Covariance Functions for a Finite-Width Pump

To get an understanding of the effect the diffraction compensation has on the interferometer, the first step is to compare the output intensity profiles for the non-compensated and the compensated setup for different experimental gain values G_{exp}. The experimental gain is defined in Sec. 3.4 and the concrete values in for the fit constant connecting the experimental gain and the theoretical gain parameter Γ can be found in Table 3.1 therein. Naturally, for the results that will be presented below, the pump envelope is given by a Gaussian whose intensity distribution has a FWHM of 50 µm, as was the case for the fit parameters presented in Table 3.1. Likewise, the interferometer consists of two crystals, each of length $L_1 = 2\,\mathrm{mm}$.

Figures 3.4(a)–3.4(c) show the intensity output profiles of a non-compensated SU(1,1) interferometer for several parametric gain values and at different interferometric phases ϕ. Instead of the transverse wave-vector components q_s, the profiles are plotted over the *external angle* θ_s, which is the emission angle of the photons as seen from outside the BBO crystal. For small θ_s, the transverse wave-vector component is connected to the angle via $\theta_s \approx q_s/k_s^{\mathrm{vac}}$, where k_s^{vac} is the modulus of the signal wave-vector in vacuum. These profiles are obtained numerically by integrating the integro-differential equations (3.11) for the first and the second crystal separately and then combining the solutions for the transfer functions as described in Sec. 3.2. The phase-matching functions are given by Eqs. (3.30) and (3.36) for the first and second crystal, respectively.

For $\phi = 0$, the profile is sinc^2-shaped for low gain and becomes more Gaussian as the

[5] The expression for $\mathcal{N}_s^{(1)}(q_s)$ provided in Eq. (3.63) is always real-valued since $\sinh(\mathrm{i}x) = \mathrm{i}\sin(x)$ for $x \in \mathbb{R}$ [111]. See also Ref. [1].

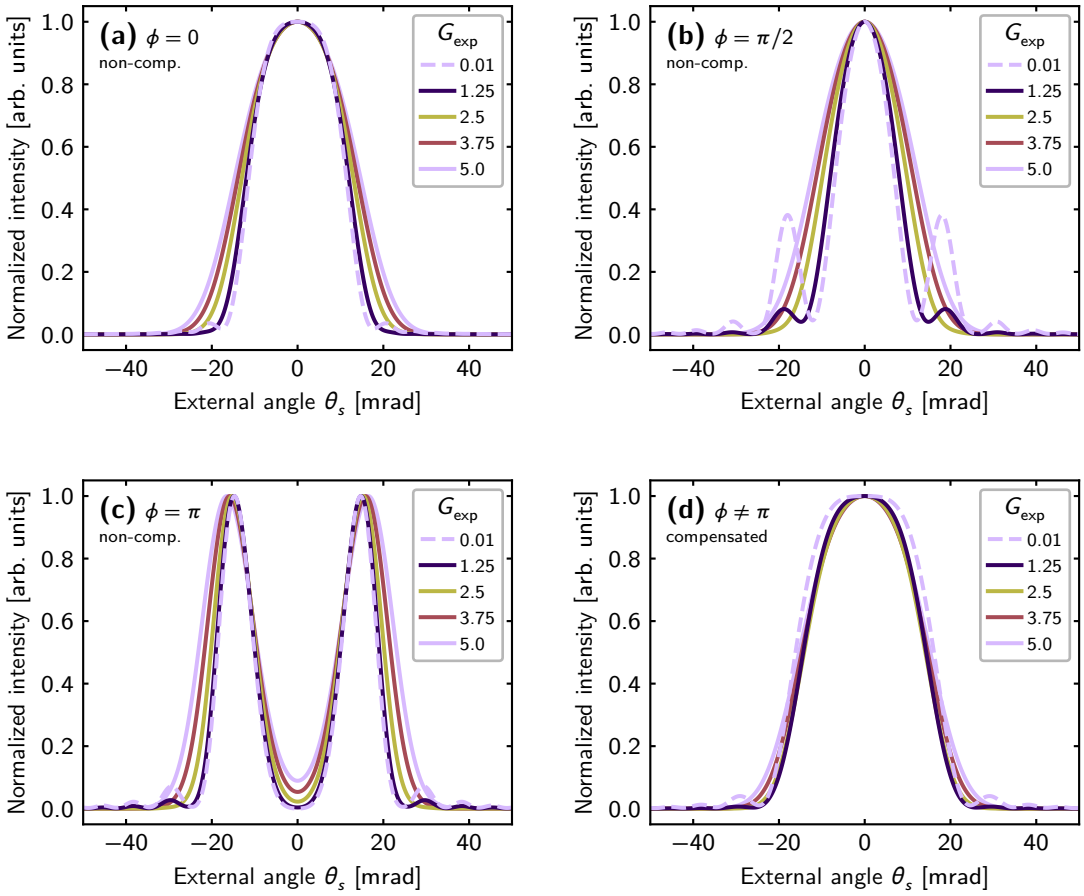

Figure 3.4: Intensity distributions for the [**(a)**–**(c)**] non-compensated interferometer for different phases ϕ and for the **(d)** compensated interferometer for $\phi \neq \pi$ for several experimental gain values G_{exp} and pumped with a pump with transverse Gaussian envelope with an intensity distribution FWHM of 50 µm. The profiles are normalized so that their peak value is 1. In the non-compensated case, for $\phi = 0$, the intensity profile is sinc^2-shaped for low gain and becomes more Gaussian as the gain is increased. As the phase approaches $\phi = \pi/2$, side peaks become more pronounced and as the phase approaches $\phi = \pi$, the intensity profile has a double-peak shape for all gains with a local minimum for the central angles. For the compensated interferometer, the intensity distribution is similarly shaped to the non-compensated interferometer at $\phi = 0$ and only scales as $\propto \cos^2(\phi/2)$ with the phase, see Eqs. (3.44a) and (3.45a). This also implies that the intensity is identically zero for $\phi = \pi$. Adapted from Ref. [1].

parametric gain increases. A similar behavior can be seen at the other two interferometric phases ϕ, where side peaks are suppressed with increasing gain. Furthermore, as the gain increases, the intensity profiles generally broaden. These observations have already been made in Sharapova *et al.* [5]. As the interferometric phase approaches $\phi = \pi$, the intensity profiles take on a shape with a double-peak structure, see Fig. 3.4(c). This is due to destructive interference, which appears for the central angles, but not for angles which are further away from the central direction. In short, the interference is *imperfect*, since there are still angles θ_s, for which the interference is not fully destructive.

For the compensated interferometer, the situation is more simple. Here, it is sufficient to compute the transfer functions $\beta^{(1)}$ and $\tilde{\eta}^{(1)}$ of a single crystal, which is the first crystal of the SU(1,1) interferometer. As described in Sec. 3.5.1, all relevant quantities of the entire interferometer can be expressed in terms of the transfer functions of the first crystal. The phase-matching function for this crystal is given in Eq. (3.30).

As was seen analytically from Eqs. (3.44a) and (3.44c), for fixed gain, the intensity profiles have a fixed shape which only scales as $\propto \cos(\phi/2)$ as the interferometric phase ϕ is varied. Hence, Fig. 3.4(d) shows the intensity profile for any interferometric phase except for $\phi = \pi$, for which the output intensity vanishes identically for all angles. Thus, compared to the non-compensated interferometer as described above, the interference is *perfect*ly destructive. As the parametric gain is increased, the intensity profiles show almost no broadening and only change shape from a sinc^2-shape at low gain to a more Gaussian shape at high gain. This is due to the fact that the effective number of modes decreases as the gain is increased, see Ref. [1] and Fig. 3.8 in Sec. 3.5.4 below.

The covariance functions $\mathrm{cov}(\theta_s, \theta_s')$ for the non-compensated and compensated interferometer setups are shown in Figs. 3.5(a) and 3.5(b), respectively, for several gain and phase values. For low gain, the plots show a clear diagonal line which represents the shot-noise term $\delta(q_s - q_s') \langle \hat{N}_s(q_s) \rangle$ as written in Eq. (3.29), while the other term contributes the ellipse-shaped region for $\phi = 0$ and $\phi = \pi/2$ and the circular shaped region for the non-compensated setup with $\phi = \pi$. This contribution dominates at higher gain, see the case $G_{\mathrm{exp}} = 3.75$, and the shot-noise term is no longer visible. Furthermore, at higher gain, the length of the minor axis of the ellipse-shaped contribution increases.

For the non-compensated setup, the ellipse-shaped contribution narrows slightly along its major axis and for $\phi = \pi$ it is split into two non-connected circular contributions, see Fig. 3.5(a). This behavior is analogous to the behavior of the intensity distribution, compare Fig. 3.4(c). Similarly, for the compensated setup, the covariance distribution is identically zero at $\phi = \pi$, see Eqs. (3.44), which is why the shown phase is $\phi = 0.995\pi$ instead. Furthermore, still analogous to the behavior of the intensity profiles shown in Fig. 3.4(d), the ellipse-shaped contribution does not change its shape as the phase is varied. As the phase approaches $\phi = \pi$, the shot-noise term contributes stronger to the function than the ellipse-shaped contribution. This can be confirmed from Eqs. (3.44a) and (3.44b): The ellipse-shaped contribution scales as $\propto \cos^4(\phi/2)$, while the shot-noise term scales as $\propto \cos^2(\phi/2)$ with the interferometric phase ϕ [1].

3.5.4. Phase Sensitivity

From the output intensity profiles and covariance functions for the output photons shown in Sec. 3.5.3, it is possible to compute the phase sensitivity $\Delta\phi$ and the corresponding normalized phase sensitivities f via Eqs. (3.1), (3.4) and (3.40). For the non-compensated setup, it is required to numerically obtain the transfer functions describing the entire interferometer, as was also the case for the intensity and covariance profiles, see Sec. 3.5.3. For the compensated setup, it is sufficient to compute the eigenvalues $\Lambda_n^{(1)}$ of a single

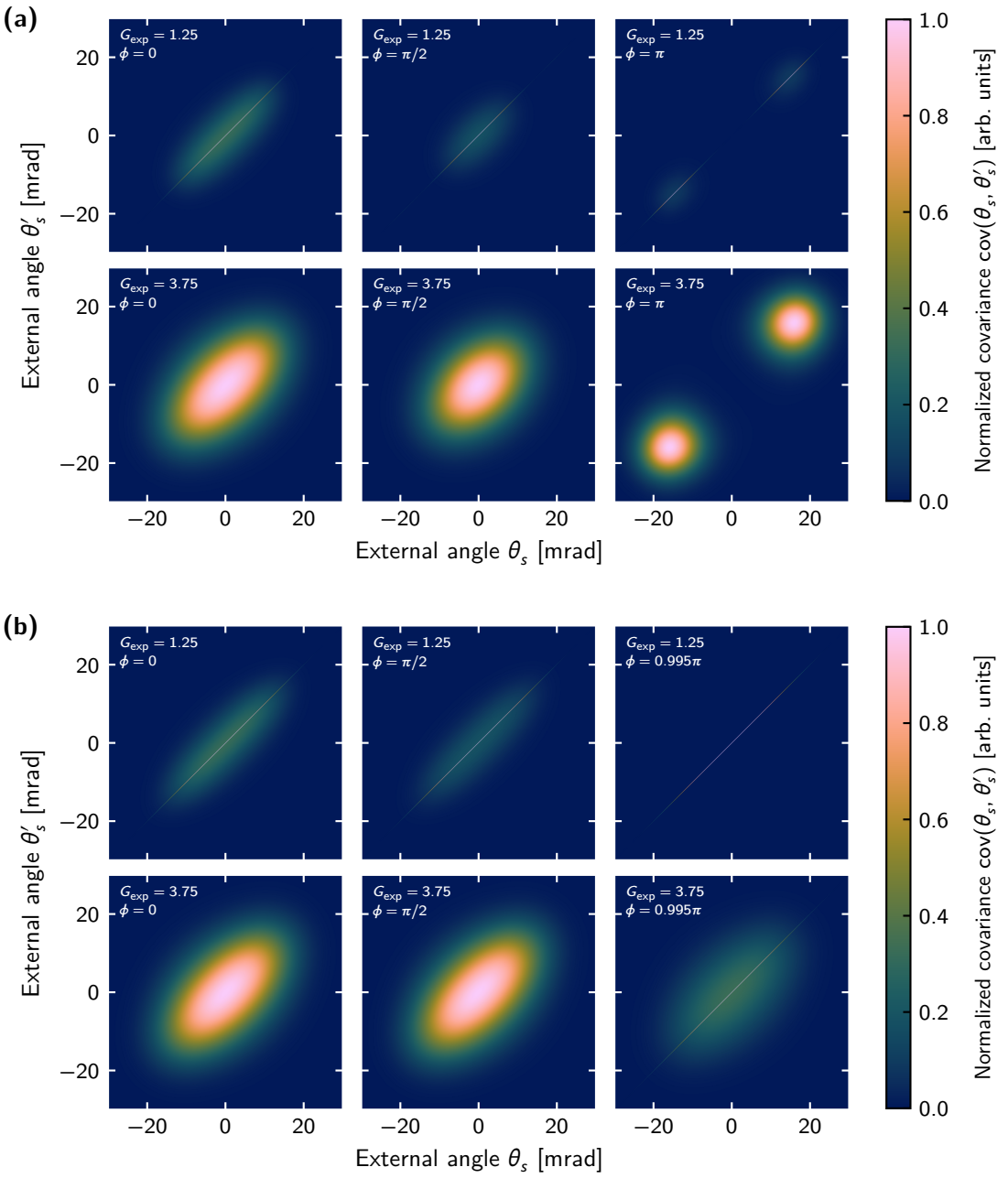

Figure 3.5: Plots of the covariance functions $\mathrm{cov}(\theta_s, \theta_s')$ of an SU(1,1) interferometer pumped with a pump with transverse Gaussian envelope with an intensity distribution FWHM of 50 µm, for the **(a)** non-compensated and for the **(b)** compensated SU(1,1) interferometer setup, for several experimental gain G_{exp} and interferometric phase values ϕ. Each plot is normalized so that the peak value $\max_{\theta_s, \theta_s'} \mathrm{cov}(\theta_s, \theta_s') = 1$. Note that for the compensated setup, the third column does not correspond to $\phi = \pi$, since for this phase the covariance function would be identically zero, see Eqs. (3.44b) and (3.44c). For low gain, a thin line along the diagonal of the plots representing the shot-noise term $\delta(q_s - q_s') \langle \hat{N}_s(q_s) \rangle$ as written in Eq. (3.29). One important aspect of the covariance distributions is their connection to an experimental procedure for obtaining approximations of the Schmidt modes as discussed in Eq. (4.86) and the surrounding text. Adapted from Ref. [1].

crystal (the first crystal of the interferometer), as was shown in Sec. 3.5.1. Equations (3.46) and (3.47), together with Eqs. (3.45c) and (3.45d) can then be used to compute f.

For the non-compensated interferometer, the phase sensitivity is shown for several experimental gain values G_{exp} over the *working point* phase ϕ in Fig. 3.6(b). Evidently, the phase sensitivity never surpasses the shot-noise level $f = 1$ for any phase ϕ and worsens as G_{exp} is increased. The optimal working points, where f is minimized, are located around $\phi = \pi$, which is the dark fringe of the interferometer where the output intensity is usually minimized. This is a common finding for SU(1,1) interferometers in the literature [6, 9, 27]. From Eq. (3.41a) and Eqs. (3.19) it is clear that the output intensity profiles, the covariance functions and therefore also f must be 2π-periodic with respect to ϕ. Thus, it is sufficient to consider a single period, which here is the interval $[0, 2\pi]$.

Figure 3.6(b) shows the phase sensitivities for the same gain values for the compensated interferometer setup around the optimal working point $\phi = \pi$. It can be seen from Eq. (3.46) that f is minimized for this point. Hence, the optimal working point is also located at the dark fringe for the compensated interferometer. Importantly, almost the entire approximately 60 mrad wide region shown in Fig. 3.6(b) lies below the shot-noise level at $f = 1$. Thus, unlike the non-compensated SU(1,1) interferometer setup, the compensated setup can beat the shot-noise level. In fact, as shown by Eqs. (3.51) and (3.52) and discussed in Sec. A.3, there always exists at least a single value for ϕ, for which $f \leq 1$. Furthermore, as the experimental gain is increased, the optimal phase sensitivity is strongly improved, while the width of the supersensitivity region (phase region that lies below $f = 1$) decreases. Similar to the compensated setup, the output intensity profiles, the covariance functions and f must be 2π-periodic with respect to ϕ. This can also be directly seen from Eq. (3.46). At the boundaries of each period interval, the phase sensitivity diverges: $\lim_{\phi \to 2\pi k} = \infty$ for $k \in \mathbb{Z}$, as can be seen from the inset plot in Fig. 3.6(b).

Note that similarly to the results discussed above for the finite-width pump, Ref. [1] also contains the corresponding results for a plane-wave pump. These results are not shown here and also not discussed in more detail since they closely resemble the corresponding finite-width pump results.

To get a better understanding of the relationship between the optimal phase sensitivity f_{min} and the supersensitivity region width Δ, both of these quantities are shown over a large range of the experimental gain G_{exp} in Figs. 3.7(a) and 3.7(b), respectively. Additionally to the results for a finite-width pump as described above, both figures also show the results for both quantities for a plane-wave pump, as they were presented in Ref. [1]. As mentioned in Sec. 3.5.2, it is necessary to define the transverse length parameter L_x in order to compute the phase sensitivity. This value L_x is chosen so that the integral output intensity of the first crystal for the plane-wave case coincides with the integral intensity for the finite-width case for the same value of G_{exp}. The concrete values of L_x in dependence on G_{exp} are presented and discussed in Ref. [1]. This choice implies that the Heisenberg limit for both cases is identical. Assuming that the Schmidt number $K^{(1)} \to 1$ as the experimental gain becomes large, it is clear from Eq. (3.51) that for high gain and

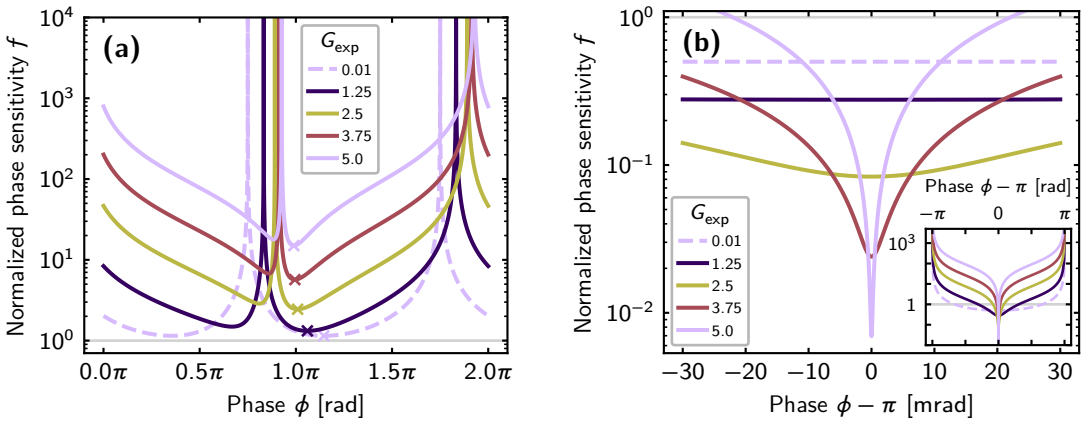

Figure 3.6: Calculated normalized phase sensitivity f for the **(a)** non-compensated and **(b)** compensated SU(1,1) interferometer over the working point phase ϕ, for several experimental gain values G_{exp}. For the non-compensated setup, the crosses mark the optimal working point, where f is minimized. The horizontal thin gray lines in all plots mark $f = 1$. For the compensated interferometer setup, the inset shows the full phase range from $\phi = 0$ to $\phi = 2\pi$. For both setups, f is 2π-periodic and only a single period is shown. Furthermore, on the full interval $[0, 2\pi]$, $f \to \infty$ for two phase values. For the compensated setup, this happens as $\phi \to 0$ and $\phi \to 2\pi$, which can be seen from the denominator in Eq. (3.46). Adapted from Ref. [1].

therefore large integral intensities of the first crystal $\langle \hat{N}^{(1)}_{s,\text{tot}} \rangle$,

$$f_{\text{min}} \approx \frac{1}{2\sqrt{\langle \hat{N}^{(1)}_{s,\text{tot}} \rangle}}. \tag{3.64}$$

The Heisenberg limit normalized with respect to the shot-noise level [compare also Eq. (3.4)] may be more precisely be defined as [1]:

$$f_{\text{HL}} = \frac{1}{2\sqrt{\langle \hat{N}^{(1)}_{s,\text{tot}} \rangle}}, \tag{3.65}$$

which defines the precise proportionality factor that was not written out in Eq. (3.5). As can be confirmed from Fig. 3.7(a), with this definition of f_{HL}, the optimal (minimal) phase sensitivity f_{min} as given in Eq. (3.51) asymptotically approaches f_{HL} for large experimental gain values G_{exp}. Additionally, Fig. 3.7(a) also shows the optimal phase sensitivity for the plane-wave pump case, which nearly coincides with the finite-width pump case for any gain and is only minimally larger. Clearly, as the experimental gain is increased, the phase sensitivity improves strongly for both the finite-width and plane-wave pump case. Physically, it is obvious that as the gain approaches zero, the integral output intensity of the first crystal vanishes: $\lim_{G_{\text{exp}} \searrow 0} \langle \hat{N}_{s,\text{tot}} \rangle = 0$. Hence, the Heisenberg limit for the phase sensitivity and the shot-noise level phase sensitivity diverge in the same limit: $\lim_{G_{\text{exp}} \searrow 0} f_{\text{HL}} = \infty$ and $\lim_{G_{\text{exp}} \searrow 0} f_{\text{SNL}} = \infty$, see Eqs. (3.65) and (3.3), respectively.

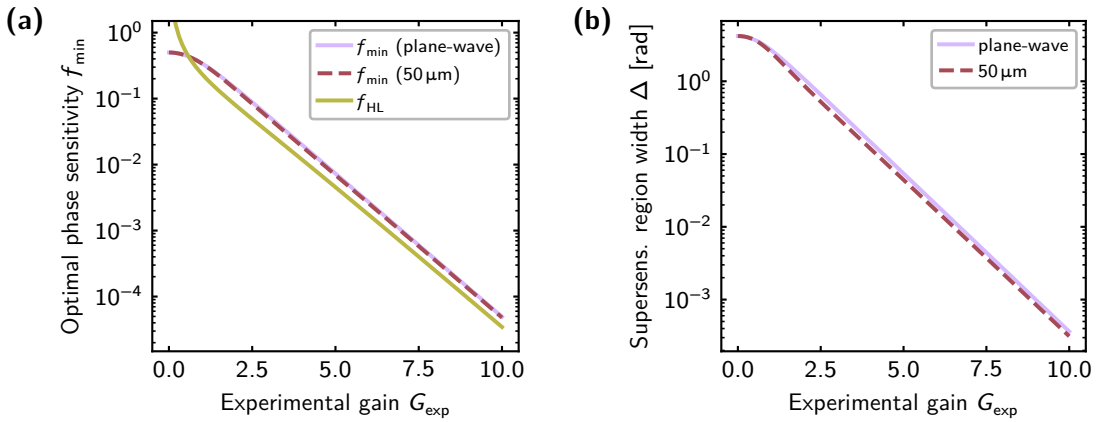

Figure 3.7: **(a)** Normalized optimal (minimal) phase sensitivities $f_{\min}$ for the finite-width pump as described in the text and for a plane-wave pump, both in comparison with the Heisenberg scaling as written in Eq. (3.65) and in dependence on the experimental gain G_{exp}. **(b)** Supersensitivity region width Δ in dependence on the experimental gain G_{exp} for the finite-width and plane-wave pump. For the finite-width pump, Δ is obtained from Eq. (3.52). More details on the plane-wave case can be found in the surrounding text, Sec. 3.5.2 and Ref. [1]. Adapted from Ref. [1].

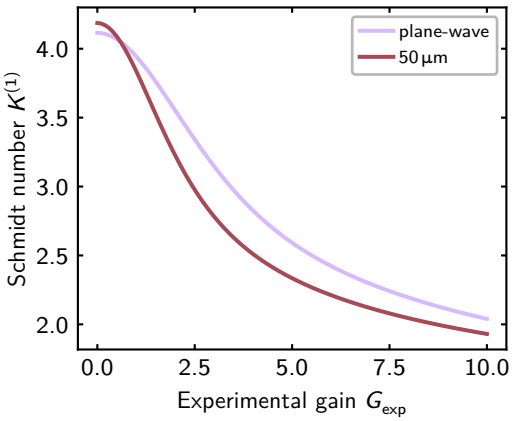

Figure 3.8: First-crystal Schmidt numbers $K^{(1)}$ for the finite-width pump with a transverse Gaussian intensity profile with a FWHM of its intensity distribution of 50 µm and for a plane-wave pump. For details regarding the definition of the Schmidt number in the plane-wave case see Ref. [1]. Adapted from Ref. [1].

Nevertheless, the calculated phase sensitivity remains finite as the gain approaches zero, compare Fig. 3.7(b) and Eq. (3.51), from which it becomes clear that $\lim_{G_{\mathrm{exp}} \searrow 0} f_{\min} = 1/2$, provided that $K^{(1)}$ remains finite as G_{exp} approaches zero[6] (compare Fig. 3.8).

As the experimental gain is increased, the supersensitivity region width Δ narrows quickly and decreases approximately by a factor of ten if G_{exp} is increased by two [1], see Fig. 3.7(b). Generally, a higher optimal phase supersensitivity comes at the cost of a narrower supersensitivity region width. If this region becomes too narrow, it is no longer possible to achieve stable measurements in experimental applications [2].

Even though the integral intensity output of the first crystal is equal for both the finite-

[6] This is not immediately obvious from the definition, see Eqs. (3.49) and (3.50), where the $\Lambda_n^{(1)}$ approach zero for vanishing experimental gain.

width and plane wave pump, both the optimal phase sensitivity $f_{\min}$ and the supersensitivity region width Δ differ slightly when comparing both cases, as discussed above. For $f_{\min}$, this can be understood by comparing the Schmidt numbers of the first crystal $K^{(1)}$ as shown in Fig. 3.8. For low gain, the Schmidt number for the finite-width pump is larger than for the plane-wave pump. At around $G_{\text{exp}} = 0.61$, both numbers coincide and for higher gains, the plane-wave pump leads to a larger Schmidt number than the finite-width pump. Thus, Eq. (3.51) predicts a slightly better optimal phase sensitivity for the finite-width case.

3.6. Conclusion

This chapter has introduced several fundamental concepts regarding SU(1,1) interferometers which will be used and investigated in more detail in the following chapters. Most importantly, in Sec. 3.2, the coupled integro-differential equations for the description of PDC at low and high parametric gain were introduced, along with the joint Schmidt decomposition of the transfer functions. The integro-differential equations were solved numerically in order to compare the phase sensitivity of two different potential setups for SU(1,1) interferometers. The simplest setup (non-compensated setup), consisting only of two consecutive crystals, shows no supersensitivity. That is, it does not surpass the shot-noise level. This is due to the diffraction of the signal and idler beams generated in the first crystal and their imperfect overlap with the pump and the radiation in the second crystal. This can be counteracted by introducing focusing elements between the two crystals or by using a single crystal and a spherical mirror, leading to compensated SU(1,1) interferometers. It has been shown that for these interferometers, it is possible to asymptotically achieve the Heisenberg scaling in the limit of high parametric gain. However, this comes at the cost of a strong reduction of the phase region where supersensitivity can be achieved, making it necessary to strike a balance between the phase sensitivity and the supersensitivity region width.

In order to improve these properties, Manceau *et al.* [9] suggests unbalancing the gain of the interferometer by increasing the gain of the second PDC section, which would lead to a broader supersensitivity region with and improved phase sensitivity. However, the authors also mention that this may lead to mode mismatches, since generally, as for example discussed in Sharapova *et al.* [5], the Schmidt modes are gain dependent[7]. This mode mismatch has been analyzed in more detail in Ref. [4] and this analysis will be presented in Chapter 4. Furthermore, the investigations presented in this chapter do not yet take losses into account, which are well known to degrade the sensitivity of SU(1,1) interferometers [6, 112]. Future studies could include these losses, for example using the formalism presented in Sec. 4.3.2 below.

[7] This is true for theoretical formalism including time-ordering effects. For Schmidt mode theory (utilized in Sharapova *et al.* [11] and Chapter 5), which neglects these effects, the Schmidt modes are gain-independent [see for example the derivations leading up to Eqs. (5.27)].

4

Simultaneous Measurement of Multimode Squeezing

While Chapter 3 was focused on the analysis of the phase sensitivity of SU(1,1) interferometers, this is not the only metrological application for which these interferometers can be used. Two further examples are Wigner function tomography as investigated in Kalash and Chekhova [29] and the measurement of multimode squeezed states as explored in Refs. [3, 4]. The latter example will be presented in this chapter. To this end, Sec. 4.1 will first introduce the concept of squeezing for both the single and multimode case. Additionally, this section will demonstrate how the joint Schmidt decomposition as previously introduced in Sec. 3.2, or, more precisely, its discrete analog, the Bloch-Messiah reduction, is linked to multimode squeezing. Immediately following that, it is first necessary to gain a good understanding of the modal structure of PDC systems and in particular SU(1,1) interferometers, in order to understand how the modes inside the interferometer interact. For this purpose, Sec. 4.2 will continue the fundamentals regarding the joint Schmidt decomposition mentioned in Sec. 3.2 and provide a thorough investigation into the modal layout of the aforementioned systems, as well as concrete examples of the Schmidt modes. Based on this, Sec. 4.3 constructs a measurement technique for multimode squeezed states generated in PDC and also connects the theoretical results with the experiment performed in Barakat *et al.* [3], while elaborating on its theoretical background.

4.1. Squeezing

Single-Mode Squeezing. *Squeezing* describes the reduction of the quantum uncertainty of one of the *quadratures* of a field mode at the expense of an increase in the uncertainty in the other quadrature. This can be illustrated as follows. For a single mode, described by

the annihilation operator $\hat{a}$ with [33]

$$[\hat{a}, \hat{a}^\dagger] = 1, \tag{4.1a}$$
$$[\hat{a}, \hat{a}] = 0, \tag{4.1b}$$
$$[\hat{a}^\dagger, \hat{a}^\dagger] = 0, \tag{4.1c}$$

the generic quadrature operator can be defined as [32]

$$\hat{p}_\vartheta = \frac{1}{2}\left(\hat{a}\mathrm{e}^{-\mathrm{i}\vartheta} + \hat{a}^\dagger \mathrm{e}^{\mathrm{i}\vartheta}\right), \tag{4.2}$$

where ϑ is the quadrature angle and with the two special cases [32, 33]

$$\hat{p}_0 = \hat{x} = \frac{1}{2}\left(\hat{a} + \hat{a}^\dagger\right), \tag{4.3a}$$
$$\hat{p}_{\frac{\pi}{2}} = \hat{y} = \frac{1}{2\mathrm{i}}\left(\hat{a} - \hat{a}^\dagger\right). \tag{4.3b}$$

Note that the above definitions, in particular the commutation relations of $\hat{a}$ in Eqs. (4.1), are not the same as those used in the rest of this work since they do not include the continuous limit[1], compare Sec. 2.2. The Heisenberg uncertainty principle in its general form states that the uncertainty product of two operators $\hat{P}$ and $\hat{Q}$ is bounded from below as [32, 33, 113]

$$\Delta^2\hat{P}\,\Delta^2\hat{Q} \geq \frac{1}{4}|\langle[\hat{P}, \hat{Q}]\rangle|^2, \tag{4.4}$$

where the uncertainties (variances) of the operators are given via[2]

$$\Delta^2\hat{P} = \langle\hat{P}^2\rangle - \langle\hat{P}\rangle^2. \tag{4.5}$$

For the vacuum state, the uncertainty product of the generalized quadrature operators $\hat{p}_\vartheta$ and $\hat{p}_{\vartheta+\frac{\pi}{2}}$ is bounded as

$$\Delta^2\hat{p}_\vartheta\,\Delta^2\hat{p}_{\vartheta+\frac{\pi}{2}} \geq \frac{1}{16}, \tag{4.6}$$

since $[\hat{p}_\vartheta, \hat{p}_{\vartheta+\frac{\pi}{2}}] = \mathrm{i}/2$. While the product of both uncertainties for the quadratures at the two angles is bound as written above, the actual squared uncertainty $\left(\Delta^2\hat{p}_\vartheta\right)^2$ for any ϑ can fall below $1/16$. If this is the case, the state is said to be a *squeezed state* [33]. An *ideal squeezed state* is a state where *equality* holds for the uncertainty product bound in Eq. (4.6) [33]. In this case, the uncertainty in the quadrature which is not squeezed is necessarily increased (*anti-squeezing*).

[1] In the continuous limit, the commutator of the plane-wave operator with its hermitian conjugate evaluated for the same mode is ill-defined and equals "$\delta(0)$" due to the unbounded volume of the system. Compare also the discussion around Eq. (3.58).

[2] This notation (using Δ^2) differs slightly from the one introduced in Eq. (3.2) for the standard deviation. It is kept here for consistency with Ref. [4] and to avoid expressions containing many parentheses due to the need to square the standard deviation.

Mathematically, squeezing is described by the unitary single-mode *squeeze operator* [32, 64, 92, 114]

$$\hat{S}_\xi = \mathrm{e}^{\frac{1}{2}\left[\xi^* \hat{a}^2 - \xi (\hat{a}^\dagger)^2\right]}, \tag{4.7}$$

where $\xi = r\mathrm{e}^{\mathrm{i}\theta}$ is the *squeeze parameter*, with $r > 0$ determining the strength of the squeezing and θ determining the squeezing angle [32]. Under the action of this operator, the plane-wave operators transform as [32, 92]

$$\hat{S}_\xi^\dagger \hat{a} \hat{S}_\xi = \hat{a} \cosh(r) - \hat{a}^\dagger \mathrm{e}^{\mathrm{i}\theta} \sinh(r), \tag{4.8a}$$

$$\hat{S}_\xi^\dagger \hat{a}^\dagger \hat{S}_\xi = \hat{a}^\dagger \cosh(r) - \hat{a} \mathrm{e}^{-\mathrm{i}\theta} \sinh(r). \tag{4.8b}$$

A *squeezed vacuum state* $|\xi\rangle$ is a state generated by applying the squeeze operator to the vacuum state: $|\xi\rangle = \hat{S}_\xi |0\rangle$. According to Eq. (21.3-13) of Mandel and Wolf [64], for this squeezed state,

$$\Delta^2 \hat{p}_\vartheta = \frac{1}{4} \left[\cosh(2r) - \sinh(2r) \cos(\theta - 2\vartheta)\right], \tag{4.9}$$

which readily follows from Eqs. (4.8). The uncertainty for the generalized quadrature in the squeezed state is (apart from the periodicity) minimized for $\vartheta = \vartheta_{\min} = \theta/2$ with the variance

$$\Delta^2 \hat{p}_{\frac{\theta}{2}} = \frac{1}{4} \mathrm{e}^{-2r}, \tag{4.10}$$

see Eq. (21.3-14) of the aforementioned reference. In contrast, for $\vartheta = \vartheta_{\max} = \vartheta_{\min} + \pi/2 = \theta/2 + \pi/2$, the variance is maximized,

$$\Delta^2 \hat{p}_{\frac{\theta}{2}+\frac{\pi}{2}} = \frac{1}{4} \mathrm{e}^{2r}, \tag{4.11}$$

corresponding to anti-squeezing. Historically, squeezed states were proposed for use in gravitational wave detection due to the fact that the uncertainty (or *quantum noise*) is reduced in one of their quadratures [92, 115]. This reduction enables a more sensitive measurement of the phase difference of the two arms inside interferometers, the same idea SU(1,1) interferometers are based on [16].

In addition to the squeeze operator, the displacement operator $\hat{D}_\alpha$ with the complex-valued displacement parameter α plays an important role in the discussion of states in quantum optics, for example for the generation of *squeezed coherent states*. However, the properties of these states are beyond the scope of this work and the displacement operator will not be needed[3].

Gaussian Unitaries and Squeezing in Multiple Modes. Squeezing as introduced above was restricted to a single mode described by a single annihilation operator $\hat{a}$. Importantly

[3] For further details, the standard literature, such as Gerry and Knight [32], Scully and Zubairy [33], and Mandel and Wolf [64] may be consulted.

however, the concept of squeezing can be extended to multiple modes. This is done as follows: Let $\hat{a}_1, \hat{a}_2, \ldots, \hat{a}_N$ be the annihilation operators describing the set of N discrete modes and let

$$\hat{\boldsymbol{a}} = \begin{bmatrix} \hat{a}_1 \\ \hat{a}_2 \\ \vdots \\ \hat{a}_N \end{bmatrix}, \tag{4.12a}$$

$$\hat{\boldsymbol{a}}^\dagger = \begin{bmatrix} \hat{a}_1^\dagger \\ \hat{a}_2^\dagger \\ \vdots \\ \hat{a}_N^\dagger \end{bmatrix}, \tag{4.12b}$$

so that the operator components of these vectors commute as [20, 64]

$$[\hat{a}_l, \hat{a}_m^\dagger] = \delta_{lm}\,, \tag{4.13a}$$

$$[\hat{a}_l, \hat{a}_m] = 0\,, \tag{4.13b}$$

$$[\hat{a}_l^\dagger, \hat{a}_m^\dagger] = 0\,. \tag{4.13c}$$

Then, a general N-mode squeezing operator may be defined as [116]:

$$\hat{\mathcal{S}}_Z = \mathrm{e}^{\frac{1}{2}\left[(\hat{\boldsymbol{a}}^\dagger)^{\mathrm{T}} Z \hat{\boldsymbol{a}}^\dagger - \hat{\boldsymbol{a}}^{\mathrm{T}} Z^{\mathrm{H}} \hat{\boldsymbol{a}}\right]}\,, \tag{4.14}$$

where $Z \in \mathbb{C}^{N\times N}$ and symmetric is the squeezing parameter matrix. Applying $\hat{\mathcal{S}}_Z$ to the vacuum state yields a multimode squeezed state: $|Z\rangle = \hat{\mathcal{S}}_Z|0\rangle$. The properties of this operator have been thoroughly investigated in the literature, see for example Ma and Rhodes [116] and Lo and Sollie [117]. However, in the context of this work, working with the multimode squeezing operator directly is not convenient due to its complex form and because a simple extension of the states under consideration enables the utilization of a much more powerful mathematical theoretical framework: Multimode squeezed states are a subset of a more general set of states, the Gaussian states.

A *Gaussian state* is any state whose Wigner function is a Gaussian function [114, 118]. Furthermore, any pure N-mode Gaussian state $|\Psi\rangle$ can be generated by applying an N-mode *Gaussian unitary transformation* $\hat{\mathcal{U}}$ to the vacuum state: $|\Psi\rangle = \hat{\mathcal{U}}|0\rangle$ [118, 119]. Generally, Gaussian unitaries and Hamiltonians which are at most quadratic in the operators are intrinsically connected. For such Hamiltonians, for example that of the PDC process, it can be shown that the time evolution of the system is described by a Gaussian unitary [116, 118]. A fundamental theorem in the theory of Gaussian unitaries is that of the Bloch-Messiah reduction [30, 31], which states that any $\hat{\mathcal{U}}$ can be decomposed (factorized) into a rotation mediated by the N-mode rotation operator

$$\hat{\mathcal{R}}_W = \mathrm{e}^{\mathrm{i}(\hat{\boldsymbol{a}}^\dagger)^{\mathrm{T}} W \hat{\boldsymbol{a}}}\,, \tag{4.15}$$

with the hermitian matrix $W \in \mathbb{C}^{N\times N}$, followed by an *independent* single-mode squeezing operation in each mode, another rotation and a single mode displacement operation independently in each mode. In the context of this work, this theorem provides an advantage compared to working with the multimode squeezing operator as written in

Eq. (4.7) since the structure of the states is better understood.

In terms of the creation and annihilation operators, *any* Gaussian unitary transformation can be written as [30]

$$\begin{bmatrix} \hat{\boldsymbol{a}}^{(\mathrm{out})} \\ \left[\hat{\boldsymbol{a}}^{(\mathrm{out})}\right]^{\dagger} \end{bmatrix} = \begin{bmatrix} \tilde{\mathrm{H}} & \mathrm{B} \\ \mathrm{B}^{*} & \tilde{\mathrm{H}}^{*} \end{bmatrix} \begin{bmatrix} \hat{\boldsymbol{a}}^{(\mathrm{in})} \\ \left[\hat{\boldsymbol{a}}^{(\mathrm{in})}\right]^{\dagger} \end{bmatrix} + \begin{bmatrix} \boldsymbol{\alpha} \\ \boldsymbol{\alpha}^{*} \end{bmatrix}, \tag{4.16}$$

where[4] $\tilde{\mathrm{H}}, \mathrm{B} \in \mathbb{C}^{N\times N}$ so that

$$\begin{bmatrix} \tilde{\mathrm{H}} & \mathrm{B} \\ \mathrm{B}^{*} & \tilde{\mathrm{H}}^{*} \end{bmatrix} \in \mathrm{Sp}(2N, \mathbb{C}), \tag{4.17}$$

with $\mathrm{Sp}(2N, \mathbb{C})$ denoting the (complex) *symplectic group* of $2N \times 2N$ matrices. The matrices $\tilde{\mathrm{H}}$ and B connect the input mode operators $\hat{a}_j^{(\mathrm{in})}$ [here stacked as a vector as written in Eqs. (4.12)] to the output operators in $\hat{\boldsymbol{a}}^{(\mathrm{out})}$. The condition in Eq. (4.17) ensures that the commutation relations of the annihilation operators as written in Eqs. (4.13) are preserved by the transformation and its inverse. For $\tilde{\mathrm{H}}, \mathrm{B} \in \mathbb{C}^{N\times N}$, it can equivalently be written as either of the following set of conditions[5] [4, 30, 31]

$$\tilde{\mathrm{H}}^{\mathrm{H}}\tilde{\mathrm{H}} - \mathrm{B}^{\mathrm{T}}\mathrm{B}^{*} = I_N, \tag{4.18a}$$
$$\tilde{\mathrm{H}}^{\mathrm{H}}\mathrm{B} - \mathrm{B}^{\mathrm{T}}\tilde{\mathrm{H}}^{*} = 0, \tag{4.18b}$$

or

$$\tilde{\mathrm{H}}\tilde{\mathrm{H}}^{\mathrm{H}} - \mathrm{B}\mathrm{B}^{\mathrm{H}} = I_N, \tag{4.19a}$$
$$\tilde{\mathrm{H}}\mathrm{B}^{\mathrm{T}} - \mathrm{B}\tilde{\mathrm{H}}^{\mathrm{T}} = 0, \tag{4.19b}$$

where I_N denotes the $N \times N$ identity matrix. Equations (4.18) ensure that the commutation relations are preserved for the transformation as written in Eq. (4.16), while Eqs. (4.19) ensure that the same holds for the inverse transform [30]. The vector $\boldsymbol{\alpha} \in \mathbb{C}^N$ in Eq. (4.16) is related to the displacement [30] and will be neglected in the following, since the states under consideration do not required it. It is well known that the matrices $\tilde{\mathrm{H}}$ and B admit the *Bloch-Messiah decomposition* (also called *Euler decomposition*) [4, 20, 30, 120]

$$\mathrm{B} = U\Sigma\Psi^{\mathrm{T}}, \tag{4.20a}$$
$$\tilde{\mathrm{H}} = U\tilde{\Sigma}\Psi^{\mathrm{H}}, \tag{4.20b}$$

with U and Ψ being two unitary matrices related to the two rotations of the factorization of the transformation and where $\Sigma = \mathrm{diag}\left(\sqrt{\Lambda_1}, \sqrt{\Lambda_2}, \ldots, \sqrt{\Lambda_N}\right)$ and $\tilde{\Sigma} = \mathrm{diag}\left(\sqrt{\tilde{\Lambda}_1}, \sqrt{\tilde{\Lambda}_2}, \ldots, \sqrt{\tilde{\Lambda}_N}\right)$, with $\Lambda_j \geq 0$ and $\tilde{\Lambda}_j = \Lambda_j + 1$. Note that both Eqs. (4.20a)

[4] The two letters H and B are the capital versions of the Greek letters η and β, respectively, and not the Latin letters H and B. The Latin letters are italicized, while the Greek letters are not.

[5] Equations (4.18a), (4.18b), (4.19a) and (4.19b) are the discretized versions of Eqs. (D3a), (D3b), (A3a) and (A3b) of Ref. [1], respectively. See also Sec. A.4, which shows these relations for the three-dimensional continuous and discrete cases.

and (4.20b) have the form of an SVD of the matrices $\tilde{\mathrm{H}}$ and B, respectively. However, both decompositions are not independent and connected by the fact that the left-hand side unitary U is equal in both cases, while the right-hand side unitary is element-wise complex conjugated when switching between B and $\tilde{\mathrm{H}}$. Analogously to the SVD, Σ and $\tilde{\Sigma}$ are usually also defined in such a way that the singular values $\sqrt{\Lambda_j}$ and $\sqrt{\tilde{\Lambda}_j}$ appear on the diagonals Σ and $\tilde{\Sigma}$, respectively, in descending order. A numerical algorithm for obtaining U and Ψ^{H} from $\tilde{\mathrm{H}}$ and B from two independent SVDs of the two matrices is outlined in Ref. [4]. This is the algorithm used in the rest of this chapter when the Schmidt modes are discussed in more detail. See also Houde *et al.* [120] for additional information regarding this decomposition.

The choice of the variable names in Eqs. (4.16) and (4.20) highlights the connection of this decomposition to the joint Schmidt decomposition as written in Eqs. (3.20): The matrices $\tilde{\mathrm{H}}$ and B are the discrete counterparts of the transfer functions $\tilde{\eta}$ and β, respectively, while Σ and $\tilde{\Sigma}$ contain the singular values. Similarly, the transformation written in Eq. (4.16) is the discrete version of the input-output relations for the plane-wave operators as written in Eqs. (3.10) and (3.16) for the degenerate case, where $\hat{a}_s = \hat{a}_i$.

In the decomposition, the two unitary matrices correspond to the rotations, while the following multiplications with the singular value matrices corresponds to the squeezing operation in each mode, as investigated in more detail in the following. After plugging the decomposition in Eqs. (4.20) back into Eq. (4.16) and setting $\boldsymbol{\alpha} = \mathbf{0}$ as described above, the upper and lower halves of the resulting vectors are given by

$$\hat{\boldsymbol{a}}^{(\mathrm{out})} = U\tilde{\Sigma}\Psi^{\mathrm{H}}\hat{\boldsymbol{a}}^{(\mathrm{in})} + U\Sigma\Psi^{\mathrm{T}}\left[\hat{\boldsymbol{a}}^{(\mathrm{in})}\right]^{\dagger}, \tag{4.21a}$$

$$\left[\hat{\boldsymbol{a}}^{(\mathrm{out})}\right]^{\dagger} = U^{*}\Sigma\Psi^{\mathrm{H}}\hat{\boldsymbol{a}}^{(\mathrm{in})} + U^{*}\tilde{\Sigma}\Psi^{\mathrm{T}}\left[\hat{\boldsymbol{a}}^{(\mathrm{in})}\right]^{\dagger}, \tag{4.21b}$$

respectively. Multiplying Eqs. (4.21a) and (4.21b) with U^{H} and U^{T} from the left, respectively, and defining

$$\hat{\boldsymbol{A}}^{(\mathrm{in})} = \begin{bmatrix} \hat{A}_1^{(\mathrm{in})} \\ \hat{A}_2^{(\mathrm{in})} \\ \vdots \\ \hat{A}_N^{(\mathrm{in})} \end{bmatrix} \overset{\mathrm{def.}}{=} \Psi^{\mathrm{H}}\hat{\boldsymbol{a}}^{(\mathrm{in})}, \tag{4.22a}$$

$$\hat{\boldsymbol{A}}^{(\mathrm{out})} = \begin{bmatrix} \hat{A}_1^{(\mathrm{out})} \\ \hat{A}_2^{(\mathrm{out})} \\ \vdots \\ \hat{A}_N^{(\mathrm{out})} \end{bmatrix} \overset{\mathrm{def.}}{=} U^{\mathrm{H}}\hat{\boldsymbol{a}}^{(\mathrm{out})}, \tag{4.22b}$$

yields[6]

$$\hat{\boldsymbol{A}}^{(\mathrm{out})} = \tilde{\Sigma}\hat{\boldsymbol{A}}^{(\mathrm{in})} + \Sigma\left[\hat{\boldsymbol{A}}^{(\mathrm{in})}\right]^{\dagger} \tag{4.23}$$

and its hermitian conjugate. Equation (4.23) is the discrete version of the Bogoliubov transformation for the Schmidt operators in the degenerate case, which are here stacked in the vectors $\hat{\boldsymbol{A}}^{(\mathrm{in})}$ and $\hat{\boldsymbol{A}}^{(\mathrm{out})}$, compare Eqs. (3.23) and (3.24) and Eq. (4.31) below. This connection to the continuous case can be more directly seen by writing the unitary

[6] Note that in the notation used above, $U^{\mathrm{T}}\left[\hat{\boldsymbol{a}}^{(\mathrm{out})}\right]^{\dagger} = \left[U^{\mathrm{H}}\hat{\boldsymbol{a}}^{(\mathrm{out})}\right]^{\dagger}$ and $\Psi^{\mathrm{T}}\left[\hat{\boldsymbol{a}}^{(\mathrm{in})}\right]^{\dagger} = \left[\Psi^{\mathrm{H}}\hat{\boldsymbol{a}}^{(\mathrm{in})}\right]^{\dagger}$.

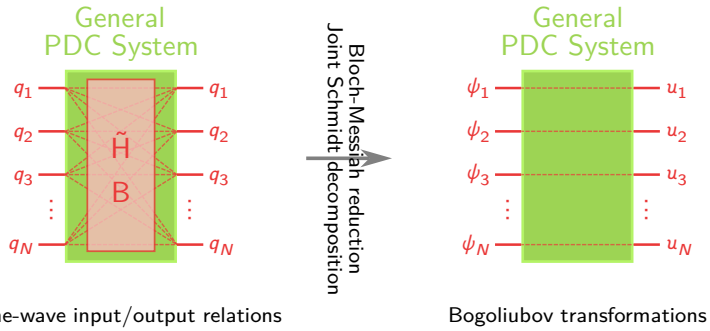

Figure 4.1: Left: For a discrete set of N plane-wave modes labeled by their transverse wave-vector components q_j ($j = 1, \dots, N$), the matrices $\tilde{H}$ and B describe their coupling during the PDC process inside the PDC system, as indicated by the red dashed lines. Right: After applying the Bloch-Messiah reduction of the matrices $\tilde{H}$ and B (joint Schmidt decomposition of the transfer functions in the continuous case) the input modes ψ_j and the output modes u_j are connected via the Bogoliubov transformations as written in Eqs. (3.23) and (4.31) which only couple input and output modes with the same index, as indicated by the horizontal red dashed lines over the PDC section.

matrices U and Ψ in terms of their columns [4]:

$$U = \begin{bmatrix} \boldsymbol{u}_1 & \boldsymbol{u}_2 & \cdots & \boldsymbol{u}_N \end{bmatrix}, \tag{4.24a}$$

$$\Psi = \begin{bmatrix} \boldsymbol{\psi}_1 & \boldsymbol{\psi}_2 & \cdots & \boldsymbol{\psi}_N \end{bmatrix}, \tag{4.24b}$$

meaning

$$u_j(q) \leftrightarrow \boldsymbol{u}_j = \begin{bmatrix} u_j(q_1) \\ u_j(q_2) \\ \vdots \\ u_j(q_N) \end{bmatrix}, \tag{4.25a}$$

$$\psi_j(q) \leftrightarrow \boldsymbol{\psi}_j = \begin{bmatrix} \psi_j(q_1) \\ \psi_j(q_2) \\ \vdots \\ \psi_j(q_N) \end{bmatrix}. \tag{4.25b}$$

This means that in the continuous case, transitioning from the plane-wave operators to the Schmidt operators corresponds to incorporating the rotations mediated by U and Ψ into new operators. As a result, the input-output relations with the newly defined Schmidt operators is diagonal in the mode index, as already seen from the Bogoliubov transformations in the continuous case, compare Eqs. (3.23).

The major difference between both cases is that in the discrete case, the number of Schmidt mode is finite, while in the continuous case, the number of modes is countably infinite. Between the two rotations, according to the theorem describing the Bloch-Messiah reduction, single-mode squeezing is applied to each mode independently. Thus, each Schmidt mode is squeezed independently of the other Schmidt modes. This diagonalization procedure is illustrated in Fig. 4.1.

Transitioning back to the continuous case, the above results suggest that the generalized quadratures for the Schmidt operators should be defined analogously to the single mode

case, that is, for each mode independently, compare Eq. (4.2) [4]:

$$\hat{P}_{l,\vartheta} = \hat{A}_l \mathrm{e}^{-\mathrm{i}\frac{\vartheta}{2}} + \hat{A}_l^\dagger \mathrm{e}^{\mathrm{i}\frac{\vartheta}{2}}. \tag{4.26}$$

Note that here, the factor 1/2 has been dropped compared to the single mode definition in Eq. (4.2) and a factor 1/2 has been added to the exponent for consistency with Ref. [4]. These quadrature operators at ϑ and $\vartheta + \pi$ commute as

$$[\hat{P}_{l,\vartheta}, \hat{P}_{l,\vartheta+\pi}] = 2\mathrm{i}, \tag{4.27}$$

meaning that the uncertainty relation for these quadratures is given by

$$\Delta^2 \hat{P}_{l,\vartheta}\, \Delta^2 \hat{P}_{l,\vartheta+\pi} \geq 1, \tag{4.28}$$

compare Eq. (4.4). Thus, if $\Delta^2 \hat{P}_{l,\vartheta} < 1$ for any ϑ, the state inside the mode is a squeezed state. The variance of the quadrature of the lth mode for an arbitrary state is given by [4]

$$\Delta^2 \hat{P}_{l,\vartheta} = 1 + 2\langle \hat{A}_l^\dagger \hat{A}_l \rangle + 2\,\mathrm{Re}\Big[\big(\langle \hat{A}_l \hat{A}_l \rangle - \langle \hat{A}_l \rangle^2\big)\, \mathrm{e}^{-\mathrm{i}\vartheta}\Big]. \tag{4.29}$$

It can be easily seen that the minimum and the maximum of $\Delta^2 \hat{P}_{l,\vartheta}$, reflecting squeezing and anti-squeezing, respectively, necessarily lie apart by π (apart from the periodicity): Equation (4.29) can be rewritten as

$$\Delta^2 \hat{P}_{l,\vartheta} = 1 + 2\langle \hat{A}_l^\dagger \hat{A}_l \rangle + 2\,\big|\langle \hat{A}_l \hat{A}_l \rangle - \langle \hat{A}_l \rangle^2\big| \cos(\Xi_l - \vartheta), \tag{4.30}$$

where $\Xi_l = \arg\big(\langle \hat{A}_l \hat{A}_l \rangle - \langle \hat{A}_l \rangle^2\big)$. Since $\langle \hat{A}_l^\dagger \hat{A}_l \rangle \geq 0$, the above expression is minimized for $\Xi_{l,\min} = 2\pi\,(n + 1/2)$, for $n \in \mathbb{Z}$ and maximized for $\Xi_{l,\max} = 2\pi n$, for $n \in \mathbb{Z}$, which lie apart by $\pi + 2\pi m$, for some $m \in \mathbb{Z}$.

In the degenerate regime, where the signal and idler plane-wave modes are indistinguishable, the Bogoliubov transformations in Eqs. (3.23) reduce to

$$\hat{A}_n^{(\mathrm{out})} = \sqrt{\tilde{\Lambda}_n}\, \hat{A}_n^{(\mathrm{in})} + \sqrt{\Lambda_n}\, \big[\hat{A}_n^{(\mathrm{in})}\big]^\dagger, \tag{4.31}$$

since then $\hat{B}_l = \hat{A}_l$, as described above. Equation (4.31) is the continuous-case analog of Eq. (4.23). For a single PDC section or the first PDC section of an SU(1,1) interferometer operating in this regime, the input Schmidt mode operators are connected to the vacuum plane-wave operators, while the output Schmidt mode operators result from the input operators via the Bogoliubov transformation in Eq. (4.31). Thus, for this particular case, [4]

$$\Delta^2 \hat{P}_{l,\vartheta} = 1 + 2\Lambda_l + 2\sqrt{\tilde{\Lambda}_l \Lambda_l}\, \cos(\vartheta). \tag{4.32}$$

The eigenvalues of the joint Schmidt decomposition can be parametrized as [80]

$$\Lambda_l = \sinh^2(r_l), \tag{4.33a}$$
$$\tilde{\Lambda}_l = \cosh^2(r_l). \tag{4.33b}$$

Clearly, with this parametrization, Eq. (4.32) takes a similar form to the variance of a single squeezed vacuum state, compare Eq. (4.9). The variance is given by

$$\Delta^2 \hat{P}_{l,\vartheta} = \cosh(2r_l) + \sinh(2r_l)\cos(\vartheta), \tag{4.34}$$

meaning that the parameter r_l is the modulus of the squeezing parameter of the mode l. The minimal and maximal values for the quadrature variance occur at $\vartheta = \pi$ and $\vartheta = 0$, respectively, and are given by

$$\min_{\vartheta} \Delta^2 \hat{P}_{l,\vartheta} = \mathrm{e}^{-2r_l}, \tag{4.35a}$$

$$\max_{\vartheta} \Delta^2 \hat{P}_{l,\vartheta} = \mathrm{e}^{2r_l}, \tag{4.35b}$$

respectively, further confirming the role of r_l as the modulus of the squeezing parameter.

4.2. Schmidt Mode Structure of PDC Systems

Before investigating the multimode squeezing in PDC systems described by the integro-differential equations as discussed in Sec. 3.2, it is helpful to analyze the Schmidt mode structure of a single crystal and an SU(1,1) interferometer with diffraction compensation in more detail. While the Schmidt decomposition for these types of systems was introduced in Sec. 3.2, the actual intensity and phase profiles of the modes have not yet been investigated. This will be addressed in the following. For simplicity, the theoretical analysis assumes a Gaussian pump so that the half width of the waist ($1/\mathrm{e}^2$-radius) of its intensity distribution is 70 µm, meaning $\sigma = \left(70/\sqrt{2}\right)$µm [compare Eqs. (3.11)]. The crystal length of the single crystal and each crystal of the interferometer will be $L_1 = 3\,\mathrm{mm}$.

For these parameters, the fitting constant connecting the theoretical and experimental gain (compare Sec. 3.4) is given by $A = 142.12$. For simplicity, this value will be used for both the low and high gain regime, even though, as was seen in Sec. 3.4, the fitting constant varies if the fit is performed in either regime alone. Similar to Ref. [2], where for a portion of the results the fitting constants for the low and high gain regime were averaged, considering only one fitting constant for both the low and high gain regime is justified by the fact that in experimental setups, the measurement error in determining A is usually large and would be smaller than the error introduced by neglecting that A may be different for both regimes.

4.2.1. Single Crystal

Before considering the full interferometer consisting of two crystals, it is instructive to consider a single crystal, which is the simplest nontrivial PDC system described by the integro-differential equations. As was the case in Chapter 3, the signal and idler photons are assumed to be distinguishable in some degree of freedom, while the refractive indices for the signal and idler plane-wave modes are assumed to be identical [compare also Sec. 3.2]. This means that in the theoretical description, there exists only one set of transfer functions β

and $\tilde{\eta}$ instead of two sets of two transfer functions. The transfer functions are obtained by integrating the integro-differential equations using the phase-matching function of a single crystal [Eq. (3.30)] over $[0, L_1]$. The joint Schmidt decomposition [Eqs. (3.20)] is then applied to the transfer functions, yielding the input Schmidt modes ψ_n and the output Schmidt modes u_n of the crystal, as well as the eigenvalues Λ_n and $\tilde{\Lambda}_n$ of β and $\tilde{\eta}$, respectively. Details on how the decomposition is implemented numerically in the context of this work can be found in Ref. [4].

Figure 4.2 shows the modulus and the phase profile (first and second column, respectively) of the first input mode (ψ_0) and the first output mode (u_0) at increasing experimental gain. The modes are plotted over the external angle $\theta_s \approx q_s/k_s^{\text{air}}$, as was also the case in Sec. 3.5.3 for the intensity profiles. Evidently, the modulus of both the input and output modes visually coincides for fixed gain, which was previously also observed in the frequency domain in Christ *et al.* [80]. Additionally, as already described in Sharapova *et al.* [5], the modulus of the modes broadens as the experimental gain is increased, which is one of the key properties of the theory of the integro-differential equations for the description of PDC. Similarly, the phase profile of the input mode ψ_0 flattens as the gain is increased, while that of the output modes steepens. As a result, the input modes have flatter phase profiles than the output modes at high gain. At low gain, $G_{\text{exp}} = 0.01$, the input and output modes coincide fully.

In order to get a better understanding of the behavior of the higher order modes in dependence on the experimental gain, the overlap integral of the input and output modes can be considered. This leads to the definition of the *same-crystal overlap coefficient* [4]:

$$\mathfrak{c}_{lm} \overset{\text{def.}}{=} \int \mathrm{d}q\, u_l(q)\, \psi_m^*(q). \tag{4.36}$$

The modulus squared of the overlap coefficient, $|\mathfrak{c}_{lm}|^2$ can be understood as a measure for the similarity of the output mode l and the input mode m. Plots of the modulus square of the first 15×15 elements of the overlap coefficient matrix are shown in the third column in Fig. 4.2.

For low gain, the input and output modes coincide, as evident from the fact that the modulus squared of $\mathfrak{c}_{lm}$ is diagonal. This can also be shown analytically by performing a first-order perturbation expansion of the integro-differential equations, as presented in Sec. A.5. At low gain, the transfer function β coincides with the two-photon amplitude of the system. As such, β is symmetric in the wave-vector arguments as long as the product of the pump function and the phase-matching function as appearing in the integro-differential equations (3.7) is symmetric in the wave-vector arguments. Since $\beta(q, q') = \beta(q', q)$, the transfer function allows for a decomposition of the form

$$\beta(q, q') = \sum_n \sqrt{\Lambda_n}\, u_n(q)\, u_n(q'), \tag{4.37a}$$

that is, with identical input and output modes. Furthermore, as shown in Eq. (A.91c), for low gain, $\tilde{\eta}(q, q') \approx \delta(q - q')$. Therefore, Eq. (4.37a) forms a joint Schmidt decomposition

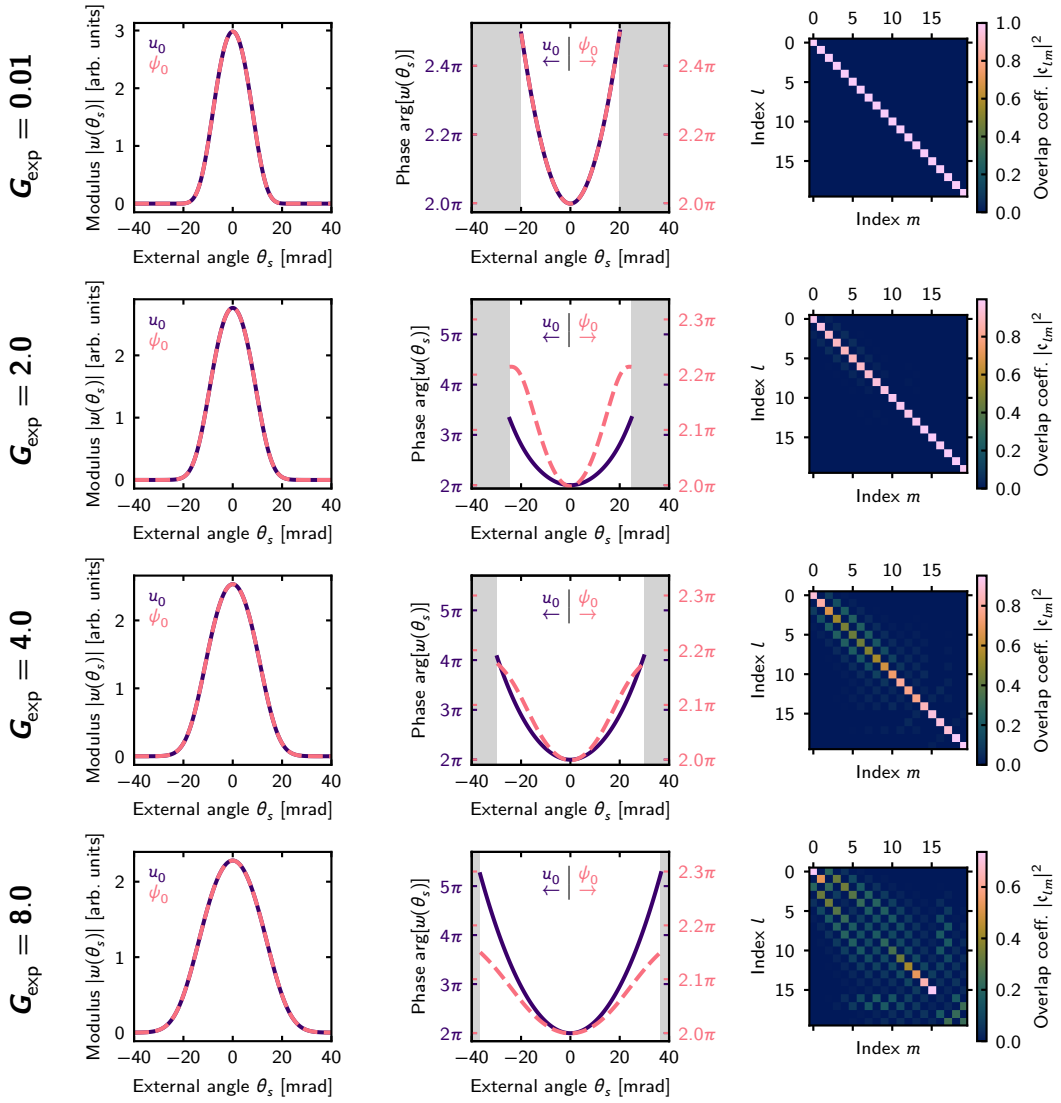

Figure 4.2: Plots of the modulus of the first input (ψ_0) and output (u_0) mode (left column), its phase distribution (middle column) and the modulus squared of the first 15×15 entries of the overlap coefficient matrix $\mathfrak{c}_{lm}$ of a single PDC section pumped at increasing experimental gain from top to bottom. Following the left column, it is clear that at increasing gain, the Schmidt modes broaden. This is a well-known result for example already described in Sharapova *et al.* [5] and Christ *et al.* [80] for the frequency domain. The phases of the first input and first output mode coincide at low gain and become more dissimilar as the gain is increased. The gray margins indicate the regions up to which the modulus of the modes has decreased by a factor of 10^{-3} compared to the peak value, meaning that the phase becomes undefined inside the margins and is characterized by random phase jumps by 2π due to the periodicity and π due to sign changes. The modulus squared of the overlap matrix elements confirms that the higher-order modes become more dissimilar as the gain is increased. The maximal values of $|\mathfrak{c}_{lm}|^2$ on the colorbars for $G_{exp} = 2.0$, $G_{exp} = 4.0$ and $G_{exp} = 8.0$ are 0.997, 0.952 and 0.737, respectively. Interestingly, the increasing dissimilarity in the modes stops as the mode index approaches 15 and continues for higher indices, which is investigated in more detail in the text and Fig. 4.3 for the modes $n = 14$, $n = 15$ and $n = 16$. Adapted from Ref. [4].

in the low gain limit, together with

$$\tilde{\eta}(q,q') = \sum_n \sqrt{\tilde{\Lambda}_n}\, u_n(q)\, u_n^*(q'), \tag{4.37b}$$

which follows from the fact that the Dirac delta can be decomposed as $\delta(q-q') = \sum_n w_n(q)\, w_n^*(q')$, where the w_n are from any set of orthonormalized functions over q, and the fact that, $\tilde{\Lambda}_n \approx 1$. Therefore, at low gain, $\mathfrak{c}_{lm} = \delta_{lm}$ since the input and output modes coincide. It should be noted that numerically, the decomposition of β as written in Eq. (4.37a) corresponds to the *Takagi factorization*[7] of the matrix representing the discrete analog of β [120].

As the experimental gain is increased, the modes become more dissimilar. Interestingly, this dissimilarity seems to mostly increase for modes $n \leq 15$ up to $G_{\text{exp}} = 4$, while the higher order modes remain more similar. For $G_{\text{exp}} = 8$, $|\mathfrak{c}_{lm}|^2$ almost becomes diagonal again as l and m approach 15 and a cutoff can be observed, meaning that for $l, m \geq 16$, the modes are less similar again. The modes $n = 14$, $n = 15$ and $n = 16$ are shown in Fig. 4.3. Evidently, the modes $n = 15$ and $n = 16$ are structurally significantly different. While for $n = 15$ (and $n = 14$), the mode approximately has a Hermite-Gaussian shape, for $n = 16$, the mode vanishes near the collinear region and consist of two series of peaks centered around $\theta = \pm 30\,\text{mrad}$.

The similarity of the modulus of the input and output modes at varying gain for $n = 0$, see Fig. 4.2, and at high gain for $n = 14$, 15 and 16, can be understood as follows. As shown in Appendix B of Ref. [4], the phase of the transfer function $\beta(q,q')$ is, to a good approximation, separable, meaning that $\beta(q,q')$ can be written as

$$\beta(q,q') \approx |\beta(q,q')| \mathrm{e}^{\mathrm{i}[\Phi_1(q)+\Phi_2(q')]}, \tag{4.38}$$

with the modulus $|\beta(q,q')|$ of β additionally being almost symmetric: $|\beta(q,q')| \approx |\beta(q',q)|$. The modulus of β can be decomposed as

$$|\beta(q,q')| \approx \sum_n \sqrt{\Lambda_n}\, v_n(q)\, v_n(q), \tag{4.39}$$

which holds more precisely for the lower order modes with larger singular values $\sqrt{\Lambda_n}$, since, as also mentioned in Appendix B of Ref. [4], the modulus of β has a small asymmetry[8].

[7] Here, it is numerically not sufficient to compute a simple SVD of the corresponding matrix and instead a proper algorithm for the computation of the Takagi factorization must be used. Otherwise, due to the non-uniqueness of the modes [see Secs. A.6 and 4.2.3] the phases of the modes may be incorrect.

[8] This asymmetry must be investigated more carefully to rule out that it originates from the solver used in the numerical solution of the integro-differential equations. During the numerical evolution, the discretized versions transfer functions, represented for example by the matrices $\tilde{\mathrm{H}}$ and B (see also the discussions in Secs. A.4.1 and A.6) must preserve the restriction imposed by Eq. (4.17) or, equivalently, Eqs. (4.18) and (4.19). To address this, as mentioned in Ref. [4], it was tested whether the asymmetry persists if the integro-differential equations are solved using a *Lie group integrator*, more precisely the *Lie-Euler method*, which are solvers explicitly constructed to ensure that the solution of a differential equation remains inside a certain Lie group, here the symplectic group $\mathrm{Sp}(2N,\mathbb{C})$ [see again Eq. (4.17)] [121, 122]. It was found that the asymmetry also appears using this method and therefore is not a result of numerical error. More details can be found in Appendix B of Ref. [4].

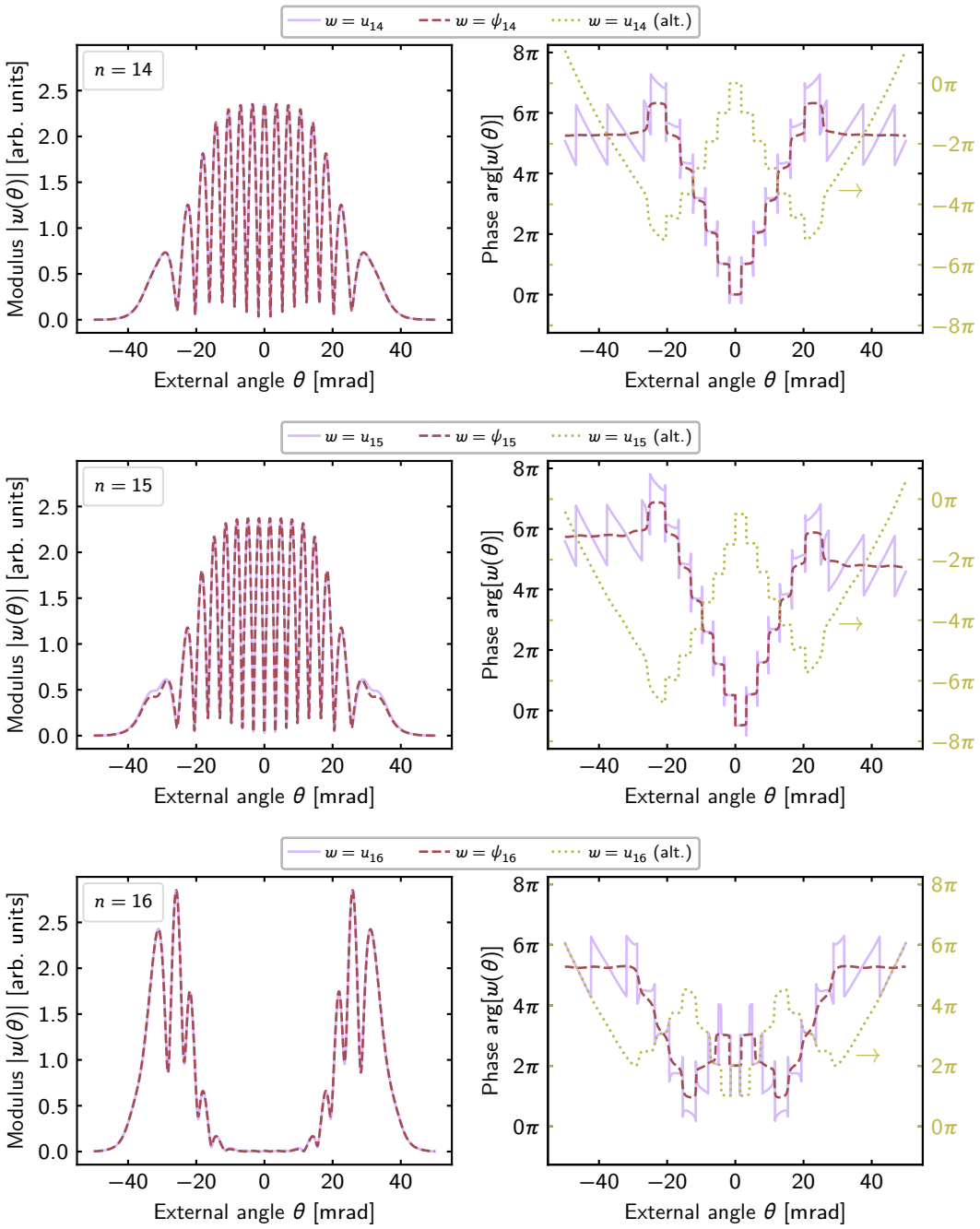

Figure 4.3: Plots of the modulus (left column) and the phase profile (right column) of the input and output modes $n = 14$, $n = 15$ and $n = 16$ of a single crystal with $G_{\text{exp}} = 8$. For all cases the modulus of the modes coincides mostly near $\theta = \pm 35\,\text{mrad}$, except for a clearly visible deviation for $n = 15$. Furthermore, for $n \leq 15$, the modes seem to be mostly localized near the collinear direction $\theta = 0$, while for $n = 16$, the mode is mostly localized starting from $\theta = \pm 10\,\text{mrad}$ and going towards broader angles. The phase profiles indicate that the input and output modes are relatively similar, but not identical. For the output modes, the light-blue and yellow lines show two possible ways of unwrapping the phase distribution from the interval $[0, 2\pi[$: The light-blue line minimizes the distance to the phase of the input mode, while the alternative unwrapping (yellow line) tries to minimize phase jumps around the collinear direction. Adapted from Ref. [4].

The modes $v_n(q)$ are orthonormalized as

$$\int \mathrm{d}q\, v_n(q)\, v_n^*(q) = \delta_{nn'}\,. \tag{4.40}$$

Since the phase of β is separable, see Eq. (4.38), the total decomposition of β can be written as

$$\beta(q,q') \approx \sum_n \sqrt{\Lambda_n}\, u_n(q)\, \psi_n(q'), \tag{4.41a}$$

where

$$u_n(q) = v_n(q)\, \mathrm{e}^{\mathrm{i}\Phi_1(q)}\,, \tag{4.41b}$$

$$\psi_n(q') = v_n(q')\, \mathrm{e}^{\mathrm{i}\Phi_2(q')}\,. \tag{4.41c}$$

The modes $u_n(q)$ and $\psi_n(q')$ are orthonormalized:

$$\int \mathrm{d}q\, u_n(q)\, u_{n'}^*(q) = \delta_{nn'}\,, \tag{4.42a}$$

$$\int \mathrm{d}q\, \psi_n(q)\, \psi_{n'}^*(q) = \delta_{nn'}\,, \tag{4.42b}$$

which follows from the orthonormality of the $v_n(q)$, see Eq. (4.40). Importantly, Eqs. (4.41b) and (4.41c) imply

$$|u_n(q)| \approx |\psi_n(q)|\,, \tag{4.43}$$

explaining the approximate equality of the moduli of the modes as described above. For the mode $n = 15$, it becomes clear that this argument only holds approximately, since a clear deviation of the moduli of the input and output modes can be observed near $\theta = \pm 35\,\mathrm{mrad}$. Note that in the above discussions, only the properties of the decomposition of the transfer function β were investigated. For these arguments, it is not necessary to explicitly consider the decomposition of $\tilde{\eta}$ assuming that the eigenvalues associated with considered modes are non-degenerate. As discussed in more detail in Secs. A.6 and 4.2.3 below, if the eigenvalues have multiplicity 1, the modes are defined up to their sign. Hence, the modes $u_n(q)$ and $\psi_n(q')$ constructed in Eqs. (4.41b) and (4.41c) above must also be (to good approximation) valid modes for the decomposition of $\tilde{\eta}$.

The phase profiles of the modes are characterized by phase jumps of π occurring near the local minima of the mode functions. Due to the fact that the phase is only defined up to adding or subtracting integer multiples of 2π, it is possible to find an *unwrapping* of the phase of the output modes that minimizes the distance of the phase-angle values to those of the input modes (light-blue line in Fig. 4.3). Here, it becomes clear that the phase profiles of the input and output modes are almost identical. This is not evident from the alternative unwrapping shown by the yellow line in Fig. 4.3, which minimizes phase jumps. However, this similarity of the phases does not explain the dissimilarity of the input and output modes for $n = 16$, since, at first glance, the phase distributions look relatively similar, while Fig. 4.2 indicates that $|\mathfrak{c}_{lm}|^2$ vanishes near the diagonal.

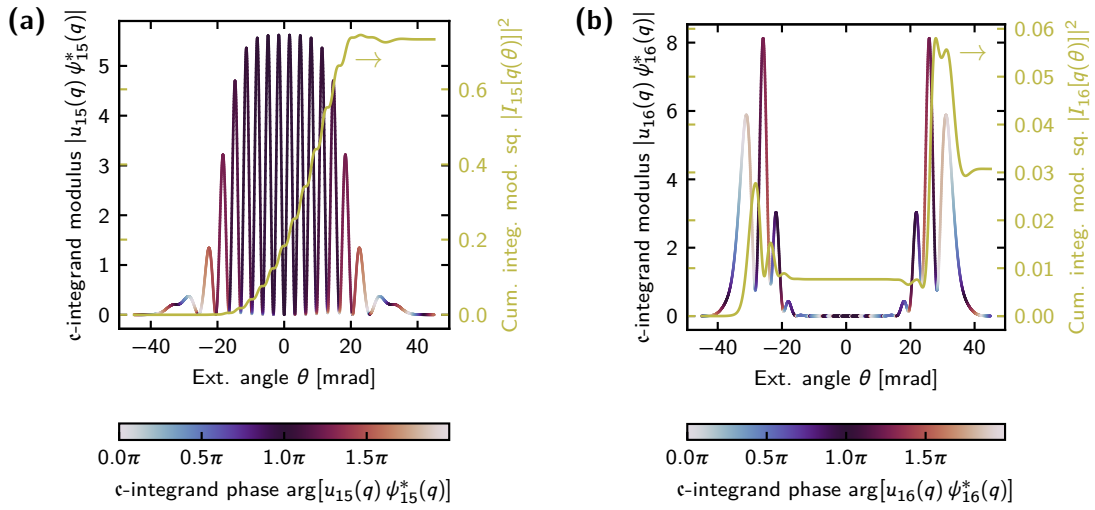

Figure 4.4: Plot of the integrand $u_n(q)\,\psi_n^*(q)$ of the overlap coefficient integral for the coefficients **(a)** $\mathfrak{c}_{15,15}$ and **(b)** $\mathfrak{c}_{16,16}$, as well as the modulus squared $|I_n(q)|^2$ of the corresponding cumulative integral $I_n(q) = \int_{-\infty}^{q} \mathrm{d}q'\, u_n(q')\,\psi_n^*(q')$, so that $\mathfrak{c}_{nn} = \lim_{q\to\infty} I_n(q)$, for a single crystal with $G_{\mathrm{exp}} = 8$. See Eq. (4.36) for the definition of the overlap coefficient. For $n = 15$, the modulus squared of the overlap coefficient reaches a relatively large value of 0.73, which is due to the fact that in the region from −20 mrad to 20 mrad, the phase is mostly constant when the modulus has a significantly positive value. This leads to a step-like increase of $|I_{15}[q(\theta)]|^2$ for increasing θ. The value of $|\mathfrak{c}_{16,16}|^2$ is comparatively small at only 0.0307. This is because the phase varies in the range over which the modulus is non-vanishing, leading to a cancellation of positive and negative contributions.

In order to understand this, it is necessary to consider the interplay of the modulus and the phase of the integrand of the overlap coefficient $\mathfrak{c}_{lm}$ as written in Eq. (4.36) in dependence on the integration variable q. For the two cases $n = 15$ and $n = 16$, Fig. 4.4 shows both the modulus and the phase of the integrand, as well as the modulus squared $|I_n(q)|^2$ of the cumulative integral $I_n(q) = \int_{-\infty}^{q} \mathrm{d}q'\, u_n(q')\,\psi_n^*(q')$, meaning that $\lim_{q\to\infty}|I_n(q)|^2 = |\mathfrak{c}_{nn}|^2$. Evidently, for $n = 15$, the phase is approximately constant in the regions between the local minima on the interval from −20 mrad to 20 mrad, where the highest peaks of the modulus are located. As such, $|I_n(q)|^2$ increases in a step-like manner with increasing q and rises to $|c_{15,15}|^2 = 0.73$ as $q \to \infty$. For $n = 16$, see Fig. 4.4(b), it can be seen that $|I_n(q)|^2$ increases and decreases due to the fact that the phase varies between the peaks. Ultimately, this leads to a smaller value of $|c_{16,16}|^2 = 0.0307$.

4.2.2. High-Gain SU(1,1) Interferometers

While the previous section explored the Schmidt mode structure of a single PDC section, this section will extend this to the modal structure of SU(1,1) interferometers consisting of two PDC sections. Unlike with single PDC sections, for SU(1,1) interferometers, the interplay between the output modes of the first section and the input modes of the second section plays a crucial role.

4.2.2.1. Balanced Fully Compensated SU(1,1) Interferometer

For a perfectly compensated SU(1,1) interferometer, where the phase-matching functions for the first crystal are given by Eqs. (3.30) and (3.37), respectively, the transfer functions of the first and second crystal are connected via

$$\beta^{(2)}(q,q') = \mathrm{e}^{\mathrm{i}\phi}\beta^{(1)}(q',q), \tag{4.44a}$$
$$\tilde{\eta}^{(2)}(q,q') = \left[\tilde{\eta}^{(1)}(q',q)\right]^*, \tag{4.44b}$$

which follows from Eqs. (3.41) and (3.43). This relationship can be used to obtain a joint Schmidt decomposition for the second crystal in terms of the Schmidt decomposition quantities of the first crystal by substituting the transfer functions of the first crystal [Eqs. (3.20)] with their joint decomposition [4]. The decomposition takes the form

$$\beta^{(2)}(q,q') = \sum_n \sqrt{\Lambda_n^{(2)}}\,\psi_n^{(2)}(q)\,u_n^{(2)}(q'), \tag{4.45a}$$
$$\tilde{\eta}^{(2)}(q,q') = \sum_n \sqrt{\tilde{\Lambda}_n^{(2)}}\,\psi_n^{(2)}(q)\left[u_n^{(2)}(q')\right]^*, \tag{4.45b}$$

where

$$\Lambda_n^{(2)} = \Lambda_n^{(1)}, \tag{4.45c}$$
$$\tilde{\Lambda}_n^{(2)} = \tilde{\Lambda}_n^{(1)}, \tag{4.45d}$$
$$u_n^{(2)}(q) = \mathrm{e}^{\frac{\mathrm{i}}{2}\phi}\psi_n^{(1)}(q), \tag{4.45e}$$
$$\psi_n^{(2)}(q') = \mathrm{e}^{\frac{\mathrm{i}}{2}\phi}u_n^{(1)}(q'). \tag{4.45f}$$

Evidently, the input modes of the first PDC section and the output modes of the second PDC section [see Eq. (4.45e)], as well as the output modes of the first PDC section and the input modes of the second PDC section [see Eq. (4.45f)] are orthonormal up to a phase $\mathrm{e}^{-\mathrm{i}\frac{\phi}{2}}$:

$$\int \mathrm{d}q\,\psi_n^{(1)}(q)\left[u_{n'}^{(2)}(q)\right]^* = \delta_{nn'}\mathrm{e}^{-\mathrm{i}\frac{\phi}{2}}, \tag{4.46a}$$
$$\int \mathrm{d}q\,u_n^{(1)}(q)\left[\psi_{n'}^{(2)}(q)\right]^* = \delta_{nn'}\mathrm{e}^{-\mathrm{i}\frac{\phi}{2}}. \tag{4.46b}$$

By utilizing the connection between the decompositions of both crystals [Eqs. (4.45)] and the connection relations between the transfer functions of the two PDC sections and the transfer functions of the entire interferometer, see Eqs. (3.19), the following expressions can be obtained for the joint Schmidt decomposition of the entire interferometer:

$$\beta^{(\mathrm{SU})}(q,q') = \sum_n \sqrt{\Lambda_n^{(\mathrm{SU})}}\,u_n^{(\mathrm{SU})}(q)\,\psi_n^{(\mathrm{SU})}(q'), \tag{4.47a}$$
$$\tilde{\eta}^{(\mathrm{SU})}(q,q') = \sum_n \sqrt{\tilde{\Lambda}_n^{(\mathrm{SU})}}\,u_n^{(\mathrm{SU})}(q)\left[\psi_n^{(\mathrm{SU})}(q')\right]^*, \tag{4.47b}$$

where

$$\Lambda_n^{(\mathrm{SU})} = 4\cos^2\left(\frac{\phi}{2}\right)\Lambda_n^{(1)}\tilde{\Lambda}_n^{(1)}, \tag{4.47c}$$

$$\tilde{\Lambda}_n^{(\mathrm{SU})} = 1 + \Lambda_n^{(\mathrm{SU})}, \tag{4.47d}$$

$$u_n^{(\mathrm{SU})}(q) = \exp\left[\frac{\mathrm{i}}{2}(\mu + \zeta_n)\right] \psi_n^{(1)}(q), \tag{4.47e}$$

$$\psi_n^{(\mathrm{SU})}(q') = \exp\left[\frac{\mathrm{i}}{2}(\mu - \zeta_n)\right] \psi_n^{(1)}(q'), \tag{4.47f}$$

and

$$\mu = \arg(1 + \mathrm{e}^{\mathrm{i}\phi}), \tag{4.47g}$$

$$\zeta_n = \arg\left[1 + \Lambda_n^{(1)}\,(1 + \mathrm{e}^{\mathrm{i}\phi})\right]. \tag{4.47h}$$

Equations (4.47a)–(4.47h) provide an analytical form for the joint Schmidt decomposition of the entire interferometer in terms of the modes $u_n^{(1)}(q)$ and $\psi_n^{(1)}(q)$, as well as the eigenvalues $\Lambda_n^{(1)}$ of the first crystal. Notably, this decomposition shows that the input and output modes of the interferometer are identical up to some q-independent phase. Hence, the system bears similarity to the idea of a *(perfectly) inline squeezer* as described in Houde and Quesada [123], which is described as a system in which the input and output modes are identical (up to some constant phase), enabling the squeezing of a temporal mode while preserving its temporal structure.

4.2.2.2. Unbalanced SU(1,1) Interferometer

More generally, the gain or other properties, such as the crystal length and the refractive indices, of the two PDC sections used to construct the SU(1,1) interferometer do not have to be identical. For example, as previously mentioned in Sec. 3.6, Manceau *et al.* [9] suggests that unbalancing the SU(1,1) interferometer improves its properties. Due to the gain dependence of the Schmidt modes, this will lead to mode mismatches between the input and output modes of the two PDC sections, as will be seen below.

A potential setup for such an unbalanced interferometer is shown in Fig. 4.5. The PDC radiation is generated in the first pass of Pump 1 (at gain $G_{\mathrm{exp}}^{(1)}$) through the crystal. The phase-matching function for this first pass is given by that of a single crystal, see Eq. (3.30). After the crystal, Pump 1 is removed, using a dichroic mirror, while the PDC radiation is reflected using a spherical mirror for diffraction compensation, as discussed in Secs. B.2 and 3.3. In this general setup, the offset of the spherical mirror from the optimal position, which would lead to perfect compensation in the balanced case, is included as δz. The mirror focuses the radiation back into the crystal, where it recombines with Pump 2, whose phase ϕ relative to Pump 1 determines the interferometric phase. In general, the experimental gain of Pump 2, $G_{\mathrm{exp}}^{(2)}$, may differ from $G_{\mathrm{exp}}^{(1)}$. The phase-matching function for the second pass is given by [4]:

$$h^{(2)}(q_s, q_i, L) = \mathrm{e}^{-\mathrm{i}\Delta k(q_s,q_i)[L-2L_1]}\mathrm{e}^{-\mathrm{i}\Delta k^{\mathrm{air}}(q_s,q_i)\delta z}\mathrm{e}^{\mathrm{i}\phi}, \tag{4.48}$$

as shown in Sec. B.2. Clearly, for $\delta z = 0$, the phase-matching function for perfect compensation in the balanced case is recovered, compare Eq. (3.37). In the following, unless specified otherwise, $G_{\mathrm{exp}}^{(2)} = 4$ and $G_{\mathrm{exp}}^{(1)} = 1$, while all other properties of the two

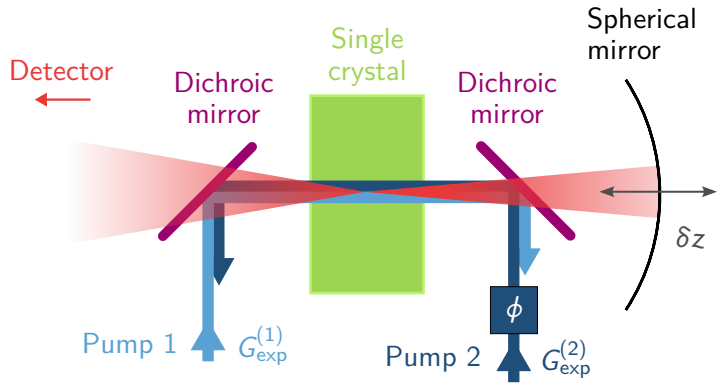

Figure 4.5: Advanced sketch of the SU(1,1) interferometer with diffraction compensation implemented using a spherical mirror (Michelson-type configuration). Compared to the simplified sketch in Fig. 3.2(b), the dichroic mirrors used to direct the pump beams into the crystals for both passes (with Pump 1 and Pump 2) are shown. Generally, the gain for both passes may be different (unbalanced case). Additionally, in the unbalanced case, the spherical mirror may be moved by δz in order to maximize the interferometric visibility, as also shown in more detail in Fig. 4.6. Compare also Fig. 2(a) of Barakat *et al.* [3] which shows another sketch of an alternative setup and Fig. S2 of the corresponding supplementary material (Ref. [103]) which shows a more elaborate sketch of the entire setup used in the experiment discussed in Sec. 4.3.2 below. Adapted from Ref. [4].

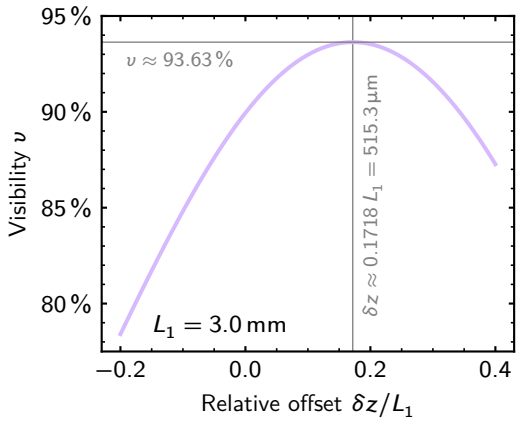

Figure 4.6: Interferometric visibility v as defined in Eq. (4.49) of the unbalanced SU(1,1) interferometer pumped at $G^{(1)}_{\text{exp}} = 1$ and $G^{(2)}_{\text{exp}} = 4$ in dependence on the relative offset $\delta z/L_1$ of the focusing element from the optimal position in the gain-balanced case. For $\delta z = 515.3\,\mu\text{m}$, the visibility reaches its local maximum with $v = 93.63\,\%$. Adapted from Ref. [4].

PDC sections are identical and the same as mentioned above.

The reason for allowing the spherical mirror to be moved by δz can be seen from Fig. 4.6, which shows the interferometric visibility

$$v = \frac{\langle \hat{N}_{\text{tot}} \rangle_{\text{bf}} - \langle \hat{N}_{\text{tot}} \rangle_{\text{df}}}{\langle \hat{N}_{\text{tot}} \rangle_{\text{bf}} + \langle \hat{N}_{\text{tot}} \rangle_{\text{df}}} \cdot 100\,\%, \tag{4.49}$$

where $\langle \hat{N}_{\text{tot}} \rangle_{\text{bf}}$ and $\langle \hat{N}_{\text{tot}} \rangle_{\text{df}}$ are the integral intensities at the bright and dark fringe over ϕ, respectively, in dependence on δz. Evidently, the dependence of v on δz is approximately quadratic, leading to a maximum at $\delta z = 515.3\,\mu\text{m}$. Thus, the visibility is no longer maximized at $\delta z = 0$, as it would be for the balanced interferometer. As was

shown analytically in Ref. [4], for the perfectly compensated and balanced interferometer, $v = 100\,\%$, regardless of the other system parameters. Thus, compared to the balanced case, the maximal visibility is reduced by around 6.4 %pt for the unbalanced interferometer discussed here.

Due to the gain dependence of the Schmidt modes, it is generally expected that the output modes of the first crystal and the input modes of the second crystal will no longer be identical up to a constant phase, as they were in Sec. 4.2.2.1 above. Hence, it is advisable to define the overlap coefficient between these modes [3, 4],

$$\mathfrak{g}_{km} \overset{\text{def.}}{=} \int \mathrm{d}q \, \left[u_k^{(1)}(q)\right]^* \psi_m^{(2)}(q), \tag{4.50}$$

to obtain a quantitative measure for their similarity. In general, this overlap coefficient will not have a diagonal form ($\mathfrak{g}_{km} \not\propto \delta_{km} \mathrm{e}^{\mathrm{i}\rho_k}$, for some phases ρ_k). Due to the fact that the properties of the first and second crystal of the interferometer are different, the connections between the transfer functions of both crystal described by Eqs. (3.43) and (4.44) no longer apply. Equations (3.41) however are still valid and describe the connection between the transfer functions for the two cases where the second crystal is integrated with a phase-matching function containing the flat-phase term $\mathrm{e}^{\mathrm{i}\phi}$ and without it (or, equivalently, for $\phi = 0$). Using this and the joint Schmidt decomposition for the second PDC section integrated without the flat phase term, it is possible to write the joint Schmidt decomposition for the transfer functions $\beta^{(2)}$ and $\tilde{\eta}^{(2)}$ including the phase [4]:

$$\beta^{(2)}(q,q') = \sum_n \sqrt{\Lambda_n^{(2)}} \, \left[\mathrm{e}^{\frac{\mathrm{i}}{2}\phi} \breve{\psi}_n^{(2)}(q)\right] \left[\mathrm{e}^{\frac{\mathrm{i}}{2}\phi} \breve{u}_n^{(2)}(q')\right], \tag{4.51a}$$

$$\tilde{\eta}^{(2)}(q,q') = \sum_n \sqrt{\tilde{\Lambda}_n^{(2)}} \, \left[\mathrm{e}^{\frac{\mathrm{i}}{2}\phi} \breve{\psi}_n^{(2)}(q)\right] \left[\mathrm{e}^{\frac{\mathrm{i}}{2}\phi} \breve{u}_n^{(2)}(q')\right]^*, \tag{4.51b}$$

where $\breve{\psi}_n^{(2)}$ and $\breve{u}_n^{(2)}$ are the Schmidt mode functions obtained from the decomposition of the transfer functions where the phase was not accounted for, see the notation introduced in Eq. (3.42) and the surrounding text. Note that $\Lambda_n^{(2)}$ and $\tilde{\Lambda}_n^{(2)}$ remain unchanged regardless of whether the phase term is accounted for in the phase-matching function. Thus, an alternative way of expressing the $\mathfrak{g}$ overlap coefficient is as [4]

$$\mathfrak{g}_{km} = \mathrm{e}^{\mathrm{i}\frac{\phi}{2}} \int \mathrm{d}q \, \left[u_k^{(1)}(q)\right]^* \breve{\psi}_m^{(2)}(q). \tag{4.52}$$

Note that the integral in the expression above is still complex-valued, meaning that the full phase dependence of $\mathfrak{g}$ is given by the product of $\mathrm{e}^{\mathrm{i}\frac{\phi}{2}}$ and some additional constant phase factor which does not depend on ϕ.

In experimental setups, the measured modes are usually the output modes of the entire interferometer $u_n^{(\mathrm{SU})}$. It should be emphasized that these modes are *not* the output modes $u_n^{(2)}$ of the second crystal alone. By definition, the former set of modes is part of the diagonalization of the plane-wave mode input-output relations of the entire interferometer, while the latter set of modes is part of the diagonalization of the second crystal, which is a

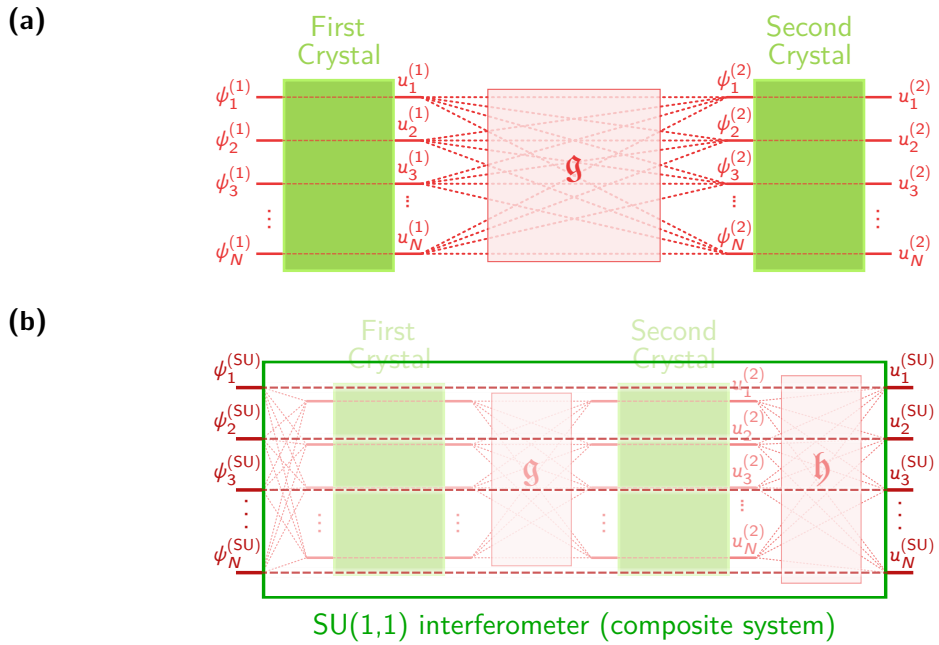

Figure 4.7: **(a)** Modal layout of a two-crystal PDC system in the discrete case. The first crystal has an associated set of N input modes $\psi_j^{(1)}$ and output modes $u_j^{(1)}$ $(j = 1, \dots, N)$ resulting from the joint Schmidt decomposition (compare Fig. 4.1). These sets of modes are connected via the Bogoliubov transformations as written in Eqs. (3.23), (3.24) and (4.31) and therefore, the input mode with index l only couples to the output mode with the same index l, as indicated by the red dashed lines overlapping the crystals. In other words, the input-output relation is diagonal. The same applies also to the second crystal with input modes $\psi_j^{(2)}$ and output modes $u_j^{(1)}$. In general, the output modes of the first crystal and the input modes of the second crystal are not identical, see Fig. 4.8. This mismatch is quantified by the overlap coefficient $\mathfrak{g}$ as defined in Eq. (4.50). Hence, despite the fact that the input-output relations for both crystals are diagonal, the relationship connecting the input modes $\{\psi_j^{(1)}\}_j$ of the first crystal to the output modes $\{u_j^{(2)}\}_j$ of the second crystal is generally not diagonal due to the fact that $\mathfrak{g}$ is not diagonal. This leads to the conclusion that $\{\psi_j^{(1)}\}_j$ and $\{u_j^{(2)}\}_j$ cannot be the input and output modes, respectively, of the composite system since the modes for the composite system need to fully diagonalize the input-output relation from the input of the first crystal to the output of the second crystal. **(b)** Modal layout of the diagonalized input-output relation of the composite PDC system [SU(1,1) interferometer] in relation to the modes of the first and second crystal seen in the background [compare **(a)**]. The input modes $\psi_j^{(\mathrm{SU})}$ and the output modes $u_{j'}^{(\mathrm{SU})}$ associated with the composite system are coupled via the diagonal Bogoliubov transformations as indicated by the dark-red dashed lines, meaning that they are only coupled by the system if their indices match $(j = j')$. The input modes of the first crystal are generally different from the input modes of the composite system since the former diagonalize the first crystal while the latter diagonalize the composite system (as mentioned above, the input modes of the first crystal do not diagonalize the composite system since $\mathfrak{g}$ is generally not diagonal). For the same reason, the output modes of the second crystal $u_j^{(2)}$ are not the same as the output modes of the interferometer $u_j^{(\mathrm{SU})}$. Their similarity is quantified by the overlap coefficient $\mathfrak{h}$ as defined in Eq. (4.53). Note that in both **(a)** and **(b)**, additional optical elements such as the phase object, the 4f-system or the spherical mirror are not explicitly shown and would be included in the description of the second crystal, see Secs. 3.3 and 4.2.2.

subsystem of the entire interferometer. Generally, $u_n^{(\mathrm{SU})}$ and $u_n^{(2)}$ therefore do not coincide. This leads to the definition of a second overlap coefficient between the output modes of the second crystal and the output modes of the entire interferometer [4]:

$$\mathfrak{h}_{nl} \overset{\text{def.}}{=} \int \mathrm{d}q \, \left[u_n^{(2)}(q)\right]^* u_l^{(\mathrm{SU})}(q). \tag{4.53}$$

The necessity to define this overlap coefficient leads to the question regarding the interpretation of the Schmidt modes. This will be explained in more detail in Sec. 4.2.3 below. Figure 4.7 summarizes the modal layouts of the two crystals and the entire interferometer system and further highlights the necessity to define the overlap coefficients $\mathfrak{g}$ and $\mathfrak{h}$.

Figure 4.8 shows the behavior of the overlap coefficient matrices $\mathfrak{g}$ and $\mathfrak{h}$ at the bright and dark fringe. Evidently, $\mathfrak{g}$ contains large off-diagonal contributions in the lower left triangle, meaning that the output modes of the first crystal and the input modes of the second crystal are mismatched. Furthermore, at the bright fringe, with $\phi \approx 0$, the phases of the low-order modes (those with the largest eigenvalues) are aligned so that $\mathfrak{g}_{km} \approx \pm 1$, while at the dark fringe, with $\phi \approx \pi$, $\mathfrak{g}_{km} \approx \pm \mathrm{i}$. Overall, the overlap coefficient matrix $\mathfrak{h}$ is much closer to being diagonal than $\mathfrak{g}$. Additionally, here, $\mathfrak{h}_{nl} \approx \pm 1$ for the bright and the dark fringe. A more detailed analysis of the behavior of the phases in dependence on δz is presented in Appendix E of Ref. [4]. In short, for several low-order modes, the phases of both $\mathfrak{g}$ and $\mathfrak{h}$ align at the aforementioned values as δz approaches the valued required to reach the maximal value of the visibility.

It should be noted that for the perfectly compensated interferometer, the overlap coefficients are diagonal,

$$\mathfrak{g}_{km} = \mathrm{e}^{\mathrm{i}\frac{\phi}{2}} \delta_{km}, \tag{4.54a}$$

compare also Eq. (4.46a), and

$$\mathfrak{h}_{ln} = \mathrm{e}^{\frac{\mathrm{i}}{2}\left(\mu + \zeta_n - \frac{\phi}{2}\right)} \delta_{ln}, \tag{4.54b}$$

both of which follow directly from the definitions of the overlap coefficients [Eqs. (4.50) and (4.53)] and the analytical expressions for the Schmidt decompositions of the second PDC section and the entire interferometer, see Eqs. (4.45) and (4.47), respectively.

4.2.3. Physical Interpretation and Uniqueness of the Schmidt Modes

In a broader context, the fact that the output modes of the second crystal are not automatically the output modes of the SU(1,1) interferometer, which lead to the definition of the overlap coefficient $\mathfrak{h}$ in Eq. (4.53), also leads to the question regarding the physical meaning of the input and output modes. Mathematically, the modes are obtained by performing the joint Schmidt decomposition of the transfer functions. The Schmidt modes then provide a diagonalization of the input-output relations, meaning that input and output Schmidt modes are connected via the Bogoliubov transformations [see Eqs. (3.23)] only if they have the same mode index n. More generally, different transfer functions lead

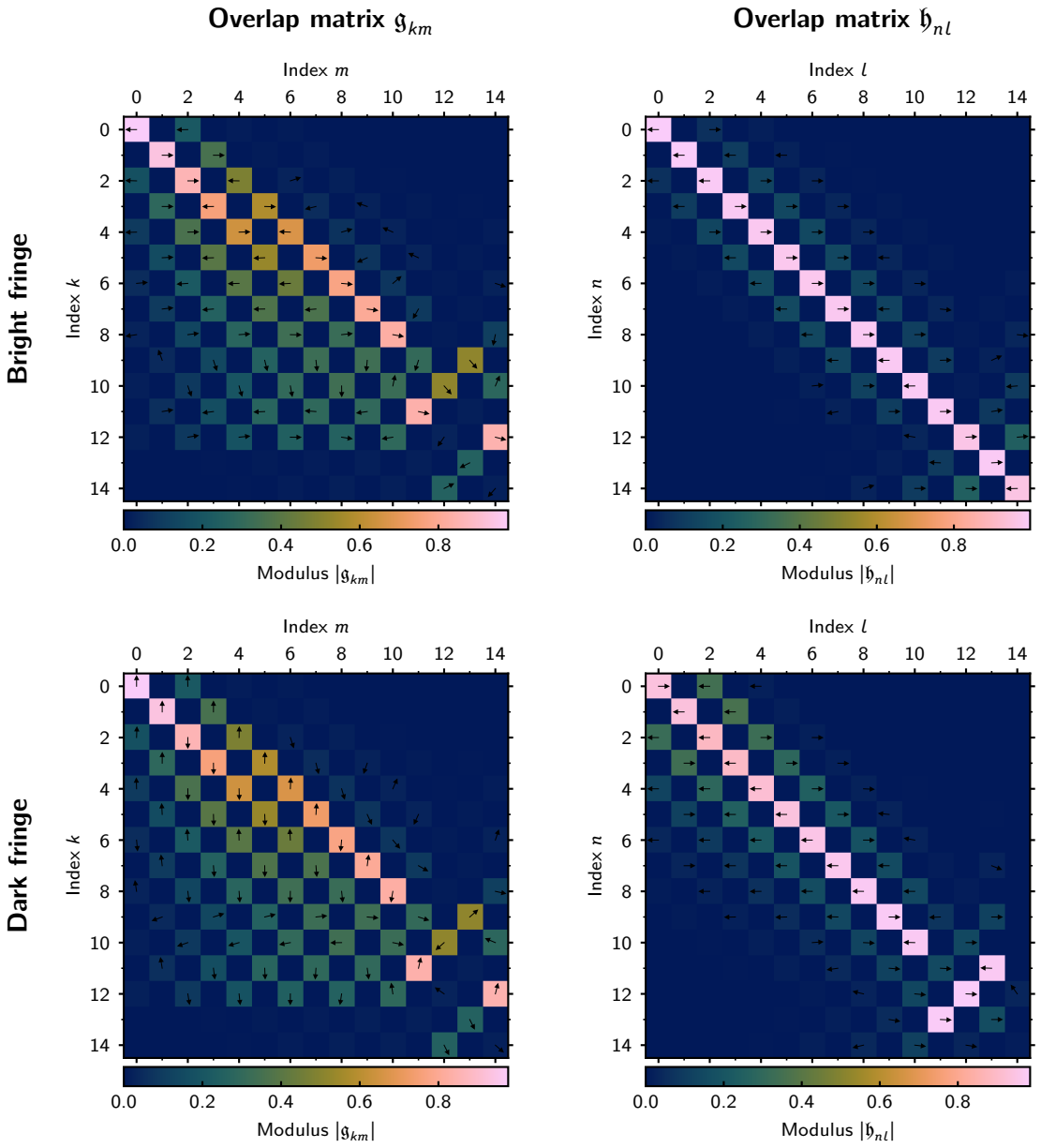

Figure 4.8: Visualization of the first 15×15 entries of the overlap matrices $\mathfrak{g}$ (left column) and $\mathfrak{h}$ (right column) at the bright (upper row; $\phi = 0.0337\pi$) and the dark (lower row; $\phi = 1.03\pi$) fringe of the unbalanced SU(1,1) interferometer with parametric gains $G^{(1)}_{\text{exp}} = 1$ and $G^{(2)}_{\text{exp}} = 4$ for of the first and second crystal, respectively. The colors correspond the modulus of the overlap coefficients as indicated by the color bars, while the handles in the cells indicate the location of the complex number in the complex plane: If the handle points to the right, the entry is purely real and positive. If the handle points upwards, the entry is purely imaginary with a positive sign. For the other directions the phase follows analogously. Handles are only shown for entries whose modulus exceeds 0.02. The maximal values of the colorbars are 0.977 for $|\mathfrak{g}_{km}|$ and 0.998 and 0.985 for $|\mathfrak{h}_{nl}|$ at the bright and dark fringe, respectively. Adapted from Ref. [4].

to different sets of modes. Naturally, this implies that the decomposition of the second crystal described by $\tilde{\eta}^{(2)}$ and $\beta^{(2)}$ will be different from that of the entire interferometer described by $\tilde{\eta}^{(\mathrm{SU})}$ and $\beta^{(\mathrm{SU})}$, since the transfer functions of the entire interferometer are constructed from those of the first *and* the second crystal in a nontrivial manner, see the connection relations in Eqs. (3.19).

Additionally, the name of "input modes" might lead to confusion since it could be interpreted in the sense that these modes are defined by the *input field* at the input face of the PDC section. Instead, as mentioned above, these modes are defined by the decomposition of the transfer functions, which connect the input plane-wave operators to the output plane-wave operators of the PDC section.

A related misconception that may arise is that the input modes, since they are associated with the "input" of the system, cannot depend on the parameters of the PDC process, such as the refractive indices and most notably the crystal length and the parametric gain, since the fields "at the input" have not yet undergone the PDC interaction. However, since the modes are obtained from the transfer functions, they cannot be determined before integrating the entire PDC section. One way to understand the dependence of the input modes on the parameters of the interaction is as follows: Since the Schmidt modes are defined by the fact that they diagonalize the input-output relations, the input modes are inevitably determined by the output modes and vice versa. Given a set of output modes $\hat{A}_n^{(\mathrm{out})}$ and $\hat{B}_n^{(\mathrm{out})}$, the input modes are determined by the fact that states in these modes do not couple to other output modes $\hat{A}_{n'}^{(\mathrm{out})}$ and $\hat{B}_{n'}^{(\mathrm{out})}$ with $n \neq n'$ during the PDC process. Mathematically, given either the set of input or output modes[9], $\{\psi_n\}_n$ or $\{u_n\}_n$, respectively, the other set of modes is immediately determined via

$$u_n(q) = \frac{1}{\sqrt{\Lambda_n}} \int \mathrm{d}q'\, \beta(q,q')\, \psi_n^*(q'), \tag{4.55a}$$

$$\psi_n(q) = \frac{1}{\sqrt{\Lambda_n}} \int \mathrm{d}q'\, \beta(q',q)\, u_n^*(q'), \tag{4.55b}$$

or

$$u_n(q) = \frac{1}{\sqrt{\tilde{\Lambda}_n}} \int \mathrm{d}q'\, \tilde{\eta}(q,q')\, \psi_n(q'), \tag{4.56a}$$

$$\psi_n(q) = \frac{1}{\sqrt{\tilde{\Lambda}_n}} \int \mathrm{d}q'\, \tilde{\eta}^*(q',q)\, u_n(q'). \tag{4.56b}$$

A more pictorial way of understanding this is by posing the question: "In which spatial mode $\psi_n(q)$ does the initial field have to be prepared in, in order to couple *only* to a single output mode $u_n(q)$ with the same fixed index n?" This question highlights that the input modes may, in principle, depend on all properties of the PDC interaction and not only

[9] In the set notation used above, $\{w_n\}_n$ is shorthand for $\{w_n\}_{n\in\mathcal{I}}$, where $\mathcal{I}$ denotes the index set for the index n of the indexed object w_n (here, the modes). The set $\{w_n\}_n$ then consists of all possible w_n, which for the modes means for example: $\{w_n\}_n = \{w_0, w_1, ...\}$ (assuming the index n starts at 0). Usually, the index set $\mathcal{I}$ follows from the context if this shorthand notation is used. The notation is contrary to that where a restriction on the index may be used to construct the set. For example, $\{w_n\}_{n\geq 5} = \{w_n | n \geq 5\} = \{w_5, w_6, ...\}$.

those that are directly causally connected to the beginning of the PDC interaction. Thus, in short, the entire PDC interaction determines the shape and phase of the input and output modes.

Naturally, the question arises as to how unique the Schmidt modes are for a given set of transfer functions β and $\tilde{\eta}$. In Appendix A 2 of Ref. [4], it was shown that due to the restrictions that the joint decomposition imposes on the modes, they are defined up to a sign change in the sense that a pair of input-output modes $u_n(q)$ and $\psi_n(q)$ may be replaced by $-u_n(q)$ and $-\psi_n(q)$ (simultaneously), if the corresponding singular value has a multiplicity of 1, that is, if it is unique for the decomposition. However, if there are degenerate singular values with multiplicity $\mu > 1$, the situation is more complex. This situation was not investigated in Ref. [4] and instead this case is addressed and described in more detail in Sec. A.6. In summary: For an eigenvalue Λ_p and the associated $\tilde{\Lambda}_p$ with multiplicity $\mu_p > 1$, let $\{\psi_r\}_r$ and $\{u_r\}_r$ $(r = 1, 2, \dots, \mu_p)$ denote the sets of input and output modes belonging to these eigenvalues, respectively. Then, as shown in Sec. A.6, *any* other two potential sets $\{\psi'_n\}_n$ and $\{u'_n\}_n$ $(n = 1, 2, \dots, \mu_p)$ for the modes are connected to the original set via a *real* orthogonal rotation, so that

$$u_n(q) = \sum_{m=1}^{\mu_p} u'_m(q)\, V_{mn}\,, \tag{4.57a}$$

$$\psi_n(q) = \sum_{m=1}^{\mu_p} \psi'_m(q)\, V_{mn}\,, \tag{4.57b}$$

with $V \in \mathrm{O}(\mu_p, \mathbb{R})$ and $\mathrm{O}(\mu_p, \mathbb{R})$ denotes the real orthogonal group of $\mu_p \times \mu_p$ matrices. In this general case, for non-degenerate singular values with $\mu_p = 1$, the result found in Ref. [4] as mentioned above is recovered. The only exception to this is the *null-block*, in which $\Lambda_p = 0$ and $\tilde{\Lambda}_p = 1$. For this block, the matrix V may instead be chosen as $V \in \mathrm{U}(\mu_p)$, with $\mathrm{U}(\mu_p)$ denoting the unitary group of $\mu_p \times \mu_p$ matrices. Additionally, it should be noted that these considerations only take into account the case where the overall number of modes is finite. Analytically, the Schmidt decomposition always yields a countably infinite number of modes. The abovementioned results are obtained by considering the discrete cases or, equivalently, by truncating the Schmidt decomposition at a certain index. In the low-gain limit, due to the vanishing eigenvalues $\sqrt{\Lambda_p}$ of β, the restriction to real orthogonal rotations is again lifted, and the modes may be connected via unitary rotations V.

4.3. Multimode Squeezing Measurements

For the experiment performed in Barakat *et al.* [3], it is helpful to first think of the SU(1,1) as a sequence of two PDC sections instead of one system. The first crystal can then be understood as a squeezer, which prepares a multimode squeezed vacuum state, while the second crystal serves as an analyzer. Ultimately, the goal is to obtain information regarding the squeezing in each output mode of the squeezer from the output of the interferometer. While the squeezer operates at low gain, it is generally useful to operate the second crystal

at high gain in order to obtain large output intensities. Due to the differing gains in both crystals, the output modes of the first crystal are mismatched with respect to the input modes of the second crystal, as seen in Sec. 4.2.2.2. As a consequence, the information regarding the nth output mode of the squeezer is spread over many output modes of the entire interferometer, which defines the measured modes (that is, the detected modes are ultimately those of the entire interferometer). As such, it is necessary to develop a processing method to extract the squeezing of the modes of the first crystal from the modes of the entire interferometer.

4.3.1. Development of the Processing Method

4.3.1.1. Exact Reconstruction of the Squeezing

Between the two crystals, the plane-wave operators are connected via Eqs. (3.14): In general, the output plane-wave operators of a PDC section are the input plane-wave operators of the following section. A similarly simple relation does not exist for the Schmidt operators. Since they diagonalize the input-output relations of different systems, the Schmidt operators of two different sections have, in general, no physical connection (as also indicated in Fig. 4.7). However, since the Schmidt modes form complete orthonormalized systems, they can always be expanded in terms of each other. Using the $\mathfrak{g}$ overlap coefficient, the output modes $\psi_m^{(2)}$ of the first crystal can be expanded in terms of the input modes $u_k^{(1)}$ of the second crystal:

$$\left[u_k^{(1)}(q')\right]^* = \sum_m \mathfrak{g}_{km} \left[\psi_m^{(2)}(q')\right]^*. \tag{4.58}$$

Since the output plane-wave operators of the first PDC section are the input plane-wave operators of the second PDC section, it follows that the output Schmidt operators of the first section are connected to the input operators of the second section via [3, 4]

$$\hat{A}_l^{(1,\mathrm{out})} = \sum_m \mathfrak{g}_{lm} \hat{A}_m^{(2,\mathrm{in})}, \tag{4.59}$$

compare the definitions of the Schmidt operators in Eqs. (3.24). The input operator $\hat{A}_m^{(2,\mathrm{in})}$ can be rewritten in terms of the output operators of the second PDC section by using the inverse transform of the Bogoliubov transformation as written in Eq. (4.31):

$$\hat{A}_m^{(\mathrm{in})} = \sqrt{\tilde{\Lambda}_m}\, \hat{A}_m^{(\mathrm{out})} - \sqrt{\Lambda_m} \left[\hat{A}_m^{(\mathrm{out})}\right]^\dagger. \tag{4.60}$$

Plugging the inverse transform into Eq. (4.59) yields

$$\hat{A}_l^{(1,\mathrm{out})} = \sum_m \mathfrak{g}_{lm} \left[\sqrt{\tilde{\Lambda}_m}\, \hat{A}_m^{(2,\mathrm{out})} - \sqrt{\Lambda_m} \left(\hat{A}_m^{(2,\mathrm{out})}\right)^\dagger\right]. \tag{4.61}$$

Similarly to the connection between $u_k^{(1)}$ and $\psi_m^{(2)}$ in Eq. (4.58), the output modes of the second crystal and those of the entire interferometer can be expanded in terms of one

another using the overlap coefficient $\mathfrak{h}$ as defined in Eq. (4.53):

$$\hat{A}_m^{(2,\mathrm{out})} = \sum_k \mathfrak{h}_{mk} \hat{A}_k^{(\mathrm{SU},\mathrm{out})}. \tag{4.62}$$

Plugging this into Eq. (4.61) yields an equation connecting the output modes of the first crystal to the output modes of the entire interferometer [4]:

$$\hat{A}_l^{(1,\mathrm{out})} = \sum_{m,k} \mathfrak{g}_{lm} \left[\sqrt{\tilde{\Lambda}_m^{(2)}}\, \mathfrak{h}_{mk} \hat{A}_k^{(\mathrm{SU},\mathrm{out})} - \sqrt{\Lambda_m^{(2)}}\, \mathfrak{h}_{mk}^* \left(\hat{A}_k^{(\mathrm{SU},\mathrm{out})} \right)^\dagger \right]. \tag{4.63}$$

Thus, given the output Schmidt modes of the interferometer, as well as the eigenvalues of the second crystal and the overlap coefficients $\mathfrak{g}$ and $\mathfrak{h}$, the output Schmidt operators of the first crystal can be reconstructed using the above equation. The output Schmidt operator can then be used to determine the level of squeezing in the Schmidt modes using Eq. (4.29), which expresses the variance of the generalized quadrature of the Schmidt mode in terms of the expectation values $\langle \hat{A}_l^\dagger \hat{A}_l \rangle$, $\langle \hat{A}_l \hat{A}_l \rangle$ and $\langle \hat{A}_l \rangle$, where the Schmidt mode operators $\hat{A}_l$ refers to the output operators of the first crystal. Clearly, $\langle \hat{A}_l^{(1,\mathrm{out})} \rangle = 0$ since $\langle \hat{A}_l^{(\mathrm{SU},\mathrm{out})} \rangle = 0$, which can be evaluated by using Eq. (4.31). Using Eq. (4.63), the remaining two expectation values can be expressed in terms of the output operators of the entire interferometer as [4]

$$\begin{aligned}
\langle \hat{A}_l^{(1,\mathrm{out})} \hat{A}_l^{(1,\mathrm{out})} \rangle = \sum_{n,n',k} \mathfrak{g}_{ln} \mathfrak{g}_{ln'} \Big[& \mathfrak{h}_{nk} \mathfrak{h}_{n'k} \sqrt{\left(\Lambda_n^{(2)} + 1\right)\left(\Lambda_{n'}^{(2)} + 1\right)} \sqrt{\left(\Lambda_k^{(\mathrm{SU})} + 1\right)\Lambda_k^{(\mathrm{SU})}} \\
& + \mathfrak{h}_{nk}^* \mathfrak{h}_{n'k}^* \sqrt{\Lambda_n^{(2)} \Lambda_{n'}^{(2)}} \sqrt{\Lambda_k^{(\mathrm{SU})}\left(\Lambda_k^{(\mathrm{SU})} + 1\right)} \\
& - \mathfrak{h}_{nk} \mathfrak{h}_{n'k}^* \sqrt{\left(\Lambda_n^{(2)} + 1\right)\Lambda_{n'}^{(2)}} \left(\Lambda_k^{(\mathrm{SU})} + 1\right) \\
& - \mathfrak{h}_{nk}^* \mathfrak{h}_{n'k} \sqrt{\Lambda_n^{(2)}\left(\Lambda_{n'}^{(2)} + 1\right)} \Lambda_k^{(\mathrm{SU})} \Big],
\end{aligned} \tag{4.64a}$$

and

$$\begin{aligned}
\langle \left[\hat{A}_l^{(1,\mathrm{out})}\right]^\dagger \hat{A}_l^{(1,\mathrm{out})} \rangle = \sum_{n,n',k} \mathfrak{g}_{ln}^* \mathfrak{g}_{ln'} \Big[& \mathfrak{h}_{nk}^* \mathfrak{h}_{n'k} \sqrt{\left(\Lambda_n^{(2)} + 1\right)\left(\Lambda_{n'}^{(2)} + 1\right)} \Lambda_k^{(\mathrm{SU})} \\
& + \mathfrak{h}_{nk} \mathfrak{h}_{n'k}^* \sqrt{\Lambda_n^{(2)} \Lambda_{n'}^{(2)}} \left(\Lambda_k^{(\mathrm{SU})} + 1\right) \\
& - \mathfrak{h}_{nk}^* \mathfrak{h}_{n'k}^* \sqrt{\left(\Lambda_n^{(2)} + 1\right)\Lambda_{n'}^{(2)}} \sqrt{\Lambda_k^{(\mathrm{SU})}\left(\Lambda_k^{(\mathrm{SU})} + 1\right)} \\
& - \mathfrak{h}_{nk} \mathfrak{h}_{n'k} \sqrt{\Lambda_n^{(2)}\left(\Lambda_{n'}^{(2)} + 1\right)} \sqrt{\Lambda_k^{(\mathrm{SU})}\left(\Lambda_k^{(\mathrm{SU})} + 1\right)} \Big],
\end{aligned} \tag{4.64b}$$

where it has been used that

$$\langle \hat{A}_l^{(\mathrm{SU},\mathrm{out})} \hat{A}_l^{(\mathrm{SU},\mathrm{out})} \rangle = \langle \left[\hat{A}_l^{(\mathrm{SU},\mathrm{out})}\right]^\dagger \left[\hat{A}_l^{(\mathrm{SU},\mathrm{out})}\right]^\dagger \rangle = \sqrt{\left(1 + \Lambda_l^{(\mathrm{SU})}\right)\Lambda_l^{(\mathrm{SU})}}, \tag{4.65a}$$

$$\langle \left[\hat{A}_l^{(\mathrm{SU},\mathrm{out})}\right]^\dagger \hat{A}_l^{(\mathrm{SU},\mathrm{out})} \rangle = \langle \hat{A}_l^{(\mathrm{SU},\mathrm{out})} \left[\hat{A}_l^{(\mathrm{SU},\mathrm{out})}\right]^\dagger \rangle - 1 = \Lambda_l^{(\mathrm{SU})}, \tag{4.65b}$$

and the expectation values are over the vacuum state. Given the eigenvalues of the second crystal and the entire interferometer, as well as the overlap coefficients $\mathfrak{g}$ and $\mathfrak{h}$, Eqs. (4.64) allow for the retrieval of the variance of the quadrature of each output mode of the first crystal of the interferometer via Eq. (4.29).

4.3.1.2. High-Gain Approximation

The expressions for the reconstruction of the quadrature variance for each mode obtained with Eqs. (4.31) and (4.64) are impractical due to their cumbersome structure. Furthermore, applying these equations requires the eigenvalues of the second PDC section and the interferometer, which correspond to the absolute photon numbers in the Schmidt modes (since $\langle \left[\hat{A}_l^{(\mathrm{out})}\right]^\dagger \hat{A}_l^{(\mathrm{out})} \rangle = \Lambda_l$) and are challenging to obtain in experiments [4]. Instead, it is much more convenient find an expression for $\Delta^2 \hat{P}_{l,\vartheta}$ in terms of the eigenvalue ratios, which correspond to intensity ratios and are easier to obtain. This can be done at high gain, where $\Lambda_j^{(2)}, \tilde{\Lambda}_j^{(2)}, \Lambda_j^{(\mathrm{SU})}, \tilde{\Lambda}_j^{(\mathrm{SU})} \gg 1$ for at least some low order modes. Then,

$$\sqrt{\tilde{\Lambda}_n^{(2)}} = \sqrt{\Lambda_n^{(2)} + 1} \approx \sqrt{\Lambda_n^{(2)}} \left(1 + \frac{1}{2\Lambda_n^{(2)}}\right), \tag{4.66a}$$

$$\sqrt{\tilde{\Lambda}_k^{(\mathrm{SU})}} = \sqrt{\Lambda_k^{(\mathrm{SU})} + 1} \approx \sqrt{\Lambda_k^{(\mathrm{SU})}} \left(1 + \frac{1}{2\Lambda_k^{(\mathrm{SU})}}\right), \tag{4.66b}$$

which follows from the binomial approximation as $\sqrt{x+1} = \sqrt{x}\sqrt{1+1/x} \approx \sqrt{x}\,[1 + 1/(2x)]$ for large x. It should be noted that for the entire interferometer, $\Lambda_j^{(\mathrm{SU})}, \tilde{\Lambda}_j^{(\mathrm{SU})} \gg 1$ is not necessarily true at high gain, due to the fact that, the eigenvalues are generally much smaller at the dark fringe than at the bright fringe.

Figure 4.9 shows the eigenvalues for the second crystal and the interferometer at the dark and bright fringe for several values of the experimental gain $G_{\mathrm{exp}}^{(2)}$ of the second crystal. The experimental gain $G_{\mathrm{exp}}^{(1)} = 1$ of the first crystal is fixed. Clearly, the eigenvalues increase strongly with the experimental gain and with increasing gain, more and more modes fulfill $\Lambda_j^{(2)} \gg 1$ and $\Lambda_j^{(\mathrm{SU})}, \tilde{\Lambda}_j^{(\mathrm{SU})} \gg 1$ both for the dark and the bright fringe.

Plugging the inverse transformation of the Bogoliubov transformation [Eq. (4.61)] again into Eq. (4.63) and applying the approximations in Eqs. (4.66) yields the following expression for the output operators of the first PDC section:

$$\begin{aligned}
\hat{A}_l^{(1,\mathrm{out})} = 2\mathrm{i} &\sum_{n,k} \mathfrak{g}_{ln} \sqrt{\Lambda_n^{(2)}} \sqrt{\Lambda_k^{(\mathrm{SU})}}\, \mathrm{Re}(\mathfrak{h}_{nk}) \left[\hat{A}_k^{(\mathrm{SU,in})} + \left(\hat{A}_k^{(\mathrm{SU,in})}\right)^\dagger\right] \\
&+ \frac{1}{2} \sum_{n,k} \mathfrak{g}_{ln} \sqrt{\frac{\Lambda_n^{(2)}}{\Lambda_k^{(\mathrm{SU})}}} \left[\mathfrak{h}_{nk} \hat{A}_k^{(\mathrm{SU,in})} - \mathfrak{h}_{nk}^* \left(\hat{A}_k^{(\mathrm{SU,in})}\right)^\dagger\right] \\
&+ \frac{1}{2} \sum_{n,k} \mathfrak{g}_{ln} \sqrt{\frac{\Lambda_k^{(\mathrm{SU})}}{\Lambda_n^{(2)}}}\, \mathfrak{h}_{nk} \left[\hat{A}_k^{(\mathrm{SU,in})} + \left(\hat{A}_k^{(\mathrm{SU,in})}\right)^\dagger\right] \\
&+ \frac{1}{4} \sum_{n,k} \mathfrak{g}_{ln} \mathfrak{h}_{nk} \frac{1}{\sqrt{\Lambda_n^{(2)}}} \frac{1}{\sqrt{\Lambda_k^{(\mathrm{SU})}}} \hat{A}_k^{(\mathrm{SU,in})}.
\end{aligned} \tag{4.67}$$

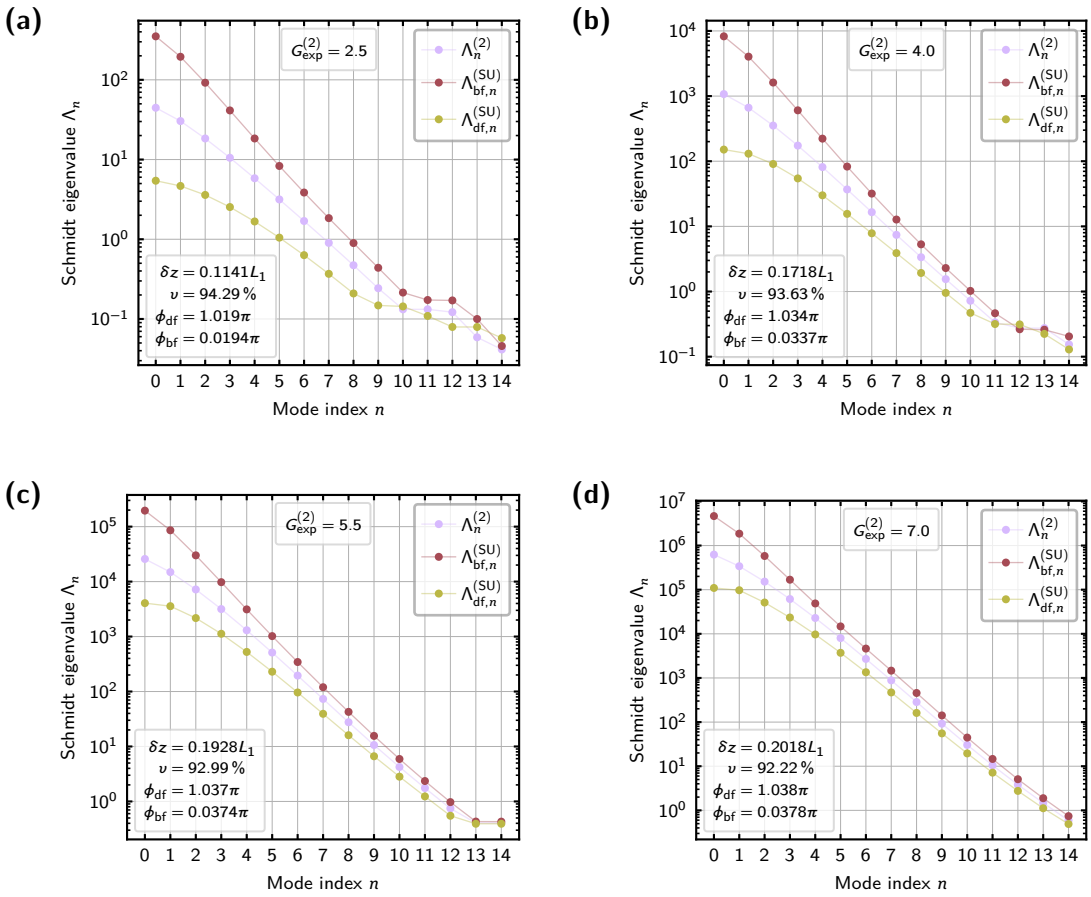

Figure 4.9: Eigenvalues for the first 15 modes of the second crystal and the unbalanced interferometer at the bright and dark fringe for increasing parametric gain of the second crystal. The ordering criterion $\Lambda^{(\mathrm{SU})}_{\mathrm{df},n} < \Lambda^{(2)}_n < \Lambda^{(\mathrm{SU})}_{\mathrm{bf},n}$ required for the validity of the high-gain approximation method derived in the text around Eq. (4.74) below holds true up to $n = 9$ for $G^{(2)}_{\mathrm{exp}} = 2.5$, up to $n = 11$ for $G^{(2)}_{\mathrm{exp}} = 4.0$, up to $n = 15$ for $G^{(2)}_{\mathrm{exp}} = 5.5$ (not visible) and up to $n = 17$ for $G^{(2)}_{\mathrm{exp}} = 7.0$ (not visible). Furthermore, the requirement $\Lambda_n \gg 1$ holds only up to at most $n = 5$ for $G^{(2)}_{\mathrm{exp}} = 2.5$, $n = 8$ for $G^{(2)}_{\mathrm{exp}} = 4.0$, $n = 11$ for $G^{(2)}_{\mathrm{exp}} = 5.5$ and $n = 13$ for $G^{(2)}_{\mathrm{exp}} = 7.0$. Since $\tilde{\Lambda}_n = 1 + \Lambda_n$, see Eq. (3.21), separate plots of $\tilde{\Lambda}_n$ are not shown. The lines connecting the data points were added for orientation purposes only. Adapted from Ref. [4].

Here, the second and third term already only contain the ratios of the eigenvalues. Additionally, if $\Lambda_n^{(2)}, \Lambda_k^{(\mathrm{SU})} \gg 1$, for low order modes n and k, the fourth term can be neglected, since $1/\sqrt{\Lambda_n^{(2)}\Lambda_k^{(\mathrm{SU})}} \ll 1$. As shown in Appendix D of Ref. [4], if the offset of the spherical mirror in the setup is adjusted carefully, it is possible to achieve $\mathrm{Re}(\mathfrak{h}_{nk}) \to 0$ for low order modes. This behavior is further confirmed by Fig. 4.8, which shows $\arg(\mathfrak{h}_{nk}) \approx 0$ or $\arg(\mathfrak{h}_{nk}) \approx \pi$ for low order modes. In this case, the first term may also be neglected. With these additional modifications applied, Eq. (4.67) becomes

$$\begin{aligned}\hat{A}_l^{(1,\mathrm{out})} = \frac{1}{2}\sum_{n,k}\mathfrak{g}_{ln}\Bigg\{&\sqrt{\frac{\Lambda_n^{(2)}}{\Lambda_k^{(\mathrm{SU})}}}\left[\mathfrak{h}_{nk}\hat{A}_k^{(\mathrm{SU,in})} - \mathfrak{h}_{nk}^*\left(\hat{A}_k^{(\mathrm{SU,in})}\right)^\dagger\right] \\ &+ \sqrt{\frac{\Lambda_k^{(\mathrm{SU})}}{\Lambda_n^{(2)}}}\,\mathfrak{h}_{nk}\left[\hat{A}_k^{(\mathrm{SU,in})} + \left(\hat{A}_k^{(\mathrm{SU,in})}\right)^\dagger\right]\Bigg\}.\end{aligned} \tag{4.68}$$

This expression for the output Schmidt mode operators of the first crystal only depends on the ratios $\Lambda_n^{(2)}/\Lambda_k^{(\mathrm{SU})}$ and $\Lambda_k^{(\mathrm{SU})}/\Lambda_n^{(2)}$ of the eigenvalues of the second crystal and of the interferometer and no longer on the absolute values.

If the output modes of the interferometer and the output modes of the second crystal are sufficiently similar, the overlap coefficient $\mathfrak{h}$ becomes diagonal and it is possible to approximate:

$$\mathfrak{h}_{nk} = \pm\delta_{nk}, \tag{4.69}$$

where the $\pm$ indicates that the sign of the output modes of the second crystal and of the interferometer are not well-defined, see Sec. 4.2.3, leading to an undefined sign of $\mathfrak{h}$. Comparing with the plots of the overlap coefficients in Fig. 4.8 shows that $\mathfrak{h}_{nk}$ is indeed approximately diagonal for the low order modes. Applying Eq. (4.69) to Eq. (4.68) yields

$$\begin{aligned}\hat{A}_l^{(1,\mathrm{out})} = \frac{1}{2}\sum_{n}\pm\mathfrak{g}_{ln}\Bigg\{&\sqrt{\frac{\Lambda_n^{(2)}}{\Lambda_n^{(\mathrm{SU})}}}\left[\hat{A}_n^{(\mathrm{SU,in})} - \left(\hat{A}_n^{(\mathrm{SU,in})}\right)^\dagger\right] \\ &+ \sqrt{\frac{\Lambda_n^{(\mathrm{SU})}}{\Lambda_n^{(2)}}}\left[\hat{A}_n^{(\mathrm{SU,in})} + \left(\hat{A}_n^{(\mathrm{SU,in})}\right)^\dagger\right]\Bigg\}.\end{aligned} \tag{4.70}$$

Ultimately, as will be shown below, the variance of the quadratures of the Schmidt modes does not depend on which of the two signs in Eq. (4.70) is chosen. This is a necessary requirement to assign physical meaning to the Schmidt modes: If the quadrature variance were to depend on the sign of $\mathfrak{h}$, it would also depend on the sign of the Schmidt modes, from which it originates. However, as seen in Sec. 4.2.3, the sign of the Schmidt modes is undefined, meaning that the quadrature variance would be ill-defined. Ultimately, the approximated form of the output operators written in Eq. (4.70) can be used to obtain an approximation of the level of squeezing in the corresponding quadratures using the eigenvalues of the second crystal and the entire interferometer, as well as the overlap coefficient matrix $\mathfrak{g}$.

Using the approximated form of the output Schmidt mode operator constructed above and written in Eq. (4.70), the generalized quadratures of the Schmidt modes take the form

$$\hat{P}_{l,\vartheta} = \sum_n \left[\mathrm{Re}\left(\mathfrak{g}_{ln} \mathrm{e}^{-\mathrm{i}\frac{\vartheta}{2}}\right) \sqrt{\frac{\Lambda_n^{(\mathrm{SU})}}{\Lambda_n^{(2)}}}\, \hat{X}_n^{(\mathrm{SU,in})} - \mathrm{Re}\left(\mathfrak{g}_{ln} \mathrm{e}^{-\mathrm{i}\frac{\vartheta}{2}}\right) \sqrt{\frac{\Lambda_n^{(2)}}{\Lambda_n^{(\mathrm{SU})}}}\, \hat{Y}_n^{(\mathrm{SU,in})} \right], \tag{4.71a}$$

where

$$\hat{X}_l \overset{\mathrm{def.}}{=} \hat{P}_{l,0} = \hat{A}_l + \hat{A}_l^\dagger, \tag{4.71b}$$

$$\hat{Y}_l \overset{\mathrm{def.}}{=} \hat{P}_{l,\pi} = -\mathrm{i}\left(\hat{A}_l - \hat{A}_l^\dagger\right), \tag{4.71c}$$

are two special quadrature operators defined analogously to Eqs. (4.3).

Since the quadrature operator $\hat{P}_{l,\vartheta}$ is linear in the Schmidt mode operators, see Eqs. (4.71), $\langle \hat{P}_{l,\vartheta} \rangle = 0$. Thus, according to Eq. (4.29), the variance of the quadrature is given by

$$\Delta^2 \hat{P}_{l,\vartheta} = \sum_n |\check{\mathfrak{g}}_{ln}|^2 \left[\cos^2\left(\arg(\check{\mathfrak{g}}_{ln}) + \frac{\phi - \vartheta}{2}\right) \frac{\Lambda_n^{(\mathrm{SU})}}{\Lambda_n^{(2)}} + \sin^2\left(\arg(\check{\mathfrak{g}}_{ln}) + \frac{\phi - \vartheta}{2}\right) \frac{\Lambda_n^{(2)}}{\Lambda_n^{(\mathrm{SU})}} \right], \tag{4.72}$$

where it has been used that

$$\mathfrak{g}_{ln} = \check{\mathfrak{g}}_{ln} \mathrm{e}^{\mathrm{i}\frac{\phi}{2}}, \tag{4.73}$$

which follows from comparing Eqs. (4.50) and (4.52).

Further simplifications of the expression for the variance of the quadrature operator in Eq. (4.72) are possible by closely inspecting the behavior of $\mathfrak{g}$. As shown in Appendix D of Ref. [4], similar to the behavior of $\mathrm{Re}(\mathfrak{h})$ mentioned above, $\check{\mathfrak{g}}_{ln} \to \pm 1$ for several low order modes as δz reaches the position that maximizes the visibility. This is again confirmed by the plots of the overlap coefficients in Fig. 4.8, which show that the phase dependence of $\mathfrak{g}$ is mainly determined by the term $\mathrm{e}^{\mathrm{i}\frac{\phi}{2}}$ for the low order modes, as expected from the analytic expression for the connection between $\check{\mathfrak{g}}$ and $\mathfrak{g}$ in Eq. (4.73). These observations imply that $\arg(\check{\mathfrak{g}}_{ln}) \approx m\pi$, for $m \in \mathbb{Z}$. Due to the π-periodicity of $\cos^2$ and $\sin^2$, these two trigonometric functions as they appear in Eq. (4.72) are essentially independent of l and n for the low-order modes and the $\arg(\check{\mathfrak{g}}_{ln})$ summand in their arguments can be neglected.

Depending on whether $\Lambda_n^{(\mathrm{SU})}$ or $\Lambda_n^{(2)}$ is larger for a given mode, either the $\cos^2$-term or the $\sin^2$-term is larger for a fixed $\phi - \vartheta$ (unless $\Lambda_n^{(\mathrm{SU})} = \Lambda_n^{(2)}$). Generally, the eigenvalues are ordered as

$$\Lambda_{\mathrm{df},n}^{(\mathrm{SU})} < \Lambda_n^{(2)} < \Lambda_{\mathrm{bf},n}^{(\mathrm{SU})}, \tag{4.74}$$

where the subscripts $_{\mathrm{df}}$ and $_{\mathrm{bf}}$ label the eigenvalues of the interferometer at the dark and bright fringe, respectively. As shown in Fig. 4.9, this ordering relation usually holds up to some index n, which increases as the experimental gain is increased. Thus, the phase differences $\phi - \vartheta$ for which the summands in Eq. (4.72) are maximized and minimized (at

least for the low-order modes, to which all the abovementioned conditions apply) can be determined as follows[10]:

- At the dark fringe, $\Lambda_n^{(2)} > \Lambda_n^{(\mathrm{SU})}$, see Eq. (4.74). This means that the prefactor of the $\cos^2$-contribution is smaller than that of the $\sin^2$-contribution. The term inside the brackets is then maximized if the $\cos^2$-term vanishes and the $\sin^2$-term is maximized, which occurs for $\vartheta = \phi_{\mathrm{df}} + 2\pi\,(m+1)$, for $m \in \mathbb{Z}$, and where ϕ_{df} is the interferometric phase at the dark fringe. Conversely, the term inside the brackets is minimized if the $\sin^2$-term vanishes and only the $\sin^2$-term remains. This occurs for $\vartheta = \phi_{\mathrm{df}} + 2\pi m$, $m \in \mathbb{Z}$.

- At the bright fringe, $\Lambda_n^{(\mathrm{SU})} > \Lambda_n^{(2)}$, see Eq. (4.74). Hence, the roles of the $\cos^2$-contribution and that of the $\sin^2$-contribution are reversed. The term inside the brackets is maximized for $\vartheta = \phi_{\mathrm{bf}} + 2\pi m$, for $m \in \mathbb{Z}$, when the $\sin^2$-term vanishes and the $\cos^2$-term is maximized. Analogously to above, ϕ_{bf} is the interferometric phase at the bright fringe. Similarly, the term in the brackets is minimized for $\vartheta = \phi_{\mathrm{bf}} + 2\pi\,(m+1)$, $m \in \mathbb{Z}$.

These observations show that the variance for the squeezed and the anti-squeezing quadrature can be obtained at either the dark fringe or the bright fringe. In concrete terms, at the dark fringe, the extremal levels of the quadrature variance follow from Eqs. (4.77) as

$$\min_{\vartheta} \Delta^2 \hat{P}_{l,\vartheta} \simeq \sum_n |\mathfrak{g}_{ln}|^2 \frac{\Lambda_{\mathrm{df},n}^{(\mathrm{SU})}}{\Lambda_n^{(2)}}, \tag{4.75a}$$

$$\max_{\vartheta} \Delta^2 \hat{P}_{l,\vartheta} \simeq \sum_n |\mathfrak{g}_{ln}|^2 \frac{\Lambda_n^{(2)}}{\Lambda_{\mathrm{df},n}^{(\mathrm{SU})}}, \tag{4.75b}$$

while at the bright fringe, they are given by

$$\min_{\vartheta} \Delta^2 \hat{P}_{l,\vartheta} \simeq \sum_n |\mathfrak{g}_{ln}|^2 \frac{\Lambda_{\mathrm{bf},n}^{(2)}}{\Lambda_n^{(\mathrm{SU})}}, \tag{4.76a}$$

$$\max_{\vartheta} \Delta^2 \hat{P}_{l,\vartheta} \simeq \sum_n |\mathfrak{g}_{ln}|^2 \frac{\Lambda_{\mathrm{bf},n}^{(\mathrm{SU})}}{\Lambda_n^{(2)}}. \tag{4.76b}$$

It should be noted that the value for ϑ that minimizes the quadrature variance in Eqs. (4.75a) and (4.76a) is different for both equations and normally both values are apart by around π. Similarly, the values for ϑ corresponding to the values that maximize the variances in Eqs. (4.75b) and (4.76b) are generally different and apart by π. The main difference between the expressions for the dark fringe and bright fringe is that the reciprocal of the eigenvalues appears in the sum. It should be noted that these results are heuristic in the sense that they to not take into account the precise behavior of the higher order modes and

[10] These observations can be analyzed more formally by defining a function $f(x) = a\sin^2(x) + b\cos^2(x)$ for $a, b > 0$. Then, $\mathrm{d}f/\mathrm{d}x = (a-b)\sin(2x)$ and $\mathrm{d}^2 f/\mathrm{d}^2 x = 2\,(a-b)\cos(2x)$ and the problem of finding the minima and maxima of f in the two cases where $a > b$ and $a < b$.

rely on the fact that the approximations made throughout this derivation apply sufficiently well to the lower-order modes.

4.3.1.3. Theoretical Application

Generally, the *level of squeezing* S_l and the *level of anti-squeezing* AS_l for the mode l can be defined via the logarithm of the ratio of the quadratures over the quadratures of the vacuum:

$$\mathrm{S}_l \overset{\text{def.}}{=} 10 \log_{10} \left[\frac{\min_\vartheta \, \Delta^2 \hat{P}_{l,\vartheta}}{\Delta^2 \hat{P}^{(\mathrm{vac})}} \right] \mathrm{dB}, \tag{4.77a}$$

$$\mathrm{AS}_l \overset{\text{def.}}{=} 10 \log_{10} \left[\frac{\max_\vartheta \, \Delta^2 \hat{P}_{l,\vartheta}}{\Delta^2 \hat{P}^{(\mathrm{vac})}} \right] \mathrm{dB}, \tag{4.77b}$$

where[11] $\Delta^2 \hat{P}^{(\mathrm{vac})} = 1$ denotes the variance of the vacuum quadrature operator (which does not depend on the mode index), and S_l and AS_l denote the levels of squeezing and anti-squeezing for the lth mode, respectively. As described in Sec. 4.1, the ϑ corresponding to the minimum and maximum of $\Delta^2 \hat{P}_{l,\vartheta}$ and thus the maximally squeezed and anti-squeezed quadratures lie apart by π.

Figures 4.10(a) and 4.10(b) show the computed values for the levels of squeezing and anti-squeezing in the first 15 modes for the SU(1,1) as described above using several methods. The experimental gain of the second crystal is $G^{(2)}_{\mathrm{exp}} = 4$. The light-blue and red-brown lines show the levels of squeezing and anti-squeezing obtained via directly evaluating the analytic expression for the quadrature variance in Eq. (4.32) and via using the exact procedure outlined in Sec. 4.3.1.1. Unsurprisingly, both of these lines coincide. This is due to the fact that the exact approach does not apply any approximations and only uses the exact analytic expressions when ultimately expressing the output Schmidt operators of the first crystal via the eigenvalues and overlap coefficients. Furthermore, for these two methods, $\mathrm{S}_l + \mathrm{AS}_l = 0$, which can also be easily seen analytically from Eqs. (4.35), which express the minimal and maximal variance of the quadrature via the squeezing parameter r_l of each mode. Clearly,

$$\mathrm{S}_l = -\frac{20 r_l}{\ln(10)} \mathrm{dB}, \tag{4.78a}$$

$$\mathrm{AS}_l = \frac{20 r_l}{\ln(10)} \mathrm{dB}, \tag{4.78b}$$

which follows directly from plugging Eqs. (4.35) into the definitions of the levels of squeezing and anti-squeezing written in Eqs. (4.77). Equations (4.78) immediately show that $\mathrm{S}_l + \mathrm{AS}_l = 0$. This is always the case for ideal squeezed states, as can be seen from taking $\log_{10}$ of both sides of $\left(\min_\vartheta \, \Delta^2 \hat{P}_{l,\vartheta}\right) \left(\max_\vartheta \, \Delta^2 \hat{P}_{l,\vartheta}\right) = 1$ and applying the definitions of the levels of squeezing and anti-squeezing [Eqs. (4.77)].

[11] The concrete value provided for $\Delta^2 \hat{P}^{(\mathrm{vac})}$ follows directly from Eq. (4.29), which reduces to 1 if the Schmidt operators are connected to the vacuum plane-wave operators.

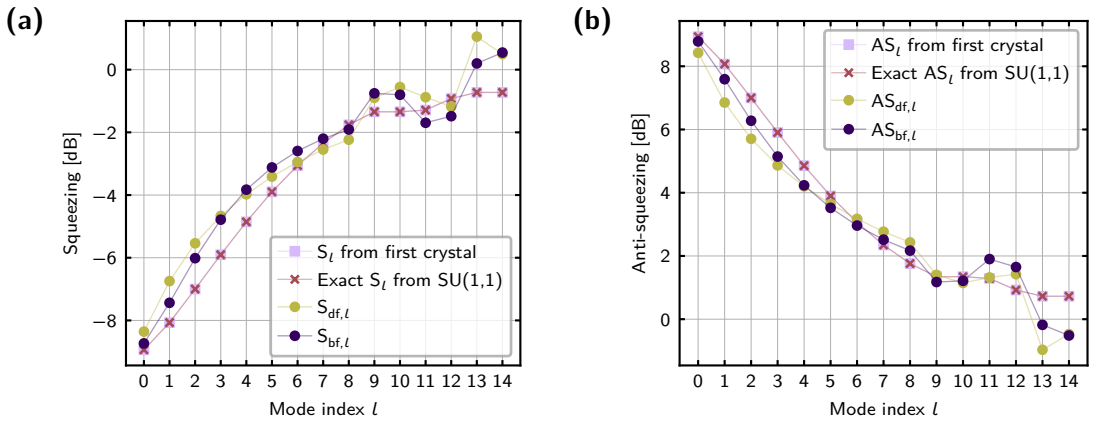

Figure 4.10: Computed values for the levels of **(a)** squeezing and **(b)** anti-squeezing using the eigenvalues of the first crystal directly (light-blue line), using the exact method outlined in Sec. 4.3.1.1 (red-brown line), and the high-gain approximation as outline in Sec. 4.3.1.2 at the dark fringe (yellow line) and the bright fringe (dark-blue line). The lines connecting the data points were added for orientation purposes only. Adapted from Ref. [4].

For the methods, where the levels of squeezing and anti-squeezing are obtained using the high-gain approximation at either the dark or the bright fringe, it is less obvious whether S_l and AS_l have the same value but with the opposite sign. Evidently, for the lower-order modes, the approximated methods underestimate the strength of the squeezing, leading to larger values for S_l, while also underestimating the anti-squeezing, leading to smaller values for AS_l.

Starting at $l = 9$, the behavior of S_l and AS_l becomes non-monotonic. This is due to the fact that $\Lambda_l^{(SU)}, \Lambda_l^{(2)} \gg 1$ and the ordering requirement in Eq. (4.74) are no longer sufficiently well satisfied, compare Fig. 4.9(b). Overall, the theoretical application shows that the approximated methods are well-suited for extracting the levels of squeezing and anti-squeezing for the lower-order modes from the eigenvalues of the interferometer and the second crystal, as well as the modulus squared of the overlap coefficient $\mathfrak{g}_{ln}$.

4.3.2. Experimental Application

This section describes several aspects and results of the experiment conducted as described in Barakat *et al.* [3] by collaborators. Supplementary material can be found in Chekhova *et al.* [103].

Modelling of Losses. Unlike for the purely theoretical application in Sec. 4.3.1.3, the comparison between the theory and the experiment must take into account the imperfections of the experimental setup. Most importantly, losses need to be taken into account since they lead to a degradation of squeezed states, reducing the strength of the squeezing and thereby increasing the quadrature variance. For SU(1,1) interferometers, at least two kinds of losses are relevant: *Internal losses*, the fields incur between the two PDC sections of the interferometer and *detection losses* occurring between the second crystal and the detector

and in the detector itself. It is well known that internal losses are more detrimental to the performance of SU(1,1) interferometers than detection losses [6, 93, 112, 124].

In a theoretical model, both types of losses can be implemented using a "virtual" (or "fictitious") beamsplitter placed between the two crystals (internal losses) and after the second crystal (detection losses) [4, 9, 17, 20, 124, 125]. This beamsplitter is only included in the model and not the actual experimental setup. For the internal losses, the input-output relations for the plane-wave operators shown in Eqs. (3.10) and (3.18) are modified by including the ancillary vacuum modes, described by their plane-wave operators $\hat{c}$, which are introduced from the open port of the virtual beamsplitter between the two crystals. The output of the second output port of the beamsplitter, which does not lead to the second crystal, is ignored. Thus, for the second crystal, the input-output relations take the form [4]:

$$\begin{aligned}\hat{a}_s^{(2,\mathrm{out})}(q_s) = \sqrt{1-\iota}\,\left[\int \mathrm{d}q_s'\,\tilde{\eta}^{(2)}(q_s,q_s')\,\hat{a}_s^{(2,\mathrm{in})}(q_s') + \int \mathrm{d}q_i'\,\beta^{(2)}(q_s,q_i')\left[\hat{a}_i^{(2,\mathrm{in})}(q_i')\right]^\dagger\right] \\ + \sqrt{\iota}\,\left[\int \mathrm{d}q_s'\,\tilde{\eta}_0^{(2)}(q_s,q_s')\,\hat{c}_s^{(2,\mathrm{in})}(q_s') + \int \mathrm{d}q_i'\,\beta_0^{(2)}(q_s,q_i')\left[\hat{c}_i^{(2,\mathrm{in})}(q_i')\right]^\dagger\right],\end{aligned} \tag{4.79a}$$

$$\begin{aligned}\left[\hat{a}_i^{(2,\mathrm{out})}(q_i)\right]^\dagger = \sqrt{1-\iota}\,\left[\int \mathrm{d}q_i'\,\left[\tilde{\eta}^{(2)}(q_i,q_i')\right]^*\left[\hat{a}_i^{(2,\mathrm{in})}(q_i')\right]^\dagger + \int \mathrm{d}q_s'\,\left[\beta^{(2)}(q_i,q_s')\right]^*\hat{a}_s^{(2,\mathrm{in})}(q_s')\right] \\ + \sqrt{\iota}\,\left[\int \mathrm{d}q_i'\,\left[\tilde{\eta}_0^{(2)}(q_i,q_i')\right]^*\left[\hat{c}_i^{(2,\mathrm{in})}(q_i')\right]^\dagger + \int \mathrm{d}q_s'\,\left[\beta_0^{(2)}(q_i,q_s')\right]^*\hat{c}_s^{(2,\mathrm{in})}(q_s')\right],\end{aligned} \tag{4.79b}$$

where ι denotes the loss factor and where β_0 and $\tilde{\eta}_0$ are the new transfer functions connecting the newly introduced vacuum modes to the output modes, meaning that $\hat{c}_{s/i}^{(2,\mathrm{in})}|0\rangle = 0$. The new plane-wave operators $\hat{c}$ commute as

$$[\hat{c}_s(q), \hat{c}_s^\dagger(q')] = \delta(q-q'), \tag{4.80a}$$
$$[\hat{c}_i(q), \hat{c}_i^\dagger(q')] = \delta(q-q'), \tag{4.80b}$$
$$[\hat{c}_s(q), \hat{c}_i^\dagger(q')] = 0, \tag{4.80c}$$

following the commutation relations of the plane-wave operator $\hat{a}$ for this model, where the plane-wave modes are assumed to be distinguishable in some degree of freedom, compare Eqs. (3.8), and, since they describe states that are orthogonal to those of the original modes $\hat{a}$, they unconditionally commute with the $\hat{a}$-operators, so that

$$[\hat{c}(q), \hat{a}^\dagger(q')] = 0, \tag{4.81a}$$
$$[\hat{c}(q), \hat{a}(q')] = 0, \tag{4.81b}$$
$$[\hat{c}^\dagger(q), \hat{a}^\dagger(q')] = 0, \tag{4.81c}$$

regardless of whether the operators belong to the signal or idler fields. Additionally, due to the fact that the states for the $\hat{c}$-operators are orthogonal to those of the $\hat{a}$-operators, the integro-differential equations describing the evolution of each set of operators through

the crystals can be different. In fact, the $\hat{c}$-operators start at the vacuum state and then see the second crystal of the interferometer as their first PDC section, meaning that for the integration of the integro-differential equations of the $\hat{c}$-operators, the phase-matching function of a single crystal [Eq. (3.30)] has to be used and not that of the second crystal of a diffraction-compensated SU(1,1) interferometer [Eq. (3.37)]. Hence, overall, additionally to the transfer functions of the two crystals, it is always necessary to obtain the transfer functions for a PDC section that uses the phase-matching function of a single crystal and has otherwise identical properties as the second crystal.

By applying the input-output relations for the plane-wave operators for the first crystal, meaning $\hat{a}_{s/i}^{(1,\mathrm{out})} = \hat{a}_{s/i}^{(2,\mathrm{in})}$ and $\hat{a}_{s/i}^{(2,\mathrm{out})} = \hat{a}_{s/i}^{(\mathrm{SU},\mathrm{out})}$, the input-output relations for the second crystal including the internal losses [Eqs. (4.79)] can be written as

$$\begin{aligned}\hat{a}_s^{(\mathrm{SU},\mathrm{out})}(q_s) = \sqrt{1-\iota}\,\Bigg[\int \mathrm{d}q_s'\,\tilde{\eta}^{(\mathrm{SU})}(q_s,q_s')\,\hat{a}_s^{(1,\mathrm{in})}(q_s') + \int \mathrm{d}q_i'\,\beta^{(\mathrm{SU})}(q_s,q_i')\left[\hat{a}_i^{(1,\mathrm{in})}(q_i')\right]^\dagger\Bigg] \\ + \sqrt{\iota}\,\Bigg[\int \mathrm{d}q_s'\,\tilde{\eta}_0^{(2)}(q_s,q_s')\,\hat{c}_s^{(2,\mathrm{in})}(q_s') + \int \mathrm{d}q_i'\,\beta_0^{(2)}(q_s,q_i')\left[\hat{c}_i^{(2,\mathrm{in})}(q_i')\right]^\dagger\Bigg],\end{aligned} \tag{4.82a}$$

$$\begin{aligned}\left[\hat{a}_i^{(\mathrm{SU},\mathrm{out})}(q_i)\right]^\dagger = \sqrt{1-\iota}\,\Bigg\{\int \mathrm{d}q_i'\,\left[\tilde{\eta}^{(\mathrm{SU})}(q_i,q_i')\right]^*\left[\hat{a}_i^{(1,\mathrm{in})}(q_i')\right]^\dagger \\ + \int \mathrm{d}q_s'\,\left[\beta^{(\mathrm{SU})}(q_i,q_s')\right]^*\hat{a}_s^{(1,\mathrm{in})}(q_s')\Bigg\} \\ + \sqrt{\iota}\,\Bigg[\int \mathrm{d}q_i'\,\left[\tilde{\eta}_0^{(2)}(q_i,q_i')\right]^*\left[\hat{c}_i^{(2,\mathrm{in})}(q_i')\right]^\dagger + \int \mathrm{d}q_s'\,\left[\beta_0^{(2)}(q_i,q_s')\right]^*\hat{c}_s^{(2,\mathrm{in})}(q_s')\Bigg],\end{aligned} \tag{4.82b}$$

where the transfer functions $\beta^{(\mathrm{SU})}$ and $\tilde{\eta}^{(\mathrm{SU})}$ result from those of the first and second crystal via the connection relations as written in Eqs. (3.19). In general, $\beta^{(2)}(q,q') \neq \beta_0^{(2)}(q,q')$ and $\tilde{\eta}^{(2)}(q,q') \neq \tilde{\eta}_0^{(2)}(q,q')$, as well as $\beta^{(\mathrm{SU})}(q,q') \neq \beta_0^{(2)}(q,q')$ and $\tilde{\eta}^{(\mathrm{SU})}(q,q') \neq \tilde{\eta}_0^{(2)}(q,q')$. After plugging in the joint Schmidt decompositions for $\beta^{(2)}$ and $\tilde{\eta}^{(2)}$, as well as $\beta_0^{(2)}$ and $\tilde{\eta}_0^{(2)}$ into Eqs. (4.79) or $\beta^{(\mathrm{SU})}$ and $\tilde{\eta}^{(\mathrm{SU})}$, as well as $\beta_0^{(2)}$ and $\tilde{\eta}_0^{(2)}$ into Eqs. (4.82), it becomes clear that the resulting expressions can, in general, no longer be brought to the same form as the Bogoliubov transformations for the Schmidt operators, see Eqs. (3.23) and (3.24) and the surrounding text. This is due to the fact that both the input and output Schmidt modes of the two joint decomposition are, in general, different and, for non-degenerate eigenvalues, unique up to their signs, so that it is not possible to choose a set of modes that satisfies both the decomposition of β and $\tilde{\eta}$ (for the second crystal or the interferometer) and that of β_0 and $\tilde{\eta}_0$. Similar observations were made in Christ *et al.* [126]. As argued in Kopylov *et al.* [20], the joint Schmidt decomposition is no longer applicable to this system including losses, since it is essentially an open system.

As already indicated with the commutator between the signal and idler operators in Eq. (4.80c), the signal and idler photons are assumed to be distinguishable. In the experiment, this is realized by recording the full two-dimensional intensity spectra at the

output of the second crystal and only selecting radiation from a line at a certain angular offset from the center of the radially symmetric intensity distribution [3, 99, 103]. Due to the conservation of the transverse momentum, each photon detected on this line is either the signal or the idler photon of a signal-idler photon pair, but both photons of the pair cannot be detected on this same line[12].

In order to remedy the fact that the joint Schmidt decomposition is not applicable to systems including losses, a hybrid approach can be used instead, where the overlap coefficients $\mathfrak{g}_{ln}$ are obtained from the system without losses ($\iota = 0\,\%$), while the eigenvalues are obtained including the losses, as described in more detail below. Using these quantities, Eqs. (4.75)–(4.77) can be used to obtain the levels of squeezing and anti-squeezing. The eigenvalues are obtained analogously to the experimental procedure, which is, by performing a Schmidt decomposition (singular value decomposition in the discrete experimental case) of the covariance function[13] $\mathrm{cov}(q,q')$ as defined in Eq. (3.28). Using the input output relations for the interferometer as in Eqs. (4.82) to compute the intensity profile as in Eq. (3.27) yields

$$\langle \hat{N}_s(q)\rangle = (1-\iota)\int \mathrm{d}q'\,|\beta(q,q')|^2 + \iota\int \mathrm{d}q'\,|\beta_0(q,q')|^2. \tag{4.83}$$

In words, the intensity profile is just the sum of the two intensity profiles, weighted with the loss factor. This is due to the fact that the $\hat{a}$ and $\hat{c}$-operators commute, see Eqs. (4.81). Similarly, the covariance function as defined in Eq. (3.28) takes the form[14]:

$$\begin{aligned}\mathrm{cov}(q,q') = {}& (1-\iota)^2\,\mathrm{cov}_{\beta^{(\mathrm{SU})}}(q,q') + \iota^2\,\mathrm{cov}_{\beta_0^{(2)}}(q,q') \\ & + \iota\,(1-\iota)\left\{\delta(q-q')\left[N_{\beta^{(\mathrm{SU})}}(q) + N_{\beta_0^{(2)}}(q)\right] + 2\,\mathrm{Re}\left[\mathcal{C}_{\beta_0^{(\mathrm{SU})}}(q,q')\,\mathcal{C}^*_{\beta_0^{(2)}}(q,q')\right]\right\},\end{aligned} \tag{4.84}$$

where $\mathrm{cov}_{\beta'}$ refers to the covariance function as written in Eq. (3.29) and evaluated for β'; $N_{\beta'}(q) = \int \mathrm{d}q'\,|\beta'(q,q')|^2$ refers to the intensity profile, see Eq. (3.27), and where

$$\mathcal{C}_\beta(q,q') = \int \mathrm{d}\bar{q}\,\beta^*(q,\bar{q})\,\beta(q',\bar{q}). \tag{4.85}$$

At high gain, the covariance function (for any system considered in the context of this work) can be decomposed as [3–5, 100, 103, 127]

$$\sqrt{\mathrm{cov}(q,q')} = \sum_m \lambda_m v_m(q)\,v_m(q'), \tag{4.86}$$

[12] The idea behind this can also be seen more directly in a more idealized scenario, for example using a plane-wave pump. As seen in Sec. 3.5.2, the photons are perfectly anti-correlated, meaning that their transverse wave-vector components are equal in modulus and have opposite signs. For a finite-width pump, this condition is slightly relaxed, as can be seen from the plots of the covariance function shown in Fig. 3.5.

[13] The covariance function can be evaluated, even though the joint Schmidt decomposition can no longer be applied. For this, Eq. (3.28) is evaluated directly using Eqs. (4.82).

[14] To see this, use the commutation relations between the plane-wave operators as written in Eqs. (4.80) and (4.81), as well as Eq. (A3a) of Ref. [1].

which can be shown from Eq. (3.29) by plugging in the Schmidt decomposition for β and using $\Lambda_n \gg 1$. This is the procedure applied in the experiment. From the recorded one-dimensional slices of the intensity profile mentioned above, the covariance is determined and decomposed according to Eq. (4.86) to obtain the modal weights λ_m. These are connected to the eigenvalues of the transfer function β via

$$\frac{\Lambda_n}{\langle \hat{N}_{\mathrm{tot}} \rangle} \approx \frac{\lambda_n}{\sum_m \lambda_m}. \tag{4.87}$$

If applied in the context of the experiment, $\langle \hat{N}_{\mathrm{tot}} \rangle$ refers to the integral intensity on the line at which the intensity is recorded. It should be noted that the approximate connection between the eigenvalues in Eq. (4.87) only holds well for the lower order modes, since the λ_n and Λ_n are monotonically decreasing, meaning that after some index, they are no longer large enough for the approximation $\Lambda_n \gg 1$ to hold. This method for obtaining the eigenvalues is applied both for the second crystal and the entire interferometer. Similarly, the v_m in Eq. (4.86) can be seen as approximations to the modulus[15] of the output modes u_m of the system for which the covariance function was obtained [5], which allows for a method of extracting the modes from the covariance function [103]. It should be noted that this approximation also requires that the cross-correlation term of the covariance is not present, see Chekhova *et al.* [103]. This is achieved by measuring only the photon distributions on the line at a certain offset, as mentioned above. However, this is ultimately only an approximation and does not necessarily guarantee a full removal of the corresponding contributions in the experimentally obtained covariance matrices, see for example Fig. S4 of Chekhova *et al.* [103].

Detection Losses for Direct Detection. The goal of the setup is determining the squeezing in the quadratures of the output Schmidt modes of the first crystal. As mentioned above, in the SU(1,1) interferometer setup, internal losses will affect the detected levels of squeezing and anti-squeezing. More generally, if an alternative detection method for the squeezing is used, which directly obtains the levels of squeezing and anti-squeezing from the output of the first crystal, these internal losses can be understood as detection losses for this alternative method instead. In the theoretical description, these losses are again implemented by placing a virtual beamsplitter between the output of the first crystal and the detector. Then, the signal output operators $\hat{a}_s^{(\mathrm{BS,out})}(q_s)$ after the beamsplitter take the form

$$\begin{aligned}\hat{a}_s^{(\mathrm{BS,out})}(q_s) = \sqrt{1-\iota}\left\{\int \mathrm{d}q_s'\, \tilde{\eta}^{(1)}(q_s, q_s')\, \hat{a}_s^{(1,\mathrm{in})}(q_s') + \int \mathrm{d}q_i'\, \beta^{(1)}(q_s, q_i')\left[\hat{a}_i^{(1,\mathrm{in})}(q_i')\right]^\dagger\right\} \\ + \sqrt{\iota}\,\hat{c}^{(\mathrm{BS,in})}(q_s),\end{aligned} \tag{4.88}$$

where $\hat{c}^{(\mathrm{BS,in})}(q_s)$ is the annihilation operator of the vacuum mode introduced from the second input of the beamsplitter. The commutations relations here are the same as the

[15] Evidently, Eq. (4.86) describes the continuous analog of a singular value decomposition. Since $\sqrt{\mathrm{cov}(q, q')}$ is real-valued, the modes v_m can therefore always be chosen to be real-valued.

ones given above, see Eqs. (4.80) and (4.81). Applying the joint Schmidt decomposition to the transfer functions of the first crystal ($\tilde{\eta}^{(1)}$ and $\beta^{(1)}$) to Eq. (4.88) and following the steps which lead to the Bogoliubov transformations [Eqs. (3.23)] yields

$$\hat{A}_n^{(\mathrm{out})} = \sqrt{1-\iota}\left\{\sqrt{\tilde{\Lambda}_n}\,\hat{A}_n^{(\mathrm{in})} + \sqrt{\Lambda_n}\left[\hat{A}_n^{(\mathrm{in})}\right]^\dagger\right\} + \sqrt{\iota}\,\hat{C}_n\,, \tag{4.89}$$

where it has been used that $\hat{A}_n = \hat{B}_n$ for the degeneracy conditions used in this chapter and where

$$\hat{C}_n = \int \mathrm{d}q\, u_n^*(q)\,\hat{c}^{(\mathrm{BS,in})}(q). \tag{4.90}$$

Evaluating the variance of the generalized quadrature operator for $\hat{A}_n^{(\mathrm{out})}$ as written above by plugging Eq. (4.89) into Eq. (4.29) yields

$$\Delta^2\hat{P}_{l,\vartheta} = 1 + (1-\iota)\left[2\sinh^2(r_l) + \sinh(2r_l)\cos(\vartheta)\right], \tag{4.91}$$

where the parametrization of the eigenvalue in terms of r_l has been used, see Eqs. (4.33). Minimizing and maximizing this expression yields

$$\min_\vartheta \Delta^2\hat{P}_{l,\vartheta} = \iota + \mathrm{e}^{-2r_l}(1-\iota), \tag{4.92a}$$

$$\max_\vartheta \Delta^2\hat{P}_{l,\vartheta} = \iota + \mathrm{e}^{2r_l}(1-\iota). \tag{4.92b}$$

Clearly, in the limit $\iota \to 100\,\%$, both the minimal and maximal quadrature are identical, which can also be seen from Eq. (4.91), and the measured state is no longer squeezed. Moreover, for the levels of squeezing and anti-squeezing associated with Eqs. (4.92), the inequality

$$-\mathrm{S}_l < \mathrm{AS}_l \tag{4.93}$$

holds for $\iota > 0$ (as long as $r_l > 0$). Thus, for non-vanishing losses, $\mathrm{AS}_l + \mathrm{S}_l > 0$, which reflects the well-known result that the level of squeezing is usually more strongly affected by losses than the level of anti-squeezing, see for example Refs. [128–130].

Imperfections of the Pump Beam. Apart from losses, a second important factor is a potential non-Gaussianity of the pump beam. This can for example lead to an effectively larger area of the crystal being illuminated than would be the case for a Gaussian function that bests approximates the actual shape of the pump. It was found[16] for the experiment in Barakat *et al.* [3] that the spatial cross-section intensity distribution had, apart from a central peak, several smaller side-peaks, as can be seen in Fig. 4.11. This also leads to a small asymmetry of the pump, which was found to only minimally affect the intensity profiles. Additionally, since the integro-differential equations which are used for the description of the experiment only take into account a single transverse dimension, it should be taken into account that

[16]This was noticed after the experiment was completed and was not intended.

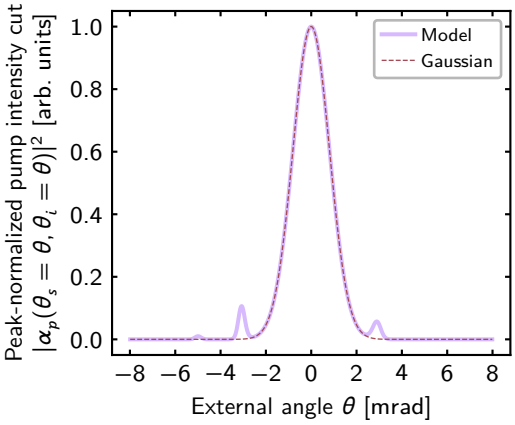

Figure 4.11: Cross-section of the intensity distribution of the pump beam used in the theoretical calculations in wave-vector space (light-blue line). The pump beam is not a simple Gaussian with $\sigma = \left(70/\sqrt{2}\right)$ µm (red-brown line, compare Sec. 4.2) and instead has three visible side-peaks and a very small asymmetry of the central peak (not visible). Along the line $\theta_s = -\theta_i$, both pump functions are constant. Additionally, both lines shown here already takes into account that the intensity is sampled at a line $\theta_{\text{line},y} = 6.5\,\text{mrad}$ away from the collinear direction, see the text.

the intensity distribution is sampled on a line with a certain angular offset from the center (or, equivalently, from the z-axis), as described above. If the full two-dimensional pump profile in wave-vector space is described by a function[17] $\alpha_p(q_{s,x}, q_{s,y}; q_{i,x}, q_{i,y})$, this can be, as a first approximation, achieved by using[18] $\alpha_p(q_{s,x}, q_{s,y} = q_{\text{line},y}; q_{i,x}, q_{i,y} = -q_{\text{line},y})$ as the pump envelope inside the integro-differential equations, where $q_{\text{line},y}$ is the transverse wave-vector component corresponding to the external angle $\theta_{\text{line},y}$ at which the line along which the intensity is recorded lies with respect to the pump axis. It should be noted that this line of reasoning requires that the signal and idler fields do not propagate too far away from the pump axis. The difference in the sign of $q_{s,y}$ and $q_{i,y}$ is due to the fact that the transverse wave-vector components of the signal and idler photons that reach the line at which the intensity is measured are, to a good approximation, anti-correlated (meaning they have the opposite sign). In the following, in accordance with Barakat *et al.* [3], $\theta_{\text{line},y} = 6.5\,\text{mrad}$ (*external* angle). Note that this offset is already included in Fig. 4.11. Due to this modification of the pump beam, the fitting constant A connecting the theoretical gain parameter Γ and the experimental gain G_{exp} is modified, so that, in the following, $A = 157.07$, independently of the gain. In the experiment, the connection between the gain and the pump power is made by a similar fitting procedure as for the theory, see Sec. 3.4 and Chekhova *et al.* [103] for details.

Comparison of the Theoretical and Experimental Results. Figures 4.12(a) and 4.12(b) compare the values for the levels of squeezing and anti-squeezing, respectively, which are obtained using theoretical calculations and experimental data for the lowest 8 modes. The theoretical results (light-blue line) are obtained by solving the integro-differential equations for first crystal with $G^{(1)}_{\text{exp}} = 1.05$, applying the joint Schmidt decomposition to obtain the gain parameters r_l via Eqs. (4.33) and then using Eqs. (4.77) and (4.92) to obtain the levels of squeezing and anti-squeezing for each mode. The gain value is in agreement with the value of $G^{(1)}_{\text{exp}} = 1.1 \pm 0.3$ chosen in the experiment [3]. The loss factor is chosen as $\iota = 15\,\%$.

[17] In the integro-differential equations as written in Eqs. (3.7), this function is given by the Gaussian term. For the full three-dimensional system, it would appear as a factor in the function f in Eqs. (A.17).

[18] When using this approximation, it must be ensured that the pump beam is sufficiently symmetric so that setting $q_{s,y}$ and $q_{i,y}$ does not distort the pump beam too much.

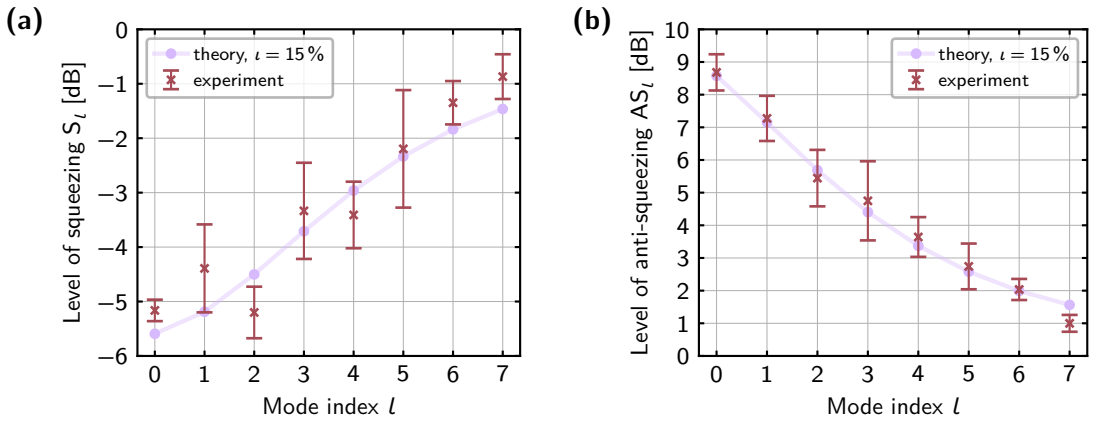

Figure 4.12: Values for the levels of **(a)** squeezing and **(b)** anti-squeezing obtained directly by solving the integro-differential equations for the first crystal and computing the squeezing assuming 15 % loss (theory) and by applying the processing method developed in Sec. 4.3.1.1 in the high-gain approximation [using Eqs. (4.75a) and (4.76b)], where the overlap matrix elements $\mathfrak{g}_{ln}$ are computed also by solving the integro-differential equations (experiment). Evidently, the processing method provides a good prediction of the levels of squeezing and anti-squeezing. The lines connecting the data points for the theoretical results is for orientation purposes only. The experimental data were generated and provided by collaborators. Adapted from Ref. [3].

For the experimental results (red-brown data points with error bars), the experimentally obtained eigenvalues are combined with the overlap matrix elements $\mathfrak{g}_{ln}$ obtained from the theory using the processing method in the high-gain approximation as described in Sec. 4.3.1.2. The gain of the second crystal is set as $G^{(2)}_{\text{exp}} = 4.0$ in the theoretical calculations, which agrees with the experimentally set value of $G^{(2)}_{\text{exp}} = 4.0 \pm 0.4$ [3]. The optimal visibility is reached for $\delta z = 0.1550 L_1$ with $v = 94.35\,\%$. As discussed above, the losses are not included in the computation of the overlap coefficient $\mathfrak{g}_{ln}$. Clearly, the levels of squeezing and anti-squeezing predicted by the processing method are in good agreement with the purely theoretical values including 15 % losses. As mentioned above, since the squeezing is affected more strongly by losses, the absolute values for S_l are lower than those of AS_l.

4.4. Conclusion

In this chapter, several aspects of the Schmidt modes that were introduced in Sec. 3.2 were investigated in more detail for both single PDC sections and SU(1,1) interferometers. It was found that while the modulus of the input and output modes is identical for the low-order modes, their phase profiles differ strongly as the parametric gain is increased. Based on this observation, overlap coefficients $\mathfrak{g}$ and $\mathfrak{h}$ were introduced, which quantify the mode mismatch inside unbalanced SU(1,1) interferometers. While $\mathfrak{h}$ is approximately diagonal for the unbalanced SU(1,1) interferometer as investigated in this chapter, where

the second crystal operates at much higher gain than the first crystal, the overlap coefficient matrix $\mathfrak{g}$, describing the mismatch of the output modes of the first crystal and the input modes of the second crystal, contains strong off-diagonal components.

Furthermore, this chapter discusses a method for the measurement of multimode squeezing as generated in the output modes of a single PDC section (squeezer). For this, a second PDC section (amplifier) pumped at high gain is placed after the squeezer, so that both sections form an SU(1,1) interferometer. Based on the observation that the overlap of the output modes of the first crystal and the input modes of the second crystal is nontrivial, an approximate processing method was developed which allows for the extraction of the squeezing information from the eigenvalues of the second crystal, the eigenvalues of the interferometer in dependence on the interferometric phase and the theoretically calculated overlap matrix $\mathfrak{g}$. This method was then applied theoretically and was found to align well with the precise results. Furthermore, the method was applied with experimental data input and was found to be in good agreement with the theoretically predicted values including losses [3]. The method is by itself quite general and the idea behind it can be extended to other multimode PDC systems.

As noted in Chekhova *et al.* [103], one possible approach to reduce the mismatch between the output modes of the squeezer and the input modes of the amplifier is by pump-shape engineering. In the simplest case, this could for example mean increasing the pump width for the second crystal. Generally, more complex pump shaping can be applied for more complicated systems. Additionally, as of writing this, there seems to be no in-depth experimental studies regarding the input and output Schmidt modes of PDC sections and how they interact. The multimode squeezing measurement technique therefore provides an incentive to perform further experimental studies in this direction.

5

PDC with Laguerre-Gaussian Pump Beams

As an alternative to the integro-differential equation approach utilized in Chapters 3 and 4, Schmidt mode theory as for example investigated in Sharapova *et al.* [11] provides a more analytical framework for the description of PDC and therefore allowing for a more in-depth understanding of the PDC process. In Sharapova *et al.* [11], it was additionally shown that the modes of the PDC process in this formalism are given by modes carrying orbital angular momentum (OAM), which will be introduced more formally in Sec. 5.1 below. As will be seen, a proper description of the PDC systems such as single PDC sections and SU(1,1) interferometers requires a fully three-dimensional description of the system, which is contrary to Chapters 3 and 4, where only one transverse dimension was included in the model.

Section A.4 provides a supplementary overview over the integro-differential equations for the fully three-dimensional system. This and the results of Sec. A.5 show that the Schmidt mode theory formalism can be understood as a low-gain approximation for the integro-differential equation approach. Without further approximations, the integro-differential equation approach for the full three-dimensional system is numerically very challenging in terms of memory and computation time[1]. Hence, the Schmidt mode theory approach has an additional advantage: Since it does not require numerical integration, it leads to a strong reduction in the numerical complexity.

Due to the fact that the modes of the PDC process carry OAM, it stands to reason that a pump beam carrying OAM can be used to modify the modal structure of the process, since OAM is usually conserved. This is investigated in Sec. 5.2 below, which provides a thorough derivation and analysis of PDC with Laguerre-Gaussian beams used as the pump

[1]This was noted during work on Barakat *et al.* [3] using the integro-differential equations for the fully three-dimensional system, which however was not used for the final publication. The title figure of this work originates from the data generated from these computations.

beam, which are a prominent example of light beams carrying OAM. Such beams can also be used for the detection of rotations (angular displacement measurements). Naturally, the formalism presented in Chapter 3 for the phase sensitivity of phase-shift measurements can be adapted to these angular displacement measurements, as will be shown and investigated in Sec. 5.4.

5.1. Orbital Angular Momentum and Laguerre-Gaussian Beams

It is well known that electromagnetic fields can carry angular momentum in two different ways [50, 131]: Via its polarization, the field can carry *spin angular momentum* (SAM) and via its spatial distribution it can carry *orbital angular momentum* (OAM). Mathematically, the total angular momentum operator $\hat{\boldsymbol{J}}$ for the total angular momentum about the coordinate origin[2] $\boldsymbol{r} = \boldsymbol{0}$ can be expressed in the form [46, 64, 133, 134]

$$\hat{\boldsymbol{J}} = \hat{\boldsymbol{L}} + \hat{\boldsymbol{S}}, \tag{5.1}$$

where $\hat{\boldsymbol{L}}$ is the OAM operator and $\hat{\boldsymbol{S}}$ is the SAM operator. It should be noted that generally, the identification of the OAM and SAM components from the total orbital angular momentum is not straightforward, see Allen *et al.* [46] and Bliokh *et al.* [133] and references therein. Furthermore, OAM and SAM are also generally coupled, which is called the *spin-orbit interaction* (SOI) of light [133, 135, 136]. However, for *paraxial optics*, where the light fields propagate close to a specified axis (in the context of this work, the axis defined by the pump or the z-axis), the identification of OAM and SAM is possible [133] and leads to eigenstates for the $\hat{\boldsymbol{L}}$ operator which have well-defined orbital angular momenta, as will be seen below in more detail. Nevertheless, even in paraxial optics, OAM and SAM may still be coupled and converted into each other inside anisotropic media, see for example Ciattoni *et al.* [137]. In the following, as was the case in Ref. [2], all interactions between OAM and SAM are neglected for simplicity, which allows for an independent treatment of both components.

More explicit expressions for $\hat{\boldsymbol{S}}$ and $\hat{\boldsymbol{L}}$ can be obtained by starting with the classical expression for the total angular momentum of the electromagnetic field and plugging in the quantized versions of the electric and magnetic field. Following Mandel and Wolf [64], the SAM operator can be, in the continuous limit, written in the following form:

$$\hat{\boldsymbol{S}} = \int \mathrm{d}^3k\, \hbar \frac{\boldsymbol{k}}{|\boldsymbol{k}|} \left(\hat{n}_{\boldsymbol{k},+} - \hat{n}_{\boldsymbol{k},-}\right), \tag{5.2}$$

where $\hat{n}_{\boldsymbol{k},+}$ and $\hat{n}_{\boldsymbol{k},-}$ refer to the photon number operators for right-hand and left-hand polarized photons, respectively. Thus, a right-hand polarized photon in the plane-wave basis carries a spin angular momentum of $+\hbar$ about its wave-vector $\boldsymbol{k}$, while a left-hand polarized photon carries an SAM of $-\hbar$ [64]. However, as for example noted by Enk and

[2] Generally, as in the classical case with angular momentum, the OAM contribution $\hat{\boldsymbol{L}}$ depends on the choice of the origin, see for example Mandel and Wolf [64] and Allen *et al.* [132].

Nienhuis [138] and Calvo *et al.* [139], the components of $\hat{\boldsymbol{S}}$ commute:

$$[\hat{S}_i, \hat{S}_j] = 0\,, \tag{5.3}$$

meaning that $\hat{\boldsymbol{S}}$ does not form an angular momentum algebra with the common quantum mechanical angular momentum commutation relations. Moreover, as discussed in Sec. 2.3.1, for type-I and type-II PDC, the linear polarization directions are fixed by the phase-matching conditions of the PDC process and therefore, SAM will not play a role in the rest of this chapter.

Similar to Eq. (5.2), it is possible to obtain an expression for $\hat{\boldsymbol{L}}$ in terms of the plane-wave operators, see Mandel and Wolf [64]. This operator and its components also do not fulfill the typical angular momentum operator commutation relations [133, 138]. While the SAM depends on the polarization direction of the light field, the OAM depends on the actual spatial distribution of the field. As such, it is advisable to consider explicit expressions for the field modes in the paraxial approximation, where both the SAM and OAM are well-defined [140]. This leads to an expression for the orbital angular momentum operator acting on these modes. In cylindrical coordinates[3] $(r_\perp, \varphi, z)$, where $r_\perp = |\boldsymbol{r}_\perp|$, and $\boldsymbol{r}_\perp = [x \;\; y]^\mathrm{T}$ denotes the transverse components of the coordinate vector, the z-component of this orbital angular momentum operator then takes the form [132, 140–142]:

$$\hat{L}_z = -\mathrm{i}\hbar \frac{\partial}{\partial \varphi}\,. \tag{5.4}$$

In the following, it will be assumed that only the z-component of the OAM is non-vanishing. The eigenfunctions then have an azimuthal phase dependence of the form $\mathrm{e}^{-\mathrm{i}l\varphi}$ and

$$\hat{L}_z \mathrm{e}^{-\mathrm{i}l\varphi} = -l\hbar \mathrm{e}^{-\mathrm{i}l\varphi}\,, \tag{5.5}$$

meaning their associated eigenvalues are $-l\hbar$. The sign in the exponent is chosen by convention, as will be explained in more detail below. Plots of the phase profiles of these functions are shown in Fig. 5.1.

Within the paraxial equation, where the fields only propagates close to and only with small angles towards the propagation axis, the relevant wave equation is the *paraxial wave equation* [64, 143]

$$\left(\nabla_\perp^2 + 2\mathrm{i}k\frac{\partial}{\partial z}\right)\psi(r_\perp, \varphi, z) = 0\,, \tag{5.6}$$

where ψ denotes the scalar electric field, $k = |\boldsymbol{k}|$ is the modulus of the wave vector and where $\nabla_\perp^2 = \nabla^2 - (\partial^2/\partial z^2)$ denotes the transverse part of the Laplace operator ∇^2. As pointed out in Marcuse [144], Eq. (5.6) has a similar structure as the time-independent Schrödinger equation, which allows an analogy between paraxial optics and quantum mechanics [132], where the operator $\hat{L}_z$ in Eq. (5.4) originates from.

[3] In this chapter, the symbol φ will be used for the direct-space azimuthal angle, while ϕ will be used for the azimuthal angle in wave-vector space.

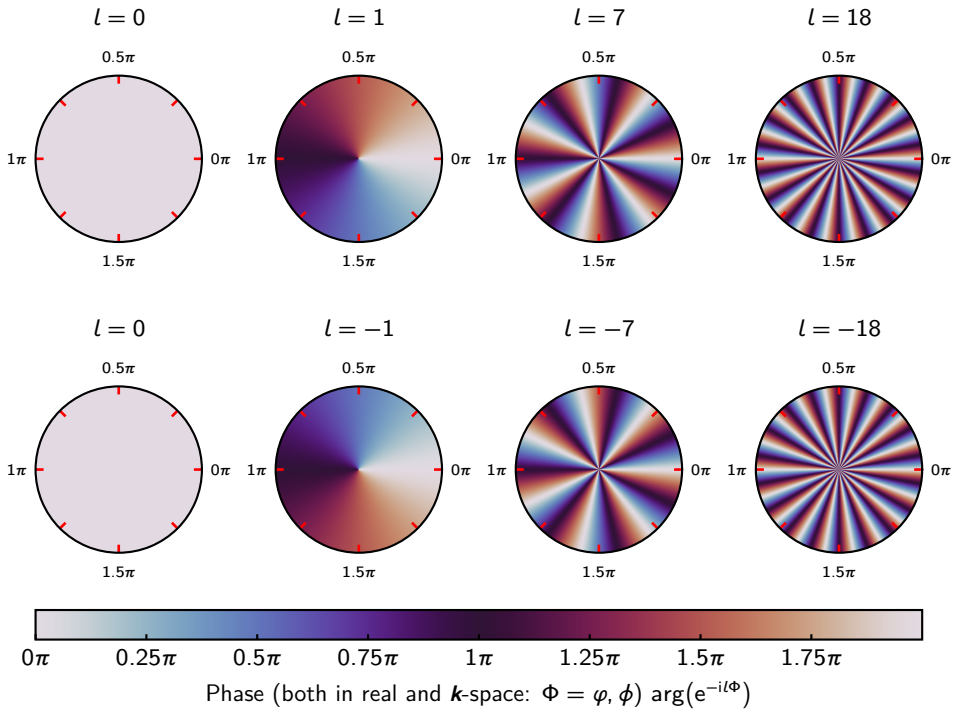

Figure 5.1: Plots of the phase profiles of the eigenfunctions $e^{-il\Phi}$ of $\hat{L}_z$, [compare Eq. (5.5)] where Φ may represent the direct space or $\boldsymbol{k}$-space azimuthal angle. See also the discussion around Eq. (5.31), where the $\hat{L}_z$ operator in wave-vector space is discussed. Evidently, the phase profiles have l-fold discrete rotational symmetry. For $l = 0$, the phase profile is flat, meaning it is constant over the entire transverse plane. Changing the sign of l_p changes the helicity of the phase profile.

One example for light beams carrying OAM are *Laguerre-Gaussian beams* [46, 145, 146], which are the solutions of the paraxial wave equation (5.6) in free space [143]. The Laguerre-Gaussian field modes can be written as[4,5] [46, 140, 143, 146, 147]:

$$\psi_{lm}(r_\perp, \varphi, z) = \sqrt{\frac{2m!}{\pi\,(m+|l|)!}}\,\frac{1}{w(z)}\left(\frac{r_\perp\sqrt{2}}{w(z)}\right)^{|l|} L_m^{|l|}\left(\frac{2r_\perp^2}{w^2(z)}\right) e^{-\frac{r_\perp^2}{w^2(z)}} e^{i\Psi(z)} e^{-il\varphi}\,, \tag{5.7}$$

where $l \in \mathbb{Z}$ is the orbital angular momentum index, as will be seen below, $m \in \mathbb{N}_0$ is the *radial index*, $L_m^{|l|}$ are the associated Laguerre polynomials, $w(z) = w_0\left[1 + (z/z_R)^2\right]^{1/2}$ is the $1/e^2$-radius of the Gaussian term of the beam, with w_0 being the $1/e^2$-radius at the beam waist ($z = 0$), and $\Psi(r_\perp, z) = \Psi_S(r_\perp, z) + \Psi_G(r_\perp, z)$ is the sum of the phase terms $\Psi_S(r_\perp, z) = -kr_\perp^2 z/\left[2\left(z^2 + z_R^2\right)\right]$, which represents a spherical phase front,

[4] In Eq. (5.7), the expression for the Laguerre-Gaussian mode function is normalized so that the normalization condition $\iint \mathrm{d}r_\perp\, \mathrm{d}\varphi\, r_\perp |\psi_{lm}(r_\perp, \varphi, z)|^2 = 1$ is satisfied for all z. Several other conventions exist in the literature for the normalization choice and the choice of the signs in the exponent (replacing for example ψ_{lm} with ψ_{lm}^*), compare Refs. [46, 143, 145, 146].

[5] The function $\psi_{lm}(r_\perp, \varphi, z)$ written in Eq. (5.7) is the slowly varying envelope of the electric field. The full time-independent part of the electric field is given by $\psi_{lm}(r_\perp, \varphi, z)\, e^{-ikz}$ [46]. See also Sec. B.1 for more details regarding the slowly varying envelope and the paraxial approximation.

and $\Psi_G(r_\perp, z) = (2m + |l| + 1)\arctan(z/z_R)$, which is the *Gouy phase*. The variable z_R refers to the Rayleigh length of the Laguerre-Gaussian beam, which is the distance from the waste along the z-axis at which the cross-section area of the beam is doubled [143]. Clearly, the field distribution described by $\psi_{lm}(r_\perp, \varphi, z)$ carries an OAM index of $l\hbar$ about the z-axis, since these functions are eigenstates of $\hat{L}_z$ with eigenvalues $-l\hbar$:

$$\hat{L}_z \psi_{lm}(r_\perp, \varphi, z) = -l\hbar \psi_{lm}(r_\perp, \varphi, z). \tag{5.8}$$

In the following, a mode function associated with the $\hat{L}_z$-eigenvalue $-l\hbar$ is said to carry an OAM of[6] l. With this definition, if the beam is said to have a positive OAM, the phase angle *decreases* in the counterclockwise direction in the transverse plane, apart from the 2π-periodicity.

In its general form, the Laguerre-Gaussian beam has a complicated dependence on the z-coordinate via the width function $w(z)$. Usually, if the system of interest is sufficiently small along the propagation direction of the Laguerre-Gaussian beam (here the z-axis) it is possible to approximate the above expression as

$$\psi_{lm}(r_\perp, \varphi, z) = \sqrt{\frac{2m!}{\pi\,(m+|l|)!}}\,\frac{1}{w_0}\left(\frac{r_\perp\sqrt{2}}{w_0}\right)^{|l|} L_m^{|l|}\left(\frac{2r_\perp^2}{w_0}\right) \mathrm{e}^{-\frac{r_\perp^2}{w_0}}\,\mathrm{e}^{-\mathrm{i}l\varphi}\,, \tag{5.9}$$

which can be understood as the result of taking the limit[7] $z_R \to \infty$ in Eq. (5.7).

5.2. Schmidt-Mode Theory with Laguerre-Gaussian Pump Beams

5.2.1. The Two-Photon Amplitude for Laguerre-Gaussian Pump Beams

The theoretical formalism (*Schmidt-mode theory*) presented in Ref. [2] is based mainly on Sharapova *et al.* [11] and extends this work by allowing the pump to have nonzero orbital angular momentum. More precisely, the pump is given by a Laguerre-Gaussian beam which is assumed to not broaden significantly over the relevant interaction regions of interest [a single crystal or the two crystals of an SU(1,1) interferometer]. This is usually satisfied if the crystals are not too long. Within the undepleted pump approximation as described in Sec. 2.3.2, the pump envelope is therefore of the form [2]:

$$\tilde{\alpha}_p(\boldsymbol{r}, t) = \frac{r_\perp^{|l_p|}}{w_0^{|l_p|+1}} L_{m_p}^{|l_p|}\left(\frac{2r_\perp^2}{w_0^2}\right) \mathrm{e}^{-\left(\frac{r_\perp}{w_0}\right)^2}\,\mathrm{e}^{-\mathrm{i}l_p\varphi}\,, \tag{5.10}$$

which follows directly from Eqs. (2.42) and (5.9).

Compared to the integro-differential equation approach for the description of PDC, which introduced in Sec. 3.2, used throughout Chapters 3 and 4, and ultimately requires that the

[6] This definition also keeps consistency with Ref. [2]. Overall, changing the sign of l only changes the helicity of the phase, compare Fig. 5.1.

[7] Equivalently, this result can be obtained by directly replacing the width function $w(z)$ and the phase $\Psi(r_\perp, z)$ with their values at $z = 0$.

transfer functions are computed numerically, the Schmidt mode theory approach developed by Sharapova *et al.* [11] attempts to find an analytic expression describing the connection between the input and output operators of the system. To this end, certain approximations are required, the most important of which is the assumption of monochromatic signal and idler fields (the pump field is always assumed to be monochromatic throughout this work). This is achieved by fixing a single frequency for the integral over ω_ν in the expressions for the electric field operators as written in Eq. (2.41) (see also Karan *et al.* [72]). The pump field is assumed to be undepleted and described by Eqs. (2.42) and (5.10), as mentioned above. Since all three fields are monochromatic, an energy conserving process is only achieved for perfect frequency matching, meaning

$$\omega_p - \omega_s - \omega_i = 0\,. \tag{5.11}$$

Overall, this assumption neglects the energy mismatch between the three field in the PDC Hamiltonian [5] and, as a result, removes its explicit time dependence.

After plugging the abovementioned expressions for the three fields into the PDC Hamiltonian [Eq. (2.37)], the spatial integral can be split into a transverse part over the xy-plane and a longitudinal part over the z-axis, so that the Hamiltonian can be brought to the form [2]

$$\hat{H}_{\mathrm{PDC}} = \mathrm{i}\hbar\Gamma \iint \mathrm{d}^2q_s\, \mathrm{d}^2q_i\, F(\boldsymbol{q}_s, \boldsymbol{q}_i)\, \hat{a}_s^\dagger(\boldsymbol{q}_s)\, \hat{a}_i^\dagger(\boldsymbol{q}_i) + \mathrm{h.c.}\,, \tag{5.12a}$$

where

$$F(\boldsymbol{q}_s, \boldsymbol{q}_i) = C g_{xy}(\boldsymbol{q}_s, \boldsymbol{q}_i)\, g_z(\boldsymbol{q}_s, \boldsymbol{q}_i) \tag{5.12b}$$

is the *two-photon amplitude* (TPA) which describes the PDC process and g_{xy} and g_z are the two functions containing the transverse and longitudinal spatial integrals, respectively.

It should be noted that unlike in Chapters 3 and 4, here, the full two-dimensional transverse plane is taken into account instead of only a single transverse dimension, meaning that the transverse wave-vector components $\boldsymbol{q}_s$ and $\boldsymbol{q}_i$ are two-dimensional vectors. Thus, the commutation relations for the signal and idler plane-wave operators read

$$[\hat{a}_s(\boldsymbol{q}_s), \hat{a}_s^\dagger(\boldsymbol{q}_s')] = \delta(\boldsymbol{q}_s - \boldsymbol{q}_s'), \tag{5.13a}$$

$$[\hat{a}_i(\boldsymbol{q}_i), \hat{a}_i^\dagger(\boldsymbol{q}_i')] = \delta(\boldsymbol{q}_i - \boldsymbol{q}_i'). \tag{5.13b}$$

Generally, the commutation relation between the signal and idler plane-wave operators is, in the context of this theoretical formalism, given by $[\hat{a}_s(\boldsymbol{q}_s), \hat{a}_i^\dagger(\boldsymbol{q}_i)] = (\mathcal{D}_{si} - 1)\,\delta(\boldsymbol{q}_s - \boldsymbol{q}_i)$, with $\mathcal{D}_{si}$ as defined in Eq. (2.35). In this chapter and Ref. [2], the PDC process is assumed to be degenerate, meaning the signal and idler photons are indistinguishable. Thus, $\mathcal{D}_{si} - 1 = 1$ and

$$[\hat{a}_s(\boldsymbol{q}_s), \hat{a}_i^\dagger(\boldsymbol{q}_i)] = \delta(\boldsymbol{q}_s - \boldsymbol{q}_i). \tag{5.13c}$$

The variable

$$\Gamma = \frac{4}{\hbar}\mathcal{D}_{si}\mathcal{E}_p\mathcal{E}_s\mathcal{E}_i\varepsilon_0\chi^{(2)}_{\text{eff}}\frac{1}{C} \tag{5.14}$$

introduced in Eqs. (5.12) is the theoretical gain parameter. Depending on the literature, its precise form may differ, which is the consequence of the different choices for the prefactor of the PDC Hamiltonian, as mentioned in Sec. 2.3.2. Its precise form is however not relevant for the rest of this work, since the value for Γ [or more precisely, for the re-scaled theoretical gain parameter G as defined in Eq. (5.34) below] will be connected to the experimental gain G_{exp} via the fitting procedure already described in Sec. 3.4 for the integro-differential equation approach. Furthermore, the introduced normalization constant C ensures the normalization of the TPA to unity, meaning [2]

$$\iint \mathrm{d}^2q_s\,\mathrm{d}^2q_i\,|F(\boldsymbol{q}_s,\boldsymbol{q}_i)|^2 = 1\,. \tag{5.15}$$

Generally,

$$C = \left(\iint \mathrm{d}^2q_s\,\mathrm{d}^2q_i\,|g_{xy}(\boldsymbol{q}_s,\boldsymbol{q}_i)\,g_z(\boldsymbol{q}_s,\boldsymbol{q}_i)|^2\right)^{-\frac{1}{2}} \tag{5.16}$$

will depend on the parameters of the system, such as the crystal length (appearing in g_z) and the pump parameters, such as the radial index, the OAM value and the pump width (appearing in g_{xy}).

The spatial integral appearing in g_{xy} is essentially the Fourier transform of the spatial pump envelope, which is easily solved in polar coordinates $\boldsymbol{q}_j \equiv (q_j,\phi_j)$, for $j = s,i$, and analogous for the real-space coordinate vector $\boldsymbol{r}_\perp$. Details on how this Fourier integral is evaluated can be found in Ref. [2]. Ultimately, with the evaluated integral, the TPA can be written as [2]

$$F(q_s,q_i,\phi_s,\phi_i) = R(q_s,q_i,\phi_s-\phi_i)\,\mathrm{e}^{-\mathrm{i}l_p\phi_i}\,, \tag{5.17}$$

where

$$\begin{aligned} R(q_s,q_i,\phi_s-\phi_i) = 2\pi C\,(-1)^{l_p+m_p}\,\mathrm{i}^{|l_p|}\left(\frac{w_0}{2}\right)^{|l_p|+1} L^{|l_p|}_{m_p}\left(\frac{(w_0\xi)^2}{2}\right)\mathrm{e}^{-\left(\frac{w_0\xi}{2}\right)^2} \\ \times\left[q_s\mathrm{e}^{-\mathrm{i}\,\mathrm{sgn}(l_p)(\phi_s-\phi_i)}+q_i\right]^{|l_p|} g_z(q_s,q_i,\phi_s-\phi_i) \end{aligned} \tag{5.18}$$

and $\xi = |\boldsymbol{q}_p| = \sqrt{q_s^2+q_i^2+2q_sq_i\cos(\phi_s-\phi_i)}$ [148].

Evidently, compared to Sharapova *et al.* [11], which this description of the Schmidt mode theory is based on, the TPA F can now no longer be written in terms of the signal-idler angle difference due to the nonzero OAM of the pump beam, which can be seen from the additional $\mathrm{e}^{-\mathrm{i}l_p\phi_i}$ in Eq. (5.17). This means that in the numerical implementation of this formalism, the TPA F would be represented by four-dimensional arrays, where the four axes represent the x- and y-coordinates of the signal and idler wave-vectors, leading to high memory and computational demands. As such, in this modified approach with nonzero

OAM for the pump beam, the phase factor $\mathrm{e}^{-\mathrm{i}l_p\phi_i}$ has been separated out so that the remaining function R as defined in Eq. (5.18) *can* be written in terms of the angle difference and the formalism developed in Sharapova *et al.* [11] will be applied to R instead of the full TPA. For $l_p = 0$, the separation of the TPA into the function R and an additional phase factor $\mathrm{e}^{-\mathrm{i}l_p\phi_i}$ as written in Eq. (5.17) is not necessary and the description coincides again with the one given in Sharapova *et al.* [11].

Since R as defined in Eq. (5.18) is written in terms of the signal-idler angle difference, the normalization condition of the TPA F in Eq. (5.15) takes the following form: $\iiint \mathrm{d}q_s\,\mathrm{d}q_i\,\mathrm{d}(\phi_s-\phi_i)\,q_sq_i|R(q_s,q_i,\phi_s-\phi_i)|^2 = 1/(2\pi)$ [2]. Clearly, R has a similar form to the Laguerre-Gaussian pump envelope as shown in Eq. (5.10), consisting of a Laguerre polynomial and a Gaussian term. This is due to the fact that Laguerre-Gaussian functions are fixed points/eigenfunctions of the Fourier transform, meaning that the Fourier transform of a Laguerre-Gaussian function is again of the form of a Laguerre-Gaussian function, possibly with additional scaling factors [2, 149].

The spatial integral over the z-axis, which in Eq. (5.18) is hidden inside g_z, depends on the concrete setup under consideration, such as a single crystal or an SU(1,1) interferometer consisting of two crystals with an air gap in-between. The concrete expressions will be provided in Secs. 5.3.1 and 5.3.2 below.

5.2.2. Separation of the Signal and Idler Variables

Following Sharapova *et al.* [11] and Miatto *et al.* [42], in order to separate the signal and idler variables, that is, perform the Schmidt decomposition of the TPA, the first step is in separating the radial variables q_s and q_i from the angle difference $\phi_s - \phi_i$ using a Fourier decomposition of the function R defined in Eq. (5.18) over the angle difference [2, 11, 42]:

$$R(q_s,q_i,\phi_s-\phi_i) = \frac{1}{2\pi}\sum_{n=-\infty}^{\infty}\chi_n(q_s,q_i)\,\mathrm{e}^{-\mathrm{i}n(\phi_s-\phi_i)}\,. \tag{5.19}$$

The Fourier coefficient integral determining the Fourier coefficients $\chi_n(q_s,q_i)$ takes the form [2]:

$$\chi_n(q_s,q_i) = \int_0^{2\pi}\mathrm{d}(\phi_s-\phi_i)\,R(q_s,q_i,\phi_s-\phi_i)\,\mathrm{e}^{\mathrm{i}n(\phi_s-\phi_i)}\,. \tag{5.20}$$

Plugging Eq. (5.19) back into Eq. (5.17) yields a modified form of the Fourier decomposition for the TPA, which accounts for the non-vanishing OAM of the pump [2]:

$$F(q_s,q_i,\phi_s,\phi_i) = \frac{1}{2\pi}\sum_n \chi_n(q_s,q_i)\,\mathrm{e}^{-\mathrm{i}n\phi_i}\mathrm{e}^{-\mathrm{i}(l_p-n)\phi_i}\,. \tag{5.21}$$

In order to fulfill the normalization condition for the TPA [see Eq. (5.15)], the Fourier coefficients must fulfill $\sum_n \iint \mathrm{d}q_s\,\mathrm{d}q_i\,q_sq_i|\chi_n(q_s,q_i)|^2 = 1$, which is analogous to *Parseval's theorem*, which connects the integral over the modulus squared of a function [the *norm* of the function and the right-hand side in Eq. (5.15)] to the sum over the modulus squared

over its Fourier coefficients [111].

Next, the *Schmidt decomposition* is applied to the Fourier coefficients, leading to the separation of the radial signal and idler variables q_s and q_i. This decomposition takes the same form as in Sharapova *et al.* [5] because the radial variables are unrelated to the OAM:

$$\chi_n(q_s, q_i) = \sum_{m=0}^{\infty} \sqrt{\lambda_{mn}} \frac{u_{mn}(q_s)}{\sqrt{q_s}} \frac{v_{mn}(q_i)}{\sqrt{q_i}}, \tag{5.22}$$

where λ_{mn} are the *Schmidt eigenvalues* and $u_{mn}(q_s)$ and $v_{mn}(q_i)$ are the (radial) *Schmidt mode functions*. Numerically, this decomposition corresponds to a simple singular-valued decomposition (SVD), unlike the joint Schmidt decomposition of the transfer functions as written in Eqs. (3.20). To obtain the singular values $\sqrt{\lambda_{mn}}$ and the modes u_{mn} and v_{mn}, the SVD of the matrix containing the numerical representation of $\sqrt{q_s q_i}\,\chi_n(q_s, q_i)$ can be taken. More details regarding the computation can be found in Appendix B of Ref. [2]. Due to this connection, the square roots of the Schmidt eigenvalues $\sqrt{\lambda_{mn}}$ will be referred to as the *singular values* in the following, analogous to the naming of the $\sqrt{\Lambda_n}$ of the joint Schmidt decomposition, see Secs. 3.2 and 4.1. Usually, by convention, the singular values are sorted in descending order over m. The mode functions of the Schmidt decomposition are orthonormalized [2, 11]:

$$\int \mathrm{d}q_s\, u_{mn}(q_s)\, u^*_{kn}(q_s) = \delta_{mk}, \tag{5.23a}$$

$$\int \mathrm{d}q_i\, v_{mn}(q_i)\, v^*_{kn}(q_i) = \delta_{mk}. \tag{5.23b}$$

By applying the Schmidt decomposition for the radial variables as written in Eq. (5.22) to the full TPA as written in Eq. (5.21), the TPA can be written as [2]

$$F(q_s, q_i, \phi_s, \phi_i) = \frac{1}{2\pi} \sum_{m,n} \sqrt{\lambda_{mn}} \frac{u_{mn}(q_s)}{\sqrt{q_s}} \frac{v_{mn}(q_i)}{\sqrt{q_i}} \mathrm{e}^{-\mathrm{i}n\phi_s} \mathrm{e}^{-\mathrm{i}(l_p - n)\phi_i}, \tag{5.24}$$

which implies that the normalization condition for the TPA [Eq. (5.15)] takes the form $\sum_{m,n} \lambda_{mn} = 1$. Clearly, for fixed m and n, each summand of the sum in Eq. (5.24) can be written as a product of one term containing only the signal variables and one containing only the idler variables. Thus, this form of the TPA allows for the introduction of the Schmidt operators

$$\hat{A}^\dagger_{mn} = \frac{1}{\sqrt{2\pi}} \int \mathrm{d}^2 q_s \, \frac{u_{mn}(q_s)}{\sqrt{q_s}} \mathrm{e}^{-\mathrm{i}n\phi_s} \hat{a}^\dagger_s(\boldsymbol{q}_s), \tag{5.25a}$$

$$\hat{B}^\dagger_{mn} = \frac{1}{\sqrt{2\pi}} \int \mathrm{d}^2 q_i \, \frac{v_{mn}(q_i)}{\sqrt{q_i}} \mathrm{e}^{-\mathrm{i}(l_p - n)\phi_i} \hat{a}^\dagger_i(\boldsymbol{q}_i), \tag{5.25b}$$

where $\mathrm{d}^2 q_j = q_j \mathrm{d}q_j \mathrm{d}\phi_j$ for $j = s, i$, so that the PDC Hamiltonian from Eqs. (5.12) is diagonalized and takes the form

$$\hat{H}_{\mathrm{PDC}} = \mathrm{i}\hbar\Gamma \sum_{m,n} \sqrt{\lambda_{mn}} \left(\hat{A}^\dagger_{mn} \hat{B}^\dagger_{mn} - \hat{A}_{mn} \hat{B}_{mn} \right). \tag{5.26}$$

Equations (5.25) suggest that the Schmidt mode operators $\hat{A}^\dagger_{mn}$ and $\hat{B}^\dagger_{mn}$ create broadband photons in the modes described by the functions

$$\mathcal{U}_{mn}(\boldsymbol{q}) = \frac{1}{\sqrt{2\pi}} \frac{u_{mn}(q)}{\sqrt{q}} \mathrm{e}^{-\mathrm{i}n\phi}, \tag{5.27a}$$

$$\mathcal{V}_{mn}(\boldsymbol{q}) = \frac{1}{\sqrt{2\pi}} \frac{v_{mn}(q)}{\sqrt{q}} \mathrm{e}^{-\mathrm{i}(l_p-n)\phi}, \tag{5.27b}$$

respectively. These mode functions fulfill the orthonormality relations:

$$\int \mathrm{d}^2q\, \mathcal{U}_{mn}(\boldsymbol{q})\, \mathcal{U}^*_{kl}(\boldsymbol{q}) = \delta_{mk}\delta_{nl}, \tag{5.28a}$$

$$\int \mathrm{d}^2q\, \mathcal{V}_{mn}(\boldsymbol{q})\, \mathcal{V}^*_{kl}(\boldsymbol{q}) = \delta_{mk}\delta_{nl}, \tag{5.28b}$$

$$\int \mathrm{d}^2q\, \mathcal{U}_{mn}(\boldsymbol{q})\, \mathcal{V}^*_{kl}(\boldsymbol{q}) = \delta_{mk}\delta_{n,l_p-l}. \tag{5.28c}$$

The Schmidt operators follow the commutation relations [2]

$$[\hat{A}_{mn}, \hat{A}^\dagger_{kl}] = \delta_{mk}\delta_{nl}, \tag{5.29a}$$

$$[\hat{B}_{mn}, \hat{B}^\dagger_{kl}] = \delta_{mk}\delta_{nl}, \tag{5.29b}$$

which follow directly from the commutation relations of the plane-wave operators and the orthonormality of the mode functions, see Eqs. (5.13) and Eqs. (5.28a) and (5.28b), respectively. These commutation relations coincide with the ones from Sharapova *et al.* [11], as evident from the fact they do not depend on l_p. Furthermore, generally, the commutation relation between the signal and idler Schmidt mode operators is given by $[\hat{A}_{mn}, \hat{B}^\dagger_{kl}] = \delta_{mk}\delta_{n,l_p-l}\,(\mathcal{D}_{si} - 1)$, with $\mathcal{D}_{si}$ as defined in Eq. (2.35). As already stated in Sec. 5.2.1, the signal and idler photons are assumed to be indistinguishable in this chapter and Ref. [2] (degenerate PDC), so that, by Eq. (5.28c), [2]

$$[\hat{A}_{mn}, \hat{B}^\dagger_{kl}] = \delta_{mk}\delta_{n,l_p-l}, \tag{5.29c}$$

which for $l_p = 0$, reduces to the equivalent commutation relation in Sharapova *et al.* [11].

The degeneracy of the PDC process also leads to special symmetries for the Schmidt mode functions and singular values, which read

$$u_{mn}(q) = v_{m,l_p-n}(q), \tag{5.30a}$$

$$v_{mn}(q) = u_{m,l_p-n}(q), \tag{5.30b}$$

$$\lambda_{mn} = \lambda_{m,l_p-n}. \tag{5.30c}$$

These symmetries are investigated and explicitly shown in more detail in Ref. [2].

In the wave-vector domain, the operator associated with the z-component of the OAM [compare Eq. (5.4)] takes the same form as in direct space [133]:

$$\hat{L}_z = -\mathrm{i}\hbar \frac{\partial}{\partial\phi}, \tag{5.31}$$

as for example shown in Simmons and Guttmann [150]. Clearly, the mode functions $\mathcal{U}_{mn}$ and $\mathcal{V}_{mn}$ are eigenstates of this operator:

$$\hat{L}_z \mathcal{U}_{mn}(\boldsymbol{q}) = -n\hbar \mathcal{U}_{mn}(\boldsymbol{q}), \tag{5.32a}$$

$$\hat{L}_z \mathcal{V}_{mn}(\boldsymbol{q}) = -\left(l_p - n\right)\hbar \mathcal{V}_{mn}(\boldsymbol{q}), \tag{5.32b}$$

which implies that a photon in the mode $\mathcal{U}_{mn}$ carries an OAM of n about the z-axis, while a photon in the mode $\mathcal{V}_{mn}$ carries the complementary value $l_p - n$. Therefore, the signal Schmidt operator $\hat{A}^\dagger_{mn}$ creates a spatially broadband photon containing an OAM of n, while the corresponding signal Schmidt operator $\hat{B}^\dagger_{mn}$ creates a photon with the complementary OAM $l_p - n$. Combined, the products of these two operators as they appear in the Hamiltonian in Eq. (5.26) create or annihilate photon pairs whose combined OAM corresponds to that of one pump photon: $l_p = n + \left(l_p - n\right)$.

5.2.3. Input-Output Relations for Schmidt Mode Theory

Using the commutation relations between the Schmidt mode operators, see Eqs. (5.29), the Heisenberg equation can be used to obtain the equations of motion for the Schmidt operators using the Hamiltonian from Eq. (5.26). Integrating these equations of motion (see Ref. [2] for details) from the beginning of the interaction to the end of the interaction yields input-output relations for the Schmidt mode operators, which take the form of Bogoliubov transformations, analogous to Eqs. (3.23) [2, 11]:

$$\hat{A}^{(\mathrm{out})}_{mn} = \hat{A}^{(\mathrm{in})}_{mn} \cosh\!\left(G\sqrt{\lambda_{mn}}\right) + \left(\hat{B}^{(\mathrm{in})}_{mn}\right)^\dagger \sinh\!\left(G\sqrt{\lambda_{mn}}\right), \tag{5.33a}$$

$$\hat{B}^{(\mathrm{out})}_{mn} = \hat{B}^{(\mathrm{in})}_{mn} \cosh\!\left(G\sqrt{\lambda_{mn}}\right) + \left(\hat{A}^{(\mathrm{in})}_{mn}\right)^\dagger \sinh\!\left(G\sqrt{\lambda_{mn}}\right). \tag{5.33b}$$

Similar to the notation introduced in Sec. 3.2, the superscript $^{(\mathrm{out})}$ denotes the Schmidt operators at the end of the interaction and therefore the output of the PDC section, while $^{(\mathrm{in})}$ denotes the Schmidt operators at the beginning of the interaction and thus the input of the PDC section. Furthermore, [2, 11]

$$G = 2\int \mathrm{d}t\, \Gamma \tag{5.34}$$

is the new re-scaled theoretical gain parameter, with the integral being over the interaction time and the additional factor 2 resulting from the fact that the signal and idler photons are indistinguishable (see Ref. [2]).

Similarly, it is possible to arrive at equations of motion for the plane-wave operators by using the commutation relations between the plane-wave operators and the Schmidt mode operators [2]

$$[\hat{a}(\boldsymbol{q}), \hat{A}^\dagger_{mn}] = \mathcal{U}_{mn}(\boldsymbol{q}), \tag{5.35a}$$

$$[\hat{a}(\boldsymbol{q}), \hat{B}^\dagger_{mn}] = \mathcal{V}_{mn}(\boldsymbol{q}), \tag{5.35b}$$

with $\mathcal{U}_{mn}$ and $\mathcal{V}_{mn}$ as defined in Eqs. (5.27a) and (5.27b), respectively, and where the subscripts $_s$ and $_i$ have been dropped because the plane-wave operators coincide [$a_s(\boldsymbol{q}) = a_i(\boldsymbol{q})$] due to the fact that the considered PDC process is degenerate. However, the Schmidt mode operators do not coincide, as seen from their definitions in Eqs. (5.25). It should be noted that the labels of "signal" and "idler" are now only meaningful in the sense that the corresponding photons carry complementary OAM values which add up to the pump OAM value l_p [2]. Thus, also in the following, the subscripts $_s$ and $_i$ will be dropped from the operators and the wave-vector variables.

Setting up the equations of motion for the plane-wave operator using the commutation relations as written in Eqs. (5.35) and integrating them yields [2]

$$\begin{aligned}\hat{a}^{(\mathrm{out})}(\boldsymbol{q}) = \hat{a}^{(\mathrm{in})}(\boldsymbol{q}) + \frac{1}{\sqrt{2\pi}} \sum_{m,n} \frac{u_{mn}(q)}{\sqrt{q}} \mathrm{e}^{-\mathrm{i}n\phi} \Big\{ \hat{A}^{(\mathrm{in})}_{mn} \Big[\cosh\Big(G\sqrt{\lambda_{mn}}\Big) - 1\Big] \\ + \Big(\hat{B}^{(\mathrm{in})}_{mn}\Big)^{\dagger} \sinh\Big(G\sqrt{\lambda_{mn}}\Big)\Big\},\end{aligned} \tag{5.36}$$

where the same notation using $^{(\mathrm{in})}$ and $^{(\mathrm{out})}$ superscripts as introduced in Sec. 3.2 has been used (see above). These input-output relation for the plane-wave operators can be brought to the same form as the solution of the integro-differential equations as written in Eqs. (3.10), which here, in the two-dimensional case for degenerate PDC reads

$$\hat{a}^{(\mathrm{out})}(\boldsymbol{q}) = \int \mathrm{d}^2q'\, \tilde{\eta}(\boldsymbol{q},\boldsymbol{q}')\, \hat{a}^{(\mathrm{in})}(\boldsymbol{q}') + \int \mathrm{d}^2q'\, \beta(\boldsymbol{q},\boldsymbol{q}')\, \big[\hat{a}^{(\mathrm{in})}(\boldsymbol{q}')\big]^{\dagger}. \tag{5.37}$$

Comparing this with Eq. (5.36) reveals that the transfer functions $\tilde{\eta}$ and β take have the form [2]

$$\beta(\boldsymbol{q},\boldsymbol{q}') = \sum_{m,n} \sqrt{\Lambda_{mn}}\, \mathcal{U}_{mn}(\boldsymbol{q})\, \mathcal{U}_{m,l_p-n}(\boldsymbol{q}'), \tag{5.38a}$$

$$\tilde{\eta}(\boldsymbol{q},\boldsymbol{q}') = \sum_{m,n} \sqrt{\tilde{\Lambda}_{mn}}\, \mathcal{U}_{mn}(\boldsymbol{q})\, \mathcal{U}^{*}_{mn}(\boldsymbol{q}'), \tag{5.38b}$$

where

$$\Lambda_{mn} = \sinh^2\Big(G\sqrt{\lambda_{mn}}\Big), \tag{5.39a}$$

$$\tilde{\Lambda}_{mn} = \cosh^2\Big(G\sqrt{\lambda_{mn}}\Big) \tag{5.39b}$$

are the high-gain eigenvalues of β and the corresponding eigenvalues of $\tilde{\eta}$, respectively. Compare also Eqs. (4.33), which shows a similar parametrization of the high-gain eigenvalues in the context of the integro-differential equation approach. Obviously,

$$\Lambda_{mn} + 1 = \tilde{\Lambda}_{mn}\,, \tag{5.40}$$

compare Eq. (3.21). Equations (5.38) are similar to the form of the joint Schmidt decomposition of the transfer functions obtained from the integro-differential equation approach for the full three-dimensional system as written in Eqs. (A.77). However, note that in the integro-differential equation approach, the two sets of modes do not correspond to

the signal and idler modes and are instead associated with the input and output Schmidt operators. Moreover, the input and output modes are, in general, not identical and only coincide approximately in the low-gain regime. This can be seen from the fact that the Schmidt mode theory formalism can be regarded as a low gain approximation for the integro-differential equation approach, see Secs. A.4.2 and A.5.

Using Eq. (5.36) to obtain the intensity distribution by evaluating the expectation value of the photon number operator $\hat{N}(\boldsymbol{q}) = \left[\hat{a}^{(\mathrm{out})}(\boldsymbol{q})\right]^{\dagger} \hat{a}^{(\mathrm{out})}(\boldsymbol{q})$ yields[8] [2]

$$\langle \hat{N}(\boldsymbol{q}) \rangle = \frac{1}{2\pi} \sum_{m,n} \frac{|u_{mn}(q)|^2}{q} \Lambda_{mn} \,, \tag{5.41}$$

which expresses the intensity distribution in terms of the sum of the intensity distributions[9] $\Lambda_{mn} |\mathcal{U}_{mn}(\boldsymbol{q})|^2$ of each mode (m,n). Note that the right-hand side of Eq. (5.41) has no dependence on ϕ, meaning that the intensity profiles are radially symmetric. The relative contribution of each mode is given, analogous to the one-dimensional case as written in Eq. (3.50), by [2, 11]

$$\bar{\Lambda}_{mn} = \frac{\Lambda_{mn}}{\langle \hat{N}_{\mathrm{tot}} \rangle} \,, \tag{5.42}$$

where the integral intensity is given by

$$\langle \hat{N}_{\mathrm{tot}} \rangle = \sum_{m,n} \Lambda_{mn} \,, \tag{5.43}$$

compare also Eq. (3.47). The normalization implies $\sum_{m,n} \bar{\Lambda}_{mn} = 1$. Contrary to the normalized low-gain eigenvalues λ_{mn}, the $\bar{\Lambda}_{mn}$ take the parametric gain into account. In addition to the actual modal weight distribution $\bar{\Lambda}_{mn}$, the Schmidt number K provides a measure for the effective number of modes, compare Eq. (3.49). For the two-dimensional case discussed in this chapter, the Schmidt number is given by

$$K = \left[\sum_{m,n} \left(\bar{\Lambda}_{mn} \right)^2 \right]^{-1} . \tag{5.44}$$

In the following, the modal weight distributions and the Schmidt number will be analyzed for several systems.

5.3. Schmidt-Mode Structure

In this section, the modal structure of a single PDC section and an SU(1,1) interferometer consisting of two PDC sections with an air-gap in-between will be analyzed for various

[8] Equation (5.41) also follows from applying Eq. (3.27) to Eq. (5.38a), since the former is derived from the form of the solution of the integro-differential equations [Eqs. (3.10)], which have the same form as Eq. (5.36), see Eq. (5.37).

[9] The integral intensity (photon number) in the mode (m,n) is given by $\langle \left(A_{mn}^{(\mathrm{out})} \right)^{\dagger} A_{mn}^{(\mathrm{out})} \rangle = \Lambda_{mn}$.

values of the radial (m_p) and OAM (l_p) index of the pump. The pump width is, in accordance with Ref. [2], chosen as $w_0 = 50\,\mu\text{m}$ at a wavelength of 354.7 nm. Each crystal in the setup has a length of $L_1 = 2\,\text{mm}$. As will be seen in Sec. 5.4 below in more detail, it is sufficient to restrict this analysis to the cases $l_p \in \mathbb{N}_{\geq 0}$, see the text surrounding Eqs. (5.65). Under the exchange $l_p \to -l_p$, the eigenvalue distributions and the Schmidt modes only change by certain symmetry operations and do not change quantitatively.

5.3.1. Single Crystal

For a single crystal of length L_1, the function g_z containing the longitudinal part of the spatial integral of the PDC Hamiltonian [see also the text leading up to Eq. (5.12b)] takes the form

$$g_z(\boldsymbol{q}_s, \boldsymbol{q}_i) = \int_0^{L_1} \mathrm{d}z\, \mathrm{e}^{\mathrm{i}\Delta k(\boldsymbol{q}_s, \boldsymbol{q}_i) z}, \tag{5.45}$$

with the longitudinal (collinear) phase mismatch $\Delta k(\boldsymbol{q}_s, \boldsymbol{q}_i)$ as defined in Eq. (3.31a) and taking the following form for the two-dimensional case:

$$\Delta k(\boldsymbol{q}_s, \boldsymbol{q}_i) = \sqrt{k_p^2 - |\boldsymbol{q}_s + \boldsymbol{q}_i|^2} - \sqrt{k_s^2 - |\boldsymbol{q}_s|^2} - \sqrt{k_i^2 - |\boldsymbol{q}_i|^2}\,. \tag{5.46}$$

It should be noted that Eq. (5.45) corresponds to the integral over the phase-matching function h as defined for the integro-differential equation approach, compare Eq. (3.30).

Equation (5.46) provides an expression for the phase mismatch which is rather cumbersome for an analytical treatment and cannot be written in terms of the difference of the signal and idler wave-vector angle $\phi_s - \phi_i$. However, within the paraxial approximation[10], the square root terms in Eq. (5.46) may be approximated as [2, 72]

$$\sqrt{k_j^2 - |\boldsymbol{q}_j|^2} \approx \left(1 - \frac{|\boldsymbol{q}_j|^2}{2k_j}\right) k_j, \tag{5.47}$$

since $|\boldsymbol{q}_j| \ll k_j$, for $j = p, s, i$, if the fields are restricted to paraxial propagation. Note that $\boldsymbol{q}_p = \boldsymbol{q}_s + \boldsymbol{q}_i$ [2]. With the Fresnel approximation, and the fact that for degenerate PDC[11] $k_s = k_i = k_p/2$, the phase mismatch as written in Eq. (5.47) becomes

$$\Delta k(\boldsymbol{q}_s, \boldsymbol{q}_i) \approx \frac{|\boldsymbol{q}_s - \boldsymbol{q}_i|^2}{2k_p}, \tag{5.48}$$

where the modulus squared of the signal-idler wave-vector difference may be expressed in terms of the signal-idler angle difference as $|\boldsymbol{q}_s - \boldsymbol{q}_i|^2 = q_s^2 + q_i^2 - 2q_s q_i \cos(\phi_s - \phi_i)$ [2]. Thus, after evaluating the integral in Eq. (5.45), the function g_z may ultimately be written

[10] Note that the validity of the Laguerre-Gaussian pump beams is also restricted to this approximation, since they are the solutions to the paraxial wave equation.

[11] See also the discussion regarding the angle phase-matching procedure in Sec. 2.3.1, which also implies $n_p = n_s = n_i$.

Table 5.1: Fitting parameter A for selected experimental gain values G_{exp} for several combinations of the pump radial (m_p) and OAM (l_p) indices. Unlike in Table I of Ref. [2], for the values presented here, the prefactor $2\pi\,(w_0/2)^{|l_p|+1}$ of the function R as written in Eq. (5.18) was taken into account.

l_p	m_p	Fitting parameter A'	
		$G_{\text{exp}} = 0.01$	$G_{\text{exp}} = 4$
0	0	2230	2710
0	7	691	1470
0	18	404	912
7	0	6360	6930
7	7	1.90×10^5	2.47×10^5
7	18	1.49×10^6	2.01×10^6
18	0	1.24×10^8	1.34×10^8
18	7	4.63×10^{10}	5.37×10^{10}
18	18	4.43×10^{12}	5.39×10^{12}

in the form

$$g_z(q_s, q_i, \phi_s - \phi_i) = L_1 \operatorname{sinc}\left(L_1 \frac{|\boldsymbol{q}_s - \boldsymbol{q}_i|^2}{4k_p}\right) \mathrm{e}^{\mathrm{i}L_1 \frac{|\boldsymbol{q}_s - \boldsymbol{q}_i|^2}{4k_p}}, \tag{5.49}$$

with the sinc-function as defined in Eq. (2.28).

Equations (5.17), (5.18) and (5.49) fully define the TPA for the single crystal. As mentioned in Sec. 5.2.1, the numerical computations focus on the function R defined in Eq. (5.18), since, unlike the TPA, it can be written in terms of three variables instead of four. The numerical computation follows the steps outlined in Secs. 5.2.2 and 5.2.3. This way, the Schmidt eigenvalue distributions, Schmidt modes and intensity spectra for PDC using Laguerre-Gaussian pump beams can be obtained.

Similar to the integro-differential equation approach for the description of PDC, the first step when obtaining these numerical results is connecting the theoretical gain parameter G [see Eq. (5.34)] to the experimental gain G_{exp} defined via a fitting procedure of the intensity curve of a single crystal over G. Here, procedure is the same as for the integro-differential equation approach described in Sec. 3.4. Furthermore, the connection between the fitting constant and the experimental gain is slightly adapted to improve the numerical stability, accounting for the fact that the behavior of the collinear output intensity strongly depends on the pump radial (m_p) and OAM (l_p) number, meaning it varies over several orders of magnitude for different pump parameters. In Ref. [2], the prefactor $2\pi\,(w_0/2)^{|l_p|+1}$ of R as written in Eq. (5.18) was additionally neglected, since for large l_p, this prefactor becomes very large. This must be taken into account when computing the value for G using the fitting constant. Here however, this prefactor is taken into account and the exact form of R must not be modified since the fitting constant depends on its prefactors. The same applies to g_z The values for the re-scaled fitting constant A', in the following just called

the fitting constant, are listed in Table 5.1. The connection between this constant and the experimental gain is [2]:

$$G_{\text{exp}} = \frac{C}{2} A' G. \tag{5.50}$$

Note that C in Eq. (5.50) refers to the normalization constant of the system under consideration and not necessarily the normalization of a single crystal for which the fit was performed. To reduce the numerical complexity, the following analysis will focus on two experimental gain values, $G_{\text{exp}} = 0.01$ for the low-gain regime and $G_{\text{exp}} = 4$ for the high-gain regime. Again, as described in Sec. 3.4, the fit constant differs when comparing the low and high-gain regime, which is why Table 5.1 lists two different values for A' for each combination (l_p, m_p). Furthermore, for the following results, it should be noted that a precise agreement with Ref. [2] is not expected due to rounding errors, which may appear due to the fact that more decimals of the fit constants are used to relate the gain parameter G and the experimental gain.

Figure 5.2 shows the modal eigenvalue distributions for a single crystal and the above-mentioned parameters for various radial (m_p) and OAM (l_p) indices of the pump for low parametric gain $G_{\text{exp}} = 0.01$. Evidently, with increasing radial and OAM number for the pump, the distribution of the eigenvalues broadens in the direction of the radial and OAM mode number, respectively. As a consequence, the Schmidt number K as defined in Eq. (5.44) also increases when either m_p or l_p or both are increased. As such, varying l_p and m_p allows for some control over the width of the eigenvalue distribution.

The eigenvalue distributions show a mirror symmetry around the line $m_p = l_p/2$. This follows due to the fact that the eigenvalues fulfill the symmetry relation written in Eq. (5.30c), which also implies that for odd l_p, the eigenvalue distribution must be flat around $n = l_p/2$, since $\Lambda_{m,n=\lceil \frac{l_p}{2} \rceil} = \Lambda_{m,n=\lfloor \frac{l_p}{2} \rfloor}$ [2].

As the parametric gain is increased, only the modes with larger eigenvalues remain compared to those with lower eigenvalues, which was one of the main results of Sharapova *et al.* [11]. This can be seen from Fig. 5.3, which shows the same eigenvalue distributions as in Fig. 5.2 but for $G_{\text{exp}} = 4$. Most notably, this redistribution of the eigenvalues due to the increased gain [11] seems to almost completely eliminate the contributions of eigenvalues with nonzero radial index $m > 0$. The reason for this redistribution is the $\sinh^2$-dependence of the modal weights on G and G_{exp}, see Eq. (5.39a), which leads to a stronger amplification for larger singular values $\sqrt{\lambda_{mn}}$, while smaller $\sqrt{\lambda_{mn}}$ are suppressed in comparison [11]. As a consequence, the Schmidt number K is also considerably reduced compared to the low-gain case, regardless of the combination of m_p and l_p, compare Fig. 5.2. Interestingly, the Schmidt number decreases with increasing m_p, which is the opposite of what was observed for the low-gain regime shown in Fig. 5.2.

The only exception to this is the transition from $m_p = 7$ to $m_p = 18$ for $l_p = 0$, compare Figs. 5.3(b) and 5.3(c), which still shows a small increase. This effect must be related to the shape of the eigenvalue distributions: At low gain (Fig. 5.3), the eigenvalue distributions are generally more flat at $m_p = 0$ and as m_p is increased, the distributions take the form

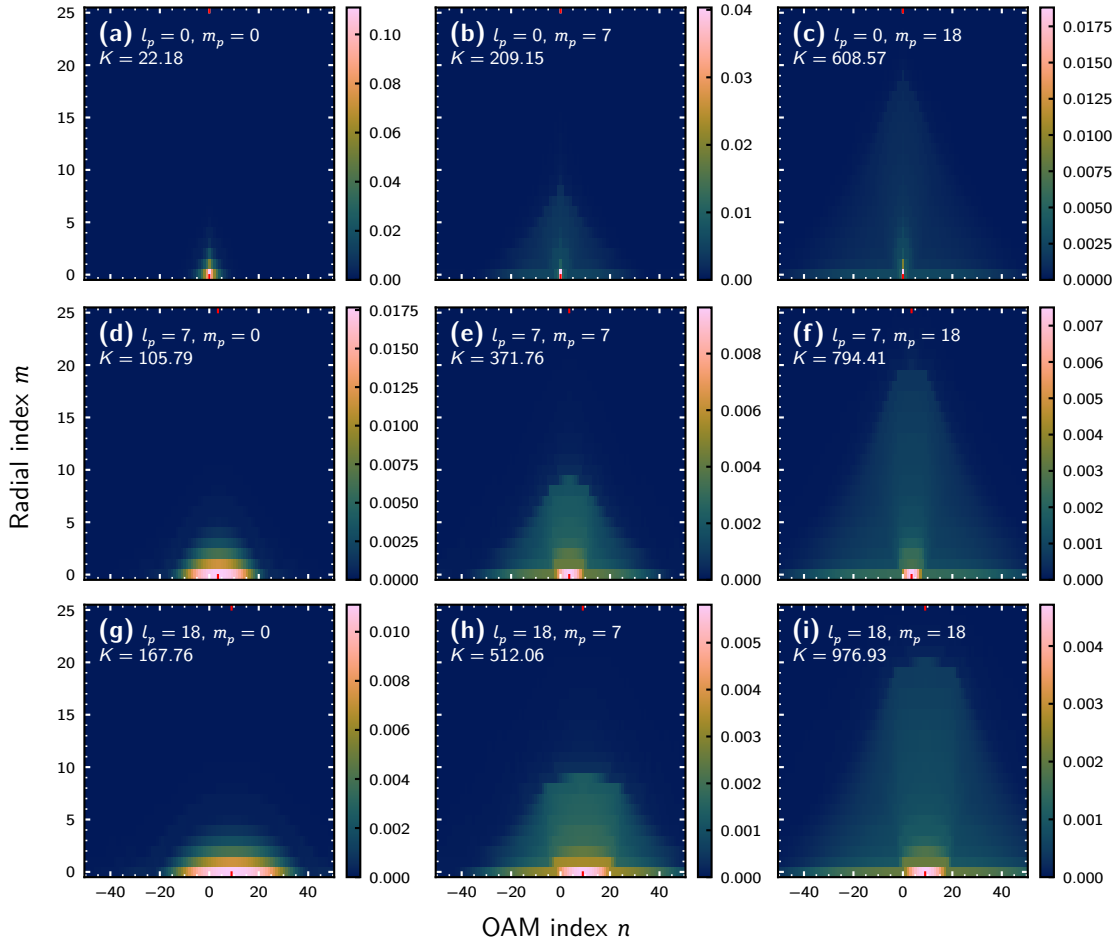

Figure 5.2: Plots of the normalized Schmidt mode weights $\bar{\Lambda}_{mn}$ as defined in Eq. (5.42) for a single BBO crystal of length $L_1 = 2\,\text{mm}$ pumped by a Laguerre-Gaussian beam for various radial (m_p) and OAM (l_p) indices (as written in the plots) at low gain $G_{\text{exp}} = 0.01$. The red ticks on the n-axis mark $n = l_p/2$, which is the symmetry line for the eigenvalue distribution. Evidently, an increase in the radial number m_p of the pump leads to a broadening of modal weight distribution along the radial index m. Similarly, increasing l_p leads to a broadening of the eigenvalue distribution along n. This is also confirmed by comparing with a Schmidt number K [defined in Eq. (5.44)], which indicates that increasing either m_p or l_p increases the number of effectively occupied modes. See also Fig. 5.3 which shows the eigenvalues for $G_{\text{exp}} = 4$. Adapted from Ref. [2], where the underlying data and the plot were produced by L. Gehse.

of a narrow region with large occupations, and a larger region with a broad tail, where many modes have smaller eigenvalues. It is this tail which gets most strongly suppressed at high gain, in contrast to the narrow regions with larger eigenvalues. Thus, in general, distributions with a large tail of eigenvalues with smaller occupations are affected more by an increase in the gain, leading to a stronger reduction in the Schmidt number compared to more narrow eigenvalue distributions. See also Fig. 5.14(b) further down in this chapter, which shows the behavior of the Schmidt number K over a wide range of values for the experimental gain. Note however that Fig. 5.14(b) uses different fit constants A than the figures shown here.

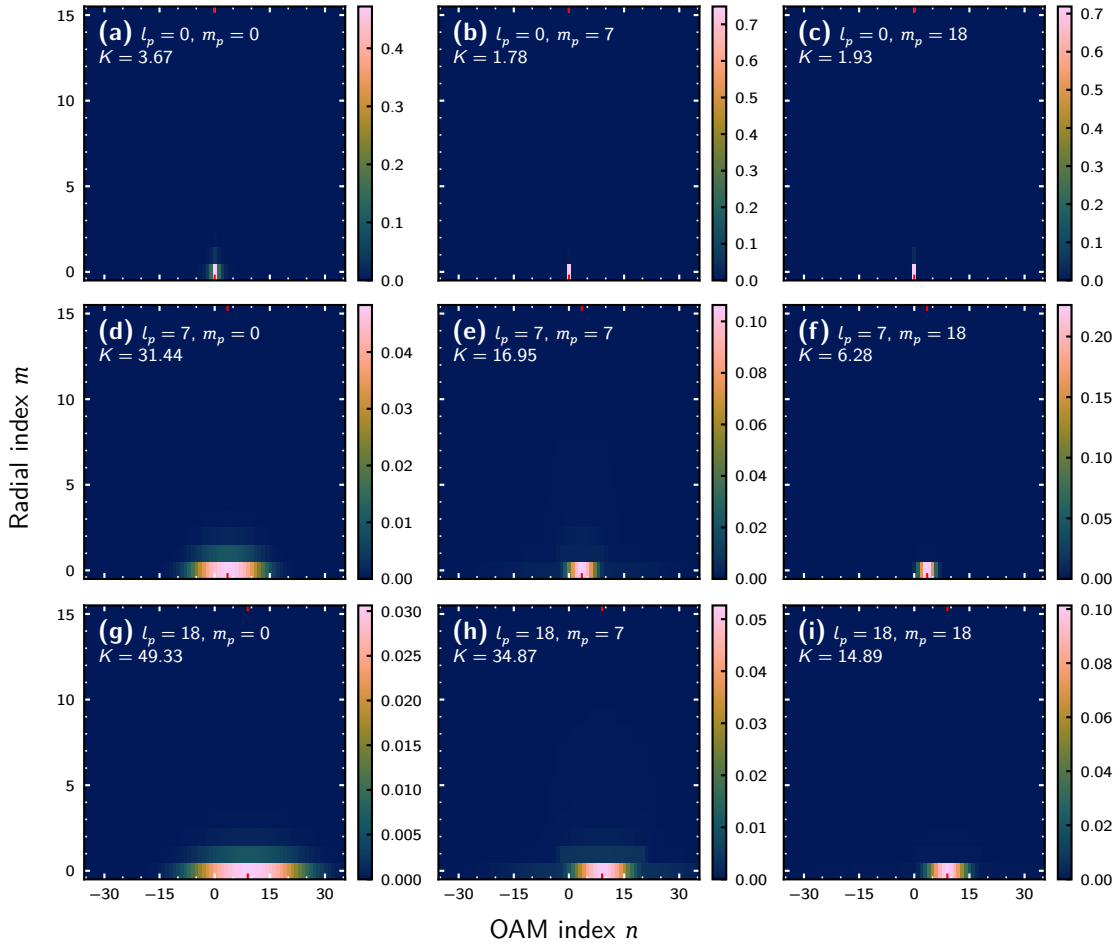

Figure 5.3: Plots of the normalized Schmidt mode weights $\bar{\Lambda}_{mn}$ as defined in Eq. (5.42) for a single BBO crystal of length $L_1 = 2\,\mathrm{mm}$ pumped by a Laguerre-Gaussian beam for various radial (m_p) and OAM (l_p) indices (as written in the plots) at high gain $G_{\mathrm{exp}} = 4$. The red ticks on the n-axis mark $n = l_p/2$, which is the symmetry line for the eigenvalue distribution. As was the case for low gain, see Fig. 5.3, the width of the distribution along m and n is increased if m_p and l_p are increased, respectively. Similarly, the Schmidt number increases if either m_p or l_p or both are increased. As described in Sharapova *et al.* [11], for the Schmidt mode formalism, increasing the parametric gain leads to a redistribution of the modal weights due to their $\sinh^2$-dependence on G_{exp} [via Eq. (5.50)]. See also Fig. 5.2 which shows the eigenvalues for low gain $G_{\mathrm{exp}} = 0.01$.

Figure 5.4 shows the radial intensity profiles for a single crystal at low and high parametric gain. The intensity profiles are plotted over the external angle[12] $\theta_s \approx q_s/k_s^{\mathrm{air}}$, where k_s^{air} is the signal wave-vector modulus in air (compare Sec. 3.5.3). As mentioned above, Eq. (5.41) shows that the intensity profiles are radially symmetric and thus the shown profiles contain the full information regarding the intensity distributions. For low parametric gain and $l_p = m_p = 0$, see Fig. 5.4(a), the intensity profile has a sinc^2-shape, which was already described in Sharapova *et al.* [11] and was also observed in Sec. 3.5.3, see Fig. 3.4. Notably,

[12]Note that in Ref. [2], Θ_s was used as the designation for the external angle.

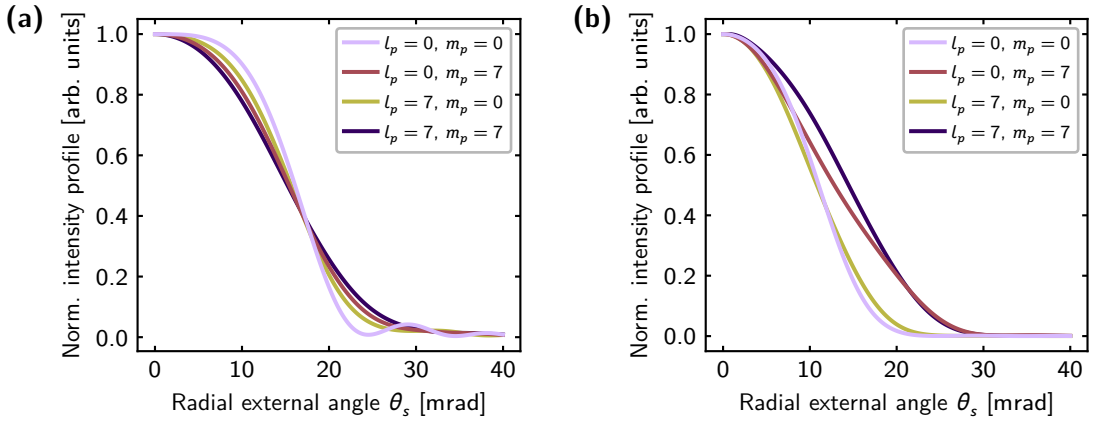

Figure 5.4: Normalized radial intensity profiles [so that $\langle \hat{N}(0) \rangle = 1$] of a single crystal pumped with a Laguerre-Gaussian pump beam for several combinations of the radial (m_p) and OAM (l_p) index for **(a)** low parametric gain $G_{\text{exp}} = 0.01$ and **(b)** high parametric gain $G_{\text{exp}} = 4$. For the low-gain regime, see also Fig. 5.5 which shows the intensity profile curves in the low-gain approximation separated into different plots. Adapted from Ref. [2], where the underlying data and the plot were produced by L. Gehse.

if the radial or OAM index of the pump is increased, the intensity profile approaches a more Gaussian shape.

In order to understand these intensity profiles in terms of the change in l_p and m_p, it is useful to consider the low-gain limit of Eq. (5.41). In this limit, $G \ll 1$ so that the high-gain eigenvalues as written in Eq. (5.39a) may be approximated using $\sinh(x) \approx x$ for $x \ll 1$ (since also $\lambda_{mn} < 1$):

$$\Lambda_{mn} \approx G^2 \lambda_{mn} \,. \tag{5.51}$$

Using the normalization of the eigenvalues, this approximation leads to

$$\langle \hat{N}(\boldsymbol{q}) \rangle \approx \frac{G^2}{2\pi} \sum_{m,n} \frac{|u_{mn}(q)|^2}{q} \lambda_{mn} \,, \tag{5.52}$$

which can also be written in terms of the TPA, compare Eqs. (5.21) and (5.22):

$$\langle \hat{N}(\boldsymbol{q}) \rangle \approx G^2 \iint \mathrm{d}q_i \, \mathrm{d}\phi_i \, q_i |F(q_s, q_i, \phi_s, \phi_i)|^2 \,, \tag{5.53}$$

where the right-hand side no longer depends on ϕ_s, as can be seen from comparing with Eq. (5.24). Alternatively, this approximation can be written in terms of R:

$$\langle \hat{N}(\boldsymbol{q}) \rangle \approx 2\pi G^2 \iint \mathrm{d}q_i \, \mathrm{d}(\phi_s - \phi_i) \, q_i |R(q_s, q_i, \phi_s - \phi_i)|^2 \,. \tag{5.54}$$

Note that in Eqs. (5.52)–(5.54), the gain parameter G still depends on the geometry of the system, due to the dependence on C, see Eqs. (5.14) and (5.34). In words, the intensity profile can be approximated by averaging the modulus squared of the TPA F or the

function R over the idler variables. Note that the factor 2π in Eq. (5.54) results from the normalization of the function R and the fact that it is integrated over the angle difference instead of both angles separately. If only the relative shape of the intensity profile is relevant, the constant G in Eqs. (5.52)–(5.54) may additionally be set to unity: $G = 1$.

It is well-understood and follows from Eq. (5.53) that the sinc^2-shape of the intensity profile at low gain and for $l_p = m_p = 0$ results from the sinc-term in the function g_z, see Eq. (5.49). If either m_p or l_p are nonzero, the Laguerre polynomial term $L_{m_p}^{|l_p|}$ and the term [2]

$$W(q_s, q_i, \phi_s - \phi_i) = \left[q_s \mathrm{e}^{-\mathrm{i}\,\mathrm{sgn}(l_p)(\phi_s - \phi_i)} + q_i\right]^{|l_p|}, \tag{5.55}$$

of R as written in Eq. (5.18), respectively, are the only relevant additional term compared to the case $l_p = m_p = 0$ and must therefore be responsible for the change of the intensity profile to a more Gaussian shape.

As the gain is increased to $G_{\mathrm{exp}} = 4$, the redistribution of the eigenvalues Λ_{mn} due to the $\sinh^2$-dependence means that only modes with higher occupation, as indicated by larger eigenvalues, contribute considerably to the intensity profiles. As such, the shapes of the intensity profiles change significantly and become more Gaussian since the low-order modes, which are normally Gaussian shaped for simple PDC sections, generally have larger eigenvalues [2]. This can be seen in Fig. 5.4(b), where even for the case $l_p = m_p = 0$ the intensity profile has become Gaussian.

Figure 5.5 provides further insight into the suppression of the side-peaks for nonzero radial and OAM indices of the pump in the low-gain approximation. The figure shows the quantity $\mathcal{I}(q_s, \phi_s - \phi_i) = \int \mathrm{d}q_i\, q_i |R(q_s, q_i, \phi_s - \phi_i)|^2$ for each combination of m_p and l_p also shown in Fig. 5.4(a). From this quantity, the intensity profile can be obtained by integrating over the azimuthal angle difference $\phi_s - \phi_i$: $\langle \hat{N}(\boldsymbol{q}_s)\rangle \approx \int \mathrm{d}(\phi_s - \phi_i)\, \mathcal{I}(q_s, \phi_s - \phi_i)$, compare Eq. (5.54). As such, $\mathcal{I}$ provides information regarding the values $\phi_s - \phi_i$ from which contributions in the intensity profile originate. As an example, for $l_p = m_p = 0$, see Fig. 5.5(a), the side peaks leading to the sinc^2 profile of the photon number distribution can be seen to originate mostly from the line $\phi_s - \phi_i = \pi$. Analytically, this observation can be validated as follows: Equation (5.49) shows that the dependence of the sinc-term on q_s and the angle difference is of the form $|\boldsymbol{q}_s - \boldsymbol{q}_i|^2 = q_s^2 + q_i^2 - 2q_s q_i \cos(\phi_s - \phi_i)$, which is maximized as $\phi_s - \phi_i$ approaches π, so that $|\boldsymbol{q}_s - \boldsymbol{q}_i|^2 = (q_s + q_i)^2$.

For $m_p = 7$, $l_p = 0$, see Fig. 5.5(b), it becomes clear that the Laguerre polynomial term in R, see Eq. (5.18), leads to a strong broadening of the distribution of $\mathcal{I}$ along q_s (shown as the external angle θ_s) and a smaller broadening along $\phi_s - \phi_i$. Oscillations appear below the line $\phi_s - \phi_i = \pi$ and, due to the symmetry, also above it. The contribution along said line which lead to the sinc^2-shaped intensity profile in the case $l_p = m_p = 0$ [compare Fig. 5.5(a)] is still visible, but due to the broadening about the line $\phi_s - \phi_i = \pi$ and the contributions at $\theta_s = 20\,\mathrm{mrad}$, they are not seen as distinct side peaks of the distribution.

For $m_p = 0$, $l_p = 7$ as shown in Fig. 5.5(c), the sinc^2-contribution is eliminated along the line $\phi_s - \phi_i = \pi$, which follows analytically from the fact that $W(q_s, q_i, \pi) =$

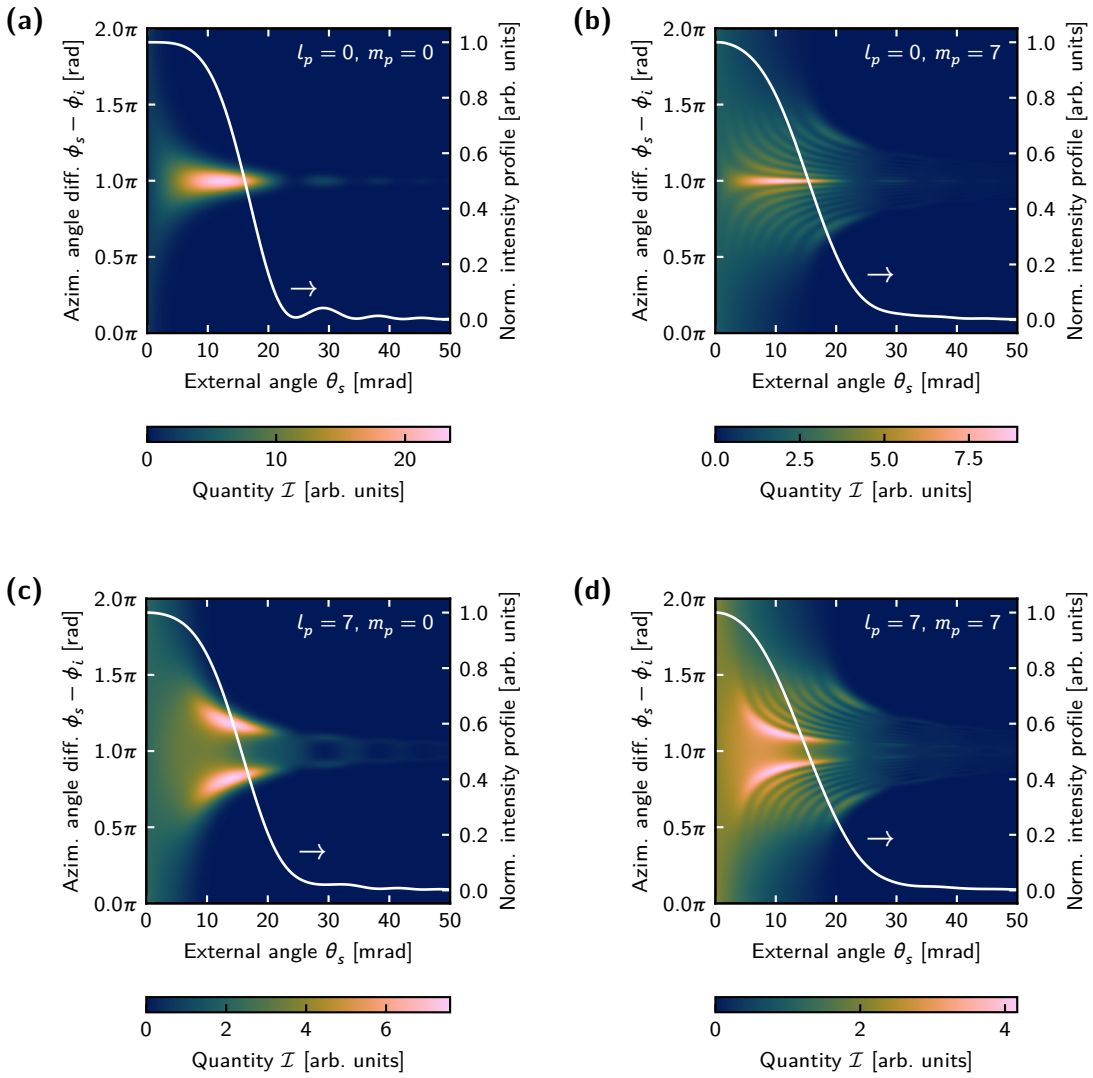

Figure 5.5: Plots of the quantity $\mathcal{I}(q_s, \phi_s - \phi_i) = \int \mathrm{d}q_i\, q_i |R(q_s, q_i, \phi_s - \phi_i)|^2$ for several combinations of the pump radial (m_p) and OAM (l_p) index. Note that the q_s variable has been expressed in terms of the external angle θ_s in the plot. The white line, corresponding to the right-hand side vertical axis, shows the intensity profile in the low-gain approximation obtained as the integral of $\mathcal{I}$ over the azimuthal angled difference $\phi_s - \phi_i$: $\langle \hat{N}(\boldsymbol{q}) \rangle \approx \int \mathrm{d}(\phi_s - \phi_i)\, \mathcal{I}(q_s, \phi_s - \phi_i)$, compare Eq. (5.54), which essentially corresponds to the integral over the (left-hand side) vertical axis (azimuthal angle difference $\phi_s - \phi_i$) of the shown plot. See also Fig. 5.4(a), which shows all four radial intensity profiles in a single plot at $G_{\mathrm{exp}} = 0.01$.

$(q_s - q_i)^{|l_p|}\,(-1)^{|l_p|}$, compare Eq. (5.55), which vanishes when the sinc-term of g_z is maximized for $q_s = q_i$, see above. This also means that the contributions are shifted away from the line $\phi_s - \phi_i = \pi$ to smaller and larger angle differences, leading to the ring shaped structures along the line $\phi_s - \phi_i = \pi$, at $\theta_s = 30\,\mathrm{mrad}$ and $\theta_s = 38\,\mathrm{mrad}$ seen in Fig. 5.5(c). A similar redistribution can be seen from the strongest contributions from $\theta_s = 10\,\mathrm{mrad}$ to $20\,\mathrm{mrad}$.

Figure 5.5(d) shows the case $m_p = 7$, $l_p = 7$, which shows both broadening mechanisms

discussed above for the cases $m_p = 7$, $l_p = 0$ an $m_p = 0$, $l_p = 7$ combined. Overall, this leads again to a suppression of the side peaks originating from the sinc^2-term.

5.3.2. Non-Compensated SU(1,1) Interferometers

For an SU(1,1) interferometer consisting of two crystals with an air-gap in-between, the integral over the z-axis from Eq. (5.45) is extended over the second crystal and an additional phase $\mathrm{e}^{\mathrm{i}\Delta k^{\mathrm{air}}(\boldsymbol{q}_s,\boldsymbol{q}_i)d}$ resulting from the air gap is added. Thus, the function g_z is given by

$$g_z(\boldsymbol{q}_s,\boldsymbol{q}_i) = \int_0^{L_1} \mathrm{d}z\, \mathrm{e}^{\mathrm{i}\Delta k(\boldsymbol{q}_s,\boldsymbol{q}_i)z} + \mathrm{e}^{\mathrm{i}\Delta k^{\mathrm{air}}(\boldsymbol{q}_s,\boldsymbol{q}_i)d} \int_{L_1}^{2L_1} \mathrm{d}z\, \mathrm{e}^{\mathrm{i}\Delta k(\boldsymbol{q}_s,\boldsymbol{q}_i)z}, \tag{5.56}$$

where d is the length of the air gap and $\Delta k^{\mathrm{air}}(\boldsymbol{q}_s,\boldsymbol{q}_i)$ is the two-dimensional form of the difference of the z-components of the wave-vectors, as written in Eq. (3.35):

$$\Delta k^{\mathrm{air}}(\boldsymbol{q}_s,\boldsymbol{q}_i) = \sqrt{\left(k_p^{\mathrm{air}}\right)^2 - |\boldsymbol{q}_s+\boldsymbol{q}_i|^2} - \sqrt{\left(k_s^{\mathrm{air}}\right)^2 - |\boldsymbol{q}_s|^2} - \sqrt{\left(k_i^{\mathrm{air}}\right)^2 - |\boldsymbol{q}_i|^2}\,. \tag{5.57}$$

Considerations regarding refraction at the crystal-air and air-crystal boundaries can be found in Sec. A.2. Therein, it is also shown that when transitioning between different materials (refractive indices), the transverse wave-vector components are preserved, meaning that the wave-vector components as written in Eq. (5.57) are the same as inside the PDC sections. Again, as for Eqs. (5.45) and (5.46), the function g_z is the integrated phase-matching function h, compare Eq. (3.30) for the contribution of the first PDC section and Eqs. (3.32) and (3.34) for the contribution of the second crystal.

For the phase mismatch in air, the Fresnel approximation contains an additional term related to the refractive index difference [1, 11]:

$$\Delta k^{\mathrm{air}}(\boldsymbol{q}_s,\boldsymbol{q}_i) \approx k_p^{\mathrm{vac}}\delta n + \frac{|\boldsymbol{q}_s-\boldsymbol{q}_i|^2}{2k_p^{\mathrm{air}}}, \tag{5.58}$$

where $\delta n = n_p^{\mathrm{air}} - (n_s^{\mathrm{air}} + n_i^{\mathrm{air}})/2 = n_p^{\mathrm{air}} - n_s^{\mathrm{air}}$ (since $n_s^{\mathrm{air}} = n_i^{\mathrm{air}}$) and n_j^{air} for $j = p, s, i$, are the refractive indices of the pump, signal and idler radiation in the air gap. The additional term $k_p^{\mathrm{vac}}\delta n$ appears due to the fact that the refractive indices are chosen for collinear phase-matching, see Sec. 2.3.1. This implies $k_p - k_s - k_i = 0$ due to the degeneracy of the PDC process and as consequence, in general, $k_p^{\mathrm{air}} - k_s^{\mathrm{air}} - k_i^{\mathrm{air}} \neq 0$, since the refractive indices in air differ from those in the PDC sections.

Evaluating the integrals in Eq. (5.56), applying the Fresnel approximations as written in Eqs. (5.48) and (5.58) and using $k_p^{\mathrm{vac}} = 2k_s/n_s$ yields the following expression for the function g_z for an SU(1,1) interferometer [2, 11]:

$$\begin{aligned} g_z(q_s,q_i,\phi_s-\phi_i) = 2L_1\,\mathrm{sinc}\left(L_1\frac{|\boldsymbol{q}_s-\boldsymbol{q}_i|^2}{4k_p}\right)\cos\left(L_1\frac{|\boldsymbol{q}_s-\boldsymbol{q}_i|^2}{4k_p} + \frac{\delta n k_s d}{n_s} + d\frac{|\boldsymbol{q}_s-\boldsymbol{q}_i|^2}{4k_p^{\mathrm{air}}}\right) \\ \times \exp\left[\mathrm{i}\left(L_1\frac{|\boldsymbol{q}_s-\boldsymbol{q}_i|^2}{2k_p} + \frac{\delta n k_s d}{n_s} + d\frac{|\boldsymbol{q}_s-\boldsymbol{q}_i|^2}{4k_p^{\mathrm{air}}}\right)\right]. \end{aligned} \tag{5.59}$$

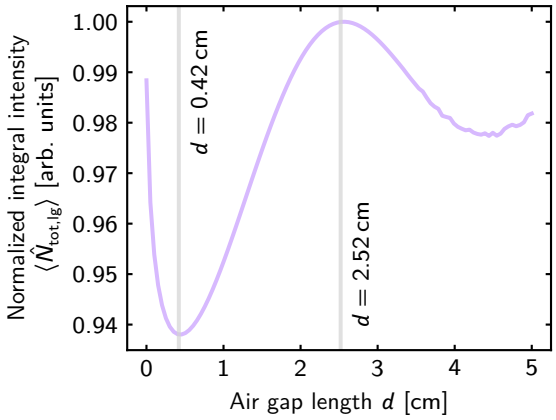

Figure 5.6: Normalized integral intensity obtained using the intensity profile in the low-gain approximation [see Eq. (5.61)] for an SU(1,1) interferometer in dependence on the length of the air gap d between the two crystals. The first local minimum (first dark fringe) at $d = 0.42\,\mathrm{cm}$ and the first local maximum (first bright fringe, apart from $d = 0$) at $d = 2.52\,\mathrm{cm}$ are marked with vertical gray lines. The relative evolution of the integral intensity in the low-gain approximation seems to be independent of l_p and m_p: Varying these parameters only seems to shift the curve by a constant amount, which was manually confirmed for all 64 combinations $0 \leq l_p, m_p \leq 7$ in Ref. [2]. The noise in the integral intensity appearing after $d = 3.5\,\mathrm{cm}$ is discussed in more detail in the main text. Adapted from Ref. [2], where the underlying data for all combinations and the plot were produced by L. Gehse. The (non-normalized) data for this plot were obtained from the dataset associated with Ref. [2], see Ref. [151].

The interferometer described by this function is non-compensated, as per the definitions in Sec. 3.3. A sketch of this setup is given in Fig. 3.2(a). The goal with using this setup is to manipulate the PDC state generated by the SU(1,1) interferometer by varying the distance d between the crystals. As such, it is not necessary to consider a compensated configuration for the interferometer, as was the case for the metrological applications discussed in Chapters 3 and 5.

It was shown with Eqs. (3.45a) and (3.45c) that the integral intensity $\langle \hat{N}_{\mathrm{tot}} \rangle$ [see also Eq. (3.39)] of a fully compensated SU(1,1) interferometer has a $\cos^2$-dependence on the interferometric phase ϕ. For a non-compensated interferometer, the dependence of the integral intensity on the distance d between the two crystals is more complex due to the diffraction of the radiation and must be, in general, computed numerically. Figure 5.6 shows this dependence for the interferometer as described in this section, using the TPA constructed from Eqs. (5.17), (5.18) and (5.59) and using the low-gain approximation for the radial intensity profile as described by Eqs. (5.52)–(5.54). By splitting the gain constant G as

$$G = \frac{\Gamma_{\mathrm{int}}}{C}, \tag{5.60}$$

where Γ_{int} is the component of the gain parameter which no longer depends on the geometry of the setup [compare Eq. (5.14)], the integral intensity in the low-gain approximation

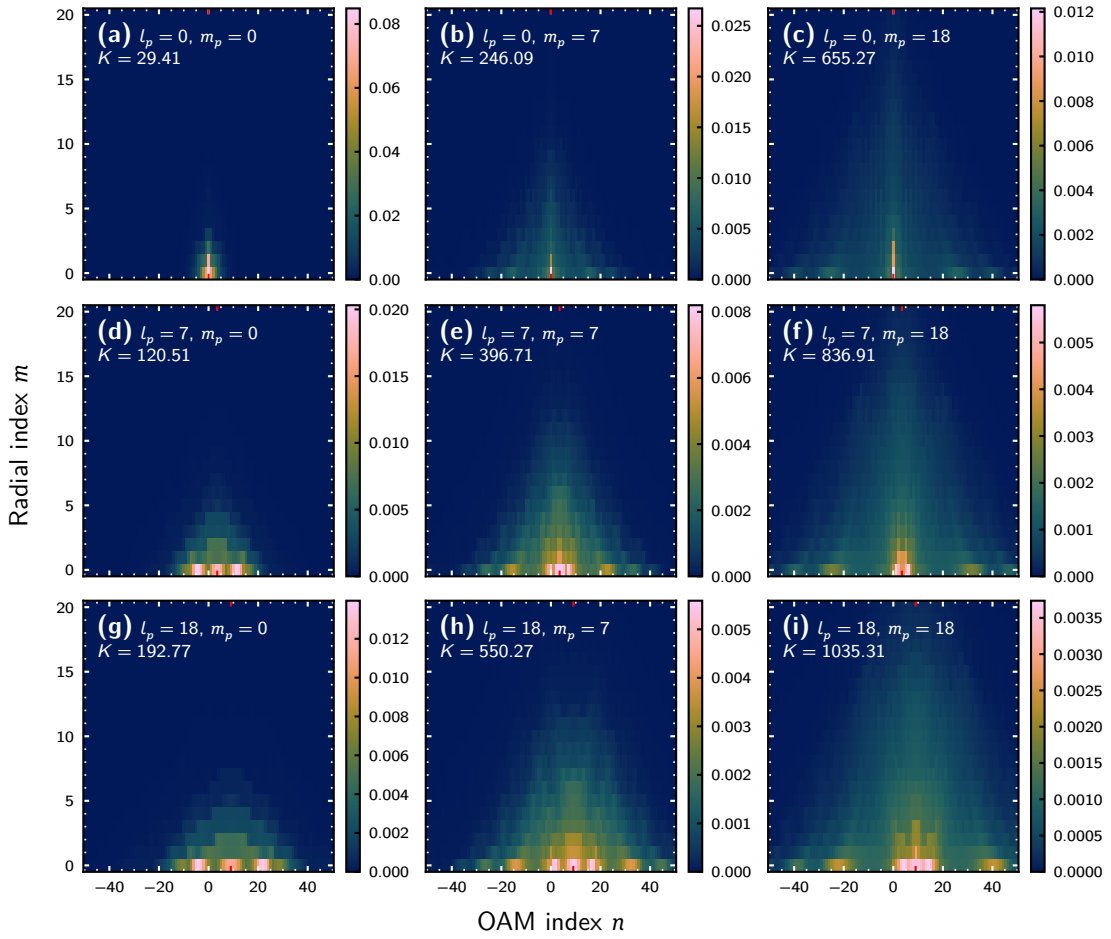

Figure 5.7: Plots of the normalized modal weights $\bar{\Lambda}_{mn}$ for an SU(1,1) interferometer consisting of two BBO crystals of length $L_1 = 2\,\mathrm{mm}$ with an air gap of length $d = 0.42\,\mathrm{cm}$ in-between (dark fringe) and pumped at low parametric gain $G_{\mathrm{exp}} = 0.01$ for varying radial (m_p) and OAM (l_p) index of the Laguerre-Gaussian pump beam. The red ticks on the n-axis mark $n = l_p/2$, which is the symmetry line for the eigenvalue distribution. The eigenvalue distributions exhibit non-monotonic behavior along the OAM n mode index, which was not observed for the single crystal, see Figs. 5.2 and 5.3. See also Fig. 5.8, which shows the eigenvalue distribution for high parametric gain $G_{\mathrm{exp}} = 4$. Adapted from Ref. [2], where the underlying data and the plot were produced by L. Gehse.

obtained from Eqs. (5.53) and (5.54) may be rewritten as

$$\langle \hat{N}_{\mathrm{tot,lg}} \rangle = \frac{\Gamma_{\mathrm{int}}^2}{C^2}\,. \tag{5.61}$$

The factor $1/C$ in Eq. (5.60) may be regarded as the *geometric component* of the gain parameter, which originates from properties of the system such as whether the system consists of a single crystal or two crystals with an air gap in-between. For the latter example, the factor $1/C$ also depends on the distance d between the two crystals. Thus, this factor determines the evolution of $\langle \hat{N}_{\mathrm{tot,lg}} \rangle$ over d.

Evidently, the integral intensity is not π-periodic as was the case for the compensated

SU(1,1) interferometer. Starting at around $d = 3.5\,\mathrm{cm}$, noise can be observed in Fig. 5.6. This results from interference fringes appearing in the intensity profile $\langle \hat{N}(q) \rangle$, which become unresolved as d grows [2]. This does not pose an issue here, since, in the following, the focus will be on the first dark fringe, which is reached at $d = 0.42\,\mathrm{cm}$, while further investigations in Ref. [2] also focus on the first bright fringe (after the initial drop of the total intensity) at $d = 2.52\,\mathrm{cm}$ and both values for d are sufficiently far away from the noise.

At the dark fringe, the PDC radiation generated in the first crystal interferes destructively in the first crystal, leading to a local minimum in the output integral intensity of the SU(1,1) interferometer. This leads to significant modification of the intensity profile and the Schmidt mode weight distribution, as can be seen from Fig. 5.7. As was the case for the single crystal, see Fig. 5.2, increasing m_p and l_p significantly increases the width of the eigenvalue distribution along m and n, respectively. However, unlike the eigenvalue distributions for a single crystal, the distributions for the SU(1,1) interferometer exhibit a non-monotonic behavior with local minima and maxima along the OAM index n, which is most clearly visible for $m = 0$. Note that contrary to that, by definition, the eigenvalues along m are sorted in descending order, meaning that for fixed n, no non-monotonic behavior can appear along m.

The non-monotonic behavior is even more strongly visible as the parametric gain is increased, see Fig. 5.8, where only the modes with the larges eigenvalues remain, while the others are suppressed. As was the case for a single crystal, see Fig. 5.3, only modes with $m = 0$ have significantly large eigenvalues. As suggested in Ref. [2], increasing the gain can thus be utilized as a filtration mechanism which allows for the selection of only the most strongly occupied modes.

Additionally, this behavior suggests an interesting application: As seen throughout Secs. 4.2.2.2 and 4.3.1, when dealing with unbalanced SU(1,1) interferometers in the model where only a single transverse dimension is considered, one of the major issues is that the output modes of the first crystal and the input modes of the second crystal share nontrivial overlap, requiring elaborate techniques to for example extract information of the first crystal from the full interferometer. The results mentioned above in this section suggest that when instead focusing on the OAM modes of PDC, this overlap is simplified. At first, it is immediately obvious that between the PDC sections of the interferometer, only modes with the same OAM index may share some overlap. Additionally, due to the fact that almost no modes with $m > 0$ are occupied at high gain, as mentioned above, all overlap coefficients should be, to a good approximation, diagonal. Further research is required to confirm these conjectures and apply them in the context of multimode squeezing measurements as investigated in Chapter 4.

Figures 5.7(g) and 5.8(g) demonstrate that for the case $l_p = 18$, $m_p = 0$ the maximally occupied modes occur at $m = 0$ and $n = -4$ and $n = 22$. This indicates that the non-monotonic behavior of the eigenvalue distribution can be used to prepare PDC states where one photon of the signal-idler pair carries larger OAM than the pump photons. Here, the

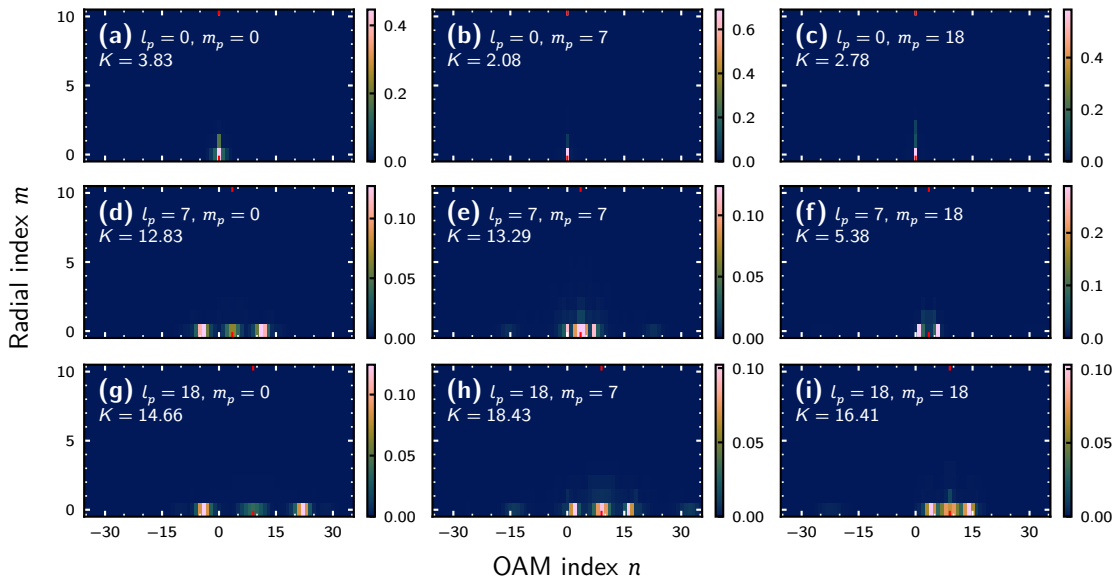

Figure 5.8: Plots of the normalized modal weights $\bar{\Lambda}_{mn}$ for an SU(1,1) interferometer consisting of two BBO crystals of length $L_1 = 2\,\text{mm}$ with an air gap of length $d = 0.42\,\text{cm}$ in-between (dark fringe) and pumped at high parametric gain $G_{\text{exp}} = 4$ for varying radial (m_p) and OAM (l_p) index of the Laguerre-Gaussian pump beam. The red ticks on the n-axis mark $n = l_p/2$, which is the symmetry line for the eigenvalue distribution. As was the case for low gain, see Fig. 5.7, the eigenvalue distributions exhibit non-monotonic behavior along the OAM n mode index, which was not observed for the single crystal, see Figs. 5.2 and 5.3. Due to the redistribution of the eigenvalues (see the main text), the number of populated modes is strongly reduced and only highly populated modes remain. Similar to the single crystal case (Fig. 5.3), this eliminates almost all modes $m > 0$ so that only the modes $m = 0$ have significant eigenvalues.

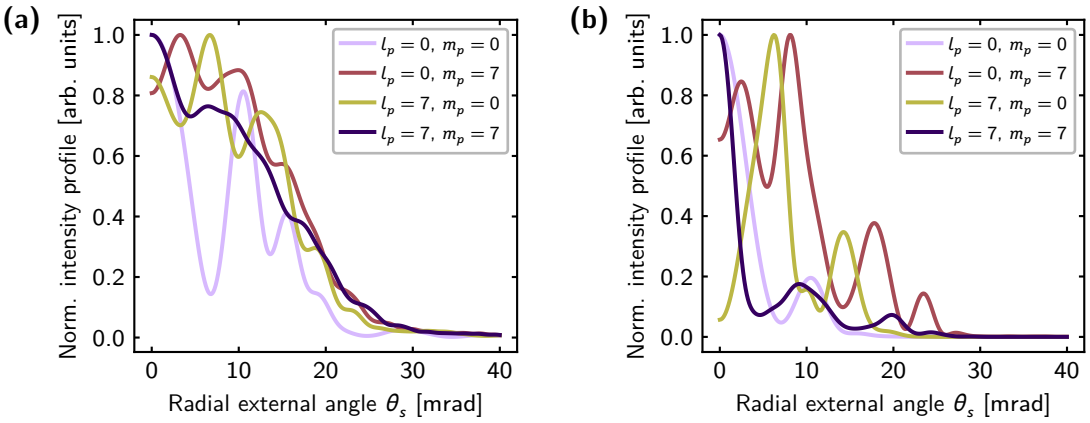

Figure 5.9: Normalized radial intensity profiles [so that $\max_{\theta_s}\langle\hat{N}(\theta_s)\rangle = 1$] of an SU(1,1) interferometer consisting of two BBO crystals of length $L_1 = 2\,\text{mm}$ with an air gap of length $d = 0.42\,\text{cm}$ in-between (dark fringe) and pumped at **(a)** low parametric gain $G_{\text{exp}} = 0.01$ and **(b)** high parametric gain $G_{\text{exp}} = 4$ for varying radial (m_p) and OAM (l_p) index of the Laguerre-Gaussian pump beam. Adapted from Ref. [2].

photon pair consists of one photon with OAM $n = -4$ and one photon with OAM $n = 22$, so that the total OAM is conserved: $22 + (-4) = 18 = l_p$. See also Figs. 5(a) and 5(b) of Ref. [2], which provides plots of the cuts $\bar{\Lambda}_{m=0,n}$.

Figures 5.9(a) and 5.9(b) show the output intensity profiles for the SU(1,1) interferometer at the dark fringe for low ($G_{\text{exp}} = 0.01$) and high gain ($G_{\text{exp}} = 4$), respectively, for several combinations of l_p and m_p. Compared to the intensity profiles of a single crystal shown in Figs. 5.4(a) and 5.4(b), the intensity profile shows a strongly non-monotonic behavior with many side peaks and local minima. Of the intensity profiles shown, the most interesting case is the case $l_p = 7$, $m_p = 0$. For high gain, Fig. 5.9(b) shows that the intensity is strongly reduced near the collinear direction $\theta_s = 0$. This could imply that the Schmidt modes with the largest eigenvalues λ_{mn} are no longer Gaussian and must instead be closer to a donut shape. At increasing gain, these Schmidt modes are amplified, while the other Schmidt modes are suppressed, as already described above.

Figure 5.10 shows the shape of the first 34 modes with the largest eigenvalues and the corresponding values of the *normalized* eigenvalues $\bar{\Lambda}_{mn}$. It confirms that the modes with the largest contributions are no longer Gaussian shaped. Instead, the modes with the largest contributions consist of one or more rings located several mrad away from the collinear direction $\theta_s = 0$. The first mode with significant collinear contribution is $m = n = 0$ and its normalized eigenvalue is 1.9 % of the maximal value for the mode $m = 0$, $n = -4$. This mode at $m = n = 0$ has an approximately Gaussian shape near the collinear direction but also shows two additional local maxima between $\theta_s = 5\,\text{mrad}$ and $15\,\text{mrad}$.

Strictly speaking, when trying to determine the contribution of each mode to the intensity profile, it is necessary to consider the weighted moduli squared $\Lambda_{mn}|u_{mn}(q_s)|^2$ instead of only the normalized modes. These weighted modes are shown in Fig. 5.11, which indicates that the peak contribution to the intensity profile of the mode $m = 0$, $n = -5$ is larger than that of the modes $m = 0$, $n = 11, 12$, which have larger eigenvalues. Hence, the normalized eigenvalue $\bar{\Lambda}_{mn}$ can be understood as a measure for the relative contribution of each mode to the integral intensity $\langle \hat{N}_{\text{tot}} \rangle$ which can be calculated as the sum over the eigenvalues Λ_{mn}, see Eq. (5.43). Contrary to that, the eigenvalue Λ_{mn} is not directly a measure for the contribution of each mode at a fixed transverse wave-vector q_s (or external angle θ_s) due to the fact that the shape of the modes differ and narrow modes generally have larger maxima than broad modes. The mode with the first significant contribution for the collinear direction is $m = n = 0$, as seen from Fig. 5.11. Ultimately however, this contribution is still small compared to that of the modes with the larger weights $\bar{\Lambda}_{mn}$, leading to the intensity profile shape as seen in Fig. 5.9(b). See also Fig. 16 of Ref. [2], which shows two-dimensional *mode profiles* for the case $l_p = 7$, $m_p = 0$ discussed here.

At the bright fringe, the behavior of the eigenvalue distributions is similar to the dark fringe. The main difference compared to the dark fringe is that the non-monotonic behavior of the eigenvalues along n is less pronounced. More details, including plots of the eigenvalues, can be found in Ref. [2]. Furthermore, the aforementioned work also provides a more detailed analysis (performed by L. Gehse) regarding the origin of the non-monotonic

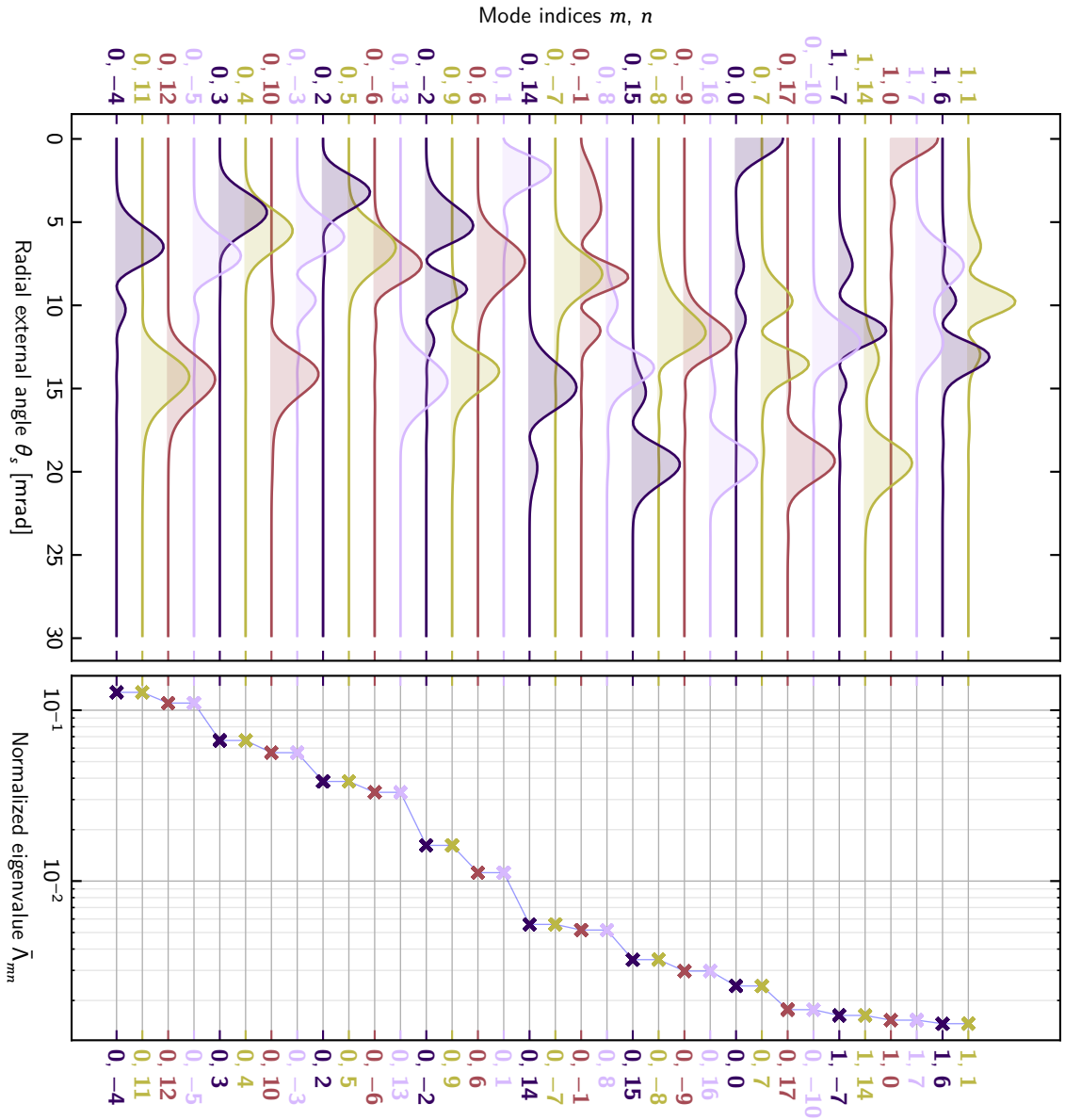

Figure 5.10: Left: Ridgeline plot of the modulus squared $|u_{mn}(q_s)|^2$ of the first 34 radial mode functions of an SU(1,1) interferometer pumped at high gain $G_{\text{exp}} = 4$ with $l_p = 7$, $m_p = 0$ sorted according to their eigenvalues in ascending order from bottom to top. The radial mode functions are normalized so that $\max_{q_s} |u_{mn}(q_s)|^2 = 1$. Right: Normalized eigenvalues corresponding to the modes on the left. Evidently, the modes with the largest contributions are donut-shaped with a local minimum in the collinear direction $\theta_s = 0$. The first mode with a significant contribution in the collinear direction is $n = m = 0$. Note that the symmetry property $\bar{\Lambda}_{mn} = \bar{\Lambda}_{m,l_p-n}$ following from Eq. (5.30c) can be observed from the fact that the normalized eigenvalues always appear pairwise, so that the sum of their OAM indices adds up to l_p (for example, for $m = 0$, the first three are the pairs $n = -4$, $n = 11$; $n = 12$, $n = -5$ and $n = 3$, $n = 4$). The blue line connecting the eigenvalue data points is added for orientation purposes only.

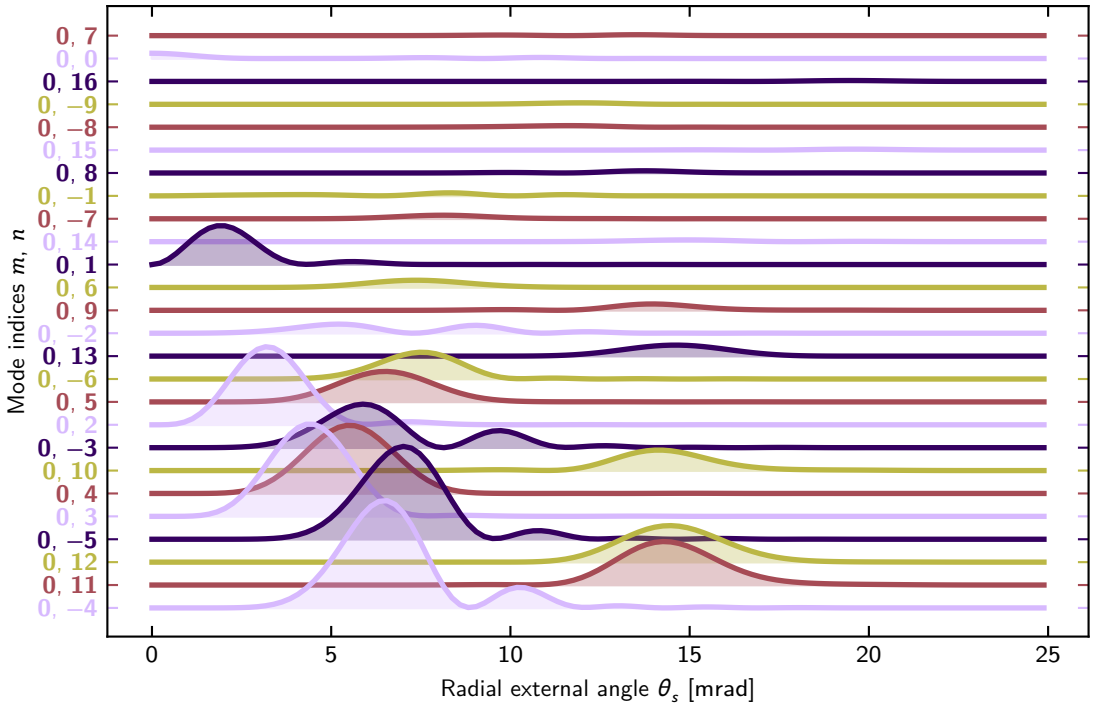

Figure 5.11: Ridgeline plot of the modulus squared of the first 26 radial mode functions weighted with the corresponding normalized eigenvalues $[\bar{\Lambda}_{mn}|u_{mn}(q_s)|^2]$ of an SU(1,1) interferometer pumped at high gain $G_{\text{exp}} = 4$ with $l_p = 7$, $m_p = 0$ sorted according to the eigenvalues in ascending order from bottom to top. Compared to Fig. 5.10, which shows the modulus squared of the normalized mode functions and the corresponding eigenvalues, this figure portrays the relative contribution of each mode to the intensity distribution more correctly.

behavior under the *double-Gaussian approximation* for the TPA (see also Miatto *et al.* [42] for details). In short, the behavior can be, at low gain, understood as resulting from the interference of Bessel function terms.

5.4. Angular Displacement Measurements

5.4.1. SU(1,1) Interferometers for Angular Displacement Measurements

In Sec. 5.3.2, a non-compensated SU(1,1) interferometer was used to modify the PDC state generated when the PDC sections of the interferometer are pumped with a Laguerre-Gaussian beam carrying OAM. Another application for beams carrying OAM is in the detection of angular displacements, that is, the detection of rotations of objects about one of their axes. This idea is based on previous works, in which quantum states of light and classical interferometers were used for angular displacement measurements, resulting in a reduction of the measurement uncertainty by a factor of $1/n$, where n is the OAM of the light states probing the rotation [48, 54, 55, 152]. This is analogous to the development from classical interferometers using coherent states to classical interferometer setups utilizing quantum light and further to SU(1,1) interferometers in the case of the phase sensitivity

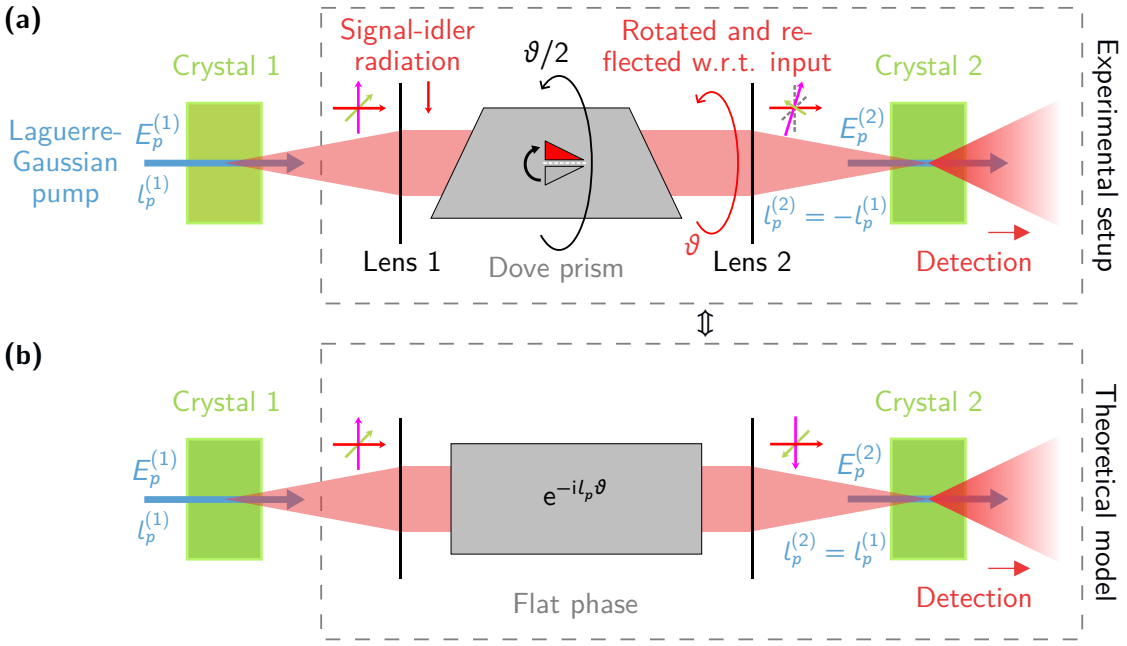

Figure 5.12: **(a)** Sketch of the experimental setup for performing angular displacement measurements using a Dove prism placed between the two lenses of a diffraction-compensated SU(1,1) interferometer in transmission geometry [compare Fig. 3.2(c)]. The prism flips the image upside down as indicated by the symbol placed over it, and, if rotated by an angle $\vartheta/2$, rotates the image by ϑ. Additionally, the 4f-system causes a central inversion (point reflection) if the input image about the origin (the point in which each transverse plane intersects with the z-axis). In this setup, the second crystal is pumped with a Laguerre-Gaussian pump of opposite helicity as the first crystal since the Dove prism also flips the helicity of the OAM modes of the signal-idler radiation [153]. **(b)** Sketch of the theoretical model equivalent to the experimental setup shown in **(a)**, in which the Dove prism is replaced by a flat phase $e^{-il_p\vartheta}$ added to the signal-idler radiation, accounting for the rotation of the beam due to the prism and the helicity of the pump beam for the second crystal is the same as for the first crystal. In both **(a)** and **(b)**, the green, magenta and red arrows at the input of the 4f-system (in front of Lens 1) represent the x-, y- and z-axis, respectively. For the setup as shown in **(a)**, after Lens 2 and the Dove prism, the x- and y-axis are shown rotated about the z-axis from their original positions (indicated by the dashed lines) and both mirrored about the y-axis and the origin. The rotation and former mirroring represent the actions of the Dove prism, while the latter mirroring is due to the 4f-system. For the theoretical setup as shown in **(b)**, where the Dove prism has been replaced by a flat phase, only the inversion due to the 4f-system is shown since the rotation induced by the Dove prism is replaced by a phase shift by $e^{-il_p\vartheta}$. Adapted from Ref. [2].

as touched on in Sec. 3.1.

Figure 5.12(a) shows the proposed experimental setup for performing these *angular displacement measurements*. A *Dove prism* is placed inside the signal-idler radiation between the two lenses of a diffraction-compensated SU(1,1) interferometer in transmission geometry [4f-setup, see Fig. 3.2(c)] and rotated about its longitudinal axis by an angle[13] $\vartheta/2$.

[13]To avoid confusion with the external angle $\theta_{(s)}$ over which the intensity profiles are shown (for example in Sec. 5.3.1, see Fig. 5.4), ϑ is used here for the rotation angle instead of θ, which was used in Ref. [2].

This transforms the signal-idler radiation in two significant ways, as described in González *et al.* [153]: First, the Dove prism flips the image of the input radiation about the plane which contains its longitudinal axis and lies parallel to its base and top area, meaning that input OAM modes with an azimuthal dependence $\mathrm{e}^{-\mathrm{i}n\phi}$ get transformed into OAM modes with the dependence $\mathrm{e}^{\mathrm{i}n\phi}$. Second, the prism applies a rotation to the field given by twice its rotation angle. For the OAM mode $\mathrm{e}^{-\mathrm{i}n\phi}$, this phase term is of the form $\mathrm{e}^{\mathrm{i}n\vartheta}$. Overall, the transformation relation for the aforementioned OAM mode is therefore of the form $\mathrm{e}^{-\mathrm{i}n\phi} \to \mathrm{e}^{\mathrm{i}n(\phi+\vartheta)}$ [55]. In addition to the Dove prism, the 4f-system also transforms the incoming OAM modes: As seen in Sec. B.2, which illustrates the properties of the 4f-system and in particular in Eq. (B.27), the 4f-system performs a central inversion of its input image, which for the transverse wave-vector components means[14] $\boldsymbol{q} \to -\boldsymbol{q}$. In the polar coordinates of the transverse plane, this transformation reads

$$\begin{cases} |\boldsymbol{q}| \to |\boldsymbol{q}| \\ \phi \to \phi + \pi\,. \end{cases} \tag{5.62}$$

For an OAM mode, this means that the azimuthal dependence changes as $\mathrm{e}^{\mathrm{i}n\phi} \to (-1)^n\,\mathrm{e}^{\mathrm{i}n\phi}$. Thus, the 4f-system affects even and odd OAM modes differently, unlike the Dove prism.

Before constructing the TPA for the SU(1,1) interferometer with the Dove prism for the angular displacement measurements, it is helpful to consider several symmetries of the TPA described by Eqs. (5.17) and (5.18) under the exchange of the sign of the pump OAM index l_p. For this, superscripts $^{[l_p]}$ and $^{[-l_p]}$ will be added to the relevant quantities to indicate the sign change of l_p. With this notation defined, it is directly clear from Eq. (5.18) that for the function R, the angle difference axis is inverted if the sign of l_p is changed[15]:

$$R^{[l_p]}(q_s, q_i, \phi_s - \phi_i) = R^{[-l_p]}(q_s, q_i, \phi_i - \phi_s). \tag{5.63}$$

It is well known that for a Fourier decomposition, an inversion of the angle axis is equivalent to a sign change in the index of the Fourier coefficients. Here, this leads to the following symmetry relation for the $\chi_n(q_s, q_i)$ when applying Eq. (5.63) to Eq. (5.20):

$$\chi_n^{[l_p]}(q_s, q_i) = \chi_{-n}^{[-l_p]}(q_s, q_i). \tag{5.64}$$

Since the Schmidt decomposition for the separation of q_s and q_i does not affect the OAM index n of the modes, the same property also applies to the Schmidt modes and eigenvalues:

$$\lambda_{mn}^{[l_p]} = \lambda_{m,-n}^{[-l_p]}\,, \tag{5.65a}$$

$$u_{mn}^{[l_p]} = u_{m,-n}^{[-l_p]}\,, \tag{5.65b}$$

$$v_{mn}^{[l_p]} = v_{m,-n}^{[-l_p]}\,. \tag{5.65c}$$

[14] This effect has been neglected in Ref. [2], since, as will be seen further below, it only adds a constant phase shift to the fields which can be neglected.

[15] Note that Eq. (5.63) can optionally also be written with q_s and q_i swapped on the right-hand side. This is due to fact that the signal and idler photons are indistinguishable. Overall, this implies the change $\boldsymbol{q}_s \leftrightarrow \boldsymbol{q}_i$ when the OAM index of the pump is swapped.

These symmetry relations are the reason for why the restriction to the case $l_p \geq 0$ is sufficient for the analysis of the Schmidt mode structure of the single crystal and the SU(1,1) interferometer with an air gap between the two crystals, as done in Sec. 5.3. Under the exchange $l_p \to -l_p$, the eigenvalue distributions and the Schmidt mode only change in the sense that $n \to -n$.

In order to describe the interferometer mathematically, an approach similar to the splitting of the interferometer into the first and the second crystal as described in Secs. 3.2 and 4.2.2 can be used. To this end, two TPA functions describing the first and second crystal separately must be found, which can then, after a Schmidt decomposition, be combined using the transfer functions as written in Eqs. (5.38) in terms of the Schmidt modes and high-gain eigenvalues and the equivalent of the connection relations written in Eqs. (3.19) for the full three-dimensional system. Similar to the description provided for the integro-differential equation approach throughout Secs. 3.2, 3.3 and 3.5.1, the TPA of the second crystal will include the modifications brought to the signal-idler radiation by the 4f-system and the Dove prism between the two lenses. Following the above discussions, this TPA can be written in the following form, under the assumption that the OAM index of the pump is[16] $-l_p$ [compare Eq. (5.21)]:

$$F^{(2,D),[-l_p]}(q_s, q_i, \phi_s, \phi_i) = \frac{(-1)^{l_p}}{2\pi} \sum_n \chi_n^{(2),[-l_p]}(q_s, q_i)\, \mathrm{e}^{\mathrm{i}n\phi_s} \mathrm{e}^{\mathrm{i}n\vartheta} \mathrm{e}^{\mathrm{i}(-l_p-n)\phi_i} \mathrm{e}^{\mathrm{i}(-l_p-n)\vartheta}\,. \tag{5.66}$$

Here, the superscript $^{(2,D)}$ has been added to the TPA to indicate that it describes the second crystal including the Dove prism (and the 4f-system). The signs of the exponents have been modified and an additional phase $\mathrm{e}^{\mathrm{i}n\vartheta}\mathrm{e}^{\mathrm{i}(-l_p-n)\vartheta}$ has been added to account for the modifications of the field resulting from the Dove prism, as described above. To account for the 4f-system, an additional factor $(-1)^{n+(l_p-n)} = (-1)^{l_p}$ has been added. Since neither the 4f-system nor the Dove prism affect the radial Schmidt modes or the Schmidt eigenvalues, the superscript $^{(2)}$ was added to the Fourier coefficients χ_n to indicate that they are the same for the second crystal regardless of whether the Dove prism is placed inside the interferometer or not.

After simplifying the exponential terms containing ϑ, flipping the sign of the summation index ($n \to -n$), and using Eq. (5.64), the TPA reduces to

$$F^{(2,D),[-l_p]}(q_s, q_i, \phi_s, \phi_i) = (-1)^{l_p} \frac{\mathrm{e}^{-\mathrm{i}l_p\vartheta}}{2\pi} \sum_n \chi_n^{(2),[l_p]}(q_s, q_i)\, \mathrm{e}^{-\mathrm{i}n\phi_s} \mathrm{e}^{-\mathrm{i}(l_p-n)\phi_i}\,, \tag{5.67}$$

where the right-hand side can be identified as the TPA of the second crystal without the Dove prism multiplied by a phase factor, so that

$$F^{(2,D),[-l_p]}(\boldsymbol{q}_s, \boldsymbol{q}_i) = (-1)^{l_p}\, \mathrm{e}^{-\mathrm{i}l_p\vartheta} F^{(2),[l_p]}(\boldsymbol{q}_s, \boldsymbol{q}_i). \tag{5.68}$$

[16] Strictly speaking, l_p in Eq. (5.66) also requires indices $^{(2)}$ and $^{(2,D)}$. However, these indices are dropped here for readability. Clearly, $l_p^{(2)} = l_p^{(2,D)}$. This notation is used in Fig. 5.12 for clarity.

This connection is analogous to Eq. (3.41a), except for the fact that it involves the *TPAs* of the second crystal with and without the additional optical elements included, instead of the transfer function β. This is not surprising, since in the low-gain regime, the TPA provides an approximation for the transfer function β, as for example seen in Sec. A.5 and throughout the rest of this section.

Furthermore, the connection expresses the equivalence of the systems depicted in Fig. 5.12(a) [left-hand side of Eq. (5.69)] and Fig. 5.12(b) [right-hand side of Eq. (5.69)]: The effect of the Dove prism on the signal-idler radiation can be understood as adding a flat phase $\mathrm{e}^{-\mathrm{i}l_p\vartheta}$ while also flipping the helicity of the pump beam. Additionally, the 4f-system contributes a phase $(-1)^{l_p}$. Equivalently, it is therefore possible to instead only add a flat phase to the signal-idler radiation (or, equivalently, twice the phase to the pump beam) while pumping the second crystal with a pump beam of the opposite helicity and accounting for the phase shift $(-1)^{l_p}$. Since this phase shift is constant with respect to the wave-vectors, it may be added to ϑ: $(-1)^{l_p}\,\mathrm{e}^{-\mathrm{i}l_p\vartheta} = \mathrm{e}^{-\mathrm{i}l_p(\vartheta+\pi)}$. In the following, this constant phase shift by π will be neglected, since it only shifts the variable[17] ϑ. Furthermore, this phase shift would lead to a qualitative difference in the behavior of even and odd l_p, which would make the following investigations more cumbersome. As such, Eq. (5.68) is reduced to

$$F^{(2,D),[-l_p]}(\boldsymbol{q}_s,\boldsymbol{q}_i) = \mathrm{e}^{-\mathrm{i}l_p\vartheta}F^{(2),[l_p]}(\boldsymbol{q}_s,\boldsymbol{q}_i). \tag{5.69}$$

In experimental setups, this additional offset by π can for example also be achieved by applying a phase shift to the pump beam. Conversely, in a setup where both crystals are pumped with two separate pump beams (compare Fig. 5.12), their relative phases must be stabilized and this can additionally introduce phase shifts. Overall, any relative flat-phase shift by δ is equivalent to a shift in the rotation angle ϑ via $\mathrm{e}^{-\mathrm{i}\delta} = \mathrm{e}^{-\mathrm{i}l_p(\delta/l_p)}$, meaning that the rotation angle is shifted by δ/l_p. Thus, these constant phase offset have no direct physical meaning that affects the metrological applications discussed in the rest of this section.

Next, the diffraction compensation of the 4f-system must be included in the description of the system. The function g_z describing the second crystal can be obtained from the phase-matching function for the second crystal of a diffraction-compensated interferometer as written in Eq. (3.37):

$$g_z^{(2)}(\boldsymbol{q}_s,\boldsymbol{q}_i) = \int_{L_1}^{2L_1}\mathrm{d}z\,\mathrm{e}^{-\mathrm{i}\Delta k(\boldsymbol{q}_s,\boldsymbol{q}_i)[z-2L_1]} \tag{5.70a}$$

$$= \int_{0}^{L_1}\mathrm{d}z\,\mathrm{e}^{\mathrm{i}\Delta k(\boldsymbol{q}_s,\boldsymbol{q}_i)z} \tag{5.70b}$$

$$= g_z^{(1)}(\boldsymbol{q}_s,\boldsymbol{q}_i), \tag{5.70c}$$

compare Eq. (5.45). Thus, the TPA for the second crystal without the Dove prism and the

[17] Equivalently, ϑ can simply be redefined to absorb the constant π: $\vartheta+\pi\to\vartheta$.

central inversion brought about by the 4f-system can be expressed in terms of the TPA of the first crystal as

$$F^{(2),[l_p]}(\boldsymbol{q}_s, \boldsymbol{q}_i) = F^{(1),[l_p]}(\boldsymbol{q}_s, \boldsymbol{q}_i). \tag{5.71}$$

Combining Eqs. (5.69) and (5.71) yields a connection to the TPA of the second crystal including the Dove prism:

$$F^{(2,D),[-l_p]}(\boldsymbol{q}_s, \boldsymbol{q}_i) = F^{(1),[l_p]}(\boldsymbol{q}_s, \boldsymbol{q}_i)\, \mathrm{e}^{-\mathrm{i}l_p\vartheta}. \tag{5.72}$$

This relationship is similar to the connection of the transfer function β for the integro-differential equation approach as given by Eq. (3.41a) and Eq. (3.43a).

This implies a connection between the eigenvalues and Schmidt modes of the first crystal and the second crystal including the Dove prism:

$$u^{(1)}_{mn}(q)\, \mathrm{e}^{-\mathrm{i}\frac{l_p}{2}\vartheta} = u^{(2,D)}_{mn}(q), \tag{5.73a}$$

$$v^{(1)}_{mn}(q)\, \mathrm{e}^{-\mathrm{i}\frac{l_p}{2}\vartheta} = v^{(2,D)}_{mn}(q), \tag{5.73b}$$

$$\lambda^{(1)}_{mn} = \lambda^{(2,D)}_{mn}. \tag{5.73c}$$

Thus, as was the case in Sec. 3.5.1, the quantities related to the second crystal can be expressed fully in terms of the quantities of the first crystal due to the symmetry introduced by the focusing elements.

The *angular displacement measurement uncertainty* for the angle ϑ is defined analogously to the phase sensitivity in Eq. (3.1) via the error propagation relation [2, 54, 55]:

$$\Delta\vartheta = \frac{\Delta N_{\mathrm{tot}}}{\left|\frac{\mathrm{d}\langle\hat{N}_{\mathrm{tot}}\rangle}{\mathrm{d}\vartheta}\right|}, \tag{5.74}$$

with ΔN_{tot} as defined in Eq. (3.2). As was the case in Sec. 3.1, the uncertainty will therefore be determined for the integral intensity. As was touched on in Sec. 3.1, the quantity defined via Eqs. (3.1) and (5.74) is a standard deviation representing an *uncertainty* of a measurable quantity. However, in the context of phase measurements, this quantity is often referred to as the *phase sensitivity*, which would imply that its numerical value is to be maximized, while in actuality, the goal of improving the phase sensitivity implies a reduction of its numerical value, compare Sec. 3.5.4. As noted in Ref. [2], in the context of angular displacement measurements, this quantity is instead more correctly referred to as the angular displacement *uncertainty*. As such, this term will be used in the following to keep consistency with the literature. Similar to the phase sensitivity, the angular displacement measurement uncertainty is usually normalized with respect to the standard quantum limit. Thus, Eqs. (3.3) and (3.4) apply here directly as they are written in Sec. 3.1 and the normalized angular phase uncertainty f defined via Eq. (3.4) will be mostly used in the following. It should be noted that the integral intensity operator here is given by

$$\hat{N}_{\mathrm{tot}} = 2\int \mathrm{d}^2q\, \hat{N}_s(\boldsymbol{q}), \tag{5.75}$$

where the factor 2 arises due to the fact that the signal and idler photons are indistinguishable, compare Eq. (3.25).

Using the relations derived above, there are two possible ways of setting up a theoretical description for the SU(1,1) interferometer, which, as will be seen below, are not equivalent and lead to differing results for the normalized angular phase uncertainty at increasing experimental gain.

Transfer-Function (TF) Approach. As already mentioned above, by using the two-dimensional form of the connection relations connecting the transfer functions of each crystal of the interferometer to the transfer functions of the entire interferometer, it is possible to describe the angular displacement measurement uncertainty using the formalism developed in Secs. 3.2, 3.3 and 3.5.1. These connection relations read, in accordance with Eqs. (3.19), [2]

$$\beta^{(\mathrm{SU})}(\boldsymbol{q},\boldsymbol{q}') = \int \mathrm{d}^2\bar{q}\,\tilde{\eta}^{(2,D)}(\boldsymbol{q},\bar{\boldsymbol{q}})\,\beta^{(1)}(\bar{\boldsymbol{q}},\boldsymbol{q}') + \int \mathrm{d}^2\bar{q}\,\beta^{(2,D)}(\boldsymbol{q},\bar{\boldsymbol{q}})\left[\tilde{\eta}^{(1)}(\bar{\boldsymbol{q}},\boldsymbol{q}')\right]^*. \tag{5.76a}$$

$$\tilde{\eta}^{(\mathrm{SU})}(\boldsymbol{q},\boldsymbol{q}') = \int \mathrm{d}^2\bar{q}\,\tilde{\eta}^{(2,D)}(\boldsymbol{q},\bar{\boldsymbol{q}})\,\tilde{\eta}^{(1)}(\bar{\boldsymbol{q}},\boldsymbol{q}') + \int \mathrm{d}^2\bar{q}\,\beta^{(2,D)}(\boldsymbol{q},\bar{\boldsymbol{q}})\left[\beta^{(1)}(\bar{\boldsymbol{q}},\boldsymbol{q}')\right]^*, \tag{5.76b}$$

where the subscripts as introduced above have been used to label the transfer functions of the first crystal, the second crystal and the entire interferometer. The transfer functions are constructed from the Schmidt decomposition as detailed in Eqs. (5.27), (5.38) and (5.39) and, due to Eqs. (5.73), they are connected via [2]

$$\beta^{(2,D)}(\boldsymbol{q},\boldsymbol{q}') = \beta^{(1)}(\boldsymbol{q},\boldsymbol{q}')\,\mathrm{e}^{-\mathrm{i}l_p\vartheta}. \tag{5.77a}$$

$$\tilde{\eta}^{(2,D)}(\boldsymbol{q},\boldsymbol{q}') = \tilde{\eta}^{(1)}(\boldsymbol{q},\boldsymbol{q}'), \tag{5.77b}$$

which is a variation of the relations discovered for the diffraction compensated SU(1,1) interferometer described by the integro-differential equation formalism, see Eqs. (3.43). The main difference to the case here is that the modes v_{mn} and u_{mn} (or $\mathcal{V}_{mn}$ and $\mathcal{U}_{mn}$) do not originally have the meaning of the input and output modes of the PDC section, as is the case in the integro-differential equation formalism. Instead, they are associated with the signal and idler Schmidt mode operators.

The transfer functions for the full interferometer in Eqs. (5.76) can be evaluated by first expressing the transfer functions of the second crystal in terms of those of the first crystal using Eqs. (5.77), followed by plugging Eqs. (5.38) (as applying to the first crystal) into the resulting expression and using

$$\mathcal{U}_{mn}(q) = \mathcal{V}_{m,l_p-n}(q), \tag{5.78a}$$

$$\mathcal{V}_{mn}(q) = \mathcal{U}_{m,l_p-n}(q), \tag{5.78b}$$

$$\Lambda_{mn} = \Lambda_{m,l_p-n} \tag{5.78c}$$

(for the quantities of the first crystal), which follow from Eqs. (5.27), (5.28), (5.30) and (5.40). Ultimately, it can be shown that the transfer functions for the full interferometer take the

following form:

$$\beta^{(\mathrm{SU})}(\boldsymbol{q},\boldsymbol{q}') = \sum_{m,n} \sqrt{\Lambda_{mn}^{(\mathrm{SU})}}\, \mathcal{U}_{mn}^{(\mathrm{SU})}(\boldsymbol{q})\, \mathcal{V}_{mn}^{(\mathrm{SU})}(\boldsymbol{q}'), \tag{5.79a}$$

$$\tilde{\eta}^{(\mathrm{SU})}(\boldsymbol{q},\boldsymbol{q}') = \sum_{m,n} \sqrt{\tilde{\Lambda}_{mn}^{(\mathrm{SU})}}\, \mathcal{U}_{mn}^{(\mathrm{SU})}(\boldsymbol{q}) \left[\mathcal{V}_{m,l_p-n}^{(\mathrm{SU})}(\boldsymbol{q}')\right]^*, \tag{5.79b}$$

where $\Lambda_{mn}^{(\mathrm{SU})}$ and $\tilde{\Lambda}_{mn}^{(\mathrm{SU})}$ are connected via Eq. (5.40) and where

$$\Lambda_{mn}^{(\mathrm{SU})} = 4\Lambda_{mn}^{(1)}\left(\Lambda_{mn}^{(1)}+1\right)\cos^2\left(\frac{l_p}{2}\vartheta\right), \tag{5.79c}$$

$$\mathcal{U}_{mn}^{(\mathrm{SU})}(\boldsymbol{q}) = \mathcal{U}_{mn}^{(1)}(\boldsymbol{q})\, \mathrm{e}^{\frac{\mathrm{i}}{2}(\mu+\zeta_{mn})}, \tag{5.79d}$$

$$\mathcal{V}_{mn}^{(\mathrm{SU})}(\boldsymbol{q}) = \mathcal{V}_{mn}^{(1)}(\boldsymbol{q})\, \mathrm{e}^{\frac{\mathrm{i}}{2}(\mu-\zeta_{mn})}, \tag{5.79e}$$

and

$$\mu = \arg\left(1+\mathrm{e}^{-\mathrm{i}l_p\vartheta}\right), \tag{5.79f}$$

$$\zeta_{mn} = \arg\left[1+\Lambda_{mn}^{(1)}\left(1+\mathrm{e}^{-\mathrm{i}l_p\vartheta}\right)\right]. \tag{5.79g}$$

Note that $\zeta_{mn} = \zeta_{m,l_p-n}$. Unlike in Eqs. (5.38), the transfer functions can now no longer be expressed just in terms of $\mathcal{U}_{mn}^{(\mathrm{SU})}$ due to the presence of the generally non-vanishing phase ζ_{mn}. Furthermore, in general, the symmetry relations in Eqs. (5.78a) and (5.78b) no longer apply to the modes $\mathcal{U}_{mn}^{(\mathrm{SU})}$ and $\mathcal{V}_{mn}^{(\mathrm{SU})}$. This is not unexpected since the modes in the transfer function approach, which is based on the integro-differential equation formalism (see Sec. 3.2), have different physical meanings than the modes obtained from the Schmidt decomposition which are then used to construct the transfer functions. In the integro-differential equation formalism, the two sets of modes are the input and output Schmidt modes associated with the input and output Schmidt operators of the PDC system, respectively. Here however, as follows from the description in Secs. 5.2.2 and 5.2.3, the input and output Schmidt modes can be described by a single set of modes $\{\mathcal{U}_{mn}\}_{mn}$, see Eqs. (5.38). The difference in $\mathcal{U}_{mn}$ and $\mathcal{V}_{mn}$ is that they describe the signal and idler modes, not the input and output modes. Ultimately, applying the connection relations does therefore not guarantee that the resulting transfer functions can again be written solely in terms of $\{\mathcal{U}_{mn}\}_{mn}$. Nevertheless, Eqs. (5.79) still have the form of the joint Schmidt decomposition for the full three-dimensional system, compare Eqs. (A.77) [with $\mathcal{U}_{mn}^{(\mathrm{SU})} \equiv U_{mn}$ and $\mathcal{V}_{m,l_p-n}^{(\mathrm{SU})} \equiv \Psi_{mn}$, compare Eqs. (A.75)].

Equations (5.79) are analogous to Eqs. (4.47), which provide the analytical expressions for the joint Schmidt decomposition of a perfectly compensated SU(1,1) interferometer in the integro-differential equation approach. Using the transfer functions for the entire interferometer, it is immediately possible to follow Sec. 3.5.1 in order to obtain an expression for the normalized angular displacement uncertainty [2]:

$$\Delta\vartheta_{\mathrm{TF}} = \frac{\sqrt{2}}{2}\frac{\sqrt{\mathcal{A}+4\mathcal{B}\cos^2\left(\frac{l_p}{2}\vartheta\right)}}{\mathcal{A}|l_p|\left|\sin\left(\frac{l_p}{2}\vartheta\right)\right|}, \tag{5.80}$$

with $\mathcal{A}, \mathcal{B} > 0$ as defined in Eqs. (3.45c) and (3.45d), respectively. In Eq. (5.80), the subscript $_{\mathrm{TF}}$ has been added to distinguishing the angular displacement measurement uncertainty from the one obtained using the Schmidt mode theory approach described below. This expression is very similar in structure to Eq. (3.46), with the major differences being the prefactor $\sqrt{2}/2$ due to the indistinguishability of the photons [in Eq. (3.46) the photons were assumed to be distinguishable] and the appearance of l_p.

Schmidt Mode Theory (SMT) Approach. Alternatively to connecting the two crystals of the SU(1,1) interferometer via the connection relations for the transfer functions, it is possible to construct the TPA of the entire interferometer via

$$F^{(\mathrm{SU})}(\boldsymbol{q}_s, \boldsymbol{q}_i) = F^{(1)}(\boldsymbol{q}_s, \boldsymbol{q}_i) + F^{(2,D)}(\boldsymbol{q}_s, \boldsymbol{q}_i), \tag{5.81}$$

which follows directly by extending the integral over the z-axis in the function g_z over both crystals and then splitting it into one integral for the first and one for the second crystal, both of which use different parameters, for example different pump OAM indices. This is analogous to how the TPA was constructed for the SU(1,1) interferometer with an air gap between the crystals, compare Eq. (5.56). Using the connection between the TPA of the first crystal and the second crystal including the Dove prism [Eq. (5.72)], this means

$$F^{(\mathrm{SU})}(\boldsymbol{q}_s, \boldsymbol{q}_i) = 2F^{(1)}(\boldsymbol{q}_s, \boldsymbol{q}_i) \cos\left(\frac{l_p}{2}\vartheta\right) \mathrm{e}^{-\mathrm{i}\frac{l_p}{2}\vartheta}. \tag{5.82}$$

By comparing this with the decompositions described by Eq. (5.24), it follows that

$$\lambda_{mn}^{(\mathrm{SU})} = 4\lambda_{mn}^{(1)} \cos^2\left(\frac{l_p}{2}\vartheta\right), \tag{5.83}$$

which implies that the high-gain eigenvalues for the entire interferometer are given by [2]

$$\Lambda_{mn}^{(\mathrm{SU})} = \sinh^2\left[2G\sqrt{\lambda_{mn}}\,\cos\left(\frac{l_p}{2}\vartheta\right)\right]. \tag{5.84}$$

Clearly, this expression is generally different from the one obtained using the transfer function approach, compare Eq. (5.79c). However, for low gain ($G \ll 1$), it follows from both expressions [Eqs. (5.79c) and (5.84)] that

$$\Lambda_{mn}^{(\mathrm{SU})} \approx 4G^2\lambda_{mn} \cos^2\left(\frac{l_p}{2}\vartheta\right). \tag{5.85}$$

Note that this uses $\Lambda_{mn}^{(\mathrm{SU})} \ll 1$ in Eq. (5.79c), which implies low gain. Evidently, both approaches will generally only coincide for low gain. Evaluating the expressions leading to the normalized angular displacement uncertainty by following Sec. 3.5.1 results in

$$\Delta\vartheta_{\mathrm{SMT}} = \frac{\sqrt{2}}{2} \frac{1}{G|l_p|\left|\sin\left(\frac{l_p}{2}\vartheta\right)\right|} \frac{\sqrt{\sum_{m,n} \sinh^2\left[4G\sqrt{\lambda_{mn}}\,\cos\left(\frac{l_p}{2}\vartheta\right)\right]}}{\sum_{m,n}\sqrt{\lambda_{mn}}\,\sinh\left[4G\sqrt{\lambda_{mn}}\,\left|\cos\left(\frac{l_p}{2}\vartheta\right)\right|\right]}. \tag{5.86}$$

This expression clearly differs from Eq. (5.80) and is more complex. At low gain, using $\sinh(x) \approx x$ for small $x \ll 1$, the third fraction in Eq. (5.86) can be approximated as

$$\frac{\sqrt{\sum_{m,n} \sinh^2\left[4G\sqrt{\lambda_{mn}}\,\cos\left(\frac{l_p}{2}\vartheta\right)\right]}}{\sum_{m,n}\sqrt{\lambda_{mn}}\,\sinh\left[4G\sqrt{\lambda_{mn}}\,\left|\cos\left(\frac{l_p}{2}\vartheta\right)\right|\right]} \approx 1, \tag{5.87}$$

so that

$$\Delta\vartheta_{G\ll 1} = \frac{\sqrt{2}}{2}\frac{1}{G|l_p|\left|\sin\left(\frac{l_p}{2}\vartheta\right)\right|}. \tag{5.88}$$

The same expression can be obtained for the transfer function approach by approximating the sinh-terms appearing in the eigenvalues in $\mathcal{A}$ and $\mathcal{B}$ in Eq. (5.80) (where then $\mathcal{A} \approx G^2$ and $\mathcal{B} \approx 0$). Thus, $\Delta\vartheta$ and, following directly from that, also the normalized angular displacement uncertainty f, coincide for both approaches at low gain.

As a sidenote, it should be mentioned that a similar expression to the low gain approximation for $\Delta\vartheta$ in Eq. (5.88) can be obtained for the phase sensitivity $\Delta\phi$ as discussed throughout Chapter 3. At low gain, Eq. (3.46) then becomes

$$\Delta\phi_{G\ll 1} = \frac{1}{2}\frac{1}{G\left|\sin\left(\frac{\phi}{2}\right)\right|}. \tag{5.89}$$

Remarkably, this expression is independent of any properties of the pump, except for properties that may affect the normalization constant C [since $1/C$ appears as a factor of G, compare Eqs. (5.14) and (5.34)]. As such, it is clear that the phase sensitivity f cannot be improved by using Laguerre-Gaussian pump pulses. Ultimately, in general, the structure of the pump beam has no direct influence on the phase sensitivity f at low gain.

5.4.2. Results

In the previous section (Sec. 5.4.1), two approaches were derived to obtain the angular displacement uncertainty for an SU(1,1) interferometer pumped with Laguerre-Gaussian beams. Both approaches result in formulas which only coincide in the low-gain regime. This is also illustrated in Fig. 5.13(a) and Figs. 5.13(b)–5.13(e), which show the normalized angular displacement uncertainty for both approaches at low gain ($G_{\text{exp}} = 0.01$) and medium gain ($G_{\text{exp}} = 2$), respectively, for various combinations of the pump radial and OAM index. For the results presented in this section, only a single fitting constant A connecting the theoretical and experimental gain will be used, which is the average of the value for the low-gain and high-gain regime (compare Sec. 5.3.1). This will greatly simplify the computation of later results, which are in dependence on wide ranges of the experimental gain and is justified by the fact that the experimental measurement error determining A would be larger than the error introduced by averaging the fitting constants [2, 104].

Evidently, both approaches show a periodic behavior for the normalized angular dis-

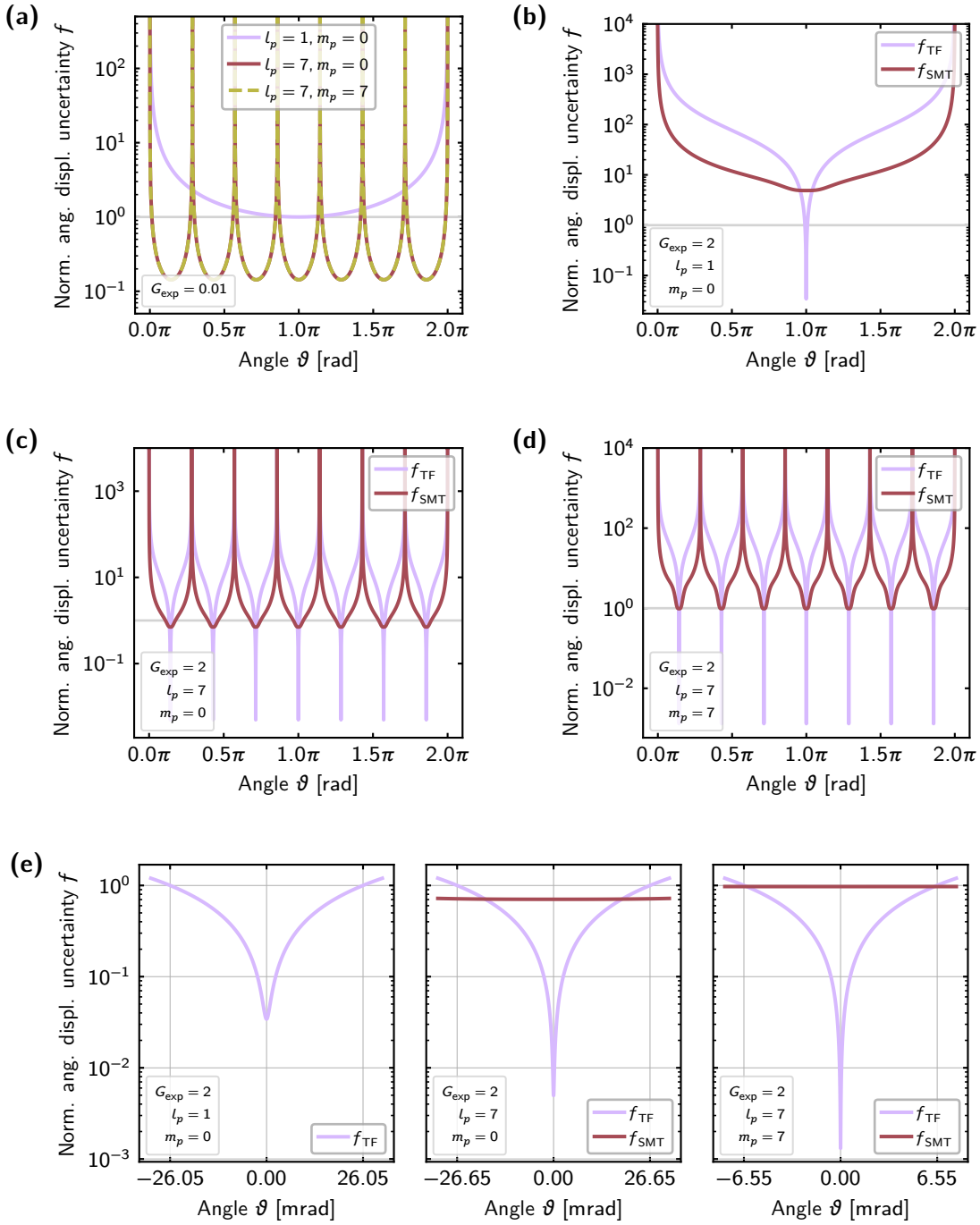

Figure 5.13: Plots of the normalized angular displacement uncertainty f in dependence on the rotation angle of the fields ϑ for **(a)** low gain $G_{exp} = 0.01$ and [**(b)**–**(e)**] medium gain $G_{exp} = 2$ for the transfer function and Schmidt mode theory approaches as indicated in the plots. Note that for low gain [**(a)**] both approaches coincide as discussed in Sec. 5.4.1. The thin horizontal gray lines in **(a)**–**(d)** indicate the standard quantum limit, meaning that all angular regions where f lies below the line display supersensitivity. Figure **(e)** shows zoomed cut-outs of **(b)**–**(d)** highlighting the behavior in the very narrow supersensitivity regions. Adapted from Ref. [2] using the dataset associated with the publication, see Ref. [151].

placement uncertainty. Since the standard quantum limit does not depend on ϑ, most of the behavior of f can be understood by analyzing the (not normalized) angular displacement uncertainty $\Delta\vartheta$. For both approaches it is immediately obvious from their respective expressions for $\Delta\vartheta$ [Eqs. (5.80) and (5.86)] that f has periodic behavior with period length $2\pi/|l_p|$.

Physically, this can be explained as follows [2]: Excluding the pump beam and the Dove prism, the two crystals of the interferometer are *continuously* rotationally symmetric due to their large (infinite) transverse size. Introducing the Dove prism does not break this symmetry, as long as the signal and idler fields themselves are rotationally symmetric, since it only rotates and mirrors the two fields. For $l_p = 0$ the pump is also rotationally symmetric (Gaussian) and therefore, the entire system has *continuous* rotational symmetry about the z-axis. However, for $l_p \neq 0$, the pump only has an l_p-fold discrete rotational symmetry due to its $\mathrm{e}^{-\mathrm{i}l_p\varphi}$ phase profile (compare also Fig. 5.1 for plots of the phase profiles of the functions of the form $\mathrm{e}^{-\mathrm{i}l\phi}$). This symmetry of the pump beam is transferred to the signal and idler radiation generated by the first crystal. This can be seen from the fact that in Eq. (5.24), for $l_p = 0$, the TPA does only depend on the azimuthal angle difference $\phi_s - \phi_i$ but not on the absolute values of these angles [2, 11], while for $l_p \neq 0$, the additional term $\mathrm{e}^{-\mathrm{i}l_p\phi_i}$ introduces the l_p-fold discrete rotational symmetry. The Dove prism mirrors the radiation field, inverting the helicity of each OAM component, which is accounted for by pumping the second crystal with the Laguerre-Gaussian mode of the opposite helicity. The second crystal itself also has an l_p-fold rotational symmetry due to the pump. Thus, a rotation of the radiation field by $2\pi/|l_p|$ maps the radiation field onto itself from the viewpoint of the second crystal, resulting in the period length of $2\pi/|l_p|$.

As $\vartheta \to 2\pi m/|l_p|$, for $m \in \mathbb{Z}$, the factor $1/|\sin(l_p\vartheta/2)|$ in both expression leads to a divergence of $\Delta\vartheta$. This is for the same reason as described above: A rotation of the signal-idler radiation field by $2\pi/|l_p|$ about the azimuthal axis is indistinguishable from no rotation being applied to the field. Thus, it is not possible to detect rotation angles of the Dove prism which lead to rotations of the fields which are integer multiples of $2\pi/|l_p|$. By the same argument, for a Gaussian pump ($l_p = 0$), no rotations of the Dove prism can be detected at all, since the system always has continuous rotational symmetry meaning that rotations of the Dove prism do not modify the signal and idler fields in a discernible (detectable) way. This leads to an undefined or infinitely large angular displacement measurement uncertainty.

Regarding the angular displacement uncertainty, Fig. 5.13(a) indicates that at low gain, where both approaches coincide, supersensitivity (uncertainties lower than those of the standard quantum limit, $f < 1$) can be reached as long as $l_p \neq 1$. The precise condition for the existence of an angular region over which $f < 1$ will be discussed below. At increasing gain, see Figs. 5.13(b)–5.13(e), the transfer function approach shows a strongly pronounced minimum over a narrow angular range. Thus, the angular displacement uncertainty is reduced at high gain and for increasing l_p and m_p. The Schmidt mode theory approach does not predict such a pronounced minimum and generally shows a

much smaller reduction in the uncertainty. Clearly, for both cases, f and $\Delta\vartheta$ reach their global minimum at $\vartheta_{\mathrm{min},m} = \pi\,(2m+1)/l_p$, for $m \in \mathbb{Z}$. For the transfer function approach, this is immediately obvious from the fact that in Eq. (5.80), the numerator is maximized (globally) at $\vartheta_{\mathrm{min},m}$, while the denominator is maximized [globally; the same argument was applied in Sec. 3.5.1, leading to Eq. (3.51)]. For the Schmidt mode theory approach, it is more difficult to show that the minimum is reached at the same phase values $\vartheta_{\mathrm{min},m}$ due to the more complex structure of Eq. (5.86). As $\vartheta \to \vartheta_{\mathrm{min},m}$, the third fraction in Eq. (5.86) assumes the indeterminate form "0/0" due to the cos-terms. This limit can be evaluated by expanding the third fraction in Eq. (5.86) with $\left|\cos\left(\frac{l_p}{2}\vartheta\right)\right|^{-1}$ and using

$$\lim_{\vartheta\to\vartheta_{\mathrm{min},m}} \frac{\sinh\left[4G\sqrt{\lambda_{mn}}\,\left|\cos\left(\frac{l_p}{2}\vartheta\right)\right|\right]}{\left|\cos\left(\frac{l_p}{2}\vartheta\right)\right|} = 4G\sqrt{\lambda_{mn}}\,, \tag{5.90}$$

which follows from l'Hospital's rule [111], leading to

$$\lim_{\vartheta\to\vartheta_{\mathrm{min},m}} \frac{\sqrt{\sum_{m,n}\sinh^2\left[4G\sqrt{\lambda_{mn}}\cos\left(\frac{l_p}{2}\vartheta\right)\right]}}{\sum_{m,n}\sqrt{\lambda_{mn}}\,\sinh\left[4G\sqrt{\lambda_{mn}}\,\left|\cos\left(\frac{l_p}{2}\vartheta\right)\right|\right]} = 1\,. \tag{5.91}$$

Furthermore, by the Cauchy-Schwarz inequality [2],

$$\sum_{m,n}\sqrt{\lambda_{mn}}\,\sinh\left[4G\sqrt{\lambda_{mn}}\,\left|\cos\left(\frac{l_p}{2}\vartheta\right)\right|\right] \leq \sqrt{\sum_{m,n}\sinh^2\left[4G\sqrt{\lambda_{mn}}\,\cos\left(\frac{l_p}{2}\vartheta\right)\right]}\,, \tag{5.92}$$

since $\sum_{m,n}\lambda_{mn} = 1$. Combined, Eqs. (5.91) and (5.92) show that the global minimum of the third fraction in Eq. (5.86) over ϑ is 1. Since the fraction assumes this value at $\vartheta_{\mathrm{min},m}$ and the denominator of the second fraction in Eq. (5.86) reaches its global maximum at $\vartheta_{\mathrm{min},m}$, it is clear that $\Delta\vartheta_{\mathrm{SMT}}$ is also minimized at $\vartheta_{\mathrm{min},m}$.

At the global minimum, f_{TF} takes the value [2]

$$f_{\mathrm{TF,min}} = \frac{1}{|l_p|}\sqrt{\frac{\langle\hat{N}_{s,\mathrm{tot}}\rangle}{\mathcal{A}}}\,. \tag{5.93}$$

While the factor $1/|l_p|$ in this equation seemingly suggests that $f_{\mathrm{TF,min}}$ scales as $1/|l_p|$ with the OAM of the light interacting with the rotated object, as is also described in the literature [48, 54, 55, 152], it should be noted that for fixed gain, both $\langle\hat{N}_{s,\mathrm{tot}}\rangle$ and $\mathcal{A}$ still depend on l_p, meaning that the actual scaling of $f_{\mathrm{TF,min}}$ with $|l_p|$ is less obvious. Note that here, the signal and idler beams carry OAM which adds to l_p, as described in Sec. 5.4.1 above, although each individual photon may carry *arbitrary* OAM n or $l_p - n$, for $n \in \mathbb{Z}$. However, for fixed experimental gain G_{exp}, both the eigenvalue distributions and the fitting constant A vary as l_p and m_p are changed. The scaling behavior as $\propto 1/|l_p|$ is however recovered exactly in the low-gain limit:

$$\lim_{G_{\mathrm{exp}}\searrow 0} f_{\mathrm{TF,min}} = \frac{1}{|l_p|}\,. \tag{5.94}$$

This follows similarly to the low-gain approximations performed above. Similarly, the minimal angular displacement measurement uncertainty for the Schmidt mode theory approach is given by

$$f_{\mathrm{SMT,min}} = \frac{1}{|l_p|} \frac{\sqrt{\langle \hat{N}_{s,\mathrm{tot}} \rangle}}{G}, \tag{5.95}$$

which follows from Eqs. (5.86) and (5.91).

Figure 5.13 suggests that $f_{\mathrm{TF,min}} < f_{\mathrm{SMT,min}}$, which can be shown directly follows: As an analytic function, the $\sinh^2$ function is defined everywhere by its power series, which can be used to estimate [2]

$$\langle \hat{N}_{s,\mathrm{tot}} \rangle = \sum_{m,n} \sum_{l=1}^{\infty} \frac{2^{-1+2l} \left(G\sqrt{\lambda_{mn}} \right)^{2l}}{(2l)!} = G^2 + \mathcal{O}(G^4) > G^2, \tag{5.96}$$

since the higher order terms $\mathcal{O}(G^4)$ are all positive, so that [2]

$$G < \sqrt{\langle \hat{N}_{s,\mathrm{tot}} \rangle} < \sqrt{\mathcal{A}}, \tag{5.97}$$

as long as $G > 0$, compare the definition of $\mathcal{A}$ in Eq. (3.48). This immediately proves that the angular displacement uncertainty for the transfer function approach is always lower or equal to that of the Schmidt mode theory approach: $f_{\mathrm{TF,min}} < f_{\mathrm{SMT,min}}$.

Ultimately, the reason for why both methods yield different results for the angular displacement uncertainty must be related to the (spatial) ordering in which the phase is included in the system. In the transfer function approach, the equations of motion are solved for both crystals separately. This means that the solution of the first crystal and the corresponding transfer functions are known. This is not the case for the Schmidt mode theory approach, where only the transfer functions for the entire interferometer are known. Mathematically, this leads to the different expressions for the eigenvalues of the entire interferometer, as seen in Eqs. (5.79c) and (5.84). This is because in the Schmidt mode theory approach, the TPA is the sum of the TPAs of both crystals [see Eq. (5.81)] and ultimately acquires the $\cos\left(l_p\vartheta/2\right)$ term as seen in Eq. (5.82). Thus, the entire TPA and its low-gain eigenvalues $\sqrt{\lambda_{mn}}$ scale as $\propto \cos\left(l_p\vartheta/2\right)$. Contrary to that, when first constructing both TPAs and combining them using the transfer function approach, only the high-gain eigenvalues of the full interferometer scale as $\propto \cos\left(l_p\vartheta/2\right)$, see Eq. (5.79c).

It is well known that Schmidt mode theory leads to incorrect results at high parametric gain [5]. Hence, the aforementioned observations regarding the differences of the two approaches are unsurprising. The transfer function approach is based on the connection of the two PDC sections as it follows from the integro-differential equation formalism, while in the Schmidt mode theory approach the TPAs are simply added. As such, the transfer function approach can be expected to yield more accurate results at high gain. In this context, it is therefore also unsurprising that the Schmidt mode theory approach does not predict a strong supersensitivity, which would be expected due to the identical

mathematical structure of the formalisms for angular displacement measurements and phase measurements as described in Chapter 3. As such, in the following, only the angular displacement uncertainty for the transfer function approach will be analyzed further.

Figure 5.14(a) shows the minimal angular displacement uncertainty for several combinations of l_p and m_p as also seen in Fig. 5.13. The behavior is generally similar to the behavior of the optimal phase sensitivity (compare Fig. 3.7) and shows a strong reduction of the uncertainty with increasing gain. Interestingly, both an increase in l_p and an increase in m_p lead to an improvement of the optimal angular displacement uncertainty. To get a better understanding of this behavior, $f_{\mathrm{TF,min}}$ may be rewritten in terms of the Schmidt number of the first crystal $K^{(1)}$ as:

$$f_{\mathrm{TF,min}} = \frac{1}{|l_p|} \frac{1}{\sqrt{1 + \frac{\langle \hat{N}^{(1)}_{s,\mathrm{tot}} \rangle}{K^{(1)}}}}. \tag{5.98}$$

This follows analogously to Eq. (3.51) as outlined in Sec. 3.5.1. Equation (5.98) implies that lowering the number of effective modes leads to an improvement of the optimal angular displacement measurement uncertainty.

Figure 5.14(b) shows the behavior of the Schmidt number at increasing experimental gain. Due to the redistribution of the eigenvalues, the Schmidt number strongly decreases with increasing gain, as described in Sec. 5.3.1 and Sharapova *et al.* [11]. As was already observed in the plots of the eigenvalue distributions shown in Figs. 5.2 and 5.3, at low gain, increasing m_p leads to an increase in the Schmidt number, while at high gain, the Schmidt number is decreased. This behavior can also be seen in Fig. 5.14(b). As a consequence, the minimal normalized angular displacement uncertainty decreases more strongly for $l_p = 7$, $m_p = 7$ than for $l_p = 7$, $m_p = 0$, as the experimental gain is increased, see Fig. 5.14(a).

As was described during the analysis of the phase sensitivity of high-gain SU(1,1) interferometers, apart from the actual sensitivity/uncertainty, the width of the region in which supersensitivity is reached is also important (see Secs. 3.5.1 and 3.5.4). This is because this region must be sufficiently broad to allow for stable measurements [2]. Section A.3 provides the derivation of the analytical expression for this supersensitivity region width for the phase sensitivity. Following this derivation using the expressions of this chapter [Eq. (5.80)] yields the following expression for the supersensitivity region width for the angular displacement uncertainty [2]:

$$\Delta_{\mathrm{TF}} = \frac{2\pi}{|l_p|} - \frac{4}{|l_p|} \arctan\left(\sqrt{\frac{1 + 4\frac{\mathcal{B}}{\mathcal{A}}}{2\mathcal{A} l_p^2 \left(\Delta\vartheta_{\mathrm{SNL}}\right)^2 - 1}} \right). \tag{5.99}$$

In order for the supersensitivity region to exist, the square root in the above expression must remain real-valued. This is the case as long as

$$1 < \left(1 + \frac{\langle \hat{N}^{(1)}_{s,\mathrm{tot}} \rangle}{K^{(1)}}\right) l_p^2 = 2\mathcal{A} l_p^2 \left(\Delta\vartheta_{\mathrm{SNL}}\right)^2, \tag{5.100}$$

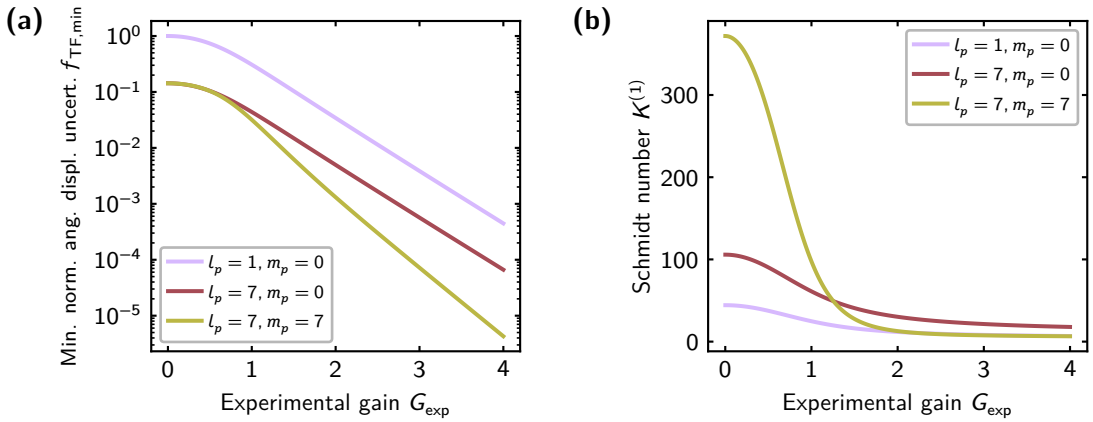

Figure 5.14: **(a)** Minimal normalized angular displacement uncertainty for the compensated SU(1,1) interferometer with a Dove prism placed between the two lenses for several combinations of the radial (m_p) and OAM (l_p) index of the Laguerre-Gaussian pump beam in dependence on the experimental gain G_{exp}. As mentioned in the text, the fitting constant A connecting the experimental gain to the theoretical gain parameter G has been chosen as the averaged values for $G_{\mathrm{exp}} = 0.01$ and $G_{\mathrm{exp}} = 4$. Note that here, only the values for the transfer function approach are shown since the Schmidt mode theory approach predicts larger uncertainties, as discussed in the text. As $G_{\mathrm{exp}} \searrow 0$, $f_{\mathrm{TF,min}}$ approaches $1/|l_p|$, see Eq. (5.94). **(b)** Schmidt number $K^{(1)}$ of the first crystal of the SU(1,1) used to carry out the angular displacement sensitivity measurements for several combinations of l_p and m_p. As the gain is increased, the Schmidt number strongly decreases due to the redistribution of the eigenvalues caused by their $\sinh^2$-dependence on G, as discussed in Sec. 5.3.1. See also Figs. 5.2(d), 5.2(e), 5.3(d) and 5.3(e) which show the eigenvalue distributions and the corresponding Schmidt numbers for the two cases where $l_p = 7$ for $G_{\mathrm{exp}} = 0.01$ and $G_{\mathrm{exp}} = 4$. Note however that here, as described in the text, the fitting constant A is averaged for the low and high-gain regime. Therefore, a precise match between these numbers is not expected. Adapted from Ref. [1].

which holds for $G > 0$ and $|l_p| \neq 0$. Thus, a supersensitivity region always exists as long as the pump beam has nonzero OAM. As mentioned above, for $l_p = 0$, the angular displacement uncertainty is undefined.

Figure 5.15(a) shows the behavior of Δ_{TF} over a range of the experimental gain G_{exp}. Evidently, the width of the supersensitivity region decreases strongly as the experimental gain is increased. Furthermore, the region shrinks more strongly for larger l_p and m_p. Generally, comparing Figs. 5.14(a) and 5.15(a) shows that an improvement in the angular displacement measurement uncertainty leads to a narrowing of the supersensitivity region. In the low gain limit, for $l_p = 1$, $m_p = 0$, the supersensitivity region degenerates into a single point. This can be seen by applying the low gain approximations discussed throughout this section to the expression for Δ_{TF} as written in Eq. (5.99) [2]:

$$\lim_{G_{\mathrm{exp}} \searrow 0} \Delta_{\mathrm{TF}} = \begin{cases} \text{undefined} & l_p = 0 \\ 0 & l_p = \pm 1 \\ \frac{2\pi}{|l_p|} - \frac{4}{|l_p|} \arctan\left(\frac{1}{\sqrt{l_p^2 - 1}}\right) & |l_p| > 1 . \end{cases} \tag{5.101}$$

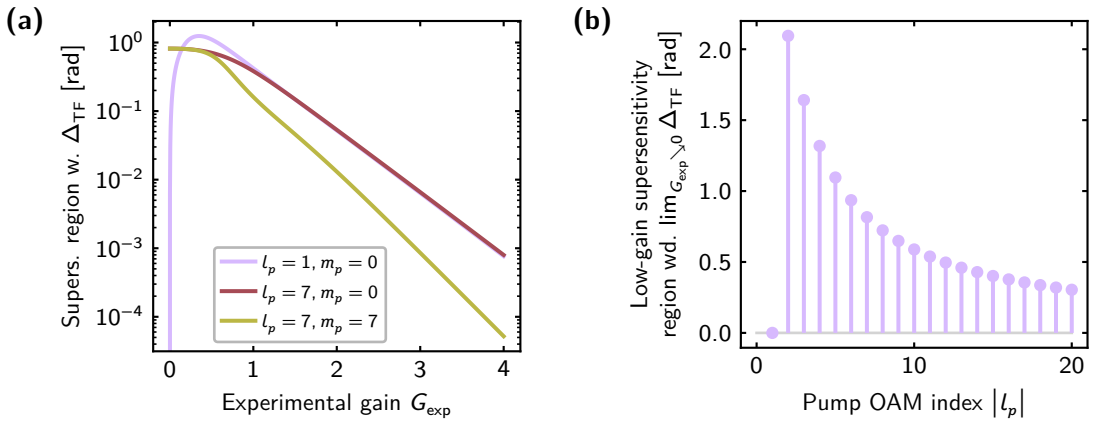

Figure 5.15: **(a)** Plot of the supersensitivity region width Δ_{TF} in dependence on the experimental gain G_{exp} for various combinations of the radial (m_p) and OAM (l_p) index of the pump beam. For $l_p = 1$, $m_p = 0$, the width approaches 0 as $G_{exp} \searrow 0$. **(b)** Width of the supersensitivity region width in dependence on the modulus of the pump OAM index in the limit of low gain as described by Eq. (5.101). For $l_p = 0$, there exists no supersensitivity and rotations of the Dove prism cannot be detected, as discussed in the text, while for $l_p = 1$, the supersensitivity region consists of a single point. Adapted from Ref. [1].

Figure 5.15(b) shows a plot of this expression in dependence on l_p. For $l_p = 2$, the width of the supersensitivity region in the low gain limit is maximized and gradually decreases as l_p is increased further.

5.5. Conclusion

This chapter, based on Ref. [2], provides an extension of the Schmidt mode theory developed in Sharapova *et al.* [11] to Laguerre-Gaussian pump envelopes carrying orbital angular momentum. It was found that the distribution of the Schmidt eigenvalues is centered around $l_p/2$, where l_p is the OAM index of the pump beam. By varying l_p and the radial index m_p, it is possible to significantly modify the eigenvalue distributions. For a single crystal, increasing these indices leads to a broadening of the eigenvalue distributions along the modal OAM index and the modal radial index, respectively. Using SU(1,1) interferometers consisting of two crystals with an air gap in-between, further modifications of the eigenvalue distributions are possible by varying the length of the gap. Most prominently, near the dark and the bright fringe of the interferometer, non-monotonic behavior along the modal OAM index n can be observed, ultimately leading to large occupations of modes with OAM larger than that of the pump. Additionally, due to the non-monotonic behavior, for certain combinations of l_p and m_p, the intensity profile approaches a donut shape due to the fact the modes with the largest occupations are no longer Gaussian shaped. For any configuration, increasing the experimental gain allows for a filtration of the highest occupied modes due to the redistribution of the eigenvalues, allowing for the extraction of the modes with OAM larger than the pump OAM and the non-Gaussian modes [11].

These observations may provide a solution to one of the major problems of the multimode squeezing measurements discussed in Chapter 4: Due to the fact that the OAM modes are orthogonal, the overlap between OAM modes with different OAM vanishes, removing the necessity to account for overlap between different OAM modes. If the system is additionally designed so that only radial modes with $m = 0$ have a significant contribution, as was for example seen for a single crystal and the interferometer at $G_{\text{exp}} = 4$, the off-diagonal overlap matrix elements are no longer relevant. Future studies may investigate this and, more generally, the role of the OAM modes in the modal overlaps inside SU(1,1) interferometers in more detail.

As an additional application of PDC pumped with Laguerre-Gaussian pump beams, it was investigated how diffraction compensated SU(1,1) interferometers as introduced in Sec. 3.3 can be used to reach supersensitivity in angular displacement measurements. This was based on the idea that using beams carrying OAM to probe the induced rotations leads to an improvement in the sensitivity. It was shown that the effective OAM interacting with the Dove prism inducing the rotation is the pump OAM l_p. The results indicated that the measurement uncertainty strongly decreases as the gain, l_p or m_p are increased. However, this increase comes at the cost of a strong reduction in the width of the angular region over which the supersensitivity can be achieved, requiring trade-off considerations between the actual supersensitivity and the width of the supersensitivity region required for stable measurements. Overall, the theoretical treatment and the results bear strong similarity to those of Chapter 3 due to the identical mathematical structure of the underlying problem. It should be noted that the abovementioned results only apply to the transfer-function approach, where the system is described in two parts, which are the first crystal and the second crystal including the Dove prism inducing the rotation of the signal and idler field. The alternative approach (Schmidt mode theory approach), where the system is described by a single TPA consisting of the sums of the TPA describing the first crystal and the second crystal predicts much larger measurement uncertainties. The reason for this is that in the transfer function approach, the phase originating from the rotation angle is included only in the description of the second crystal, so that only the low-gain eigenvalues of the second crystal are modified as the angle is varied. This is structurally different from the Schmidt mode theory approach, where the low-gain eigenvalues are directly proportional to the cosine of the angle.

Generally, it should be noted that the description of PDC with Laguerre-Gaussian pump beams presented in this chapter does not include time-ordering effects, as is typical for Schmidt mode theory. For this, a more elaborate approach such as the integro-differential equations approach described in Sec. 3.2 has to be employed. In this approach, the Schmidt modes also become gain dependent, while in the Schmidt mode theory approach only the eigenvalues are gain-dependent. However, the integro-differential equation approach can generally only be solved numerically, except when approximation such as that of the plane-wave pump are made (compare Sec. 3.5.2). The major advantage of Schmidt mode theory is providing analytical expressions for the TPA, which can be understood as an

analog to the transfer function β, and, as seen in more detail in Sec. A.5, coincides with it at low gain.

It was noted during the review phase of Ref. [2] that apart from the phase sensitivity and the angular displacement measurements, it is also possible to consider transverse displacements of the signal and idler fields between the two crystals, which were for example investigated in Grenapin *et al.* [154] and Barboza *et al.* [155]. As mentioned in Ref. [2], applying the formalism developed here to transverse displacements may have high computational demand, due to the fact that in the most general case, four-dimensional Cartesian grids have to be used for the TPA due to its dependence on the signal and idler wave vectors $\boldsymbol{q}_s$ and $\boldsymbol{q}_i$. In the formalism illustrated here, it was possible to construct a description of the system that requires only three-dimensional grids for the function R by utilizing the symmetry of the system, meaning that it can be described in terms of the signal-idler azimuthal angle-difference $\phi_s - \phi_i$. As such, it is advisable to utilize possible symmetries of the system when describing transverse displacements in order to reduce the dimensionality of the grids describing the TPA. In the simplest case, it might be possible to reduce the transverse plane, in which the displacement occurs, to a single line along the displacement, leading to a similar description as in Chapter 3, where only one transverse direction was included in the description.

6

Concluding Remarks

In this thesis, several aspects of high-gain multimode SU(1,1) interferometers were theoretically investigated. In this regard, the main focus was on metrological applications using SU(1,1) for the measurement of phases (Chapter 3), the multimode squeezing (Chapter 4) and their sensitivity for rotational displacement measurements (Chapter 5). Several conclusions can be drawn from the results presented in this thesis.

Phase Sensitivity of High-Gain SU(1,1) Interferometers. It was shown that high-gain multimode SU(1,1) interferometers can be used to beat the shot-noise level for the phase sensitivity, provided that proper diffraction compensation is applied. This means that focusing elements must be used to properly image the output field of the first crystal onto the second crystal. It then follows that at high gain, the scaling of the phase sensitivity approaches the Heisenberg scaling. These results were obtained by numerically integrating integro-differential equations describing the evolution of the plane-wave operators through the PDC sections [5]. Additionally, several useful analytical relationships between the transfer functions, which describe the solutions of the integro-differential equations, were found and used to simplify the computations. These results were enabled by applying the well-known joint Schmidt decompositions for the transfer functions, yielding the Schmidt modes and the corresponding eigenvalues. Importantly, these results illustrate that the phase sensitivity of SU(1,1) interferometers in the form analyzed here is improved by reducing the number of effective modes, increasing the parametric gain or both. Ultimately, the increase in the phase sensitivity is always accompanied by a strong decrease in the width of the phase region over which the supersensitivity can be achieved. Therefore, in experimental realizations of this setup it is always necessary to make trade-off considerations. Future investigations may focus on the inclusion of internal losses for the SU(1,1) interferometer, since these are well known to degrade the interferometer performance.

Modal Structure of SU(1,1) Interferometers. A second important consequence of the joint Schmidt decomposition is the fact that each PDC sections has an associated set of input

and output modes. These modes were analyzed in dependence on the parametric gain. In this regard, the well-known result was reproduced that the modulus of the Schmidt modes broadens as the parametric gain is increased, while the moduli of the input and output modes coincides to a good approximation. Additionally, it was discovered that the phase profiles of the modes coincide at low gain, leading to a full coincidence of the input and output modes at low gain. As the gain is increased, the phase profile of the input modes flattens, while that of the output modes steepens slightly. Overall, the input and output modes become generally more dissimilar as the parametric gain is increased. Another important result is the discovery that for non-degenerate eigenvalues, the Schmidt modes are unique up to their sign, meaning their phases are not fully arbitrary.

Multimode Squeezing Measurements. In order to measure the squeezing in each output mode of a single PDC section (squeezer), a second PDC section (amplifier) can be used to form an SU(1,1) interferometer. In principle, depending on the phase difference the light acquires between the two PDC sections, either the squeezing or anti-squeezing can be measured. However, in general, if the second crystal operates at high parametric gain, meaning that the SU(1,1) interferometer is unbalanced, the output modes of the first crystal and the input modes of the second crystal, as well as the output modes of the second crystal and those of the SU(1,1) interferometer are not identical. Based on this, a processing method was developed which facilitates obtaining the multimode squeezing data from the eigenvalues of the squeezer and the entire interferometer, provided that the overlap coefficients between the output modes of the squeezer and the input modes of the amplifier, as well as those between the output modes of the amplifier and the entire interferometer are known. Since the overlap coefficients and the eigenvalues, reflecting absolute photon numbers, are generally hard to obtain experimentally, an approximation was made to the processing method allowing for a simplified reconstruction of the levels of squeezing and anti-squeezing, given that the amplifier operates at much higher parametric gain than the squeezer. Both the approximated and exact methods were first applied theoretically and found to be in good agreement. Furthermore, this processing method was applied to experimental data obtained by collaborators in Barakat *et al.* [3] and was found to be in good agreement with the theoretically predicted values for the levels of squeezing and anti-squeezing.

Modal Structure of PDC Systems Pumped with Laguerre-Gaussian Beams. In the preceding results, the pump pulse always had a Gaussian envelope. The description of PDC was extended to Laguerre-Gaussian beams within the context of Schmidt mode theory as developed in Sharapova *et al.* [11]. This theory does not include time-ordering effects and does therefore best agree with the experiment at low gain. It was found that the occupation numbers (eigenvalues) of the Schmidt modes can be strongly modified by varying the orbital and radial indices of the Laguerre-Gaussian pump. The orbital index is associated with the orbital angular momentum (OAM) that the pump beam carries and was found to be preserved in this PDC process. By increasing the radial and orbital indices, the occupation numbers of the modes broaden along the radial and orbital index, respectively.

Then, as the gain is increased, only the modes with the highest occupation numbers remain, as described in Sharapova *et al.* [11], allowing for the filtering of the modes with the largest eigenvalues. This becomes especially useful in the case of SU(1,1) interferometers pumped with Laguerre-Gaussian beams, where at the dark and bright fringe certain configurations were shown to lead to non-monotonic behavior of the eigenvalues. As the gain is increased, the modes corresponding to these local maxima are filtered out, while the others are suppressed. In one case, it was also found that the OAM of one of the selected modes was larger than the OAM of the pump beam. Thus, overall, SU(1,1) interferometers can also be used to prepare certain states of multimode PDC light. Future studies may focus on extending this formalism to the integro-differential equation approach for the description of PDC in order to obtain more accurate results at high parametric gain. Furthermore, these findings may provide a way for the reduction of the modal overlap, for example in the context of multimode squeezing measurements, which may be investigated in more detail in future research.

Angular Displacement Sensitivity of SU(1,1) Interferometers Pumped with Laguerre-Gaussian Beams. Using light carrying OAM, it is possible to detect angular displacements (rotations) of objects. As such, following the results obtained for the phase sensitivity, it was shown that within the Schmidt mode theory approach, SU(1,1) interferometers pumped with Laguerre-Gaussian beams can be used to achieve supersensitivity of angular displacement measurements. The displacement measurement uncertainty can be reduced by increasing the pump OAM index, its radial index or the parametric gain. As was the case for the phase sensitivity, this again comes at the cost of a diminishing angular region over which the supersensitivity can be achieved. Further studies may extend this SU(1,1) interferometer setup to *transverse displacement* measurements, where objects are moved perpendicular to the pump direction, leading to a displacement of the signal and idler fields. Here, in general, Cartesian coordinates must be used, leading to a dramatic increase in the numerical complexity, unless symmetries can be utilized.

A

Appendix: Auxiliary Results, Calculations and Proofs

A.1. Integro-Differential Equations for the Transfer Functions

Finite-Width Pump. More generally, the integro-differential equations (3.7) may be written as

$$\frac{\mathrm{d}\hat{a}_s(q_s,L)}{\mathrm{d}L} = \Gamma \int \mathrm{d}q_i\, r(q_s,q_i,L)\, \hat{a}_i^\dagger(q_i,L), \tag{A.1a}$$

$$\frac{\mathrm{d}\hat{a}_i^\dagger(q_i,L)}{\mathrm{d}L} = \Gamma \int \mathrm{d}q_s\, r^*(q_s,q_i,L)\, \hat{a}_s(q_s,L), \tag{A.1b}$$

where the pump term and the phase-matching function have been absorbed into $r(q_s,q_i,L)$. Plugging Eqs. (3.10) into Eqs. (A.1) and comparing both sides yields two sets of integro-differential equations:

$$\frac{\mathrm{d}\beta(q_s,q_i',L)}{\mathrm{d}L} = \Gamma \int \mathrm{d}q_i\, r(q_s,q_i,L)\, \tilde{\eta}^*(q_i,q_i',L), \tag{A.2a}$$

$$\frac{\mathrm{d}\tilde{\eta}^*(q_i,q_i',L)}{\mathrm{d}L} = \Gamma \int \mathrm{d}q_s\, r^*(q_s,q_i,L)\, \beta(q_s,q_i',L), \tag{A.2b}$$

and

$$\frac{\mathrm{d}\beta^*(q_i,q_s',L)}{\mathrm{d}L} = \Gamma \int \mathrm{d}q_s\, r^*(q_s,q_i,L)\, \tilde{\eta}(q_s,q_s',L), \tag{A.3a}$$

$$\frac{\mathrm{d}\tilde{\eta}(q_s,q_s',L)}{\mathrm{d}L} = \Gamma \int \mathrm{d}q_i\, r(q_s,q_i,L)\, \beta^*(q_i,q_s',L), \tag{A.3b}$$

where Eqs. (A.2) coincide with Eqs. (3.11) in the main text. Clearly, these two sets are only equivalent when r is symmetric under the exchange of the two wave-vector arguments

for any L:

$$r(q_s, q_i, L) = r(q_i, q_s, L). \tag{A.4}$$

In the case where Eq. (A.4) does hold, Eqs. (A.2) and (A.3) are complex conjugates of each other. Contrary to that, if this symmetry is not fulfilled, β and β^*, as well as $\tilde{\eta}$ and $\tilde{\eta}^*$, are generally not complex conjugates of each other. As mentioned in Ref. [1], this more general case without the symmetry condition written in Eq. (A.4) requires four complex-valued transfer functions. As a consequence, the number of integro-differential equations that has to be solved numerically is doubled, since the two sets written in Eqs. (A.2) and (A.3) have to be solved independently.

Plane-Wave Pump. For a plane-wave pump, plugging Eqs. (3.56) into Eqs. (3.54) directly yields two sets of coupled differential equations:

$$\frac{\mathrm{d}\beta_{\mathrm{pw}}(q_s, L)}{\mathrm{d}L} = \Gamma_0 h_{\mathrm{pw}}(q_s, L)\, \tilde{\eta}^*_{\mathrm{pw}}(-q_s, L), \tag{A.5a}$$

$$\frac{\mathrm{d}\tilde{\eta}^*_{\mathrm{pw}}(-q_s, L)}{\mathrm{d}L} = \Gamma_0 h^*_{\mathrm{pw}}(q_s, L)\, \beta_{\mathrm{pw}}(q_s, L), \tag{A.5b}$$

and

$$\frac{\mathrm{d}\beta^*_{\mathrm{pw}}(-q_s, L)}{\mathrm{d}L} = \Gamma_0 h^*_{\mathrm{pw}}(q_s, L)\, \tilde{\eta}_{\mathrm{pw}}(q_s, L), \tag{A.6a}$$

$$\frac{\mathrm{d}\tilde{\eta}_{\mathrm{pw}}(q_s, L)}{\mathrm{d}L} = \Gamma_0 h_{\mathrm{pw}}(q_s, L)\, \beta^*_{\mathrm{pw}}(-q_s, L), \tag{A.6b}$$

where Eqs. (A.5) coincide with Eqs. (3.57) in the text. These two sets are equivalent provided that

$$h_{\mathrm{pw}}(q_s, L) = h_{\mathrm{pw}}(-q_s, L), \tag{A.7}$$

which due to the definition of h_{pw} in Eq. (3.55) is equivalent to the condition in Eq. (A.4). Again, as for a finite-width pump, if h_{pw} does not fulfill this property, β_{pw} and β^*_{pw} as well as $\tilde{\eta}$ and $\tilde{\eta}^*_{\mathrm{pw}}$ are not necessarily complex conjugates of each other and the solution consists of four complex-valued functions.

A.2. Refraction Considerations

One additional aspect that needs to be considered when treating the propagation of light from the PDC sources is refraction at the boundaries of materials with different refractive indices. In Chapters 3 and 5 this was also taken into account by considering the output intensity profiles in terms of the external angles. Similarly, as already hinted at in Sec. 3.2, refraction must also be considered when transitioning between PDC sections with different optical properties, for example different refractive indices, or when transitioning between the output of the first crystal of an SU(1,1) interferometer into the phase object. A general sketch of the geometry of the refraction of a plane wave at the boundary between two media

with different refractive indices is shown in Fig. A.1(a). In the medium 1, with refractive index n_1, the wave travels with wave-vector $\boldsymbol{k}_1 = \begin{bmatrix} q_1 & k_{z,1} \end{bmatrix}^\mathrm{T}$ in the xz-plane towards the boundary to medium 2, where the refractive index is n_2. The angles α_1 and α_2 of the wave-vectors with respect to the normal of the boundary between the media are related via *Snell's law* [60, 101, 156, 157]:

$$n_1 \sin(\alpha_1) = n_2 \sin(\alpha_2). \tag{A.8}$$

During the derivation of Snell's law, it is either initially assumed or appears as an intermediate result that the wave-vector components q_1 and q_2 of the wave vectors in medium 1 and 2, respectively, are conserved:

$$q_1 = q_2\,, \tag{A.9}$$

see also Fig. A.1(a). For more details, see for example the derivations in Landau *et al.* [60] or Bartelmann *et al.* [157]. Obviously, this connection between the transverse wave-vector components can also *a posteriori* be obtained from Snell's law since it is one of the underlying assumptions: First, note that

$$q_j = |\boldsymbol{k}_j| \sin(\alpha_j), \qquad \text{for } j = 1, 2\,. \tag{A.10}$$

Additionally, since the waves are monochromatic, the moduli $k_j = |\boldsymbol{k}_j|$ of their wave-vectors are related via

$$\frac{k_1}{n_1} = \frac{k_2}{n_2}\,, \tag{A.11}$$

which directly follows from the dispersion relation, see Eq. (2.15). Then, combining Eqs. (A.8), (A.10) and (A.11) directly leads to Eq. (A.9).

Refraction must also be considered when implementing the diffraction-compensated SU(1,1) configurations as discussed in Sec. 3.3. The sketches shown in Figs. 3.2(b) and 3.2(c) neglect the diffraction of the signal and idler radiation at the crystal-air boundaries. In a more precise treatment, it must be taken into account that the actual focal point $\mathscr{F}'$ of the radiation focused into the crystals is shifted by some distance δl from point $\mathscr{F}$, where it would lie if $n_1 = n_2$. This geometry is shown in Fig. A.1(b), which can be seen as a more precise sketch of the transitions between the first crystal and the air gap, as well as the air gap and the second crystal in Figs. 3.2(b) and 3.2(c).

Using Snell's law as written in Eq. (A.8) and the fact that

$$d = l \tan(\alpha_2) = (\delta l + l) \tan(\alpha_1), \tag{A.12}$$

see Fig. A.1(b), it can be shown that

$$\delta l = (\ell - a) \left[\frac{n_1}{n_2} \frac{\sqrt{1 - \left(\frac{n_2}{n_1}\right)^2 \sin^2(\alpha_2)}}{\cos(\alpha_2)} - 1 \right]. \tag{A.13}$$

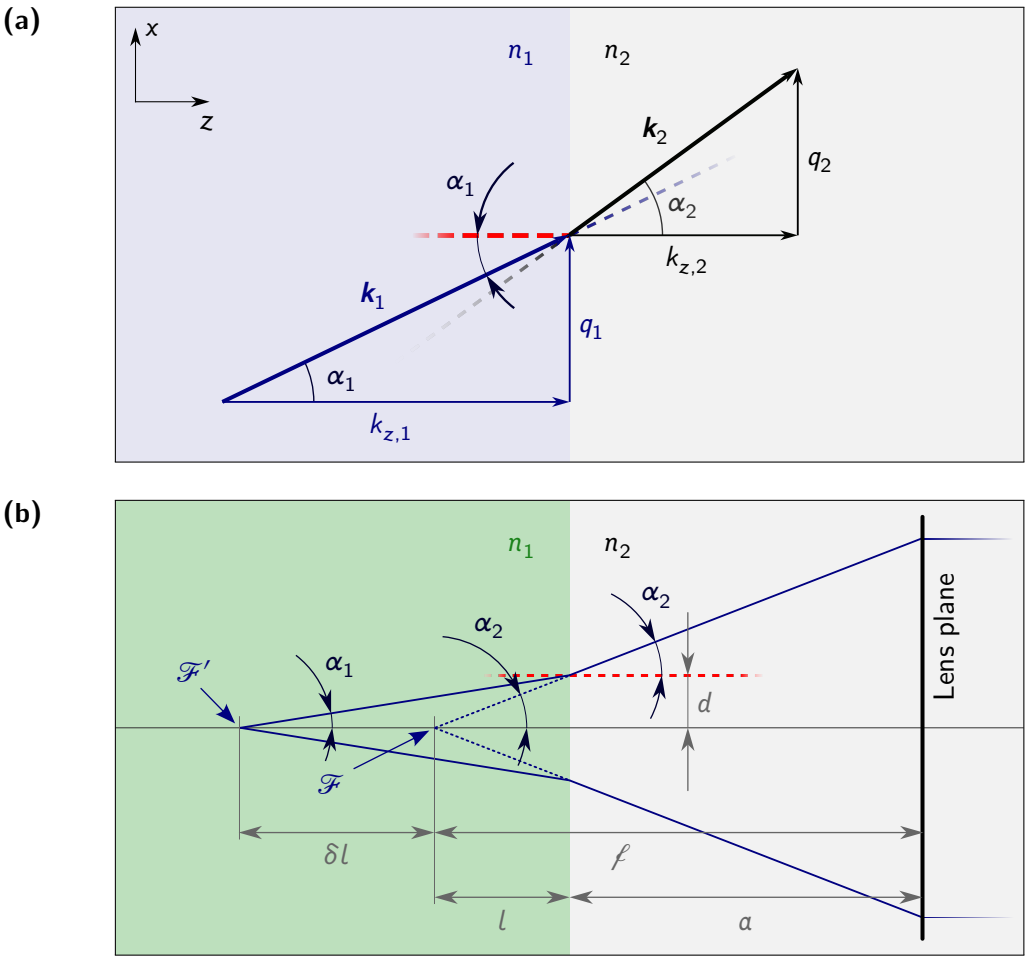

Figure A.1: **(a)** Sketch of the geometry of the refraction of a plane wave at the boundary of two materials. The plane wave impinges onto the boundary between two media from the medium with refractive index n_1 (indicated by the blue area) with the wave vector $\boldsymbol{k}_1 = [q_1 \;\; k_{z,1}]^{\mathrm{T}}$. After transitioning into the other medium with refractive index n_2 (indicated by the gray area), the wave vector becomes $\boldsymbol{k}_2 = [q_2 \;\; k_{z,2}]^{\mathrm{T}}$. The angles of incident and refraction are α_1 and α_2, respectively. **(b)** Sketch of the focusing of a collimated beam entering from the right and inside a medium with refractive index n_2 (gray region) into a medium with refractive index n_1 (green region). Equivalently, this sketch also illustrates the diffraction of a beam originating at a single point in the medium with refractive index n_1, followed by the refraction at the material boundary and subsequent collimation at the lens plane. The dashed lines indicate the continuation of the rays focused by the lens. It should be noted that in both cases the point $\mathscr{F}'$ where the beam is fully focused lies not at the focal length ℓ of the lens behind the lens plane (at the point marked with $\mathscr{F}$) but is shifted by some distance δl due to the diffraction.

Note that $l = \ell - a$. For small angles[1] α_2, so that $(n_2/n_1)^2 \sin^2(\alpha_2) \ll 1$ and $\cos(\alpha_2) \approx 1$, Eq. (A.13) can be approximated as

$$\delta l \approx (\ell - a)\left(\frac{n_1}{n_2} - 1\right). \tag{A.14}$$

With the refractive index of the crystal chosen as $n_1 = 1.6645$ as discussed in Sec. 2.3.1 and $n_2 \approx 1$ as the refractive index in air, this means $\delta l \approx 0.6645 l$. If the goal is to focus the PDC radiation into the center of a crystal with length $L = 2\,\mathrm{mm}$, requiring $l = 1\,\mathrm{mm}$, the actual focus inside the crystal will be shifted by 0.6645 mm, which is relatively large compared to the crystal size. However, it should be noted that in experimental setups the optimal position is determined by varying the position of the focusing element in order to maximize the visibility [4]. It is therefore not necessary to know the optimal position of the focusing element in advance.

A.3. Phase-Supersensitivity Region Width Δ for Compensated SU(1,1) Interferometers

The normalized phase sensitivity f as defined via Eqs. (3.4) and (3.46) is 2π-periodic and diverges towards $+\infty$ as $\phi \to 2\pi c$, for $c \in \mathbb{Z}$. Furthermore, on the intervals $I_c = [2\pi c, 2\pi(c+1)]$, f is a continuous function of ϕ. This means that in order to derive the analytic expression for the supersensitivity range width Δ, it is possible to start by solving the equation $f = 1$ for ϕ. With Eqs. (3.4) and (3.46), this equation becomes

$$1 + a\cos^2\left(\frac{\phi}{2}\right) - b\sin^2\left(\frac{\phi}{2}\right) = 0, \tag{A.15a}$$

with the two positive constants

$$a = 4\frac{\mathcal{B}}{\mathcal{A}}, \tag{A.15b}$$

$$b = 4\mathcal{A}\,(\Delta\phi_{\mathrm{SNL}})^2. \tag{A.15c}$$

Equation (A.15a) can be solved for ϕ with the help of the identity $\sin^2(x) + \cos^2(x) = 1$ [111]. This way, the solutions for ϕ can be expressed either in terms of sin or cos. Furthermore, by comparing both possibilities, the set of solutions may be written in terms of tan:

$$\phi_{c,\pm} = 2\pi c \pm 2\arctan\left(\frac{\sqrt{1+a}}{\sqrt{b-1}}\right), \qquad \text{for } c \in \mathbb{Z}. \tag{A.16}$$

Clearly, this expression requires $b > 1$ for $\phi_{c,\pm}$ to be real-valued. However, $b > 1$ is equivalent to $\langle \hat{N}^{(1)}_{s,\mathrm{tot}} \rangle / K^{(1)} > -3/4$ and is therefore always true. Unsurprisingly, the same condition also follows when setting $f_{\min} < 1$, with $f_{\min}$ as given in Eq. (3.51), which was

[1] For broad angles, the dependence on the angle α_2 in Eq. (A.13) implies that even for fixed distance a between the crystal and the lens plane (and therefore fixed l), the rays may not necessarily be focused into a single point, leading to abberations. However, this case is beyond the scope of this work.

discussed in Sec. 3.5.1. If the minimum normalized phase sensitivity f were strictly greater than 1 for all ϕ, no real-valued solutions to Eqs. (A.15) would be possible. Furthermore, $\lim_{b\searrow 1} \phi_{c,\pm} = (2c+1)\,\pi$ meaning that in this case, each of the intervals I_c contains a single point of vanishing width $\Delta = 0$ where $f = 1$.

In all other cases with $b > 1$, there are two real-valued solutions $\phi_{c,+}$ and $\phi_{c,-}$ on the intervals I_c described by Eq. (A.16) and due to the continuity and the behavior at the boundaries of these intervals discussed above, the supersensitivity region must lie between those two solutions. Its width is therefore given by $\Delta = \phi_{c+1,-} - \phi_{c,+}$, which, after applying Eq. (3.48), leads directly to Eq. (3.52).

A.4. Integro-Differential Equations for the Full Three-Dimensional System

A.4.1. Cartesian Frame

For the full three-dimensional system, where, unlike in Chapters 3 and 4, both transverse dimensions are included in the description, the integro-differential equations describing the evolution of the plane-wave operators through the PDC sections take the general form

$$\frac{\mathrm{d}\hat{a}_s(\boldsymbol{q}_s, L)}{\mathrm{d}L} = \Gamma \int \mathrm{d}^2 q_i \, f(\boldsymbol{q}_s, \boldsymbol{q}_i, L)\, \hat{a}_i^\dagger(\boldsymbol{q}_i, L), \tag{A.17a}$$

$$\frac{\mathrm{d}\hat{a}_i^\dagger(\boldsymbol{q}_i, L)}{\mathrm{d}L} = \Gamma \int \mathrm{d}^2 q_s \, f^*(\boldsymbol{q}_s, \boldsymbol{q}_i, L)\, \hat{a}_s(\boldsymbol{q}_s, L), \tag{A.17b}$$

where f is the function describing the PDC process and normally the product of the Fourier transform of the spatial envelope of the pump beam and the phase-matching function. Compared to Eqs. (3.7), the only difference is that the wave-vector variables are now vector-valued instead of scalar-valued. The commutation relations of these plane-wave operators are given by

$$[\hat{a}_s(\boldsymbol{q}_s, L), \hat{a}_s^\dagger(\boldsymbol{q}_s', L)] = \delta(\boldsymbol{q}_s - \boldsymbol{q}_s'), \tag{A.18a}$$

$$[\hat{a}_i(\boldsymbol{q}_i, L), \hat{a}_i^\dagger(\boldsymbol{q}_i', L)] = \delta(\boldsymbol{q}_i - \boldsymbol{q}_i'), \tag{A.18b}$$

$$[\hat{a}_s(\boldsymbol{q}_s, L), \hat{a}_i^\dagger(\boldsymbol{q}_i', L)] = 0, \tag{A.18c}$$

and

$$[\hat{a}_s(\boldsymbol{q}_s, L), \hat{a}_i^\dagger(\boldsymbol{q}_i, L)] = (\mathcal{D}_{si} - 1)\, \delta(\boldsymbol{q}_s - \boldsymbol{q}_i). \tag{A.19}$$

The solution of the integro-differential equations (A.17) are of the form:

$$\hat{a}_s(\boldsymbol{q}_s, L) = \int \mathrm{d}^2 q_s' \, \tilde{\eta}(\boldsymbol{q}_s, \boldsymbol{q}_s', L)\, \hat{a}_s(\boldsymbol{q}_s') + \int \mathrm{d}^2 q_i' \, \beta(\boldsymbol{q}_s, \boldsymbol{q}_i', L)\, \hat{a}_i^\dagger(\boldsymbol{q}_i'), \tag{A.20a}$$

$$\hat{a}_i^\dagger(\boldsymbol{q}_i, L) = \int \mathrm{d}^2 q_i' \, \tilde{\eta}^*(\boldsymbol{q}_i, \boldsymbol{q}_i', L)\, \hat{a}_i^\dagger(\boldsymbol{q}_i') + \int \mathrm{d}^2 q_s' \, \beta^*(\boldsymbol{q}_i, \boldsymbol{q}_s', L)\, \hat{a}_s(\boldsymbol{q}_s'). \tag{A.20b}$$

Plugging this form back into Eqs. (A.17) yields two sets of integro-differential equations for the transfer functions:

$$\frac{\mathrm{d}\beta(\boldsymbol{q}_s,\boldsymbol{q}_i',L)}{\mathrm{d}L} = \Gamma \int \mathrm{d}^2 q_i \, f(\boldsymbol{q}_s,\boldsymbol{q}_i,L)\, \tilde{\eta}^*(\boldsymbol{q}_i,\boldsymbol{q}_i',L), \tag{A.21a}$$

$$\frac{\mathrm{d}\tilde{\eta}^*(\boldsymbol{q}_i,\boldsymbol{q}_i',L)}{\mathrm{d}L} = \Gamma \int \mathrm{d}^2 q_s \, f^*(\boldsymbol{q}_s,\boldsymbol{q}_i,L)\, \beta(\boldsymbol{q}_s,\boldsymbol{q}_i',L), \tag{A.21b}$$

and

$$\frac{\mathrm{d}\beta^*(\boldsymbol{q}_i,\boldsymbol{q}_s',L)}{\mathrm{d}L} = \Gamma \int \mathrm{d}^2 q_s \, f^*(\boldsymbol{q}_s,\boldsymbol{q}_i,L)\, \tilde{\eta}(\boldsymbol{q}_s,\boldsymbol{q}_s',L), \tag{A.22a}$$

$$\frac{\mathrm{d}\tilde{\eta}(\boldsymbol{q}_s,\boldsymbol{q}_s',L)}{\mathrm{d}L} = \Gamma \int \mathrm{d}^2 q_i \, f(\boldsymbol{q}_s,\boldsymbol{q}_i,L)\, \beta^*(\boldsymbol{q}_i,\boldsymbol{q}_s',L). \tag{A.22b}$$

As described in Sec. A.1 for the two-dimensional description, $f(\boldsymbol{q}_s,\boldsymbol{q}_i,L) = f(\boldsymbol{q}_i,\boldsymbol{q}_s,L)$ is required for these two sets in Eqs. (A.21) and Eqs. (A.22) to be equivalent. Otherwise, four transfer functions are required, meaning that the above equations remain valid under the assumption that * does not denote the complex conjugate, but rather only denotes two additional transfer functions β^* and $\tilde{\eta}^*$.

Following Sec. 3.2, the initial value conditions when integrating the system section-by-section are given by

$$\beta^{(m+1,\mathrm{in})}(\boldsymbol{q},\boldsymbol{q}') = \beta^{(m,\mathrm{out})}(\boldsymbol{q},\boldsymbol{q}'), \tag{A.23a}$$

$$\tilde{\eta}^{(m+1,\mathrm{in})}(\boldsymbol{q},\boldsymbol{q}') = \tilde{\eta}^{(m,\mathrm{out})}(\boldsymbol{q},\boldsymbol{q}'), \tag{A.23b}$$

where the concrete values of L have been replaced by $^{(m+1,\mathrm{in})}$ and $^{(m,\mathrm{out})}$, labeling the input to the $(m+1)$th PDC section and the output of the mth section. For the first section, the initial value conditions are

$$\beta^{(1,\mathrm{in})}(\boldsymbol{q},\boldsymbol{q}') = 0, \tag{A.23c}$$

$$\tilde{\eta}^{(1,\mathrm{in})}(\boldsymbol{q},\boldsymbol{q}') = \delta(\boldsymbol{q}-\boldsymbol{q}'). \tag{A.23d}$$

When integrating each section separately, the initial value conditions are

$$\beta^{(m,\mathrm{in})}(\boldsymbol{q},\boldsymbol{q}') = 0, \tag{A.24a}$$

$$\tilde{\eta}^{(m,\mathrm{in})}(\boldsymbol{q},\boldsymbol{q}') = \delta(\boldsymbol{q}-\boldsymbol{q}'). \tag{A.24b}$$

for each section m and the sections are connected via the generalization of Eqs. (3.19):

$$\tilde{\eta}^{(m+1,m)}(\boldsymbol{q},\boldsymbol{q}') = \int \mathrm{d}^2\bar{q}\, \tilde{\eta}^{(m+1)}(\boldsymbol{q},\bar{\boldsymbol{q}})\, \tilde{\eta}^{(m)}(\bar{\boldsymbol{q}},\boldsymbol{q}') + \int \mathrm{d}^2\bar{q}\, \beta^{(m+1)}(\boldsymbol{q},\bar{\boldsymbol{q}})\, \left[\beta^{(m)}(\bar{\boldsymbol{q}},\boldsymbol{q}')\right]^*, \tag{A.25a}$$

$$\beta^{(m+1,m)}(\boldsymbol{q},\boldsymbol{q}') = \int \mathrm{d}^2\bar{q}\, \tilde{\eta}^{(m+1)}(\boldsymbol{q},\bar{\boldsymbol{q}})\, \beta^{(m)}(\bar{\boldsymbol{q}},\boldsymbol{q}') + \int \mathrm{d}^2\bar{q}\, \beta^{(m+1)}(\boldsymbol{q},\bar{\boldsymbol{q}})\, \left[\tilde{\eta}^{(m)}(\bar{\boldsymbol{q}},\boldsymbol{q}')\right]^*. \tag{A.25b}$$

Naturally, by generalizing from the expressions for the joint Schmidt decomposition as written in Eqs. (3.20), the joint Schmidt decomposition for the three-dimensional case can

be expected to take the following form:

$$\beta(\boldsymbol{q},\boldsymbol{q}') = \sum_n \sqrt{\Lambda_n}\, u_n(\boldsymbol{q})\, \psi_n(\boldsymbol{q}'), \tag{A.26a}$$

$$\tilde{\eta}(\boldsymbol{q},\boldsymbol{q}') = \sum_n \sqrt{\tilde{\Lambda}_n}\, u_n(\boldsymbol{q})\, \psi_n^*(\boldsymbol{q}'), \tag{A.26b}$$

where the Schmidt modes are now (complex-valued) functions over two real-valued arguments (the two components of the transverse wave-vectors). The form of the decomposition in Eqs. (A.26) can be justified as follows: Clearly, the transfer functions for the three-dimensional system must fulfill the relations

$$\int \mathrm{d}^2\bar{q}\, \beta(\bar{\boldsymbol{q}},\boldsymbol{q},L)\, \beta^*(\bar{\boldsymbol{q}},\boldsymbol{q}',L) + \delta(\boldsymbol{q}-\boldsymbol{q}') = \int \mathrm{d}^2\bar{q}\, \tilde{\eta}^*(\bar{\boldsymbol{q}},\boldsymbol{q},L)\, \tilde{\eta}(\bar{\boldsymbol{q}},\boldsymbol{q}',L), \tag{A.27a}$$

$$\int \mathrm{d}^2\bar{q}\, \tilde{\eta}^*(\bar{\boldsymbol{q}},\boldsymbol{q},L)\, \beta(\bar{\boldsymbol{q}},\boldsymbol{q}',L) = \int \mathrm{d}^2\bar{q}\, \beta(\bar{\boldsymbol{q}},\boldsymbol{q},L)\, \tilde{\eta}^*(\bar{\boldsymbol{q}},\boldsymbol{q}',L), \tag{A.27b}$$

$$\int \mathrm{d}^2\bar{q}\, \beta(\boldsymbol{q},\bar{\boldsymbol{q}},L)\, \beta^*(\boldsymbol{q}',\bar{\boldsymbol{q}},L) + \delta(\boldsymbol{q}-\boldsymbol{q}') = \int \mathrm{d}^2\bar{q}\, \tilde{\eta}(\boldsymbol{q},\bar{\boldsymbol{q}},L)\, \tilde{\eta}^*(\boldsymbol{q}',\bar{\boldsymbol{q}},L), \tag{A.27c}$$

$$\int \mathrm{d}^2\bar{q}\, \tilde{\eta}(\boldsymbol{q},\bar{\boldsymbol{q}},L)\, \beta(\boldsymbol{q}',\bar{\boldsymbol{q}},L) = \int \mathrm{d}^2\bar{q}\, \beta(\boldsymbol{q},\bar{\boldsymbol{q}},L)\, \tilde{\eta}(\boldsymbol{q}',\bar{\boldsymbol{q}},L), \tag{A.27d}$$

which follow by plugging the form of the solution of the integro-differential equations [Eqs. (A.20)] into the commutation relations [Eqs. (A.18)] and requiring that the operators at L also fulfill said commutation relations [1]. In the discrete case, the transverse wave-vectors $\boldsymbol{q}$ are sampled on equidistant grids of size N for each dimension, meaning $\boldsymbol{q}_{\varphi_x\varphi_y} = \begin{bmatrix} q_{x,\varphi_x} & q_{y,\varphi_y} \end{bmatrix}^\mathsf{T}$ with $q_{l,\varphi} = q_{l,0} + \varphi \mathrm{d}q$, where $l = x, y$, $\mathrm{d}q$ is the lattice spacing and $\varphi = 0, \ldots, N-1$. It is then possible to define a (finite) set $\{\alpha_j(\boldsymbol{q})\}_j$ of (discrete) functions

$$\alpha_j\big(\boldsymbol{q}_{\varphi_x,\varphi_y}\big) = \begin{cases} 1, & \varphi_x + N\varphi_y = j \\ 0, & \text{otherwise} \end{cases} \qquad \text{for } j = 0, \ldots, N^2-1 \tag{A.28}$$

representing orthonormalized functions, meaning that $\sum_{\boldsymbol{q}} \alpha_j(\boldsymbol{q})\, \alpha_k(\boldsymbol{q}) = \delta_{jk}$. In words, this function represents a *flattening* of the two indices φ_x and φ_y into a single index j. The discretized counterparts of the transfer functions $\tilde{\eta}$ and β can be expanded in terms of these basis functions, yielding the complex-valued coefficient matrices $\mathscr{H}$ and $\mathscr{B}$, respectively:

$$\tilde{\mathscr{H}}_{jk} = \sum_{\boldsymbol{q},\boldsymbol{q}'} \alpha_j(\boldsymbol{q})\, \alpha_k(\boldsymbol{q}')\, \tilde{\eta}(\boldsymbol{q},\boldsymbol{q}',L), \tag{A.29a}$$

$$\mathscr{B}_{jk} = \sum_{\boldsymbol{q},\boldsymbol{q}'} \alpha_j(\boldsymbol{q})\, \alpha_k(\boldsymbol{q}')\, \beta(\boldsymbol{q},\boldsymbol{q}',L). \tag{A.29b}$$

The expansions in terms of the basis functions then read

$$\tilde{\eta}(\boldsymbol{q},\boldsymbol{q}',L) = \sum_{j,k} \tilde{\mathscr{H}}_{jk} \alpha_j(\boldsymbol{q})\, \alpha_k(\boldsymbol{q}'), \tag{A.30a}$$

$$\beta(\boldsymbol{q},\boldsymbol{q}',L) = \sum_{j,k} \mathscr{B}_{jk} \alpha_j(\boldsymbol{q})\, \alpha_k(\boldsymbol{q}'). \tag{A.30b}$$

For the coefficient matrices, Eqs. (A.27) take the form

$$\tilde{\mathscr{K}}\tilde{\mathscr{K}}^{\mathsf{H}} - \mathscr{B}\mathscr{B}^{\mathsf{H}} = I_{N^2}\,, \tag{A.31a}$$

$$\tilde{\mathscr{K}}\mathscr{B}^{\mathsf{T}} - \mathscr{B}\tilde{\mathscr{K}}^{\mathsf{T}} = 0\,, \tag{A.31b}$$

and

$$\tilde{\mathscr{K}}^{\mathsf{H}}\tilde{\mathscr{K}} - \mathscr{B}^{\mathsf{T}}\mathscr{B}^{*} = I_{N^2}\,, \tag{A.32a}$$

$$\tilde{\mathscr{K}}^{\mathsf{H}}\mathscr{B} - \mathscr{B}^{\mathsf{T}}\tilde{\mathscr{K}}^{*} = 0\,, \tag{A.32b}$$

where I_N denotes the $N \times N$ identity matrix. Equations (A.31) may be written as [86]

$$\mathscr{Q}\mathcal{S}_{N^2}\mathscr{Q}^{\mathsf{H}} = \mathcal{S}_{N^2}\,, \tag{A.33}$$

where

$$\mathcal{S}_N = \begin{bmatrix} I_N & 0 \\ 0 & -I_N \end{bmatrix}, \tag{A.34}$$

$$\mathscr{Q} = \begin{bmatrix} \mathscr{K} & \mathscr{B} \\ \mathscr{B}^{*} & \mathscr{K}^{*} \end{bmatrix}. \tag{A.35}$$

Following Quesada *et al.* [86], this means that the coefficient matrices are elements of the SU(1,1) Lie group[2,3,4] and allow for a decomposition analogous to the joint Schmidt decomposition which, in matrix form, reads

$$\mathscr{B} = \mathscr{U}\mathcal{S}\mathscr{W}^{\mathsf{T}}, \tag{A.36a}$$

$$\tilde{\mathscr{K}} = \mathscr{U}\tilde{\mathcal{S}}\mathscr{W}^{\mathsf{H}}, \tag{A.36b}$$

where $\mathscr{U}$ and $\mathscr{W}$ are $N^2 \times N^2$ unitary matrices, $\mathcal{S}$ is the $N^2 \times N^2$ diagonal matrix containing the singular values and $\mathcal{S}^2 + I_{N^2} = \tilde{\mathcal{S}}^2$. Plugging Eqs. (A.36) into Eqs. (A.30) yields the discretized version of the decomposition of the transfer functions as written in Eqs. (A.26), with the modes

$$u_n(\boldsymbol{q}) = \sum_j \mathscr{U}_{jn}\alpha_j(\boldsymbol{q}), \tag{A.37a}$$

$$\psi_n(\boldsymbol{q}) = \sum_k \mathscr{W}_{kn}\alpha_k(\boldsymbol{q}), \tag{A.37b}$$

[2] For this reason, it is called "SU(1,1) interferometer".

[3] Note that Eqs. (A.33)–(A.35) is equivalent to $\mathscr{Q} \in \mathrm{Sp}(2N^2, \mathbb{C})$, compare also Eq. (4.17). This immediately implies that $\det(\mathscr{Q}) = 1$ [158–160].

[4] Strictly speaking, the SU(1,1) Lie group is usually defined via the matrices $Q = \left[\begin{smallmatrix} u & v \\ v^* & u^* \end{smallmatrix}\right] \in \mathbb{C}^{2\times 2}$ fulfilling $QSQ^{\mathsf{H}} = S$, where $S = \left[\begin{smallmatrix} 1 & 0 \\ 0 & -1 \end{smallmatrix}\right]$ [161] with $|u|^2 - |v|^2 = 1$. Hence, it would be more correct to say that $\mathscr{Q} \in \mathrm{SU}(n,n)$ (and here $n = N^2$), where $\mathrm{SU}(n,n)$ denotes the group of $n \times n$ *special pseudo-unitary matrices* which are defined by the fact that they fulfill $\mathscr{Q}\mathcal{S}_n\mathscr{Q}^{\mathsf{H}} = \mathcal{S}_n$ [see Eq. (A.33)], with $\mathcal{S}_n$ as defined in Eq. (A.34), and $\det(\mathscr{Q}) = 1$, compare Footnote 3 immediately above [162]. In the single-mode case with the plane-wave operator $\hat{a}$, the input-output relations take the form $\begin{bmatrix} \hat{a}^{(\mathrm{out})} \\ (\hat{a}^{(\mathrm{out})})^{\dagger} \end{bmatrix} = \mathscr{Q}\begin{bmatrix} \hat{a}^{(\mathrm{in})} \\ (\hat{a}^{(\mathrm{in})})^{\dagger} \end{bmatrix}$ [30, 31, 86]. By parametrizing $u = \cosh(r)$ and $v = \mathrm{e}^{\mathrm{i}\theta}\sinh(r)$, this input-output relation takes a form analogous to the Bogoliubov transformations for the Schmidt mode operators, compare Eqs. (3.23) and (4.23). Hence, for each mode, the transformation is analogous to the transformation of the SU(1,1) group.

and the singular value matrices

$$\mathcal{S} = \mathrm{diag}\Big(\sqrt{\Lambda_0}\,, \sqrt{\Lambda_1}\,, \ldots, \sqrt{\Lambda_{N^2-1}}\Big), \tag{A.37c}$$

$$\tilde{\mathcal{S}} = \mathrm{diag}\Big(\sqrt{\tilde{\Lambda}_0}\,, \sqrt{\tilde{\Lambda}_1}\,, \ldots, \sqrt{\tilde{\Lambda}_{N^2-1}}\Big). \tag{A.37d}$$

Equations (A.28)–(A.37) also reveal a way for numerically performing the joint Schmidt decomposition of the transfer functions in the three-dimensional case. First, the arrays representing β and $\tilde{\eta}$ are reshaped into $N^2 \times N^2$ matrices. Then, the algorithm performing the joint Schmidt decomposition as for example described in Ref. [4] is applied to these matrices, yielding the $N^2 \times N^2$ unitary matrices representing the modes as flattened vectors and the vector containing the singular values. Finally, the $N^2 \times N^2$ unitary matrices are reshaped into N^2 $N \times N$ matrices, which then represent the mode functions. This can be seen by following the actions of the $\alpha_j(\boldsymbol{q})$ in Eqs. (A.29) and Eqs. (A.30).

The aforementioned approach for the computation of the joint Schmidt decomposition can also be applied for the computation of the TPA in Schmidt mode theory. In general, in the three-dimensional system in Cartesian coordinates, this decomposition reads

$$F(\boldsymbol{q}_s, \boldsymbol{q}_i) = \sum_n \sqrt{\lambda_n}\, u_n(\boldsymbol{q}_s)\, v_n(\boldsymbol{q}_i). \tag{A.38}$$

This approach was utilized in Gehse [163] for the computation of the Schmidt decomposition of the TPA of SU(1,1) interferometers which can only be properly described in Cartesian coordinates. This was not necessary in Sharapova *et al.* [11] and Chapter 5 since it was possible to utilize the cylindrical symmetry of the system, see Sec. 5.2 in particular.

A.4.2. Cylindrical Frame: Pump with a Single OAM Component

A.4.2.1. General Case

Alternatively to Cartesian coordinates, the integro-differential equations (A.17) can be re-formulated in cylindrical coordinates:

$$\frac{\mathrm{d}\hat{a}_s(q_s, \phi_s, L)}{\mathrm{d}L} = \Gamma \iint \mathrm{d}q_i\, \mathrm{d}\phi_i\, q_i\, f(q_s, q_i, \phi_s, \phi_i, L)\, \hat{a}_i^\dagger(q_i, \phi_i, L), \tag{A.39a}$$

$$\frac{\mathrm{d}\hat{a}_i^\dagger(q_i, \phi_i, L)}{\mathrm{d}L} = \Gamma \iint \mathrm{d}q_s\, \mathrm{d}\phi_s\, q_s\, f^*(q_s, q_i, \phi_s, \phi_i, L)\, \hat{a}_s(q_s, \phi_s, L). \tag{A.39b}$$

Analogously, the solutions of the integro-differential equations take the form:

$$\begin{aligned} \hat{a}_s(q_s, \phi_s, L) = &\int \mathrm{d}q_s'\, \mathrm{d}\phi_s'\, q_s'\, \tilde{\eta}(q_s, \phi_s, q_s', \phi_s', L)\, \hat{a}_s(q_s', \phi_s') \\ &+ \int \mathrm{d}q_i'\, \mathrm{d}\phi_i'\, q_i'\, \beta(q_s, \phi_s, q_i', \phi_i', L)\, \hat{a}_i^\dagger(q_i', \phi_i'), \end{aligned} \tag{A.40a}$$

$$\begin{aligned} \hat{a}_i^\dagger(q_i, \phi_i, L) = &\int \mathrm{d}q_i'\, \mathrm{d}\phi_i'\, q_i'\, \tilde{\eta}^*(q_i, \phi_i, q_i', \phi_i', L)\, \hat{a}_i^\dagger(q_i', \phi_i') \\ &+ \int \mathrm{d}q_s'\, \mathrm{d}\phi_s'\, q_s'\, \beta^*(q_i, \phi_i, q_s', \phi_s', L)\, \hat{a}_s(q_s', \phi_s'). \end{aligned} \tag{A.40b}$$

By plugging the expression for the solutions into the integro-differential equations into Eqs. (A.39), the following sets of integro-differential equations for the transfer functions can be obtained:

$$\frac{\mathrm{d}\beta(q_s,\phi_s,q_i',\phi_i',L)}{\mathrm{d}L} = \Gamma \iint \mathrm{d}q_i\,\mathrm{d}\phi_i\,q_i\,f(q_s,q_i,\phi_s,\phi_i,L)\,\tilde{\eta}^*(q_i,\phi_i,q_i',\phi_i',L), \tag{A.41a}$$

$$\frac{\mathrm{d}\tilde{\eta}^*(q_i,\phi_i,q_i',\phi_i',L)}{\mathrm{d}L} = \Gamma \iint \mathrm{d}q_s\,\mathrm{d}\phi_s\,q_s\,f^*(q_s,q_i,\phi_s,\phi_i,L)\,\beta(q_s,\phi_s,q_i',\phi_i',L), \tag{A.41b}$$

as well as

$$\frac{\mathrm{d}\beta^*(q_i,\phi_i,q_s',\phi_s',L)}{\mathrm{d}L} = \Gamma \iint \mathrm{d}q_s\,\mathrm{d}\phi_s\,q_s\,f(q_s,q_i,\phi_s,\phi_i,L)\,\tilde{\eta}(q_s,\phi_s,q_s',\phi_s',L), \tag{A.42a}$$

$$\frac{\mathrm{d}\tilde{\eta}(q_s,\phi_s,q_s',\phi_s',L)}{\mathrm{d}L} = \Gamma \iint \mathrm{d}q_i\,\mathrm{d}\phi_i\,q_i\,f^*(q_s,q_i,\phi_s,\phi_i,L)\,\beta^*(q_i,\phi_i,q_s',\phi_s',L). \tag{A.42b}$$

Here, the same points regarding the symmetry $f(q_s,q_i,\phi_s,\phi_i,L) = f(q_i,q_s,\phi_i,\phi_s,L)$ as in Secs. A.1 and A.4.1 apply. Structurally, the only difference in Eqs. (A.39)–(A.42) compared to Eqs. (A.17) and (A.20)–(A.22) is that the former ones are written in terms of cylindrical coordinates. The initial value conditions are identical to Eqs. (A.23)–(A.25) with $\boldsymbol{q} \equiv (q,\phi)$ and $\mathrm{d}^2q = q\mathrm{d}q\mathrm{d}\phi$.

It should be noted that both for the Cartesian and cylindrical coordinate system, the numerical complexity is drastically increased compared to the two-dimensional system. Numerically, for the two-dimensional system, the transfer functions can be represented by $N \times N$ arrays (matrices) each, if N sampling points are used for the underlying signal and idler q-grids. For the three-dimensional system, the transfer functions are then instead represented by $N^2 \times N^2$ arrays, leading to dramatically increased memory and computation power demands. In cylindrical coordinates, this can be additionally more complicated due the fact that the point density along the azimuthal angle is lower for larger radial wave vectors.

Based on Sec. 5.2, it is possible to perform several simplifications if the function f describing the evolution of the transfer functions can be factorized in the following form:

$$f(q_s,q_i,\phi_s,\phi_i,L) = r(q_s,q_i,\phi_s-\phi_i,L)\,\mathrm{e}^{-\mathrm{i}l_p\phi_i}, \tag{A.43}$$

where now the function r can be written purely in terms of the azimuthal angle difference $\phi_s - \phi_i$. Furthermore, l_p refers to the OAM of the pump. This form for f is for example valid for PDC sections pumped with Laguerre-Gaussian beams, compare the steps leading up to Eqs. (5.17) and (5.18) and the derivation in Ref. [2]. It should be noted that, strictly speaking, l_p requires a superscript $^{(m)}$, which identifies the PDC section for which f as written above is the function that describes the evolution of the transfer functions, since, in general, l_p may differ from section to section. This index will be written out below where required.

In order to utilize the form of the function f as written in Eq. (A.43), the plane-wave operators $\hat{a}_s(q_s,\phi_s,L)$ and $\hat{a}_i^\dagger(q_i,\phi_i,L)$ are first expanded into Fourier series in terms of

the azimuthal angles ϕ_s and ϕ_i, so that

$$\hat{a}_s(q_s,\phi_s,L) = \frac{1}{2\pi}\sum_{n=-\infty}^{\infty} \hat{a}_{s,n}(q_s,L)\,\mathrm{e}^{-\mathrm{i}n\phi_s}\,, \tag{A.44a}$$

$$\hat{a}_i^\dagger(q_i,\phi_i,L) = \frac{1}{2\pi}\sum_{n=-\infty}^{\infty} \hat{a}_{i,n}^\dagger(q_i,L)\,\mathrm{e}^{\mathrm{i}n\phi_i}\,, \tag{A.44b}$$

which effectively rewrites the plane-wave operators in terms of OAM components. The integrals that can be used to obtain the (operator-valued) Fourier coefficients are given by:

$$\hat{a}_{s,n}(q_s,L) = \int_0^{2\pi} \mathrm{d}\phi_s\,\hat{a}_s(q_s,\phi_s,L)\,\mathrm{e}^{\mathrm{i}n\phi_s}\,, \tag{A.45a}$$

$$\hat{a}_{i,n}^\dagger(q_s,L) = \int_0^{2\pi} \mathrm{d}\phi_i\,\hat{a}_i^\dagger(q_i,\phi_i,L)\,\mathrm{e}^{-\mathrm{i}n\phi_i}\,. \tag{A.45b}$$

Using the Fourier expansions, the integro-differential equations for the plane wave operators take following form for f as given in Eq. (A.43):

$$\frac{\mathrm{d}\hat{a}_{s,n}(q_s,L)}{\mathrm{d}L} = \Gamma\int \mathrm{d}q_i\,q_i r_n(q_s,q_i,L)\,\hat{a}_{i,l_p-n}^\dagger(q_i,L), \tag{A.46a}$$

$$\frac{\mathrm{d}\hat{a}_{i,l_p-n}^\dagger(q_i,L)}{\mathrm{d}L} = \Gamma\int \mathrm{d}q_s\,q_s r_{-n}^*(q_s,q_i,L)\,\hat{a}_{s,n}(q_s,L). \tag{A.46b}$$

This follows from Eqs. (A.39) either by plugging in the Fourier expansions Eqs. (A.44) and sorting for terms with the same azimuthal dependence (the terms of the form $\mathrm{e}^{\mp\mathrm{i}n\phi_{s/i}}$, since they are orthogonal) or, more directly, by multiplying Eqs. (A.39a) and (A.39b) with $\mathrm{e}^{-\mathrm{i}n\phi_s}$ and $\mathrm{e}^{\mathrm{i}n\phi_i}$, respectively, and integrating over the azimuthal angle. For the latter case, the convolutions of the function r with the plane-wave operators lead to products[5] of the Fourier coefficients.

The Fourier expansion of r leading to the Fourier coefficients r_n as written in Eqs. (A.46) is given by

$$r(q_s,q_i,\phi_s-\phi_i,L) = \frac{1}{2\pi}\sum_{n=-\infty}^{\infty} r_n(q_s,q_i,L)\,\mathrm{e}^{-\mathrm{i}n(\phi_s-\phi_i)}\,, \tag{A.47}$$

while the Fourier coefficient integral is given by

$$r_n(q_s,q_i,L) = \int_0^{2\pi} \mathrm{d}(\phi_s-\phi_i)\,r(q_s,q_i,\phi_s-\phi_i,L)\,\mathrm{e}^{\mathrm{i}n(\phi_s-\phi_i)}\,. \tag{A.48}$$

Compare also Eqs. (5.19) and (5.20). Most notably, in Eqs. (A.46), the integro-differential equations only couple signal and idler operators which conserve the OAM of the pump

[5] This can be understood as a result of the convolution theorem. Let the Fourier coefficient integral for complex-valued 2π-periodic functions κ and ρ be defined as $\kappa_n = \int_0^{2\pi}\mathrm{d}\phi\,\kappa(\phi)\,\mathrm{e}^{\mathrm{i}n\phi}$ [compare Eq. (A.45a)]. Then, the two relevant forms of the convolution theorem read $\zeta(\phi) = \int_0^{2\pi}\mathrm{d}\phi'\,\kappa(\phi-\phi')\,\mathrm{e}^{-\mathrm{i}l\phi'}\,\rho^*(\phi') \Leftrightarrow \zeta_n = \kappa_n\rho_{l-n}^*$ and $\zeta^*(\phi) = \mathrm{e}^{\mathrm{i}l\phi}\int_0^{2\pi}\mathrm{d}\phi'\,\kappa^*(\phi-\phi')\,\rho(\phi') \Leftrightarrow \zeta_{l-n}^* = \kappa_{-n}^*\rho_n$, for $l\in\mathbb{Z}$. For operators, replacing * with † does not affect these statements.

[that is, $n + (l_p - n) = l_p$], unlike in Eqs. (A.39) where all azimuthal angles ϕ_s and ϕ_i are coupled via the two equations. In other words, in Eqs. (A.46), there are no sums over the OAM components on the right-hand side.

Transforming the form of the solutions [Eqs. (A.40)] to cylindrical coordinates and performing a Fourier decomposition yields

$$\begin{aligned}\hat{a}_{s,n}(q_s, L) = \frac{1}{2\pi}\sum_{n'}\int \mathrm{d}q_s'\, q_s' \tilde{\eta}_{nn'}(q_s, q_s', L)\, \hat{a}_{s,n'}(q_s') \\ + \frac{1}{2\pi}\sum_{n'}\int \mathrm{d}q_i'\, q_i' \beta_{nn'}(q_s, q_i', L)\, \hat{a}^\dagger_{i,l_p-n'}(q_i'),\end{aligned} \tag{A.49a}$$

$$\begin{aligned}\hat{a}^\dagger_{i,l_p-n}(q_i, L) = \frac{1}{2\pi}\sum_{n'}\int \mathrm{d}q_i'\, q_i' \tilde{\eta}^*_{l_p-n,l_p-n'}(q_i, q_i', L)\, \hat{a}^\dagger_{i,l_p-n'}(q_i') \\ + \frac{1}{2\pi}\sum_{n'}\int \mathrm{d}q_s'\, q_s' \beta^*_{l_p-n,l_p-n'}(q_i, q_s', L)\, \hat{a}_{s,n'}(q_s'),\end{aligned} \tag{A.49b}$$

where the expansions of the transfer functions are defined as

$$\tilde{\eta}_{nn'}(q, q') = \iint \mathrm{d}\phi\, \mathrm{d}\phi'\, \tilde{\eta}(q, \phi, q', \phi')\, \mathrm{e}^{\mathrm{i}n\phi}\mathrm{e}^{-\mathrm{i}n'\phi'}, \tag{A.50a}$$

$$\beta_{nn'}(q, q') = \iint \mathrm{d}\phi\, \mathrm{d}\phi'\, \beta(q, \phi, q', \phi')\, \mathrm{e}^{\mathrm{i}n\phi}\mathrm{e}^{\mathrm{i}(l_p-n')\phi'}, \tag{A.50b}$$

so that the Fourier coefficient integrals are given by

$$\tilde{\eta}(q, \phi, q', \phi') = \frac{1}{(2\pi)^2}\sum_{n,n'} \tilde{\eta}_{nn'}(q, q')\, \mathrm{e}^{-\mathrm{i}n\phi}\mathrm{e}^{\mathrm{i}n'\phi'}, \tag{A.51a}$$

$$\beta(q, \phi, q', \phi') = \frac{1}{(2\pi)^2}\sum_{n,n'} \beta_{nn'}(q, q')\, \mathrm{e}^{-\mathrm{i}n\phi}\mathrm{e}^{-\mathrm{i}(l_p-n')\phi'}. \tag{A.51b}$$

Comparing with Eqs. (5.38), the transfer functions appearing in Eqs. (A.49)–(A.51) depend on two indices resulting from the Fourier expansion over the two azimuthal angle arguments, so that one index is connected to the input operators and the other index is connected to the output operators.

Plugging Eqs. (A.49) into Eqs. (A.46) yields the integro-differential equations for the transfer functions:

$$\frac{\mathrm{d}\beta_{nn'}(q_s, q_i', L)}{\mathrm{d}L} = \Gamma \int \mathrm{d}q_i\, q_i\, r_n(q_s, q_i, L)\, \tilde{\eta}^*_{l_p-n,l_p-n'}(q_i, q_i', L), \tag{A.52a}$$

$$\frac{\mathrm{d}\tilde{\eta}^*_{l_p-n,l_p-n'}(q_i, q_i', L)}{\mathrm{d}L} = \Gamma \int \mathrm{d}q_s\, q_s\, r^*_{-n}(q_s, q_i, L)\, \beta_{nn'}(q_s, q_i', L), \tag{A.52b}$$

and

$$\frac{\mathrm{d}\beta^*_{l_p-n,l_p-n'}(q_i, q_s', L)}{\mathrm{d}L} = \Gamma \int \mathrm{d}q_s\, q_s\, r^*_{-n}(q_s, q_i, L)\, \tilde{\eta}_{nn'}(q_s, q_s', L), \tag{A.53a}$$

$$\frac{\mathrm{d}\tilde{\eta}_{nn'}(q_s, q_s', L)}{\mathrm{d}L} = \Gamma \int \mathrm{d}q_i\, q_i\, r_n(q_s, q_i, L)\, \beta^*_{l_p-n,l_p-n'}(q_i, q_s', L), \tag{A.53b}$$

Here, the discussions regarding the symmetry of r mentioned for Eqs. (A.41) and (A.42) above also apply. Note that if r is symmetric under the exchange of ϕ_s and ϕ_i, then $r_n = r_{-n}$, which follows from Eq. (A.48).

After dropping the $_s$ and $_i$ subscripts of the transverse wave-vector components for readability, the initial value conditions when integrating the system section-by-section take the form

$$\beta^{(m+1,\mathrm{in})}_{n,l_p^{(m+1)}-n'}(q,q') = \beta^{(m,\mathrm{out})}_{n,l_p^{(m)}-n'}(q,q'), \tag{A.54a}$$

$$\tilde{\eta}^{(m+1,\mathrm{in})}_{nn'}(q,q') = \tilde{\eta}^{(m,\mathrm{out})}_{nn'}(q,q'), \tag{A.54b}$$

$$\beta^{(1,\mathrm{in})}_{nn'}(q,q') = 0, \tag{A.54c}$$

$$\tilde{\eta}^{(1,\mathrm{in})}_{nn'}(q,q') = 2\pi\delta_{nn'}\frac{\delta(q-q')}{q}, \tag{A.54d}$$

which can be seen by writing out Eqs. (A.49) for both sections, shifting the indices of the input plane-wave operators appropriately and comparing the expression for both sections. As mentioned above, the pump OAM l_p may generally vary from PDC section to PDC section. As such, in Eqs. (A.54) above, the superscripts $^{(m)}$ and $^{(m+1)}$ have also been added to l_p.

For the case where each section is integrated separately, the initial value conditions take the (l_p-independent) form

$$\beta^{(m,\mathrm{in})}_{nn'}(q,q') = 0, \tag{A.55a}$$

$$\tilde{\eta}^{(m,\mathrm{in})}_{nn'}(q,q') = 2\pi\delta_{nn'}\frac{\delta(q-q')}{q}, \tag{A.55b}$$

for each section m. These results follow by performing the Fourier decompositions of both sides of Eqs. (A.23) and (A.24). The connection relations are constructed as described in Sec. 3.2. Here, it must again be taken into account that l_p may vary from section to section.

After combining the input-output relations for both sections, the resulting expression is again brought to the form as in Eqs. (A.49). Ultimately, the connection relations for the transfer functions of two consecutive sections with indices m and $m+1$ read:

$$\begin{aligned}\tilde{\eta}^{(m+1,m)}_{nn'}(q,q') = {}& \frac{1}{2\pi}\sum_{\bar{n}}\int \mathrm{d}\bar{q}\,\bar{q}\,\tilde{\eta}^{(m+1)}_{n\bar{n}}(q,\bar{q})\,\tilde{\eta}^{(m)}_{\bar{n}n'}(\bar{q},q') \\ & + \frac{1}{2\pi}\sum_{\bar{n}}\int \mathrm{d}\bar{q}\,\bar{q}\,\beta^{(m+1)}_{n\bar{n}}(q,\bar{q})\left[\beta^{(m)}_{l_p^{(m+1)}-\bar{n},l_p^{(m)}-n'}(\bar{q},q')\right]^*,\end{aligned} \tag{A.56a}$$

$$\begin{aligned}\beta^{(m+1,m)}_{nn'}(q,q') = {}& \frac{1}{2\pi}\sum_{\bar{n}}\int \mathrm{d}\bar{q}\,\bar{q}\,\tilde{\eta}^{(m+1)}_{n\bar{n}}(q,\bar{q})\,\beta^{(m)}_{\bar{n},l_p^{(m)}-l_p^{(m+1)}+n'}(\bar{q},q') \\ & + \frac{1}{2\pi}\sum_{\bar{n}}\int \mathrm{d}\bar{q}\,\bar{q}\,\beta^{(m+1)}_{n\bar{n}}(q,\bar{q})\left[\tilde{\eta}^{(m)}_{l_p^{(m+1)}-\bar{n},l_p^{(m+1)}-n'}(\bar{q},q')\right]^*.\end{aligned} \tag{A.56b}$$

For the input-output relations for the plane-wave operators as written in Eqs. (A.49), the relationships required for the commutation relations to be preserved [Eqs. (A.27)] can

be written in the following form after applying the Fourier decomposition to the transfer functions:

$$\begin{aligned}\frac{1}{2\pi}\sum_{\bar{n}}\int \mathrm{d}\bar{q}\,\bar{q}\,\beta_{\bar{n},l_p-n}(\bar{q},q,L)\,\beta^*_{\bar{n},l_p-n'}(\bar{q},q',L)+2\pi\delta_{nn'}\frac{\delta(q-q')}{q}\\ =\frac{1}{2\pi}\sum_{\bar{n}}\int \mathrm{d}\bar{q}\,\bar{q}\,\tilde{\eta}^*_{\bar{n}n}(\bar{q},q,L)\,\tilde{\eta}_{\bar{n}n'}(\bar{q},q',L),\end{aligned} \tag{A.57a}$$

$$\frac{1}{2\pi}\sum_{\bar{n}}\int \mathrm{d}\bar{q}\,\bar{q}\,\tilde{\eta}^*_{\bar{n}n}(\bar{q},q,L)\,\beta_{\bar{n},l_p-n'}(\bar{q},q',L)=\frac{1}{2\pi}\sum_{\bar{n}}\int \mathrm{d}\bar{q}\,\bar{q}\,\beta_{\bar{n},l_p-n}(\bar{q},q,L)\,\tilde{\eta}^*_{\bar{n},n'}(\bar{q},q',L), \tag{A.57b}$$

which are equivalent to Eqs. (4.18a) and (4.18b), respectively, and

$$\begin{aligned}\frac{1}{2\pi}\sum_{\bar{n}}\int \mathrm{d}\bar{q}\,\bar{q}\,\beta_{n,l_p-\bar{n}}(q,\bar{q},L)\,\beta^*_{n',l_p-\bar{n}}(q',\bar{q},L)+2\pi\delta_{nn'}\frac{\delta(q-q')}{q}\\ =\frac{1}{2\pi}\sum_{\bar{n}}\int \mathrm{d}\bar{q}\,\bar{q}\,\tilde{\eta}_{n\bar{n}}(q,\bar{q},L)\,\tilde{\eta}^*_{n'\bar{n}}(q',\bar{q},L),\end{aligned} \tag{A.58a}$$

$$\frac{1}{2\pi}\sum_{\bar{n}}\int \mathrm{d}\bar{q}\,\bar{q}\,\tilde{\eta}_{n\bar{n}}(q,\bar{q},L)\,\beta_{n',l_p-\bar{n}}(q',\bar{q},L)=\frac{1}{2\pi}\sum_{\bar{n}}\int \mathrm{d}\bar{q}\,\bar{q}\,\beta_{n,l_p-\bar{n}}(q,\bar{q},L)\,\tilde{\eta}_{n'\bar{n}}(q',\bar{q},L), \tag{A.58b}$$

which are equivalent to Eqs. (4.19a) and (4.19b), respectively.

By the same argument as with Eqs. (A.27) above, these relations imply that the discretized versions of the functions $\sqrt{qq'}\,\beta_{n,l_p-n'}(q,q')/(2\pi)$ and $\sqrt{qq'}\,\tilde{\eta}_{nn'}(q,q')/(2\pi)$ admit a joint Schmidt decomposition of the form

$$\beta_{n,l_p-n'}(q,q')=2\pi\sum_m\sqrt{\Lambda_{mnn'}}\,\frac{u_{mn}(q)}{\sqrt{q}}\,\frac{\psi_{mn'}(q')}{\sqrt{q'}}, \tag{A.59a}$$

$$\tilde{\eta}_{nn'}(q,q')=2\pi\sum_m\sqrt{\tilde{\Lambda}_{mnn'}}\,\frac{u_{mn}(q)}{\sqrt{q}}\,\frac{\psi^*_{mn'}(q')}{\sqrt{q'}}, \tag{A.59b}$$

so that the radial mode functions $u_{mn}(q)$ and $\psi_{mn}(q)$ fulfill the orthonormality conditions

$$\sum_n\int \mathrm{d}q\,u_{mn}(q)\,u^*_{m'n}(q)=\delta_{mm'}\,, \tag{A.60a}$$

$$\sum_n\int \mathrm{d}q\,\psi_{mn}(q)\,\psi^*_{m'n}(q)=\delta_{mm'}\,. \tag{A.60b}$$

Note that the integrals do not contain additional factors q, similar to the orthonormality relations in Eqs. (5.23) for the Schmidt decomposition in the context of the Schmidt mode theory approach. These observations follow from the same argument regarding the flattening of the indices of the numerical grids presented in Sec. A.4.1. Here, the flattening is performed over the two discrete indices of β and $\tilde{\eta}$, as well as their two discretized radial wave-vector component arguments q and q'.

Shifting $l_p-n'\to n'$ in Eq. (A.59a) and applying the Fourier decompositions backwards

to Eqs. (A.59) [see Eqs. (A.51)] yields:

$$\beta(q,\phi,q',\phi') = \frac{1}{2\pi}\sum_{m,n,n'}\sqrt{\Lambda_{mnn'}}\,\frac{u_{mn}(q)}{\sqrt{q}}\,\frac{\psi_{m,l_p-n'}(q')}{\sqrt{q'}}\mathrm{e}^{-\mathrm{i}n\phi}\mathrm{e}^{-\mathrm{i}(l_p-n')\phi'}, \tag{A.61a}$$

$$\tilde{\eta}(q,\phi,q',\phi') = \frac{1}{2\pi}\sum_{m,n,n'}\sqrt{\tilde{\Lambda}_{mnn'}}\,\frac{u_{mn}(q)}{\sqrt{q}}\,\frac{\psi^*_{mn'}(q')}{\sqrt{q'}}\mathrm{e}^{-\mathrm{i}n\phi}\mathrm{e}^{\mathrm{i}n\phi'}. \tag{A.61b}$$

A.4.2.2. Simplification for Identical Pump OAM in Each Section

General Derivation. In Eqs. (A.49)–(A.57) and (A.59)–(A.61) above, the transfer functions carry two indices related to the Fourier decompositions and later the input and output modes each carry distinct indices n and n' in Eqs. (A.59) and (A.61). Comparing Eqs. (A.61) with Eqs. (5.79) suggests that it should be possible to rewrite the equations above using a single Fourier decomposition index. In fact, this is possible as long as all PDC sections have the same value of l_p. This can be seen as follows:

- For the approach where first each PDC section is integrated separately, this can be seen as follows: The initial condition for $\tilde{\eta}$, as written in Eq. (A.55b), is only nonzero for $n = n'$. Additionally, in the integro-differential equations for the transfer functions, Eqs. (A.52) and (A.53), the second index of $\tilde{\eta}^{(*)}$ only[6] also appears as the second index of β. Thus, if $n \neq n'$, then[7] $\tilde{\eta}^{(m)} = 0$ and $\beta^{(m)} = 0$ for any m, l_p, L, $q_s^{(\prime)}$ and $q_i^{(\prime)}$. In other words, the transfer functions for each individual section are diagonal in the two indices. This is however not generally the case for the composite transfer functions connecting the input and output operators of different PDC sections, as evident from Eqs. (A.56). Here, the diagonal structure is only preserved if $l_p^{(m)} = l_p^{(m+1)}$.

- A similar observation can be made for the initial value conditions as written in Eqs. (A.54) for the approach where the sections are integrated consecutively. Initially, at the first PDC section, see Eqs. (A.54c) and (A.54d), only the diagonal elements of the transfer functions are non-vanishing. Then, when transitioning between the PDC sections, see Eqs. (A.54a) and (A.54b), the transfer function β may acquire non-vanishing off-diagonal elements if $l_p^{(m)} \neq l_p^{(m+1)}$.

With these observations, it is possible to greatly simplify the integro-differential equations and their solutions for the case when all PDC sections have the same l_p. Evidently, Eqs. (A.43)–(A.48) remain unchanged regardless of whether these simplifications are

[6] This is not the case for example for the integro-differential equations as written in Eqs. (A.21) and (A.22) when using the initial value conditions written in Eq. (A.24b): Here, due to the integral over $\boldsymbol{q}_i$ in Eq. (A.21a) and over $\boldsymbol{q}_s$ in Eq. (A.22a), the right-hand sides of the integro-differential equations are always nonzero for any $\boldsymbol{q}_i'$ and $\boldsymbol{q}_s'$, respectively.

[7] More precisely, the initial value condition first implies $\tilde{\eta}^{(m)} = 0$, meaning $\beta^{(m)} = \text{const.}$ as per Eqs. (A.52a) and (A.53a). The initial value condition for β then implies $\beta^{(m)} = 0$.

applied. Mathematically, the simplification can be implemented by setting

$$\beta_{nn'}(q,q') = 2\pi\beta_n(q,q')\,\delta_{nn'}\,, \tag{A.62a}$$

$$\tilde{\eta}_{nn'}(q,q') = 2\pi\tilde{\eta}_n(q,q')\,\delta_{nn'}\,, \tag{A.62b}$$

so that the input-output relations for the plane wave operators become

$$\hat{a}_{s,n}(q_s,L) = \int \mathrm{d}q_s'\, q_s'\,\tilde{\eta}_n(q_s,q_s',L)\,\hat{a}_{s,n}(q_s') + \int \mathrm{d}q_i'\, q_i'\,\beta_n(q_s,q_i',L)\,\hat{a}^\dagger_{i,l_p-n}(q_i'), \tag{A.63a}$$

$$\hat{a}^\dagger_{i,l_p-n}(q_i,L) = \int \mathrm{d}q_i'\, q_i'\,\tilde{\eta}^*_{l_p-n}(q_i,q_i',L)\,\hat{a}^\dagger_{i,l_p-n}(q_i') + \int \mathrm{d}q_s'\, q_s'\,\beta^*_{l_p-n}(q_i,q_s',L)\,\hat{a}_{s,n}(q_s'). \tag{A.63b}$$

Clearly, these relations only couple OAM components n and $l_p - n$ corresponding to complementary OAM values with respect to the OAM of the pump.

The Fourier expansions in Eqs. (A.51) become:

$$\beta(q,\phi,q',\phi') = \frac{\mathrm{e}^{-\mathrm{i}l_p\phi'}}{2\pi}\sum_n \beta_n(q,q')\,\mathrm{e}^{-\mathrm{i}n(\phi-\phi')}\,, \tag{A.64a}$$

$$\tilde{\eta}(q,q',\phi-\phi') = \frac{1}{2\pi}\sum_n \tilde{\eta}_n(q,q')\,\mathrm{e}^{-\mathrm{i}n(\phi-\phi')}\,. \tag{A.64b}$$

Evidently, the transfer function $\tilde{\eta}$ can be written in terms of the azimuthal angle difference $\phi - \phi'$, while β can not. The Fourier coefficient integrals take the form:

$$\tilde{\eta}_n(q,q') = \int \mathrm{d}(\phi-\phi')\,\tilde{\eta}(q,q',\phi-\phi')\,\mathrm{e}^{\mathrm{i}n(\phi-\phi')}\,, \tag{A.65a}$$

$$\beta_n(q,q') = \frac{1}{2\pi}\iint \mathrm{d}\phi\,\mathrm{d}\phi'\,\beta(q,\phi,q',\phi')\,\mathrm{e}^{\mathrm{i}n\phi}\mathrm{e}^{\mathrm{i}(l_p-n)\phi'}\,. \tag{A.65b}$$

These two equations follow for example as the inverse transformations of Eqs. (A.64) or by applying Eqs. (A.62) to Eqs. (A.50) and simplifying the azimuthal angle difference integrals for $\tilde{\eta}$. Equations (A.64a) and (A.65b) can be further rewritten as

$$\beta^{\{l_p\}}(q,q',\phi-\phi') = \frac{1}{2\pi}\sum_n \beta_n(q,q')\,\mathrm{e}^{-\mathrm{i}n(\phi-\phi')}\,, \tag{A.66a}$$

$$\beta_n(q,q') = \int \mathrm{d}(\phi-\phi')\,\beta^{\{l_p\}}(q,q',\phi-\phi')\,\mathrm{e}^{\mathrm{i}n(\phi-\phi')}\,, \tag{A.66b}$$

respectively, where

$$\beta^{\{l_p\}}(q,q',\phi-\phi') \overset{\text{def.}}{=} \beta(q,\phi,q',\phi')\,\mathrm{e}^{\mathrm{i}l_p\phi'}\,, \tag{A.66c}$$

which follows from the fact that β can be written in terms of the angle differences.

Under the abovementioned simplifications, the integro-differential equations reduce to

$$\frac{\mathrm{d}\beta_n(q_s,q_i',L)}{\mathrm{d}L} = \Gamma\int \mathrm{d}q_i\, q_i\, r_n(q_s,q_i,L)\,\tilde{\eta}^*_{l_p-n}(q_i,q_i',L), \tag{A.67a}$$

$$\frac{\mathrm{d}\tilde{\eta}^*_{l_p-n}(q_i,q_i',L)}{\mathrm{d}L} = \Gamma\int \mathrm{d}q_s\, q_s\, r^*_{-n}(q_s,q_i,L)\,\beta_n(q_s,q_i',L), \tag{A.67b}$$

and

$$\frac{\mathrm{d}\beta^*_{l_p-n}(q_i,q'_s,L)}{\mathrm{d}L} = \Gamma \int \mathrm{d}q_s\, q_s\, r^*_{-n}(q_s,q_i,L)\, \tilde{\eta}_n(q_s,q'_s,L), \tag{A.67c}$$

$$\frac{\mathrm{d}\tilde{\eta}_n(q_s,q'_s,L)}{\mathrm{d}L} = \Gamma \int \mathrm{d}q_i\, q_i\, r_n(q_s,q_i,L)\, \beta^*_{l_p-n}(q_i,q'_s,L). \tag{A.67d}$$

These can again be integrated using the sequential approach of integrating each section consecutively, with the initial value conditions given by

$$\beta_n^{(m+1,\mathrm{in})}(q,q') = \beta_n^{(m,\mathrm{out})}(q,q'), \tag{A.68a}$$

$$\tilde{\eta}_n^{(m+1,\mathrm{in})}(q,q') = \tilde{\eta}_n^{(m,\mathrm{out})}(q,q'), \tag{A.68b}$$

$$\beta_n^{(1,\mathrm{in})}(q,q') = 0, \tag{A.68c}$$

$$\tilde{\eta}_n^{(1,\mathrm{in})}(q,q') = \frac{1}{q}\delta(q-q'). \tag{A.68d}$$

Alternatively, each section can be integrated separately using the initial value conditions

$$\beta_n^{(m,\mathrm{in})}(q,q') = 0, \tag{A.69a}$$

$$\tilde{\eta}_n^{(m,\mathrm{in})}(q,q') = \frac{1}{q}\delta(q-q') \tag{A.69b}$$

in combination with the connection relations, which here take the following form:

$$\tilde{\eta}_n^{(m+1,m)}(q,q') = \int \mathrm{d}\bar{q}\,\bar{q}\,\tilde{\eta}_n^{(m+1)}(q,\bar{q})\,\tilde{\eta}_n^{(m)}(\bar{q},q') + \int \mathrm{d}\bar{q}\,\bar{q}\,\beta_n^{(m+1)}(q,\bar{q})\left[\beta_{l_p-n}^{(m)}(\bar{q},q')\right]^*, \tag{A.70a}$$

$$\beta_n^{(m+1,m)}(q,q') = \int \mathrm{d}\bar{q}\,\bar{q}\,\tilde{\eta}_n^{(m+1)}(q,\bar{q})\,\beta_n^{(m)}(\bar{q},q') + \int \mathrm{d}\bar{q}\,\bar{q}\,\beta_n^{(m+1)}(q,\bar{q})\left[\tilde{\eta}_{l_p-n}^{(m)}(\bar{q},q')\right]^*, \tag{A.70b}$$

where it has been used that $l_p = l_p^{(m+1)} = l_p^{(m)}$, compare Eqs. (A.56).

Equations (A.57), which describe restrictions to the transfer functions required for the preservation of the commutation relations for the output plane-wave operators, reduce to

$$\int \mathrm{d}\bar{q}\,\bar{q}\,\beta_n(q,\bar{q},L)\,\beta_n^*(q',\bar{q},L) + \frac{1}{q}\delta(q-q') = \int \mathrm{d}\bar{q}\,\bar{q}\,\tilde{\eta}_n(q,\bar{q},L)\,\tilde{\eta}_n^*(q',\bar{q},L), \tag{A.71a}$$

$$\int \mathrm{d}\bar{q}\,\bar{q}\,\tilde{\eta}_n(q,\bar{q},L)\,\beta_{l_p-n}(q',\bar{q},L) = \int \mathrm{d}\bar{q}\,\bar{q}\,\beta_n(q,\bar{q},L)\,\tilde{\eta}_{l_p-n}(q',\bar{q},L), \tag{A.71b}$$

$$\int \mathrm{d}\bar{q}\,\bar{q}\,\beta_{l_p-n}(\bar{q},q,L)\,\beta^*_{l_p-n}(\bar{q},q',L) + \frac{1}{q}\delta(q-q') = \int \mathrm{d}\bar{q}\,\bar{q}\,\tilde{\eta}_n^*(\bar{q},q,L)\,\tilde{\eta}_n(\bar{q},q',L), \tag{A.71c}$$

$$\int \mathrm{d}\bar{q}\,\bar{q}\,\tilde{\eta}_n^*(\bar{q},q,L)\,\beta_n(\bar{q},q',L) = \int \mathrm{d}\bar{q}\,\bar{q}\,\beta_{l_p-n}(\bar{q},q,L)\,\tilde{\eta}^*_{l_p-n}(\bar{q},q',L), \tag{A.71d}$$

meaning that the transfer functions admit a joint Schmidt decomposition of the form

$$\beta_n(q,q') = \sum_m \sqrt{\Lambda_{mn}}\,\frac{u_{mn}(q)}{\sqrt{q}}\,\frac{\psi_{m,l_p-n}(q')}{\sqrt{q'}}, \tag{A.72a}$$

$$\tilde{\eta}_n(q,q') = \sum_m \sqrt{\tilde{\Lambda}_{mn}}\,\frac{u_{mn}(q)}{\sqrt{q}}\,\frac{\psi^*_{mn}(q')}{\sqrt{q'}}, \tag{A.72b}$$

which follows by the same arguments as above. Note that in Eqs. (A.72), the index $l_p - n$ of ψ may be moved to ψ^* by redefining $\psi_{mn} \to \psi_{m,l_p-n}$. The form of the decomposition for $\beta_n(q, q')$ follows for example by comparing with Eq. (A.59a) and by closely inspecting Eqs. (A.71b) and (A.71d). Note that generally, the decomposition has not the same form as the decomposition for the two-dimensional system as introduced in Eqs. (3.20) due to the fact that different indices appear on the input modes ψ in Eqs. (A.72a) and (A.72b). The radial mode functions u_m and ψ_m are orthonormalized so that

$$\int \mathrm{d}q\, u_m(q)\, u^*_{m'}(q) = \delta_{mm'}\,, \tag{A.73a}$$

$$\int \mathrm{d}q\, \psi_m(q)\, \psi^*_{m'}(q) = \delta_{mm'}\,. \tag{A.73b}$$

Plugging the decomposition in Eqs. (A.72) into Eqs. (A.64) yields

$$\beta(q, \phi, q', \phi') = \frac{1}{2\pi} \sum_{m,n} \sqrt{\Lambda_{mn}}\, \frac{u_{mn}(q)}{\sqrt{q}}\, \frac{\psi_{m,l_p-n}(q')}{\sqrt{q'}} \mathrm{e}^{-\mathrm{i}n\phi} \mathrm{e}^{-\mathrm{i}(l_p-n)\phi'}\,, \tag{A.74a}$$

$$\tilde{\eta}(q, q', \phi - \phi') = \frac{1}{2\pi} \sum_{m,n} \sqrt{\tilde{\Lambda}_{mn}}\, \frac{u_{mn}(q)}{\sqrt{q}}\, \frac{\psi^*_{mn}(q')}{\sqrt{q'}} \mathrm{e}^{-\mathrm{i}n(\phi-\phi')}\,. \tag{A.74b}$$

These equations suggest that the Schmidt modes should be defined as

$$U_{mn}(q, \phi) = \frac{1}{\sqrt{2\pi}}\, \frac{u_{mn}(q)}{\sqrt{q}} \mathrm{e}^{-\mathrm{i}n\phi}\,, \tag{A.75a}$$

$$\Psi_{mn}(q, \phi) = \frac{1}{\sqrt{2\pi}}\, \frac{\psi_{mn}(q)}{\sqrt{q}} \mathrm{e}^{-\mathrm{i}n\phi}\,, \tag{A.75b}$$

which fulfill the orthonormality relations

$$\int \mathrm{d}^2q\, U_{mn}(q, \phi)\, U^*_{m'n'}(q, \phi) = \delta_{mm'}\delta_{nn'}\,, \tag{A.76a}$$

$$\int \mathrm{d}^2q\, \Psi_{mn}(q, \phi)\, \Psi^*_{m'n'}(q, \phi) = \delta_{mm'}\delta_{nn'}\,. \tag{A.76b}$$

Overall, the transfer functions written in terms of the Schmidt modes are given by

$$\beta(q, \phi, q', \phi') = \sum_{m,n} \sqrt{\Lambda_{mn}}\, U_{mn}(\boldsymbol{q})\, \Psi_{m,l_p-n}(\boldsymbol{q}), \tag{A.77a}$$

$$\tilde{\eta}(q, q', \phi - \phi') = \sum_{m,n} \sqrt{\tilde{\Lambda}_{mn}}\, U_{mn}(\boldsymbol{q})\, \Psi^*_{m,n}(\boldsymbol{q}). \tag{A.77b}$$

This form of the joint Schmidt decomposition is slightly different from Eqs. (3.20) and (A.26) in that the input modes appearing in $\tilde{\eta}$ and β are not simply the complex conjugate of each other. The same observation also applies to the decompositions in Eqs. (A.59) after shifting $l_p - n' \to n$ and Eqs. (A.61). This form of the decomposition coincides with the decomposition for the transfer functions for the Schmidt mode theory results as written in Eqs. (5.38) and (5.79), provided that $u_{mn}(q) = \psi_{mn}(q)$. Note however that generally $u_{mn}(q) \neq \psi_{mn}(q)$ for the integro-differential equation formalism, see Sec. 4.2.

The input-output relations for the plane-wave operators as written in Eqs. (A.63) can be rewritten in terms of the azimuthal angles using Eqs. (A.45), (A.65), (A.66b) and (A.66c). The resulting expression has the same form as Eqs. (A.40). By plugging Eqs. (A.74) into said expression, it is possible to obtain the expressions for the input and output Schmidt operators, as described in the text surrounding Eqs. (3.24). In terms of the two-dimensional mode functions, these expressions read

$$\hat{A}_{mn}^{(\mathrm{in})} = \int \mathrm{d}^2 q\, \Psi_{mn}^*(\boldsymbol{q})\, \hat{a}_s^{(\mathrm{in})}(\boldsymbol{q}), \tag{A.78a}$$

$$\hat{A}_{mn}^{(\mathrm{out})} = \int \mathrm{d}^2 q\, U_{mn}^*(\boldsymbol{q})\, \hat{a}_s^{(\mathrm{out})}(\boldsymbol{q}), \tag{A.78b}$$

$$\hat{B}_{mn}^{(\mathrm{in})} = \int \mathrm{d}^2 q\, \Psi_{m,l_p-n}^*(\boldsymbol{q})\, \hat{a}_i^{(\mathrm{in})}(\boldsymbol{q}), \tag{A.78c}$$

$$\hat{B}_{mn}^{(\mathrm{out})} = \int \mathrm{d}^2 q\, U_{m,l_p-n}^*(\boldsymbol{q})\, \hat{a}_i^{(\mathrm{out})}(\boldsymbol{q}), \tag{A.78d}$$

with $\boldsymbol{q} \equiv (q, \phi)$ and $\mathrm{d}^2 q = q \mathrm{d}q \mathrm{d}\phi$, so that the Bogoliubov transformations for the Schmidt operators read

$$\hat{A}_{mn}^{(\mathrm{out})} = \sqrt{\tilde{\Lambda}_{mn}}\, \hat{A}_{mn}^{(\mathrm{in})} + \sqrt{\Lambda_{mn}}\, \left[\hat{B}_{mn}^{(\mathrm{in})}\right]^\dagger, \tag{A.79a}$$

$$\hat{B}_{mn}^{(\mathrm{out})} = \sqrt{\tilde{\Lambda}_{m,l_p-n}}\, \hat{B}_{mn}^{(\mathrm{in})} + \sqrt{\Lambda_{m,l_p-n}}\, \left[\hat{A}_{mn}^{(\mathrm{in})}\right]^\dagger. \tag{A.79b}$$

Note that in the degenerate case where $\hat{a}_s = \hat{a}_i$, for example for frequency-degenerate type-I PDC, where the signal and idler plane-wave modes coincide, the Bogoliubov transformations written above can be reduced to a single equation, since the Schmidt operators then fulfill $\hat{A}_{mn}^{(\mathrm{in})} = \hat{B}_{m,l_p-n}^{(\mathrm{in})}$ and $\hat{A}_{mn}^{(\mathrm{out})} = \hat{B}_{m,l_p-n}^{(\mathrm{out})}$. Replacing $n \to l_p - n$ in Eq. (A.79a) then results in Eq. (A.79b) and vice versa.

Special Case: Even Function r and $l_p = 0$. If the function r describing the evolution of the integro-differential equations is even in the angle difference, meaning

$$r(q_s, q_i, \phi_s - \phi_i, L) = r(q_s, q_i, \phi_i - \phi_s, L), \tag{A.80}$$

then it follows from the Fourier coefficient integral in Eq. (A.48) that

$$r_n(q_s, q_i, L) = r_{-n}(q_s, q_i, L). \tag{A.81}$$

The property of r written in Eq. (A.80) holds for example for the special case $l_p = 0$ and in the following, the discussion will be restricted to this case. Then, the above results represent the extension of Ref. [5] to the fully three-dimensional system and the extension of Ref. [1] to the integro-differential equation formalism. Applying Eq. (A.81) to the integro-differential equations (A.67) shows that

$$\beta_n(q_s, q_i) = \beta_{-n}(q_s, q_i), \tag{A.82a}$$

$$\tilde{\eta}_n(q_s, q_i) = \tilde{\eta}_{-n}(q_s, q_i). \tag{A.82b}$$

Comparing with Eqs. (A.72) implies, due to the uniqueness of the singular values, that

$$\Lambda_{mn} = \Lambda_{m,-n}\,, \tag{A.83a}$$
$$\tilde{\Lambda}_{mn} = \tilde{\Lambda}_{m,-n}\,. \tag{A.83b}$$

Furthermore, the aforementioned equations also imply that it is possible to construct a decomposition of the transfer functions in which the modes may be chosen so that

$$u_{mn}(q) = u_{m,-n}(q), \tag{A.84a}$$
$$\psi_{mn}(q) = \psi_{m,-n}(q). \tag{A.84b}$$

Note that for *any* given decomposition of the transfer functions, the Schmidt modes do not necessarily have to fulfill the relationship written in Eqs. (A.84). This is due to the fact that for a given n, the decomposition written in Eqs. (A.72) may not be unique, meaning that different modes may be chosen for n and $-n$. In the simplest case, these may differ in their sign. Ultimately, for this particular case, the transfer functions admit a decomposition of the form

$$\beta_n(q,q') = \sum_m \sqrt{\Lambda_{mn}}\,\frac{u_{mn}(q)}{\sqrt{q}}\,\frac{\psi_{mn}(q')}{\sqrt{q'}}, \tag{A.85a}$$
$$\tilde{\eta}_n(q,q') = \sum_m \sqrt{\tilde{\Lambda}_{mn}}\,\frac{u_{mn}(q)}{\sqrt{q}}\,\frac{\psi^*_{mn}(q')}{\sqrt{q'}}, \tag{A.85b}$$

which has the same form as the joint Schmidt decomposition for the two-dimensional case as written in Eqs. (3.20), apart from the fact that the q variables refer to the radial transverse wave-vector components and the factors $1/\sqrt{q}$ and $1/\sqrt{q'}$ appearing on the right-hand side due to this.

A.5. Low-Gain Expansions of the Integro-Differential Equations

In general, the integro-differential equations as written in Eqs. (3.7) or Eqs. (A.17) can only be solved numerically. Several approximations are applicable in order to obtain an analytic approximation, for example the plane-wave pump limit as shown in Sec. 3.5.2. Another possible case where an approximation of the solutions can be obtained is in the low-gain limit for $\Gamma \ll 1$. In this case, a common approach is to perform power series expansions in terms of powers of Γ for the plane-wave operators that are the solutions of the differential equations:

$$\hat{a}_s(\boldsymbol{q}_s, L) = \sum_{n=0}^{\infty} \Gamma^n \hat{a}_s^{[n]}(\boldsymbol{q}_s, L), \tag{A.86a}$$
$$\hat{a}_i(\boldsymbol{q}_i, L) = \sum_{n=0}^{\infty} \Gamma^n \hat{a}_i^{[n]}(\boldsymbol{q}_i, L), \tag{A.86b}$$

where $\hat{a}_s^{[n]}(\boldsymbol{q}_s, L)$ and $\hat{a}_i^{[n]}(\boldsymbol{q}_i, L)$ denote the nth order components of the operator proportional to Γ^n. Note that here, the transverse wave-vector components are treated as vector-valued, as in Sec. A.4.

Plugging the expansion in Eqs. (A.86) into the integro-differential equations (A.17) and sorting by orders of Γ yields recursive integro-differential equations for the components of the plane-wave operators:

$$\frac{\mathrm{d}\hat{a}_s^{[n]}(\boldsymbol{q}_s, L)}{\mathrm{d}L} = \Gamma \int \mathrm{d}^\nu q_i \, f(\boldsymbol{q}_s, \boldsymbol{q}_i, L) \left[\hat{a}_i^{[n-1]}(\boldsymbol{q}_i, L)\right]^\dagger, \tag{A.87a}$$

$$\frac{\mathrm{d}\left[\hat{a}_i^{[n]}(\boldsymbol{q}_i, L)\right]^\dagger}{\mathrm{d}L} = \Gamma \int \mathrm{d}^\nu q_s \, f^*(\boldsymbol{q}_s, \boldsymbol{q}_i, L) \, \hat{a}_s^{[k-1]}(\boldsymbol{q}_s, L), \tag{A.87b}$$

for $n > 0$ and where $\nu = 1$ or $\nu = 2$, depending on how many transverse dimensions are included in the model, and

$$\frac{\mathrm{d}\hat{a}_s^{[0]}(\boldsymbol{q}_s, L)}{\mathrm{d}L} = 0, \tag{A.88a}$$

$$\frac{\mathrm{d}\left[\hat{a}_i^{[0]}(\boldsymbol{q}_i, L)\right]^\dagger}{\mathrm{d}L} = 0, \tag{A.88b}$$

for the lowest-order operator components. The differential equations for these lowest-order operators can be solved immediately:

$$\hat{a}_s^{[0]}(\boldsymbol{q}_s, L) = \hat{a}_s^{(\mathrm{in})}(\boldsymbol{q}_s), \tag{A.89a}$$

$$\left[\hat{a}_i^{[0]}(\boldsymbol{q}_i, L)\right]^\dagger = \left[\hat{a}_i^{(\mathrm{in})}(\boldsymbol{q}_i, L)\right]^\dagger, \tag{A.89b}$$

where the operators on the right-hand side are the input operators of the PDC section for which the integro-differential equations are to be solved.

Plugging Eqs. (A.89) into Eqs. (A.87) yields the solutions for the first order components. The full solution[8] up until (including) the first order is given by the partial sums of the expansions as written in Eqs. (A.86):

$$\hat{a}_s^{(\mathrm{out})}(\boldsymbol{q}_s, L) = \hat{a}_s^{(\mathrm{in})}(\boldsymbol{q}_s) + \Gamma \int \mathrm{d}^\nu q_i \left(\int_{L_0}^{L} \mathrm{d}L' \, f(\boldsymbol{q}_s, \boldsymbol{q}_i, L')\right) \left[\hat{a}_i^{(\mathrm{in})}(\boldsymbol{q}_i)\right]^\dagger, \tag{A.90a}$$

$$\left[\hat{a}_i^{(\mathrm{out})}(\boldsymbol{q}_i, L)\right]^\dagger = \left[\hat{a}_i^{(\mathrm{in})}(\boldsymbol{q}_i)\right]^\dagger + \Gamma \int \mathrm{d}^\nu q_s \left(\int_{L_0}^{L} \mathrm{d}L' \, f(\boldsymbol{q}_s, \boldsymbol{q}_i, L')\right)^* \hat{a}_s^{(\mathrm{in})}(\boldsymbol{q}_s), \tag{A.90b}$$

where L_0 marks the appropriate lower boundary for the PDC section under consideration. The expression in the parentheses containing the L'-integral over the function $f(\boldsymbol{q}_s, \boldsymbol{q}_i, L')$ is, apart from the normalization factor, equal to the TPA from Schmidt mode theory, compare the construction of f in Sharapova *et al.* [5] with the computation of the TPA, for example in Ref. [2]. Furthermore, comparing the input-output relations for the plane-wave

[8] Note that a proper convergence analysis of the solution is required, which is beyond the scope of this work.

operators in Eqs. (A.90) with the form of the solutions of the integro-differential equations as written in Eqs. (3.10) and (A.20), yields

$$\beta(\boldsymbol{q}_s, \boldsymbol{q}_i', L) = \Gamma \int_{L_0}^{L} \mathrm{d}L'\, f(\boldsymbol{q}_s, \boldsymbol{q}_i', L'), \tag{A.91a}$$

$$\beta^*(\boldsymbol{q}_i, \boldsymbol{q}_s', L) = \Gamma \int_{L_0}^{L} \mathrm{d}L'\, f^*(\boldsymbol{q}_s', \boldsymbol{q}_i, L'), \tag{A.91b}$$

$$\tilde{\eta}\big(\boldsymbol{q}_{s/i}, \boldsymbol{q}_{s/i}', L\big) = \delta\big(\boldsymbol{q}_{s/i} - \boldsymbol{q}_{s/i}'\big). \tag{A.91c}$$

Note that Eqs. (A.91a) and (A.91b) contradict each other unless either f is symmetrical in the wave-vector arguments or * does not actually refer to the complex conjugate for β and instead just labels β^* as different from β. This is due to the fact that the form of the solutions as written in Eqs. (3.10) and (A.20) assumes that the signal and idler photons are indistinguishable, see also Secs. A.1 and A.4. Furthermore, it should be noted that the transfer functions obtained this way do not necessarily preserve the symplectic structure of the solution as described by Eqs. (A.27) due to the truncation of the power series. For example, Eqs. (A.91) do not generally fulfill Eqs. (A.27a) and (A.27c).

Due to the connection to the TPA, it follows that, at low gain, where it is sufficient to truncate the power series for the operators after the first order,

$$\beta(\boldsymbol{q}, \boldsymbol{q}') = \frac{\Gamma}{C} F(\boldsymbol{q}, \boldsymbol{q}'), \tag{A.92}$$

where

$$F(\boldsymbol{q}, \boldsymbol{q}') = C \int \mathrm{d}L'\, f(\boldsymbol{q}_s', \boldsymbol{q}_i, L') \tag{A.93}$$

was identified as the normalized TPA and C is the normalization constant to ensure $\iint \mathrm{d}^\nu q\, \mathrm{d}^\nu q'\, |F(\boldsymbol{q}, \boldsymbol{q}')|^2 = 1$. If the photons in the plane-wave modes are indistinguishable, the function f is symmetric in the wave-vector arguments, as mentioned above. As a consequence, for low gain, $\beta(\boldsymbol{q}, \boldsymbol{q}') = \beta(\boldsymbol{q}', \boldsymbol{q})$.

A.6. Uniqueness of the Schmidt Modes in the General Case

Following the same idea as in Ref. [4], the uniqueness of the modes can be understood by considering the discretized versions of the transfer functions and their singular value decompositions. In this discretized form, the transfer functions are sampled over discrete grids representing the transverse wave-vector components q. If these q-grids consist of N points, the transfer functions are represented by complex-valued $N \times N$ matrices. Let $A \in \mathbb{C}^{N \times N}$ be such a matrix. Then, its singular value decomposition is given by [111, 164, 165]

$$A = Y \Sigma W^{\mathrm{H}}, \tag{A.94}$$

with $Y, W \in \mathrm{U}(N)$, where $\mathrm{U}(N)$ denotes the unitary group of $N \times N$ matrices, and $\Sigma = \mathrm{diag}(\sigma_1, \sigma_2, \ldots, \sigma_N)$ is a diagonal matrix with positive entries containing the singular values σ_n. Here and in the following, the symbol $^{\mathrm{H}}$ will denote the hermitian conjugate of a matrix or vector. Usually, the singular values are taken to be sorted in descending order along the diagonal of Σ. In index notation, Eq. (A.94) takes the form

$$A = \sum_{n=1}^{N} \sigma_n \boldsymbol{y}_n \otimes \boldsymbol{w}_n^{\mathrm{H}}, \tag{A.95}$$

where $\boldsymbol{y}_n, \boldsymbol{w}_n \in \mathbb{C}^N$ are the columns of Y and W, respectively, σ_n is the nth entry on the diagonal of Σ, see above, and $\otimes$ denotes the dyadic product. It is well known that this singular value matrix Σ is unique for a given choice of A [164, 165]. However, the unitary matrices Y and W are not unique, even if all singular values are unique. In general, the singular values may be repeated with multiplicities $\mu_1, \mu_2, \ldots, \mu_P \in \mathbb{N}_1$, so that $\sum_p \mu_p = N$, meaning that there are P unique singular values. By splitting the sum over n in Eq. (A.95) into a sum over the unique singular values and one sum over the multiplicity of each unique singular value, the equation may be rewritten as

$$A = \sum_{p=1}^{P} \sum_{r=1}^{\mu_p} \sigma_p \boldsymbol{y}_{p;r} \otimes \boldsymbol{w}_{p;r}^{\mathrm{H}}, \tag{A.96}$$

where σ_p is the pth singular value with multiplicity μ_p and $\boldsymbol{y}_{p;r}$ and $\boldsymbol{w}_{p;r}^{*}$ are the columns of Y and W associated with the singular value σ_p. The index $r = 1, \ldots, \mu_p$ refers to the index of each singular vector within the left and right subspaces belonging to σ_p. Note that here and in the following, for vectors and matrices, the symbol * will denote the element-wise complex conjugate. For the pth unique singular value, the vectors indexed with r are the columns with index

$$n = r + \sum_{l=1}^{p-1} \mu_l \tag{A.97}$$

of the full matrices Y and W. The notation introduced above is summarized in Fig. A.2.

Theorem 3.1.1′ of Horn and Johnson [165] states that if $A = \bar{V}\Sigma\bar{W}^{\mathrm{H}}$ is *any* SVD of A, then *all possible* SVDs can be obtained by multiplying the column vectors $\bar{\boldsymbol{y}}_p$ and $\bar{\boldsymbol{w}}_p$ (of $\bar{V}$ and $\bar{W}$, respectively) associated with the unique singular value σ_p by an arbitrary unitary matrix $V_p \in \mathrm{U}(\mu_p)$ (which may also be independently chosen for each singular value):

$$\boldsymbol{y}_{p;r} = \sum_{m=1}^{\mu_p} \bar{\boldsymbol{y}}_{p;m} V_{p;mr}, \tag{A.98a}$$

$$\boldsymbol{w}_{p;r} = \sum_{m=1}^{\mu_p} \bar{\boldsymbol{w}}_{p;m} V_{p;mr}, \tag{A.98b}$$

where $\boldsymbol{y}_{p;r}$ and $\boldsymbol{w}_{p;r}$ are the resulting possible choices for the column vectors of the unitary matrices in the SVD. Note that for simple singular values with multiplicity $\mu_p = 1$, these unitary transformations are mediated by the circle group $\mathrm{U}(1) = \{\mathrm{e}^{\mathrm{i}\Phi} | \Phi \in [0, 2\pi[\}$, that is,

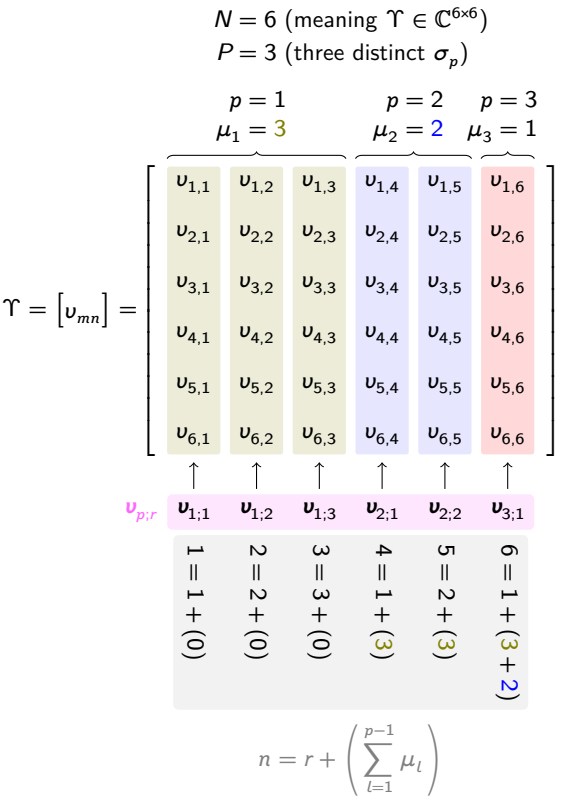

Figure A.2: Illustration of the index notation used to address the multiplicities of the singular values. The complex-valued 6×6 matrix Υ is a placeholder for either the left-hand side unitary Y or the right-hand side unitary W of the SVD as written in Eq. (A.94). Its columns $\boldsymbol{\upsilon}$ represent then either the singular vectors $\boldsymbol{y}$ or $\boldsymbol{w}$, respectively. As an example, the three unique singular values ($P = 3$) are chosen to have multiplicities $\mu_1 = 3$, $\mu_2 = 2$ and $\mu_3 = 1$ and the columns are color-coded accordingly. Below each column of the matrix, the indexed vectors $\upsilon_{p;r}$ as first introduced in Eq. (A.96) are listed. Underneath each of these vectors, it is shown how Eq. (A.97) connects the index $r = 1, \dots, \mu_p$ of the modes within the subspaces to the global index $n = 1, \dots, N$ inside the full matrix Υ. The parts in parentheses correspond to the sum over the multiplicities. For the first block ($p = 1$), the sum is empty and n and r coincide. For the second block, the sum only contains the multiplicity $\mu_1 = 3$ of the first block. For the third block, the sum is additionally over the multiplicity of the second block, $\mu_2 = 2$.

the rotations are mediated by simple phase factors $V_{p;mr} = \mathrm{e}^{\mathrm{i}\Phi_{p;mr}}$, for $\Phi_{p;mr} \in [0, 2\pi[$ and only $m = r = 1$. In words, given any potential SVD of $A = Y\Sigma W^{\mathrm{H}}$, all possible SVDs can be obtained by performing unitary rotations in the (degenerate) subspaces spanned the *any* potential set of columns of Y and W.

The discrete form of the Schmidt decomposition for N discrete modes was already described in Sec. 4.1. When the integro-differential equations are solved numerically, the transfer functions $\tilde{\eta}$ and β are represented by two matrices, which here will be labeled with the corresponding uppercase letters $\tilde{\mathrm{H}}$ and B, respectively, as was introduced above. If the underlying computational grids for the transverse wave-vector components consist of N points $q_1, q_2, \dots, q_N$, the *joint* Schmidt decomposition is, apart from lattice spacing factors $\mathrm{d}q$ resulting from the fact that integrals are replaced by sums, given by the decomposition as written in Eqs. (4.20). Since the $\boldsymbol{u}_n$ and $\boldsymbol{\psi}_n$ are the left-hand and right-hand singular vectors of $\tilde{\mathrm{H}}$, respectively, see Eq. (4.24b), they are not unique and all potential candidates for these vectors are described by Eqs. (A.98). Since the singular values are connected via $\tilde{\Lambda}_n = 1 + \Lambda_n$, compare Eq. (3.21), the multiplicities μ_p must the same for both B and $\tilde{\mathrm{H}}$. Numerically, this may not be precisely the case due to rounding errors, where then $\tilde{\Lambda}_n \neq 1 + \Lambda_n$. This issue is more prevalent for large Λ_n due to the loss of floating point precision, leading to erroneous equalities such as "$\Lambda_n + 1 = \Lambda_n$" for $\Lambda_n \ggg 0$.

Let $\bar{S} = \left(\{\bar{\boldsymbol{u}}_{p;m}\}_{pm}, \{\bar{\boldsymbol{\psi}}_{p;m}\}_{pm}\right)$ denote the column vectors of $\bar{U}$ and $\bar{\Psi}$ of any potential joint decomposition of B and $\tilde{\mathrm{H}}$ and let $S = \left(\{\boldsymbol{u}_{p;m}\}_{pm}, \{\boldsymbol{\psi}_{p;m}\}_{pm}\right)$ denote *any other* potential set that may provide an alternative result for the decomposition. The modes in these two sets must be related via Eqs. (A.98). Written out analogously to Eq. (A.96), for the set $\bar{S}$, the decomposition takes the form

$$\mathrm{B} = \sum_{p=1}^{P} \sqrt{\Lambda_p} \sum_{r=1}^{\mu_p} \bar{\boldsymbol{u}}_{p;r} \otimes \bar{\boldsymbol{\psi}}_{p;r}^{\mathtt{T}}, \tag{A.99a}$$

$$\tilde{\mathrm{H}} = \sum_{p=1}^{P} \sqrt{\tilde{\Lambda}_p} \sum_{r=1}^{\mu_p} \bar{\boldsymbol{u}}_{p;r} \otimes \bar{\boldsymbol{\psi}}_{p;r}^{\mathtt{H}}. \tag{A.99b}$$

Clearly,

$$\bar{\boldsymbol{u}}_{p';r'}^{\mathtt{H}} \mathrm{B} \bar{\boldsymbol{\psi}}_{p'';r''}^{*} = \sqrt{\Lambda_{p'}}\, \delta_{p'p''} \delta_{r'r''}, \tag{A.100a}$$

$$\bar{\boldsymbol{u}}_{p';r'}^{\mathtt{H}} \tilde{\mathrm{H}} \bar{\boldsymbol{\psi}}_{p'';r''} = \sqrt{\tilde{\Lambda}_{p'}}\, \delta_{p'p''} \delta_{r'r''}, \tag{A.100b}$$

which follows from the fact that

$$\bar{\boldsymbol{u}}_{p;r} \cdot \bar{\boldsymbol{u}}_{p';r'}^{*} = \delta_{pp'} \delta_{rr'}, \tag{A.101a}$$

$$\bar{\boldsymbol{\psi}}_{p;r} \cdot \bar{\boldsymbol{\psi}}_{p';r'}^{*} = \delta_{pp'} \delta_{rr'}, \tag{A.101b}$$

which itself follows from the unitarity of the matrices $\bar{U}$ and $\bar{\Psi}$.

Rewriting the joint decomposition in terms of the modes in the set S and applying Eqs. (A.98) yields

$$\mathrm{B} = \sum_{p=1}^{P} \sqrt{\Lambda_p} \sum_{m,m'=1}^{\mu_p} \left(\sum_{r=1}^{\mu_p} V_{p;mr} V_{p;m'r} \right) \bar{\boldsymbol{u}}_{p;m} \otimes \bar{\boldsymbol{\psi}}_{p;m'}^{\mathtt{T}}, \tag{A.102a}$$

$$\tilde{\mathrm{H}} = \sum_{p=1}^{P} \sqrt{\tilde{\Lambda}_p} \sum_{m,m'=1}^{\mu_p} \left(\sum_{r=1}^{\mu_p} V_{p;mr} V_{p;m'r}^{*} \right) \bar{\boldsymbol{u}}_{p;m} \otimes \bar{\boldsymbol{\psi}}_{p;m'}^{\mathtt{H}}. \tag{A.102b}$$

Clearly, Eqs. (A.100) must hold regardless of which set of modes (S or $\bar{S}$) is used to express the decomposition. Forming these matrix elements for the decompositions as written in Eqs. (A.102) yields

$$\bar{\boldsymbol{u}}_{p';r'}^{\mathtt{H}} \mathrm{B} \bar{\boldsymbol{\psi}}_{p'';r''}^{*} = \sqrt{\Lambda_{p'}}\, \delta_{p'p''} \left(\sum_{r=1}^{\mu_p} V_{p;r'r} V_{p;r''r} \right), \tag{A.103a}$$

$$\bar{\boldsymbol{u}}_{p';r'}^{\mathtt{H}} \tilde{\mathrm{H}} \bar{\boldsymbol{\psi}}_{p'';r''} = \sqrt{\tilde{\Lambda}_{p'}}\, \delta_{p'p''} \left(\sum_{r=1}^{\mu_p} V_{p;r'r} V_{p;r''r}^{*} \right). \tag{A.103b}$$

Comparing Eqs. (A.103) with Eqs. (A.100) shows that the V_p must be restricted by[9]

$$V_p V_p^{\mathtt{T}} = I_{\mu_p}, \tag{A.104a}$$

$$V_p V_p^{\mathtt{H}} = I_{\mu_p}, \tag{A.104b}$$

[9]Equations (A.104) follow from the fact that regardless of which form of the decomposition is used for B and $\tilde{\mathrm{H}}$, the matrix elements $\bar{\boldsymbol{u}}_{p';r'}^{\mathtt{H}} \mathrm{B} \bar{\boldsymbol{\psi}}_{p'';r''}^{*}$ and $\bar{\boldsymbol{u}}_{p';r'}^{\mathtt{H}} \tilde{\mathrm{H}} \bar{\boldsymbol{\psi}}_{p'';r''}$ must have a single, well-defined value.

respectively, where I_{μ_p} denotes the identity matrix of size μ_p. The first restriction [Eq. (A.104a)] implies that $V_p \in \mathrm{O}(\mu_p, \mathbb{C})$, where $\mathrm{O}(\mu_p, \mathbb{C})$ denotes the complex orthogonal group of size μ_p. The second restriction [Eq. (A.104b)] is fulfilled by assumption, since it only implies that $V_p \in \mathrm{U}(\mu_p)$. Combined, they imply that $V_p \in \mathrm{U}(\mu_p) \cap \mathrm{O}(\mu_p, \mathbb{C})$. The intersection of these two groups is the real orthogonal group[10] $\mathrm{O}(\mu_p, \mathbb{R})$:

$$\mathrm{U}(\mu_p) \cap \mathrm{O}(\mu_p, \mathbb{C}) = \mathrm{O}(\mu_p, \mathbb{R}), \tag{A.105}$$

meaning that the V_p are restricted to real orthogonal matrices:

$$V_p \in \mathrm{O}(\mu_p, \mathbb{R}). \tag{A.106}$$

Transferring this result back to the continuous case, it becomes clear that the joint decomposition of the transfer functions imposes a restriction on the modes, so that for each subspace associated with the unique eigenvalues, the potential choices for the modes are not connected by unitary rotations, but only by real orthogonal rotations. For *simple singular values* with multiplicity $\mu_p = 1$, this observation reduces back to the case presented in Ref. [4]: The group $\mathrm{O}(1, \mathbb{R})$ consists only of the two 1×1 matrices ± 1. Hence, the mode pair (u_p, ψ_p) may be replaced by $(-u_p, -\psi_p)$ [4].

It should be noted that the above discussion neglects the *null space* of the decomposition. In general, for a singular value decomposition as for example written in Eq. (A.95) or Eq. (A.96), only a certain number of the N singular values is nonzero. Thus, the singular values σ_n, ordered in descending order, can be split into two parts: First, M monotonically decreasing singular values, followed by K singular values which are zero (simply called the null space in the following), so that $M + K = N$. The discussions in the above part of this section apply directly to the M monotonically decreasing nonzero singular values. Due to the fact that the singular values for this part of the decomposition are all zero ($\sigma_p = 0$), the summation over r in Eq. (A.96) for this block ($\mu_p = K$) does not actually contribute to A. Instead, the purpose of the corresponding columns $\boldsymbol{y}_{p;r}$ and $\boldsymbol{w}_{p;r}$ of the left- and right-hand side unitarity matrices Y and W, which are then said to span the left- and right-hand side null space, respectively, is only to fill the matrices to N columns so that they become square matrices. As such, following again Theorem 3.1.1′ of Horn and Johnson [165], the connection between the possible singular vectors for the pth singular value as written in Eqs. (A.98) takes a different form for the null space:

$$\boldsymbol{y}_{p;r} = \sum_{m=1}^{\mu_p} \bar{\boldsymbol{y}}_{p;m} V'_{p;mr}\,, \tag{A.107a}$$

$$\boldsymbol{w}_{p;r} = \sum_{m=1}^{\mu_p} \bar{\boldsymbol{w}}_{p;m} V''_{p;mr}\,, \tag{A.107b}$$

[10] This may be seen as follows: Complex conjugating Eq. (A.104a) yields $V_p^* V_p^{\mathrm{H}} = I_{\mu_p}$. Multiplying this with V_p from the left and applying $V_p^{\mathrm{H}} V_p = I_{\mu_p}$, which follows from the unitarity of V_p [and Eq. (A.104b)], shows that $V^* = V$, meaning $V \in \mathbb{R}^{\mu_p \times \mu_p}$. Combining this with Eq. (A.104a) implies $V_p \in \mathrm{O}(\mu_p, \mathbb{R})$. Since $\mathrm{O}(N, \mathbb{R})$ is also a subgroup of both $\mathrm{U}(N)$ and $\mathrm{O}(N, \mathbb{C})$, it must be the intersection of both. See also Problem 14 of Sec. 2.1 of Ref. [166].

with $V_p', V_p'' \in \mathrm{U}(\mu_p)$, but where, compared to Eqs. (A.98), in general, $V_p' \neq V_p''$.

For the joint Schmidt decomposition as written in Eqs. (A.100), only the decomposition for B has a null space. This is due to the fact that the singular values are connected via $\sqrt{\tilde{\Lambda}_n} = \sqrt{\Lambda_n + 1}$, meaning that the decomposition of $\tilde{\mathrm{H}}$ never has singular values which are zero. Thus, both decompositions for B and $\tilde{\mathrm{H}}$ have different restrictions on the potential columns of the left- and right-hand side unitary matrices: For B, the restriction is described by Eqs. (A.107), while for $\tilde{\mathrm{H}}$, it is given by Eqs. (A.98).

Following the above discussions, Eqs. (A.103) for the null space become:

$$\bar{\boldsymbol{u}}^{\mathrm{H}}_{p';r'} \mathrm{B} \bar{\boldsymbol{\psi}}^{*}_{p'';r''} = \sqrt{\Lambda_{p'}}\, \delta_{p'p''} \left(\sum_{r=1}^{\mu_p} V_{p;r'r} V_{p;r''r} \right) = 0\,, \tag{A.108a}$$

$$\bar{\boldsymbol{u}}^{\mathrm{H}}_{p';r'} \tilde{\mathrm{H}} \bar{\boldsymbol{\psi}}_{p'';r''} = \sqrt{\tilde{\Lambda}_{p'}}\, \delta_{p'p''} \left(\sum_{r=1}^{\mu_p} V_{p;r'r} V^{*}_{p;r''r} \right) = \delta_{p'p''} \left(\sum_{r=1}^{\mu_p} V_{p;r'r} V^{*}_{p;r''r} \right), \tag{A.108b}$$

since $\sqrt{\Lambda_{p'}} = 0$ and $\sqrt{\tilde{\Lambda}_{p'}} = 1$. Note that in Eq. (A.108a), the two matrices V_p and V_p are identical, despite the fact that above, it was found that for B, the matrices for the left- and right-hand side matrices are different. This is due to the fact that the general form of the column vectors for the null space must still be compatible with the decomposition of $\tilde{\mathrm{H}}$, which imposes the restriction that the columns of the left- and right-hand side unitary matrices are multiplied by the same unitary matrix, as written in Eqs. (A.98) for the SVD. Thus, overall, the restriction on V_p for the null space is, instead of Eqs. (A.104), only

$$V_p V_p^{\mathrm{H}} = I_{\mu_p}\,. \tag{A.109}$$

Therefore, for the null space, V_p is actually allowed to be unitary instead of just real orthogonal, as was the case for all nonzero singular values, see the discussion leading up to Eq. (A.106). Overall, due to the fact that $\sqrt{\Lambda_{p'}} = 0$ for the null space, the modes associated with these singular values are solely defined by the decomposition of $\tilde{\mathrm{H}}$.

Usually, especially at high gain, the null space is only of low practical relevance for theoretical applications due to the fact that the eigenvalues for this space are very small compared to those of the lower order modes. Additionally, the fact that these modes are only used to fill the left- and right-hand unitary matrices up to N columns, implies that these modes do not actually carry any physical meaning and are not experimentally detectable. In fact, following for example the method for the experimental detection of these modes described in Sec. 4.3.2, the modes of the null space do not actually contribute to the covariance distribution and therefore, their approximate modulus cannot be obtained from the decomposition of the covariance function.

In the low gain limit, the eigenvalues of the transfer function β approach 0, while those of $\tilde{\eta}$ approach 1, compare Sec. 4.2.1. This means the overall, the entire range of eigenvalues approaches the null space and in numerical applications, they may get sufficiently small that they are effectively 0 due to the finite precision. Thus, in the low-gain limit, the modes are also only unique up to unitary rotations.

B

Appendix: Phase-Matching Functions for the Diffraction-Compensated Configuration

B.1. The Paraxial Propagation of Light

Wave Equations. In order to understand how the diffraction compensation is facilitated, it is first necessary to examine the propagation of light and its behavior under the influence of certain optical elements. The propagation of waves of the electric field $\tilde{\boldsymbol{E}}(\boldsymbol{r}, t)$ in linear homogeneous isotropic media with refractive index n for the relevant frequency components is described by the wave equation [157]

$$\nabla^2 \tilde{\boldsymbol{E}} - \frac{n^2}{c_0^2} \frac{\partial^2 \tilde{\boldsymbol{E}}}{\partial t^2} = 0, \tag{B.1}$$

which is derived from Maxwell's equations and where c_0 denotes the speed of light in vacuum [143, 156]. Assuming a monochromatic and harmonic time dependence $\mathrm{e}^{-\mathrm{i}\omega t}$ for the electric field, as well as a fixed polarization direction, so that the field can be written as $\tilde{\boldsymbol{E}}(\boldsymbol{r}, t) = \tilde{u}(\boldsymbol{r})\, \mathrm{e}^{-\mathrm{i}\omega t} \boldsymbol{e}$, with $\boldsymbol{e}$ denoting the unit polarization vector, the wave equation (B.1) reduces to the time-independent Helmholtz equation

$$\nabla^2 \tilde{u} = -k^2 \tilde{u}, \tag{B.2}$$

where $k = |\boldsymbol{k}| = n\omega/c_0$ is the modulus of the wave-vector.

Paraxial Wave Equation. Usually, the system has a distinguished direction, which is the general propagation direction of the light. For the PDC systems as described throughout this work, this direction would for example be along the z-axis, parallel to which both the pump and the signal-idler radiation primarily propagate. As such, the field is usually

split into its longitudinal and transverse components with respect to the main propagation direction of the fields in the system. Based on this, the longitudinal direction will also be chosen as the z-direction in the following. This splitting also led from the form of the electric field operator as written in Eq. (2.38), to its form in Eq. (2.41), where the integration over the spatial modes is only over the transverse plane and additionally over the frequency. The state of the electric field over different transverse planes $z = \text{const.}$ is described by the complex-valued function $\tilde{u}(x, y; z)$. The spatial propagation of the electric field is then modeled by successively applying transformations to $\tilde{u}(x, y; z)$ which correspond to the free propagation of the field or optical elements. This way, the input field $\tilde{u}(x, y; z_{\text{start}})$ at the initial coordinate z_{start} is transformed into the output field $\tilde{u}(x', y'; z_{\text{end}})$ at the final z-coordinate z_{end} of the system. Furthermore, it is often useful to further split the field $\tilde{u}(x, y; z)$ into the slowly varying envelope $\tilde{\psi}(x, y; z)$ (also called the *wavefront* in the following) and a rapidly oscillating part $\mathrm{e}^{\mathrm{i}kz}$ along the propagation axis via [143]:

$$\tilde{u}(x, y; z) = \tilde{\psi}(x, y; z)\, \mathrm{e}^{\mathrm{i}kz}. \tag{B.3}$$

When dealing with a layered system, that is, a system where the refractive index varies along the z-axis, $\tilde{u}$ may instead be written as

$$\tilde{u}(x, y; z) = \tilde{\psi}(x, y; z)\, \mathrm{e}^{\mathrm{i}S(z)}, \tag{B.4}$$

where

$$S(z) = \int_{z_{\text{ref}}}^{z} \mathrm{d}z'\, k(z') \tag{B.5}$$

is the total phase of the carrier wave at z, related to the *Eikonal phase* [60, 157] and z_{ref} is the z-coordinate defining the reference phase (often chosen as $z_{\text{ref}} = 0$). This assumes that boundary effects where the refractive index varies between the regions can be neglected. Due to the fact that $\tilde{\psi}(x, y; z)$ is slowly varying, [143]

$$\left| \frac{\partial^2 \tilde{\psi}}{\partial z^2} \right| \ll 2k \left| \frac{\partial \tilde{\psi}}{\partial z} \right|. \tag{B.6}$$

Plugging Eq. (B.3) into the Helmholtz equation (B.2) and applying Eq. (B.6) yields the paraxial wave equation as written in Eq. (5.6) (with $\psi \to \tilde{\psi}$). Intuitively, the paraxial approximation applies to fields which are propagating close to and only with small angles towards the propagation axis (here the z-axis) [143].

Diffraction Integrals. As an example for the transformations mentioned above, the free propagation of the electric field $\tilde{u}$ in a homogeneous isotropic medium from coordinates z' to $z > z'$ can be described by the *Rayleigh-Sommerfeld diffraction integral* [65, 167, 168]

$$\tilde{u}(x, y; z) = \frac{k}{2\pi\mathrm{i}} \iint \mathrm{d}x'\, \mathrm{d}y'\, \tilde{u}(x', y'; z')\, \frac{\mathrm{e}^{\mathrm{i}kr}}{r} \frac{z - z'}{r} \left(1 + \frac{\mathrm{i}}{kr}\right), \tag{B.7}$$

where k is the modulus of the wave-vector and $r = \sqrt{(x - x')^2 + (y - y')^2 + (z - z')^2}$.

Since the integral appearing in Eq. (B.7) is usually difficult if not impossible to solve analytically, the diffraction integral is usually considered within the paraxial approximation. Formally, in this approximation, r in the exponent $\mathrm{e}^{\mathrm{i}kr}$ of Eq. (B.7) may be rewritten as [65, 143]

$$r = |z - z'| \sqrt{1 + \left(\frac{x - x'}{z - z'}\right)^2 + \left(\frac{y - y'}{z - z'}\right)^2} \tag{B.8a}$$

$$\approx |z - z'| + \frac{1}{2} \frac{(x - x')^2}{|z - z'|} + \frac{1}{2} \frac{(y - y')^2}{|z - z'|} + \dots , \tag{B.8b}$$

where from the first to the second line the Taylor series of the function $f(\xi) = \sqrt{1 + \xi}$ has been applied and truncated after the second order. For the denominators containing r in the aforementioned equation a simpler approximation is used: $r \approx |z - z'|$, since $|x - x'| \ll |z - z'|$ and $|y - y'| \ll |z - z'|$ [143]. Applying this same approximation to the exponential term would neglect the approximately spherical wavefront of the complex exponential: If k is large, small variations in the transverse direction would lead to a change in the phase of the term $\mathrm{e}^{\mathrm{i}kr}$. Furthermore, $1 + \mathrm{i}/(kr) \approx 1$. Applying these approximations to Eq. (B.7) and using Eq. (B.3) to write the result in terms of the slowly varying envelope yields the *Huygens-Fresnel diffraction integral* [143]

$$\tilde{\psi}(x, y; z) \approx \frac{k}{2\pi\mathrm{i}} \frac{1}{z - z'} \iint \mathrm{d}x' \, \mathrm{d}y' \, \tilde{\psi}(x', y'; z') \, \mathrm{e}^{\mathrm{i}\frac{k}{2} \frac{(x - x')^2 + (y - y')^2}{z - z'}} . \tag{B.9}$$

This integral is usually easier to solve than Eq. (B.7) since it only contains (complex) Gaussian functions and $\tilde{\psi}(x', y'; z')$. While the Rayleigh-Sommerfeld diffraction integral as written in Eq. (B.7) is a solution to the Helmholtz equation (B.2), the Huygens-Fresnel diffraction integral is a solution to the paraxial wave equation (5.6) (provided that the initial fields are solutions to the respective wave equation) [169–171].

For simplicity, as was the case in Chapters 3 and 4, the y-direction will be neglected in the following (see also Sec. 3.2). Equation (B.9) suggests that by factorizing the integrand and the prefactors the resulting integral can be written in the following form [143]:

$$\tilde{\psi}(x; z) \approx \left[\tilde{\psi}(\,\cdot\,; z') * \tilde{\mathscr{K}}_{z - z'}\right](x), \tag{B.10}$$

where $*$ denotes the *convolution integral*, defined for two (possibly complex-valued) functions $f(x)$ and $g(x)$ as [111]

$$(f * g)(x) \overset{\text{def.}}{=} \int \mathrm{d}x' \, f(x') \, g(x - x'), \tag{B.11}$$

and where [143]

$$\tilde{\mathscr{K}}_{z - z'}(x) = \sqrt{\frac{k}{2\pi\mathrm{i}}} \frac{\mathrm{e}^{\mathrm{i}\frac{k}{2} \frac{x^2}{z - z'}}}{\sqrt{z - z'}} \tag{B.12}$$

is the *Huygens-Fresnel kernel* which characterizes the propagation of the light field described by $\tilde{\psi}$ from z' to z [143].

Wave-Vector Domain. The majority of this work describes the electric field in the wave-vector domain and not in real space. The connection between the two domains is mediated by the Fourier transform. For the rest of this chapter, the one-dimensional Fourier transform connecting a function $\tilde{f}(x)$ in the spatial domain to its Fourier transformed $f(q)$ in the wave-vector domain will be defined as [111]

$$f(q) = (\mathcal{F}\,\tilde{f})(q) \overset{\text{def.}}{=} \int \mathrm{d}x\, \tilde{f}(x)\, \mathrm{e}^{-\mathrm{i}qx}\,. \tag{B.13}$$

With this convention for the Fourier transform from wave-vector space to real space, the inverse transform is given by [111]

$$\tilde{f}(x) = (\mathcal{F}^{-1} f)(x) \overset{\text{def.}}{=} \frac{1}{2\pi} \int \mathrm{d}q\, f(q)\, \mathrm{e}^{\mathrm{i}qx}\,, \tag{B.14}$$

so that $[\mathcal{F}^{-1}(\mathcal{F}\,f)](q) = [\mathcal{F}\,(\mathcal{F}^{-1} f)](q) = f(q)$. Applying the Fourier transform as in Eq. (B.13) to both sides of the definition of the convolution as written in Eq. (B.11) leads to the *convolution theorem* [111, 156]:

$$\big[\mathcal{F}\,\big(\tilde{f} * \tilde{g}\big)\big](q) = (\mathcal{F}\,\tilde{f})(q)\,(\mathcal{F}\,\tilde{g})(q). \tag{B.15}$$

In words, this means that the Fourier transform of the convolution of two functions equals the product of the Fourier transforms of said functions.

Transforming Eq. (B.10) into the wave-vector domain by applying the convolution theorem yields

$$\psi(q; z) \approx \psi(q; z')\, \mathscr{K}_{z-z'}(q). \tag{B.16}$$

The Fourier transform of the Huygens-Fresnel propagation kernel is given by[1]

$$\mathscr{K}_{\Delta z}(q) = \mathrm{e}^{-\mathrm{i}\frac{\Delta z}{2k} q^2}\,, \tag{B.17}$$

where $\Delta z = z - z'$. An alternative way of arriving at this result is by considering the phase the light acquires by traveling along the z-axis inside a homogeneous medium. This phase factor is given by $\mathrm{e}^{\mathrm{i}k_z \Delta z}$ for the positive frequency components of the electric field, which has for example been used in the phase-matching function for the non-compensated SU(1,1) interferometer configuration to model the propagation of the light field in air, see Eqs. (3.34) and (3.35) and Refs. [1, 5, 11]. The z-component of the wave-vector can be expressed in terms of the transverse component as in Eq. (2.40) and the Fresnel approximation can then be applied to the resulting expression: $\sqrt{k^2 - q^2} \approx k - q^2/(2k)$, since $q \ll k$. Thus, $\mathrm{e}^{\mathrm{i}k_z \Delta z} \approx \mathrm{e}^{\mathrm{i}k\Delta z} \mathrm{e}^{-\mathrm{i}\frac{\Delta z}{2k} q^2}$, which is identical to the Huygens-Fresnel propagation kernel as written for the full electric field including the rapidly oscillating carrier term, compare Eqs. (B.3) and (B.17). This result is not surprising. It can be shown

[1] The Fourier integral can be solved by completing the square in the exponent and using the *(complex) Fresnel integral* $\int \mathrm{d}x\, \mathrm{e}^{\mathrm{i}x^2} = \sqrt{\mathrm{i}\pi}$ [143], which is used in the computation of the *Fresnel integrals* $\int \mathrm{d}x\, \cos(x^2) = \int \mathrm{d}x\, \sin(x^2) = \sqrt{2\pi}/2$, see for example Bronshtein *et al.* [111].

that the full two-dimensional term $\mathrm{e}^{\mathrm{i}k_z\Delta z} = \mathrm{e}^{\mathrm{i}\sqrt{k^2-q_x^2-q_y^2}\,\Delta z}$ is the Fourier transform of the full two-dimensional Rayleigh-Sommerfeld diffraction integral kernel [compare Eq. (B.7)]

$$\tilde{K}_{\Delta z}(x', y') = \frac{k}{2\pi\mathrm{i}} \frac{\mathrm{e}^{\mathrm{i}kr}}{r} \frac{\Delta z}{r} \left(1 + \frac{\mathrm{i}}{kr}\right), \tag{B.18}$$

where $r = \sqrt{(x-x')^2 + (y-y')^2 + (\Delta z)^2}$. See for example Eq. (9.21) and the text preceding it in Khare *et al.* [168].

Lenses. For the 4f-system, in addition to free-space propagation, it is also necessary to model how lenses modify the electric field. In the paraxial approximation, a thin lens with focal length ℓ adds a phase [1, 156]

$$\tilde{\mathscr{L}}_\ell(x) = \mathrm{e}^{-\mathrm{i}\frac{k}{2\ell}x^2} \tag{B.19}$$

to the slowly varying envelope in real space. The full transformation of the function $\tilde{\psi}$ therefore reads

$$\tilde{\psi}^{(\mathrm{out})}(x; z) = \tilde{\psi}^{(\mathrm{in})}(x; z)\, \mathrm{e}^{-\mathrm{i}\frac{k}{2\ell}x^2}, \tag{B.20}$$

where $\tilde{\psi}^{(\mathrm{in})}$ and $\tilde{\psi}^{(\mathrm{out})}$ describe the state of the light field before and after the lens, respectively. Writing the functions on both sides of the product as the inverse Fourier transform of their wave-vector domain counterparts leads to another version of the convolution theorem, which in its general form reads

$$\left[\mathcal{F}\left(\tilde{f}\tilde{g}\right)\right](q) = \frac{1}{2\pi}\left[\left(\mathcal{F}\,\tilde{f}\right) * \left(\mathcal{F}\,\tilde{g}\right)\right](q). \tag{B.21}$$

Thus, in the Fourier domain, Eq. (B.20) essentially becomes the convolution of the Fourier transforms of $\tilde{\psi}^{(\mathrm{in})}$ and $\tilde{\mathscr{L}}_\ell$. The Fourier integral of the *lens transmission function* $\tilde{\mathscr{L}}_\ell$ is of the same type as the Fourier transform integral leading to Eq. (B.17). The integral can be evaluted, yielding

$$\mathscr{L}_\ell(q) = \sqrt{\frac{2\pi\mathrm{i}\ell}{k}}\, \mathrm{e}^{\mathrm{i}\frac{\ell}{2k}q^2}. \tag{B.22}$$

Thus, the transformation for a lens in wave-vector space is ultimately given by

$$\psi^{(\mathrm{out})}(q; z) = \frac{1}{2\pi}\left[\psi^{(\mathrm{in})}(\,\cdot\,; z) * \mathscr{L}_\ell\right](q). \tag{B.23}$$

B.2. Diffraction Compensation

The methods presented in Sec. B.1 can be used to illustrate the behavior of the radiation inside the 4f-system used to compensate the diffraction inside an SU(1,1) interferometer as described in Sec. 3.3. Figure B.1 shows the basic setup of an SU(1,1) using a 4f-system for compensating the diffraction of the signal and idler radiation and adds additional details that were not shown in Fig. 3.2(c). Additionally, the figure illustrates the refraction at the

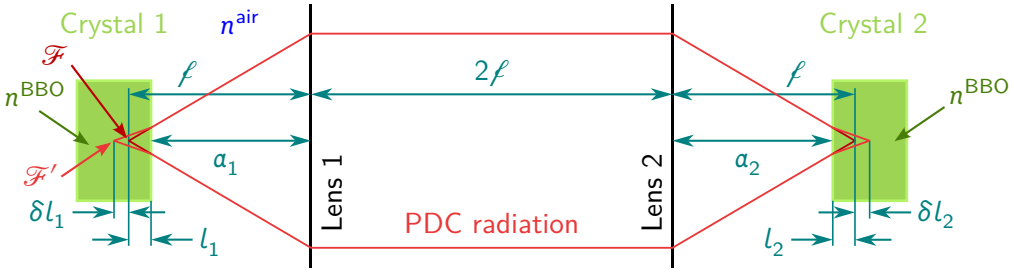

Figure B.1: Sketch of the diffraction-compensated SU(1,1) realized as a 4f-system. This figure is a more detailed version of Fig. 3.2(c) and also illustrates the refraction at the boundaries between the crystals and the air as also shown in Fig. A.1(b), from which several labels for dimensions have been adopted. As was the case in Fig. 3.2(c), the angles for the emitted and focused PDC radiation are shown exaggerated. The pump beam and the signal and idler radiation leaving the second crystal are not shown.

crystal-air boundaries as discussed in Sec. A.2.

The radiation emitted from the first crystal at its output face travels a distance of a_1 and is then collimated by Lens 1. After traveling a distance 2ℓ, the collimated beam is focused into the second crystal by Lens 2. Applying the corresponding transformation equations derived in Sec. B.1 for the propagation of the light field described by $\psi^{(1,\text{out})}$ at the output face of the first crystal yields the function $\psi^{(2,\text{in})}$ which describes the field at the input face of the second crystal:

$$\psi^{(2,\text{in})}(q) = \frac{1}{(2\pi)^2}\Big(\Big\{\Big[\Big(\psi^{(1,\text{out})}\mathscr{K}_{a_1}\Big) * \mathscr{L}_\ell\Big]\,\mathscr{K}_b\Big\} * \mathscr{L}_\ell\Big)(q)\,\mathscr{K}_{a_2}(q), \tag{B.24}$$

where, analogously to the notation introduced in Sec. 3.2, the concrete values for the z-coordinates have been dropped from the argument lists in favor of the superscripts $^{(1,\text{out})}$ and $^{(2,\text{in})}$. The expression for $\psi^{(2,\text{in})}$ written in Eq. (B.24) can be brought to the form of a single integral transform with $\psi^{(1,\text{out})}$:

$$\psi^{(2,\text{in})}(q) = \int \mathrm{d}q'\,\mathscr{T}_{a_1,a_2}(q,q')\,\psi^{(1,\text{out})}(q'), \tag{B.25}$$

where $\mathscr{T}_{a_1,a_2}$ is the transformation kernel describing the transformation from the output of the first crystal to the input of the second crystal. By explicitly calculating the integrals appearing in Eq. (B.24), $\mathscr{T}_{a_1,a_2}$ can be found to be of the following form:

$$\mathscr{T}_{a_1,a_2}(q,q') = \mathrm{i}\mathrm{e}^{\mathrm{i}\frac{q^2}{2k^{\text{air}}}(2\ell-a_1-a_2)}\delta(q+q'). \tag{B.26}$$

The full transformation as in Eq. (B.25) therefore reads

$$\psi^{(2,\text{in})}(q) = \mathrm{i}\mathrm{e}^{\mathrm{i}\frac{q^2}{2k^{\text{air}}}(2\ell-a_1-a_2)}\psi^{(1,\text{out})}(-q). \tag{B.27}$$

For $\ell = a_1 = a_2$, this transformation reflects the well-known result that the transform of a 4f-system from the input plane of the first lens to the output plane of the second lens

corresponds, apart from scaling factors and phases which are constant with respect to the coordinates, to a twofold Fourier transform, which in turn corresponds to a mirroring about the origin [172–174]. The sign change in the transverse wave-vector component becomes relevant if the system under consideration does not have inversion symmetry about $q = 0$, as was for example the case throughout Chapter 5. Therein, the symmetry was reduced to an l_p-fold discrete rotational symmetry, where l_p is the OAM quantum number of the pump beam. Thus, in Sec. 5.4.1, this inversion was explicitly accounted for when setting up the TPA for angular displacement measurements using SU(1,1) interferometers, despite not being accounted for in Chapters 3 and 4.

The exponent in Eq. (B.27) can be rewritten in terms of k^{BBO} by noticing that for one thing, from Eqs. (A.11) and (2.15), it follows that

$$\frac{k^{\mathrm{air}}}{k^{\mathrm{BBO}}} = \frac{n^{\mathrm{air}}}{n^{\mathrm{BBO}}}; \tag{B.28}$$

while for another, from Eq. (A.14), it follows that, within the paraxial approximation,

$$\delta l_1 + l_1 = l_1 \frac{n^{\mathrm{BBO}}}{n^{\mathrm{air}}}. \tag{B.29}$$

Thus, Eq. (B.27) may be written as

$$\psi^{(2,\mathrm{in})}(q) = \mathrm{i}\mathrm{e}^{\mathrm{i}\frac{q^2}{2k^{\mathrm{BBO}}}(\delta l_1 + l_1 + \delta l_2 + l_2)} \psi^{(1,\mathrm{out})}(-q), \tag{B.30}$$

where it has been used that

$$l_j = \mathscr{f} - a_j, \qquad \text{for } j = 1, 2. \tag{B.31}$$

Assuming that the system is approximately symmetric about a plane in the middle between the two lens planes, the distances $\delta l_1 + l_1$ and $\delta l_2 + l_2$ may be related via

$$\delta l_1 + l_1 = \delta l_2 + l_2 + \delta z', \tag{B.32}$$

where $\delta z'$ is some offset from the fully symmetric position. Applying the connection written in Eq. (B.32) to the transformation of the 4f-system as written in Eq. (B.30) yields

$$\psi^{(2,\mathrm{in})}(q) = \mathrm{i}\mathrm{e}^{\mathrm{i}\frac{q^2}{2k^{\mathrm{BBO}}}[2(\delta l_1 + l_1) + \delta z']} \psi^{(1,\mathrm{out})}(-q). \tag{B.33}$$

As a simple initial example, a very low-gain PDC process can be considered, where a signal-idler pair is generated at some distance z after the input face of the first crystal. As discussed throughout Chapter 3, it is generally not possible to obtain an analytic expression for the transfer functions of the PDC process at arbitrary parametric gain. However, a reasonable assumption is usually that the generated field has a quadratic phase front and originates approximately from a small region, which may be idealized as a single point. Such a field distribution can be approximated in real space by a very narrow Gaussian or a Dirac delta distribution, so that $\tilde{\psi}(x) = \delta(x)$. In the wave-vector domain, this function

is therefore a constant: $\psi(q) = 1$. Propagating the field forwards to the output face of the crystal using Eqs. (B.16) and (B.17) yields

$$\psi^{(1,\mathrm{out})}(q) = \mathrm{e}^{-\mathrm{i}\frac{q^2}{2k^{\mathrm{BBO}}}(L_1 - z)}, \tag{B.34}$$

where L_1 is the length of the first crystal. Thus, as mentioned above, the light emitted has a quadratic phase front with negative curvature $-(L_1 - z)/(2k^{\mathrm{BBO}})$. Applying the transformation of the 4f-system as written in Eq. (B.33) yields

$$\psi^{(2,\mathrm{in})}(q) = \mathrm{i}\mathrm{e}^{\mathrm{i}\frac{q^2}{2k^{\mathrm{BBO}}}[2(\delta l_1 + l_1) + \delta z']}\mathrm{e}^{-\mathrm{i}\frac{q^2}{2k^{\mathrm{BBO}}}(L_1 - z)}. \tag{B.35}$$

For the fully symmetric case, $\delta z = 0$, Eq. (B.35) reveals a special case for the shape of the wavefront curvature: Setting $\delta l_1 + l_1 = L_1/2$, $\psi^{(2,\mathrm{in})}$ takes the form

$$\psi^{(2,\mathrm{in})}(q) = \mathrm{i}\mathrm{e}^{\mathrm{i}\frac{q^2}{2k^{\mathrm{BBO}}}z}. \tag{B.36}$$

This field is again fully focused, meaning that it is constant in the wave-vector domain, after propagating further by a distance of z inside the second crystal. Thus, for $\delta l_1 + l_1 = L_1/2$, the PDC radiation is focused into the second crystal so that the distance from the focal point to the input face of the second crystal is the same as between the input face of the first crystal and the position from which the radiation originates.

More generally, the radiation field generated in the first crystal may have some approximately quadratic wavefront which depends on the parameters of the PDC process, most importantly the gain. Overall, the wavefront can be approximated as

$$\psi^{(1,\mathrm{out})}(q) = \mathrm{e}^{-\mathrm{i}\frac{q^2}{2k^{\mathrm{BBO}}}(L_1 - \varkappa)}, \tag{B.37}$$

where $\varkappa$ then denotes the effective position from which the radiation originates. The value of $\varkappa$ may depend on the gain due to stimulated emission occurring in the crystal more frequently at high gain, leading to a shift in the average position from which the PDC radiation originates (*spatial ordering*). At the input face of the second crystal, the field becomes

$$\psi^{(2,\mathrm{in})}(q) = \mathrm{i}\mathrm{e}^{\mathrm{i}\frac{q^2}{2k^{\mathrm{BBO}}}[2(\delta l_1 + l_1) + \delta z']}\mathrm{e}^{-\mathrm{i}\frac{q^2}{2k^{\mathrm{BBO}}}(L_1 - \varkappa)}. \tag{B.38}$$

Here, another special choice for $\delta l_1 + l_1$ is given by

$$\delta l_1 + l_1 = L_1 - \varkappa, \tag{B.39}$$

with which the wavefront at the input face of the second crystal becomes

$$\psi^{(2,\mathrm{in})}(q) = \mathrm{i}\mathrm{e}^{\mathrm{i}\frac{q^2}{2k^{\mathrm{BBO}}}(L_1 - \varkappa)}\mathrm{e}^{\mathrm{i}\frac{q^2}{2k^{\mathrm{BBO}}}\delta z'}. \tag{B.40}$$

Apart from the phase i and the phase due to the offset $\delta z'$, the wavefront has the same magnitude of the curvature as at the output of the first crystal, compare Eq. (B.37), but

with the opposite sign. After traveling further by a distance of $L_1 - \varkappa$, the radiation is again fully focused into a single point. This configuration with $\delta l_1 + l_1$ as chosen in Eq. (B.39) can be considered as the *diffraction-compensated configuration* due to the fact that the wavefront curvature accumulated during the propagation in the second crystal and the air gap is flipped when the radiation reaches the second crystal. Equation (B.39) implies that in the experimental setup, for each value of $\varkappa$, $\delta l_1 + l_1$ must be adjusted individually. Thus, in general, for a given set of parameters of the PDC process (such as the parametric gain), $\delta l_1 + l_1$ must generally be different to achieve diffraction compensation. This is similar to the situation for the unbalanced interferometer as discussed in Sec. 4.2.2.2. Therein, Eq. (4.52) showed that varying the position of the focal points affects the visibility.

The fact that the optimal position to achieve the compensation depends on the gain can be rather impractical for further theoretical investigations because it requires performing a fit for each value of the gain in order to maximize the visibility and determine the optimal value for $\delta l_1 + l_1$. Instead, as an idealization, it can be assumed that the setup is optimal regardless of the gain. In this case, as suggested by Eqs. (B.37)–(B.40), the action of the idealized 4f-system is simply described by a flipping of the curvature of the wavefront of the generated radiation. This leads to a modification of the phase-matching function in the second crystal. In the paraxial approximation, for frequency-degenerate parametric down-conversion, the phase mismatch can be approximated as

$$\Delta k(q_s, q_i) \approx \delta k - \frac{q_p^2}{2k_p} + \frac{q_s^2}{2k_s} + \frac{q_i^2}{2k_i}, \tag{B.41}$$

where

$$\delta k = k_p - k_s - k_i, \tag{B.42}$$

compare Eqs. (3.31), (5.46) and (5.47). Note that the superscript $^{\mathrm{BBO}}$ for the wave-vectors has been dropped here. The term δk describes the phase mismatch which may result for example from a frequency mismatch or a misalignment of the setup, or, more precisely, a mismatch of the phase-matching angle [5]. For ideal phase matching without frequency mismatch, $\delta k = 0$. The other terms on the right-hand side of Eq. (B.41) describe the wavefront of the pump, signal and idler field.

In general, if a PDC system consists of several layers with different phase-mismatch functions $\Delta k(q_s, q_i)$, the phase-matching function is given by [12, 175]

$$h(q_s, q_i, z) = \exp\left[\mathrm{i} \int_0^z \mathrm{d}z'\, \Delta k(q_s, q_i, z')\right], \tag{B.43}$$

which, using Eq. (B.41), becomes

$$h(q_s, q_i, z) = \mathrm{e}^{\mathrm{i}\delta S(z)} \exp\left[\mathrm{i} \int_0^z \mathrm{d}z'\, \kappa(z')\right], \tag{B.44}$$

where

$$\delta S(z) = S_p(z) - S_s(z) - S_i(z), \tag{B.45}$$

with $S_j(z) = \int_0^z \mathrm{d}z'\, k_j(z')$ for $j = p, s, i$ analogous to Eq. (B.5) being the difference of the

fast carrier phases and where

$$\kappa(z') = -\frac{q_p^2}{2k_p} + \frac{q_s^2}{2k_s} + \frac{q_i^2}{2k_i}. \tag{B.46}$$

Clearly, for ideal phase matching with $\delta k = 0$,

$$\Delta k \approx \kappa. \tag{B.47}$$

As described in Sec. 3.3, the 4f-system is included in the description of the PDC systems by modifying the theoretical description of the second crystal. *Full diffraction compensation* implies that the radiation arriving at the second crystal has the opposite wavefront curvature than at the output of the first crystal, see the above discussion leading from Eq. (B.37) to Eq. (B.40) and the surrounding text. Integrating this into the description of the second crystal suggests that the term κ appearing above should appear with the opposite sign in the phase matching function of the second crystal. Thus, the connection between this function for the first and second crystal is given by

$$\kappa^{(1)} = -\kappa^{(2)}. \tag{B.48}$$

For perfect phase matching with $\delta k = 0$ and within the paraxial approximation, the above connection describes full diffraction compensation under the assumption of quadratic wavefronts for the fields. Heuristically, this result may be generalized beyond the paraxial approximation by writing instead

$$\Delta k^{(1)} = -\Delta k^{(2)}, \tag{B.49}$$

Then, when applying the paraxial approximation again, Eq. (B.48) is recovered. Equation (B.49) implies that the system comprised of the optimally positioned 4f-system and the second crystal effectively acts as a simple crystal for which the exponent of the phase-mismatch function has the opposite sign. Naturally, both Eqs. (B.48) and (B.49) require that the refractive indices (and the phase-matching angle) are the same for both crystals.

Let now z label a coordinate inside the second crystal ranging from L_1 (the length and end coordinate of the *first* crystal) to $2L_1$, so that the length of the *second* crystal is also given by L_1. The phase-matching function $h(q_s, q_i, z)$ is then given by

$$h(q_s, q_i, z) = \mathrm{e}^{\mathrm{i}\Delta k^{(1)}(q_s,q_i)L_1}\mathrm{e}^{\mathrm{i}\Delta k^{(2)}(q_s,q_i)[z-L_1]}, \tag{B.50}$$

which follows from evaluating Eq. (B.43). With Eq. (B.49), which provides the connection between the phase-mismatch functions of the two crystals, Eq. (B.50) simplifies further to

$$h(q_s, q_i, z) = \mathrm{e}^{-\mathrm{i}\Delta k^{(1)}(q_s,q_i)[z-2L_1]}. \tag{B.51}$$

For positions between the two lenses of the 4f-system, the transformation describing the evolution of the output of the first crystal to the position with distance b after the first

lens is given by

$$\psi_b^{(\mathrm{mid})}(q) = \frac{1}{2\pi}\left[\left(\psi^{(1,\mathrm{out})}\mathscr{K}_{a_1}\right) * \mathscr{L}_f\right](q)\,\mathscr{K}_b(q). \tag{B.52}$$

This can be understood as an intermediate result leading from Eq. (B.24) to Eq. (B.26). For a field originating from the effective coordinate $\varkappa$ inside the first crystal, the distance a_1 between the output face and the first lens to reach optimal focusing can be obtained from the above discussions and Eqs. (B.29), (B.31) and (B.39) as

$$a_1 = f - \frac{n^{\mathrm{air}}}{n^{\mathrm{BBO}}}\,(L_1 - \varkappa). \tag{B.53}$$

Evaluating the transformation in Eq. (B.37) for the output field of the first crystal as written in Eq. (B.37) with optimal focusing by using the value of a_1 written in Eq. (B.53) yields for $\psi_b^{(\mathrm{mid})}(q)$:

$$\psi_b^{(\mathrm{mid})}(q) = \sqrt{\frac{2\pi \mathrm{i} f}{k}}\,\delta\!\left(\frac{f}{k}q\right). \tag{B.54}$$

Hence, between the two lenses, for optimal focusing, the wavefront is independent of b. In real space, the Dirac delta on the right-hand side in Eq. (B.54) corresponds to a constant, meaning that the wavefront in real space is flat. This result mirrors the well-known fact that light rays originating from the focal point of a lens become collimated after passing through the lens, leading to flat wavefronts. This is here reflected by the fact that only the plane waves for $q = 0$ appear in $\psi_b^{(\mathrm{mid})}(q)$. These are the plane waves traveling parallel to the z-axis.

The fact that the right-hand side of Eq. (B.54) does not depend on b furthermore suggests that the phase-matching function can be extended by accounting for potential phase changes ϕ which do not modify the wavefront curvature between the two crystals, leading to an extended expression compared to Eq. (B.51):

$$h(q_s, q_i, z) = \mathrm{e}^{-\mathrm{i}\Delta k^{(1)}(q_s,q_i)[z-2L_1]}\mathrm{e}^{\mathrm{i}\phi}, \tag{B.55}$$

which is the phase-matching function for the second crystal of a diffraction compensated SU(1,1) interferometer as written in Eq. (3.37). Note that the additional phase factor i appearing in Eq. (B.40) as been neglected in the above discussions and can be included in ϕ in Eq. (B.55).

In the above discussion, the phase term $\mathrm{e}^{\mathrm{i}\frac{q^2}{2k^{\mathrm{BBO}}}\delta z'}$ in Eq. (B.40) resulting from an offset of the focal points of one or both of the two lenses was first neglected. This additional phase acts similar to the phase the pump, signal and idler radiation experience in a non-compensated interferometer due to the air gap. In principle, depending on the setup, all three fields can experience such an offset. The relevant quantity is therefore:

$$\rho = -\left(\frac{q_p^2}{2k_p} - \frac{q_s^2}{2k_s} - \frac{q_i^2}{2k_i}\right)\delta z'. \tag{B.56}$$

Note that this assumes that all three fields have the same spatial offset $\delta z'$. Depending on the setup, this might not be exactly fulfilled if the pump beam is not sent through the 4f-system. This may be rewritten as

$$\rho = \frac{(q_s - q_i)^2}{2k_p}\delta z' , \tag{B.57}$$

since $k_p = 2k_s = 2k_i$ for ideal collinear degenerate PDC. Transferring this back outside the paraxial approximation, Eq. (B.57) implies that the offset adds a phase shift

$$\rho = \Delta k(q_s, q_i)\, \delta z' \tag{B.58}$$

to the phase matching function. Alternatively, Eq. (B.57) may be rewritten in terms of the wave-vectors inside air:

$$\rho = \frac{(q_s - q_i)^2}{2k_p^{\mathrm{air}}}\delta z , \tag{B.59}$$

where now $\delta z = (n^{\mathrm{air}}/n^{\mathrm{BBO}})\, \delta z'$. Thus, outside the paraxial approximation, Eq. (B.59) may be restated as simply

$$\rho = \Delta k^{\mathrm{air}}(q_s, q_i)\, \delta z - k_p^{\mathrm{vac}} \delta n \delta z, \tag{B.60}$$

where $\delta n = n_p^{\mathrm{air}} - n_s^{\mathrm{air}}$, see Eq. (5.58) and the surrounding text. The term $k_p^{\mathrm{vac}}\delta n \delta z$ in Eq. (B.60) does not depend on the transverse wave-vector components and therefore only shifts the phase ϕ added in Eq. (B.55) above. Overall, the phase matching function can be written in the form

$$h(q_s, q_i, z) = \mathrm{e}^{-\mathrm{i}\Delta k^{(1)}(q_s,q_i)[z-2L_1]}\mathrm{e}^{-\mathrm{i}\Delta k^{\mathrm{air}}(q_s,q_i)\delta z}\mathrm{e}^{\mathrm{i}\phi} , \tag{B.61}$$

which is the phase matching function used through Chapter 4, for the description of unbalanced SU(1,1) interferometers [see Eq. (4.48)]. Note that in Eq. (B.61), the sign in the exponent containing δz is arbitrary, since changing it only changes the direction in which the offset δz occurs.

Geometrically, the setup which uses a spherical mirror to compensate for the diffraction (reflection geometry) is equivalent to the 4f-system. This can be seen by first considering the fact that in the middle between the two lenses of the 4f-system, the wavefront phase must be flat, see Eq. (B.54) above and the surrounding text. As such, the half of the setup following this point can be replaced by a flat mirror placed parallel to the plane of the first lens, which sends back the signal-idler radiation (and the pump) through the first crystal. It can be easily seen that the lens and the flat mirror combined are functionally identical to a spherical mirror if the abovementioned effective point at which the PDC radiation is generated coincides with the center of the sphere from which the mirror originates. For a spherical mirror, this point is 2ℓ away from the surface, where ℓ is the focal length of a parabolic mirror that approximates the curvature of the spherical mirror [59].

References

[1] D. Scharwald, T. Meier, and P. R. Sharapova, "Phase sensitivity of spatially broadband high-gain SU(1,1) interferometers", Phys. Rev. Res. **5**, 043158 (2023).

[2] D. Scharwald, L. Gehse, and P. R. Sharapova, "Schmidt modes carrying orbital angular momentum generated by cascaded systems pumped with Laguerre–Gaussian beams", APL Photonics **10**, 016112 (2025).

[3] I. Barakat, M. Kalash, D. Scharwald, P. Sharapova, N. Lindlein, and M. Chekhova, "Simultaneous measurement of multimode squeezing through multimode phase-sensitive amplification", Opt. Quantum **3**, 36 (2025).

[4] D. Scharwald and P. R. Sharapova, "Characterization of Schmidt modes in high-gain SU(1,1) interferometers" (2025), arXiv:2504.19377 [quant-ph].

[5] P. R. Sharapova, G. Frascella, M. Riabinin, A. M. Pérez, O. V. Tikhonova, S. Lemieux, R. W. Boyd, G. Leuchs, and M. V. Chekhova, "Properties of bright squeezed vacuum at increasing brightness", Phys. Rev. Res. **2**, 013371 (2020).

[6] A. M. Marino, N. V. Corzo Trejo, and P. D. Lett, "Effect of losses on the performance of an SU(1,1) interferometer", Phys. Rev. A **86**, 023844 (2012).

[7] G. Frascella, E. E. Mikhailov, N. Takanashi, R. V. Zakharov, O. V. Tikhonova, and M. V. Chekhova, "Wide-field SU(1,1) interferometer", Optica **6**, 1233 (2019).

[8] Z. Y. Ou and X. Li, "Quantum SU(1,1) interferometers: Basic principles and applications", APL Photonics **5**, 080902 (2020).

[9] M. Manceau, F. Khalili, and M. Chekhova, "Improving the phase super-sensitivity of squeezing-assisted interferometers by squeeze factor unbalancing", New J. Phys. **19**, 013014 (2017).

[10] J. Xin, X.-M. Lu, X. Li, and G. Li, "Optimal phase point for SU(1,1) interferometer", J. Opt. Soc. Am. B **36**, 2824 (2019).

[11] P. Sharapova, A. M. Pérez, O. V. Tikhonova, and M. V. Chekhova, "Schmidt modes in the angular spectrum of bright squeezed vacuum", Phys. Rev. A **91**, 043816 (2015).

[12] A. Ferreri, M. Santandrea, M. Stefszky, K. H. Luo, H. Herrmann, C. Silberhorn, and P. R. Sharapova, "Spectrally multimode integrated SU(1,1) interferometer", Quantum **5**, 461 (2021).

[13] M. V. Chekhova and Z. Y. Ou, "Nonlinear interferometers in quantum optics", Adv. Opt. Photonics **8**, 104 (2016).

[14] M. Riabinin, P. R. Sharapova, and T. Meier, "Bright correlated twin-beam generation and radiation shaping in high-gain parametric down-conversion with anisotropy", Opt. Express **29**, 21876 (2021).

[15] F. Hudelist, J. Kong, C. Liu, J. Jing, Z. Y. Ou, and W. Zhang, "Quantum metrology with parametric amplifier-based photon correlation interferometers", Nat. Commun. **5**, 3049 (2014).

[16] B. Yurke, S. L. McCall, and J. R. Klauder, "SU(2) and SU(1,1) interferometers", Phys. Rev. A **33**, 4033 (1986).

[17] Q. Kang, Z. Zhao, T. Zhao, C. Liu, and L. Hu, "Phase estimation via a number-conserving operation inside a SU(1,1) interferometer", Phys. Rev. A **110**, 022432 (2024).

[18] W. Wasilewski, A. I. Lvovsky, K. Banaszek, and C. Radzewicz, "Pulsed squeezed light: Simultaneous squeezing of multiple modes", Phys. Rev. A **73**, 063819 (2006).

[19] G. Harder, T. J. Bartley, A. E. Lita, S. W. Nam, T. Gerrits, and C. Silberhorn, "Single-Mode Parametric-Down-Conversion States with 50 Photons as a Source for Mesoscopic Quantum Optics", Phys. Rev. Lett. **116**, 143601 (2016).

[20] D. A. Kopylov, T. Meier, and P. R. Sharapova, "Theory of Multimode Squeezed Light Generation in Lossy Media", Quantum **9**, 1621 (2025).

[21] A. Patra, R. Gupta, S. Roy, T. Das, and A. Sen(De), "Quantum dense coding network using multimode squeezed states of light", Phys. Rev. A **106**, 052607 (2022).

[22] V. Roman-Rodriguez, D. Fainsin, G. L. Zanin, N. Treps, E. Diamanti, and V. Parigi, "Multimode squeezed state for reconfigurable quantum networks at telecommunication wavelengths", Phys. Rev. Res. **6**, 043113 (2024).

[23] A. Mair, A. Vaziri, G. Weihs, and A. Zeilinger, "Entanglement of the orbital angular momentum states of photons", Nature **412**, 313 (2001).

[24] L. V. Amitonova, T. B. H. Tentrup, I. M. Vellekoop, and P. W. H. Pinkse, "Quantum key establishment via a multimode fiber", Opt. Express **28**, 5965 (2020).

[25] Y. Xu, T. Zhao, Q. Kang, C. Liu, L. Hu, and S. Liu, "Phase sensitivity of an SU(1, 1) interferometer in photon-loss via photon operations", Opt. Express **31**, 8414 (2023).

[26] S. Chang, W. Ye, H. Zhang, L. Hu, J. Huang, and S. Liu, "Improvement of phase sensitivity in an SU(1,1) interferometer via a phase shift induced by a Kerr medium", Phys. Rev. A **105**, 033704 (2022).

[27] D. Li, B. T. Gard, Y. Gao, C.-H. Yuan, W. Zhang, H. Lee, and J. P. Dowling, "Phase sensitivity at the Heisenberg limit in an SU(1,1) interferometer via parity detection", Phys. Rev. A **94**, 063840 (2016).

[28] U. L. Andersen, T. Gehring, C. Marquardt, and G. Leuchs, "30 years of squeezed light generation", Phys. Scr. **91**, 053001 (2016).

[29] M. Kalash and M. V. Chekhova, "Wigner function tomography via optical parametric amplification", Optica **10**, 1142 (2023).

[30] G. Cariolaro and G. Pierobon, "Reexamination of Bloch-Messiah reduction", Phys. Rev. A **93**, 062115 (2016).

[31] G. Cariolaro and G. Pierobon, "Bloch-Messiah reduction of Gaussian unitaries by Takagi factorization", Phys. Rev. A **94**, 062109 (2016).

[32] C. Gerry and P. Knight, *Introductory Quantum Optics* (Cambridge University Press, 2004).

[33] M. O. Scully and M. S. Zubairy, *Quantum Optics* (Cambridge University Press, 1997).

[34] B. J. Lawrie, P. D. Lett, A. M. Marino, and R. C. Pooser, "Quantum Sensing with Squeezed Light", ACS Photonics **6**, 1307 (2019).

[35] J. Fuenzalida, E. Giese, and M. Gräfe, "Nonlinear Interferometry: A New Approach for Imaging and Sensing", Adv. Quantum Technol. **7**, 2300353 (2024).

[36] S. Schaffrath, D. Derr, M. Gräfe, and E. Giese, "Quantum imaging beyond the standard-quantum limit and phase distillation", New J. Phys. **26**, 023018 (2024).

[37] F. Meylahn, B. Willke, and H. Vahlbruch, "Squeezed States of Light for Future Gravitational Wave Detectors at a Wavelength of 1550 nm", Phys. Rev. Lett. **129**, 121103 (2022).

[38] M. Tse, H. Yu, N. Kijbunchoo, A. Fernandez-Galiana, P. Dupej, L. Barsotti, C. D. Blair, D. D. Brown, S. E. Dwyer, A. Effler, *et al.*, "Quantum-Enhanced Advanced LIGO Detectors in the Era of Gravitational-Wave Astronomy", Phys. Rev. Lett. **123**, 231107 (2019).

[39] R. E. Slusher, L. W. Hollberg, B. Yurke, J. C. Mertz, and J. F. Valley, "Observation of Squeezed States Generated by Four-Wave Mixing in an Optical Cavity", Phys. Rev. Lett. **55**, 2409 (1985).

[40] Y. Zhao, N. Aritomi, E. Capocasa, M. Leonardi, M. Eisenmann, Y. Guo, E. Polini, A. Tomura, K. Arai, Y. Aso, *et al.*, "Frequency-Dependent Squeezed Vacuum Source for Broadband Quantum Noise Reduction in Advanced Gravitational-Wave Detectors", Phys. Rev. Lett. **124**, 171101 (2020).

[41] P. Gupta, R. W. Speirs, K. M. Jones, and P. D. Lett, "Effect of imperfect homodyne visibility on multi-spatial-mode two-mode squeezing measurements", Opt. Express **28**, 652 (2020).

[42] F. M. Miatto, H. Di Lorenzo Pires, S. M. Barnett, and M. P. van Exter, "Spatial Schmidt modes generated in parametric down-conversion", Eur. Phys. J. D **66**, 263 (2012).

[43] F. M. Miatto, T. Brougham, and A. M. Yao, "Cartesian and polar Schmidt bases for down-converted photons: How high dimensional entanglement protects the shared information from non-ideal measurements", Eur. Phys. J. D **66**, 183 (2012).

[44] Y. Shen, X. Wang, Z. Xie, C. Min, X. Fu, Q. Liu, M. Gong, and X. Yuan, "Optical vortices 30 years on: OAM manipulation from topological charge to multiple singularities", Light Sci. Appl. **8**, 90 (2019).

[45] J. Wang, S. Chen, and J. Liu, "Orbital angular momentum communications based on standard multi-mode fiber (invited paper)", APL Photonics **6**, 060804 (2021).

[46] L. Allen, M. W. Beijersbergen, R. J. C. Spreeuw, and J. P. Woerdman, "Orbital angular momentum of light and the transformation of Laguerre-Gaussian laser modes", Phys. Rev. A **45**, 8185 (1992).

[47] A. Forbes, "Perspectives on the orbital angular momentum of light", J. Opt. **24**, 124005 (2022).

[48] R. Fickler, R. Lapkiewicz, W. N. Plick, M. Krenn, C. Schaeff, S. Ramelow, and A. Zeilinger, "Quantum Entanglement of High Angular Momenta", Science **338**, 640 (2012).

[49] A. Forbes, A. Dudley, and M. McLaren, "Creation and detection of optical modes with spatial light modulators", Adv. Opt. Photonics **8**, 200 (2016).

[50] K. Y. Bliokh, E. Karimi, M. J. Padgett, M. A. Alonso, M. R. Dennis, A. Dudley, A. Forbes, S. Zahedpour, S. W. Hancock, H. M. Milchberg, *et al.*, "Roadmap on structured waves", J. Opt. **25**, 103001 (2023).

[51] V. D'Ambrosio, N. Spagnolo, L. Del Re, S. Slussarenko, Y. Li, L. C. Kwek, L. Marrucci, S. P. Walborn, L. Aolita, and F. Sciarrino, "Photonic polarization gears for ultra-sensitive angular measurements", Nat. Commun. **4**, 2432 (2013).

[52] B. Piccirillo, V. D'Ambrosio, S. Slussarenko, L. Marrucci, and E. Santamato, "Photon spin-to-orbital angular momentum conversion via an electrically tunable q-plate", Appl. Phys. Lett. **97**, 241104 (2010).

[53] F. Cardano, E. Karimi, S. Slussarenko, L. Marrucci, C. de Lisio, and E. Santamato, "Polarization pattern of vector vortex beams generated by q-plates with different topological charges", Appl. Opt. **51**, C1 (2012).

[54] M. Hiekkamäki, F. Bouchard, and R. Fickler, "Photonic Angular Superresolution Using Twisted N00N States", Phys. Rev. Lett. **127**, 263601 (2021).

[55] A. K. Jha, G. S. Agarwal, and R. W. Boyd, "Supersensitive measurement of angular displacements using entangled photons", Phys. Rev. A **83**, 053829 (2011).

[56] R. W. Boyd, *Nonlinear Optics*, 4th ed. (Academic Press, 2020).

[57] P. D. Drummond and M. Hillery, *The Quantum Theory of Nonlinear Optics* (Cambridge University Press, 2014).

[58] G. Harder, *Optimized down-conversion source and state-characterization tools for quantum optics*, PhD thesis (Paderborn University, 2016).

[59] B. E. A. Saleh and M. C. Teich, *Fundamentals of Photonics* (Wiley, 1991).

[60] L. D. Landau, E. M. Lifshitz, and L. P. Pitaevskii, *Electrodynamics of Continuous Media*, 2nd ed. (Butterworth-Heinemann, 1984).

[61] R. Loudon, *The Quantum Theory of Light*, 3rd ed. (Oxford University Press, 2000).

[62] P. A. Franken, A. E. Hill, C. W. Peters, and G. Weinreich, "Generation of Optical Harmonics", Phys. Rev. Lett. **7**, 118 (1961).

[63] N. Quesada and J. E. Sipe, "Why you should not use the electric field to quantize in nonlinear optics", Opt. Lett. **42**, 3443 (2017).

[64] L. Mandel and E. Wolf, *Optical Coherence and Quantum Optics* (Cambridge University Press, 1995).

[65] J. D. Jackson, *Classical Electrodynamics* (Wiley, 1999).

[66] P. A. Franken and J. F. Ward, "Optical Harmonics and Nonlinear Phenomena", Rev. Mod. Phys. **35**, 23 (1963).

[67] G. New, *Introduction to Nonlinear Optics* (Cambridge University Press, 2011).

[68] J. Tucker and D. F. Walls, "Quantum Theory of the Traveling-Wave Frequency Converter", Phys. Rev. **178**, 2036 (1969).

[69] D. B. Horoshko, G. Patera, A. Gatti, and M. I. Kolobov, "X-entangled biphotons: Schmidt number for 2D model", Eur. Phys. J. D **66**, 239 (2012).

[70] R. J. Glauber, "The Quantum Theory of Optical Coherence", Phys. Rev. **130**, 2529 (1963).

[71] G. Kulkarni, J. Rioux, B. Braverman, M. V. Chekhova, and R. W. Boyd, "Classical model of spontaneous parametric down-conversion", Phys. Rev. Res. **4**, 033098 (2022).

[72] S. Karan, S. Aarav, H. Bharadhwaj, L. Taneja, A. De, G. Kulkarni, N. Meher, and A. K. Jha, "Phase matching in β-barium borate crystals for spontaneous parametric down-conversion", J. Opt. **22**, 083501 (2020).

[73] S. E. Harris, M. K. Oshman, and R. L. Byer, "Observation of Tunable Optical Parametric Fluorescence", Phys. Rev. Lett. **18**, 732 (1967).

[74] K. Spasibko, *Spectral and statistical properties of high-gain parametric down-conversion*, PhD thesis (Friedrich-Alexander-Universität Erlangen-Nürnberg, 2019).

[75] G. Auletta, M. Fortunato, and G. Parisi, *Quantum Mechanics* (Cambridge University Press, 2009).

[76] M. V. Chekhova, G. Leuchs, and M. Żukowski, "Bright squeezed vacuum: Entanglement of macroscopic light beams", Opt. Commun. **337**, 27 (2015).

[77] N. Bloembergen, "Conservation laws in nonlinear optics", J. Opt. Soc. Am. **70**, 1429 (1980).

[78] A. Joobeur, B. E. A. Saleh, and M. C. Teich, "Spatiotemporal coherence properties of entangled light beams generated by parametric down-conversion", Phys. Rev. A **50**, 3349 (1994).

[79] A. Christ, *Theory of ultrafast waveguided parametric down-conversion: From fundamentals to applications*, PhD thesis (Paderborn University, 2013).

[80] A. Christ, B. Brecht, W. Mauerer, and C. Silberhorn, "Theory of quantum frequency conversion and type-II parametric down-conversion in the high-gain regime", New J. Phys. **15**, 053038 (2013).

[81] J. P. Fève, B. Boulanger, and G. Marnier, "Calculation and classification of the direction loci for collinear types I, II and III phase-matching of three-wave nonlinear optical parametric interactions in uniaxial and biaxial acentric crystals", Opt. Commun. **99**, 284 (1993).

[82] D. Eimerl, L. Davis, S. Velsko, E. K. Graham, and A. Zalkin, "Optical, mechanical, and thermal properties of barium borate", J. Appl. Phys. **62**, 1968 (1987).

[83] Z.-Y. J. Ou, *Multi-Photon Quantum Interference* (Springer, 2007).

[84] P. N. Butcher and D. Cotter, *The Elements of Nonlinear Optics* (Cambridge University Press, 1990).

[85] J.-S. Peng and G.-X. Li, *Introduction to Modern Quantum Optics* (World Scientific, 1998).

[86] N. Quesada, G. Triginer, M. D. Vidrighin, and J. E. Sipe, "Theory of high-gain twin-beam generation in waveguides: From Maxwell's equations to efficient simulation", Phys. Rev. A **102**, 033519 (2020).

[87] P. R. Sharapova, O. V. Tikhonova, S. Lemieux, R. W. Boyd, and M. V. Chekhova, "Bright squeezed vacuum in a nonlinear interferometer: Frequency and temporal Schmidt-mode description", Phys. Rev. A **97**, 053827 (2018).

[88] D. N. Klyshko, *Photons and Nonlinear Optics*, 1st ed. (Taylor & Francis, 1988).

[89] J. Schneeloch, S. H. Knarr, D. F. Bogorin, M. L. Levangie, C. C. Tison, R. Frank, G. A. Howland, M. L. Fanto, and P. M. Alsing, "Introduction to the absolute brightness and number statistics in spontaneous parametric down-conversion", J. Opt. **21**, 043501 (2019).

[90] M. Zhang, H.-M. Yu, H. Yuan, X. Wang, R. Demkowicz-Dobrza ński, and J. Liu, "QuanEstimation: An open-source toolkit for quantum parameter estimation", Phys. Rev. Res. **4**, 043057 (2022).

[91] G. Tóth and I. Apellaniz, "Quantum metrology from a quantum information science perspective", J. Phys. A: Math. Theor. **47**, 424006 (2014).

[92] C. M. Caves, "Quantum-mechanical noise in an interferometer", Phys. Rev. D **23**, 1693 (1981).

[93] R. Demkowicz-Dobrzański, J. Kołodyński, and M. Guţă, "The elusive Heisenberg limit in quantum-enhanced metrology", Nat. Commun. **3**, 1063 (2012).

[94] A. Ferreri, *Spectral engineering in multiphoton linear and nonlinear interferometry: the importance of being multimode*, PhD thesis (Paderborn University, 2021).

[95] Z. Y. Ou, "Fundamental quantum limit in precision phase measurement", Phys. Rev. A **55**, 2598 (1997).

[96] L. Pezzé and A. Smerzi, "Mach-Zehnder Interferometry at the Heisenberg Limit with Coherent and Squeezed-Vacuum Light", Phys. Rev. Lett. **100**, 073601 (2008).

[97] A. K. Ekert and P. L. Knight, "Relationship between semiclassical and quantum-mechanical input-output theories of optical response", Phys. Rev. A **43**, 3934 (1991).

[98] G. Triginer, M. D. Vidrighin, N. Quesada, A. Eckstein, M. Moore, W. S. Kolthammer, J. E. Sipe, and I. A. Walmsley, "Understanding High-Gain Twin-Beam Sources Using Cascaded Stimulated Emission", Phys. Rev. X **10**, 031063 (2020).

[99] V. A. Averchenko, G. Frascella, M. Kalash, A. Cavanna, and M. V. Chekhova, "Reconstructing two-dimensional spatial modes for classical and quantum light", Phys. Rev. A **102**, 053725 (2020).

[100] G. Frascella, R. V. Zakharov, O. V. Tikhonova, and M. V. Chekhova, "Experimental reconstruction of spatial Schmidt modes for a wide-field SU(1,1) interferometer", Laser Phys. **29**, 124013 (2019).

[101] D. Halliday, R. Resnick, and J. Walker, *Fundamentals of Physics, Extended*, 10th ed. (John Wiley & Sons, 2013).

[102] F. S. Roux, "Nonlinear interferometry in all spatiotemporal degrees of freedom", Phys. Rev. A **105**, 043701 (2022).

[103] M. Chekhova, I. Barakat, M. Kalash, D. Scharwald, P. Sharapova, and N. Lindlein, Supplementary document: "Supplementary document for Simultaneous measurement of multimode squeezing" (Optica Publishing Group, 2025).

[104] K. Y. Spasibko, T. S. Iskhakov, and M. V. Chekhova, "Spectral properties of high-gain parametric down-conversion", Opt. Express **20**, 7507 (2012).

[105] A. M. Pérez, K. Y. Spasibko, P. R. Sharapova, O. V. Tikhonova, G. Leuchs, and M. V. Chekhova, "Giant narrowband twin-beam generation along the pump-energy propagation direction", Nat. Commun. **6**, 7707 (2015).

[106] T. S. Iskhakov, A. M. Pérez, K. Y. Spasibko, M. V. Chekhova, and G. Leuchs, "Superbunched bright squeezed vacuum state", Opt. Lett. **37**, 1919 (2012).

[107] E. Brambilla, A. Gatti, M. Bache, and L. A. Lugiato, "Simultaneous near-field and far-field spatial quantum correlations in the high-gain regime of parametric down-conversion", Phys. Rev. A **69**, 023802 (2004).

[108] M. I. Kolobov, "The spatial behavior of nonclassical light", Rev. Mod. Phys. **71**, 1539 (1999).

[109] A. Gatti, E. Brambilla, K. Gallo, and O. Jedrkiewicz, "Golden ratio entanglement in hexagonally poled nonlinear crystals", Phys. Rev. A **98**, 053827 (2018).

[110] E. Brambilla, A. Gatti, L. A. Lugiato, and M. I. Kolobov, "Quantum structures in traveling-wave spontaneous parametric down-conversion", Eur. Phys. J. D **15**, 127 (2001).

[111] I. N. Bronshtein, K. A. Semendyayev, G. Musiol, and H. Mühlig, *Handbook of Mathematics* (Springer Berlin Heidelberg, 2015).

[112] Q. Kang, Z. Zhao, T. Zhao, C. Liu, and L. Hu, "Improved phase sensitivity of an SU(1,1) interferometer based on the internal single-path local squeezing operation" (2024), arXiv:2410.21292 [quant-ph].

[113] M. Bartelmann, B. Feuerbacher, T. Krüger, D. Lüst, A. Rebhan, and A. Wipf, *Theoretische Physik 3 / Quantenmechanik* (Springer Spektrum, 2018).

[114] M. G. Genoni, M. L. Palma, T. Tufarelli, S. Olivares, M. S. Kim, and M. G. A. Paris, "Detecting quantum non-Gaussianity via the Wigner function", Phys. Rev. A **87**, 062104 (2013).

[115] J. N. Hollenhorst, "Quantum limits on resonant-mass gravitational-radiation detectors", Phys. Rev. D **19**, 1669 (1979).

[116] X. Ma and W. Rhodes, "Multimode squeeze operators and squeezed states", Phys. Rev. A **41**, 4625 (1990).

[117] C. F. Lo and R. Sollie, "Generalized multimode squeezed states", Phys. Rev. A **47**, 733 (1993).

[118] J. B. Brask, "Gaussian states and operations – a quick reference" (2022), arXiv:2102.05748 [quant-ph].

[119] G. Cariolaro and G. Pierobon, "Fock expansion of multimode pure Gaussian states", J. Math. Phys. **56**, 122109 (2015).

[120] M. Houde, W. McCutcheon, and N. Quesada, "Matrix decompositions in quantum optics: Takagi/Autonne, Bloch–Messiah/Euler, Iwasawa, and Williamson", Can. J. Phys. **102**, 497 (2024).

[121] E. Celledoni, E. Çokaj, A. Leone, D. Murari, and B. O. and, "Lie group integrators for mechanical systems", Int. J. Comput. Math. **99**, 58 (2022).

[122] A. Iserles, H. Z. Munthe-Kaas, S. P. Nørsett, and A. Zanna, "Lie-group methods", Acta Numer. **9**, 215 (2000).

[123] M. Houde and N. Quesada, "Perfect pulsed inline twin-beam squeezers", AVS Quantum Sci. **6**, 021402 (2024).

[124] E. Giese, S. Lemieux, M. Manceau, R. Fickler, and R. W. Boyd, "Phase sensitivity of gain-unbalanced nonlinear interferometers", Phys. Rev. A **96**, 053863 (2017).

[125] C.-P. Wei, C.-G. Xu, and Q. Liu, "Phase sensitivity of a modified Grover-Michelson interferometer", Opt. Contin. **4**, 1266 (2025).

[126] A. Christ, C. Lupo, M. Reichelt, T. Meier, and C. Silberhorn, "Theory of filtered type-II parametric down-conversion in the continuous-variable domain: Quantifying the impacts of filtering", Phys. Rev. A **90**, 023823 (2014).

[127] L. Beltran, G. Frascella, A. M. Perez, R. Fickler, P. R. Sharapova, M. Manceau, O. V. Tikhonova, R. W. Boyd, G. Leuchs, and M. V. Chekhova, "Orbital angular momentum modes of high-gain parametric down-conversion", J. Opt. **19**, 044005 (2017).

[128] S. E. Dwyer, G. L. Mansell, and L. McCuller, "Squeezing in Gravitational Wave Detectors", Galaxies **10**, 46 (2022).

[129] S. Chelkowski, *Squeezed light and laser interferometric gravitational wave detectors*, PhD thesis (Gottfried Wilhelm Leibniz Universität Hannover, 2007).

[130] M. Croquette, *Optomechanics and Squeezed light*, PhD thesis (Sorbonne Université, 2022).

[131] E. Polino, M. Valeri, N. Spagnolo, and F. Sciarrino, "Photonic quantum metrology", AVS Quantum Sci. **2**, 024703 (2020).

[132] L. Allen, S. M. Barnett, and M. J. Padgett, *Optical Angular Momentum* (CRC Press, 2016).

[133] K. Y. Bliokh, M. A. Alonso, E. A. Ostrovskaya, and A. Aiello, "Angular momenta and spin-orbit interaction of nonparaxial light in free space", Phys. Rev. A **82**, 063825 (2010).

[134] J. Garrison and R. Chiao, *Quantum Optics* (Oxford University Press, 2008).

[135] K. Y. Bliokh, F. J. Rodríguez-Fortuño, F. Nori, and A. V. Zayats, "Spin–orbit interactions of light", Nat. Photonics **9**, 796 (2015).

[136] A. Niv, Y. Gorodetski, V. Kleiner, and E. Hasman, "Topological spin-orbit interaction of light in anisotropic inhomogeneous subwavelength structures", Opt. Lett. **33**, 2910 (2008).

[137] A. Ciattoni, G. Cincotti, and C. Palma, "Angular momentum dynamics of a paraxial beam in a uniaxial crystal", Phys. Rev. E **67**, 036618 (2003).

[138] S. J. van Enk and G. Nienhuis, "Spin and Orbital Angular Momentum of Photons", Europhys. Lett. **25**, 497 (1994).

[139] G. F. Calvo, A. Picón, and E. Bagan, "Quantum field theory of photons with orbital angular momentum", Phys. Rev. A **73**, 013805 (2006).

[140] W. N. Plick and M. Krenn, "Physical meaning of the radial index of Laguerre-Gauss beams", Phys. Rev. A **92**, 063841 (2015).

[141] S. J. van Enk and G. Nienhuis, "Eigenfunction description of laser beams and orbital angular momentum of light", Opt. Commun. **94**, 147 (1992).

[142] G. Nienhuis and L. Allen, "Paraxial wave optics and harmonic oscillators", Phys. Rev. A **48**, 656 (1993).

[143] A. E. Siegman, *Lasers* (University Science Books, 1986).

[144] D. Marcuse, *Light Transmission Optics* (Van Nostrand Reinhold, 1972).

[145] F. Pampaloni and J. Enderlein, "Gaussian, Hermite-Gaussian, and Laguerre-Gaussian beams: A primer" (2004), arXiv:physics/0410021 [physics.optics].

[146] R. F. Offer, D. Stulga, E. Riis, S. Franke-Arnold, and A. S. Arnold, "Spiral bandwidth of four-wave mixing in Rb vapour", Commun. Phys. **1**, 84 (2018).

[147] Y. Yang, Y. Li, and C. Wang, "Generation and expansion of Laguerre–Gaussian beams", J. Opt. **51**, 910 (2022).

[148] B. Baghdasaryan, C. Sevilla-Gutiérrez, F. Steinlechner, and S. Fritzsche, "Generalized description of the spatio-temporal biphoton state in spontaneous parametric down-conversion", Phys. Rev. A **106**, 063711 (2022).

[149] N. K. Fontaine, R. Ryf, H. Chen, D. T. Neilson, K. Kim, and J. Carpenter, "Laguerre-Gaussian mode sorter", Nat. Commun. **10**, 1865 (2019).

[150] J. W. Simmons and M. J. Guttmann, *States, Waves and Photons: A Modern Introduction to Light* (Addison-Wesley, 1970).

[151] D. Scharwald, L. Gehse, and P. R. Sharapova, Dataset: "Schmidt modes carrying orbital angular momentum generated by cascaded systems pumped with Laguerre-Gaussian beams" (Zenodo, 2024).

[152] J. Guo, S. Ming, Y. Wu, L. Q. Chen, and W. Zhang, "Super-sensitive rotation measurement with an orbital angular momentum atom-light hybrid interferometer", Opt. Express **29**, 208 (2021).

[153] N. González, G. Molina-Terriza, and J. P. Torres, "How a Dove prism transforms the orbital angular momentum of a light beam", Opt. Express **14**, 9093 (2006).

[154] F. Grenapin, D. Paneru, A. D'Errico, V. Grillo, G. Leuchs, and E. Karimi, "Superresolution Enhancement in Biphoton Spatial-Mode Demultiplexing", Phys. Rev. Appl. **20**, 024077 (2023).

[155] R. Barboza, A. Babazadeh, L. Marrucci, F. Cardano, C. de Lisio, and V. D'Ambrosio, "Ultra-sensitive measurement of transverse displacements with linear photonic gears", Nat. Commun. **13**, 1080 (2022).

[156] J. W. Goodman, *Introduction to Fourier Optics*, 2nd ed. (McGraw-Hill, 1996).

[157] M. Bartelmann, B. Feuerbacher, T. Krüger, D. Lüst, A. Rebhan, and A. Wipf, *Theoretische Physik 2 | Elektrodynamik* (Springer Spektrum, 2018).

[158] F. M. Dopico and C. R. Johnson, "Complementary bases in symplectic matrices and a proof that their determinant is one", Linear Algebra Appl. **419**, 772 (2006).

[159] D. Rim, "An Elementary Proof That Symplectic Matrices Have Determinant One" (2018), arXiv:1505.04240 [math.HO].

[160] F. Bünger and S. Rump, "Yet more elementary proofs that the determinant of a symplectic matrix is 1", Linear Algebra Appl. **515**, 87 (2017).

[161] A. B. Klimov and S. M. Chumakov, *A Group-Theoretical Approach to Quantum Optics: Models of Atom-Field Interactions* (Wiley, 2009).

[162] A. P. Isaev and V. A. Rubakov, *Theory Of Groups And Symmetries: Finite Groups, Lie Groups, And Lie Algebras* (World Scientific Publishing Company, 2018).

[163] L. Gehse, *Orbital angular momentum modes generated in advanced nonlinear interferometers*, Master's thesis (Paderborn University, 2024).

[164] L. N. Trefethen and D. Bau, III, *Numerical Linear Algebra* (Society for Industrial and Applied Mathematics, 1997).

[165] R. A. Horn and C. R. Johnson, *Topics in Matrix Analysis* (Cambridge University Press, 1991).

[166] R. A. Horn and C. R. Johnson, *Matrix Analysis* (Cambridge University Press, 1985).

[167] M. Born and E. Wolf, *Principles of optics*, 7th ed. (Cambridge University Press, 2019).

[168] K. Khare, M. Butola, and S. Rajora, *Fourier Optics and Computational Imaging*, 2nd ed. (Springer Cham, 2023).

[169] R. Grella, "Fresnel propagation and diffraction and paraxial wave equation", J. Opt. **13**, 367 (1982).

[170] W. Zhao, J. Lu, J. Ma, C. Yuan, C. Chang, and R. Zhu, "Technique for enhancing the accuracy of the Rayleigh–Sommerfeld convolutional diffraction through the utilization of independent spatial sampling", Opt. Lett. **49**, 1385 (2024).

[171] Y.-m. Gao, J.-p. Xie, and X.-y. Yu, "Rayleigh-Sommerfeld diffraction on a sub-wavelength scale: Theories and a resolution criterion", Phys. Rev. A **99**, 023814 (2019).

[172] E. Mosso, "An optical-cryptographic encryption scheme using a keystream synthesizer based on chaotic speckle nature", J. Opt. **25**, 015703 (2022).

[173] A. Al Falou (editor), *Advanced Secure Optical Image Processing for Communications* (IOP Publishing, 2018).

[174] W. Han, W. Cheng, and Q. Zhan, "Design and alignment strategies of 4f systems used in the vectorial optical field generator", Appl. Opt. **54**, 2275 (2015).

[175] D. N. Klyshko, "Parametric generation of two-photon light in anisotropic layered media", J. Exp. Theor. Phys. **105**, 1574 (1994).

[176] D. Scharwald, T. Meier, and P. R. Sharapova, Dataset: "Phase sensitivity of spatially broadband high-gain SU(1,1) interferometers" (Zenodo, 2023).

[177] D. Scharwald and P. R. Sharapova, Dataset: "Characterization of Schmidt modes in high-gain SU(1,1) interferometers" (Zenodo, 2025).

List of Scientific Contributions

Peer-Reviewed Articles in Scientific Journals

I. **D. Scharwald**, T. Meier, and P. R. Sharapova
"Phase sensitivity of spatially broadband high-gain SU(1,1) interferometers"
Physical Review Research **5**, 043158 (2023)
Appearing herein as Ref. [1]. The dataset associated with this publication is openly available, see Ref. [176].

II. **D. Scharwald**, L. Gehse, and P. R. Sharapova
"Schmidt modes carrying orbital angular momentum generated by cascaded systems pumped with Laguerre-Gaussian beams"
APL Photonics **10**, 016112 (2025)
Appearing herein as Ref. [2]. The dataset associated with this publication is openly available, see Ref. [151].

III. Ismail Barakat, Mahmoud Kalash, **Dennis Scharwald**, Polina Sharapova, Norbert Lindlein, and Maria Chekhova
"Simultaneous measurement of multimode squeezing through multimode phase-sensitive amplification"
Optica Quantum **3**, 36 (2025)
Appearing herein as Ref. [3]. Published with supplementary material, see Ref. [103].

Preprints

IV. **D. Scharwald** and P. R. Sharapova
"Characterization of Schmidt modes in high-gain SU(1,1) interferometers"
arXiv:2504.19377 (2025)
Appearing herein as Ref. [4]. The dataset associated with this publication is openly available, see Ref. [177].

Conference and Workshop Contributions

The name of the presenting author is indicated by an underline.

i. **D. Scharwald**, I. Barakat, M. Kalash, N. Lindlein, M. Chekhova, and P. Sharapova
"Metrology Based on Multimode Nonlinear Interferometers" [Revised version of Contributions ii and iv]
SFB/TRR 142-Workshop, Bad Sassendorf (Germany), November 2024 (poster)

ii. **D. Scharwald**, I. Barakat, M. Kalash, N. Lindlein, M. Chekhova, and P. Sharapova
"Metrology Based on Multimode Nonlinear Interferometers" [Revised version of Contribution iv]
Quantum Photonics Spotlight 2024 (QPS2024), Paderborn (Germany), October 2024 (poster)

iii. **D. Scharwald**, M. Kalash, I. Barakat, M. V. Chekhova, and P. R. Sharapova
"Multimode Squeezing Reconstruction Via Direct Intensity Measurement"
32nd Annual International Laser Physics Workshop (LPHYS'24), São Carlos (Brazil), July 2024 (talk)

iv. **D. Scharwald**, I. Barakat, M. Kalash, N. Lindlein, M. Chekhova, and P. Sharapova
"Metrology based on multimode nonlinear interferometers"
Central European Workshop on Quantum Optics (CEWQO), Olomouc (Czech Republic), July 2024 (poster)

v. **Dennis Scharwald** and Polina Sharapova
"Reducing Schmidt mode cross-overlap inside SU(1,1) interferometers"
DPG Spring Meeting (SAMOP), Freiburg im Breisgau (Germany), March 2024 (talk)

vi. **D. Scharwald** and P. R. Sharapova
"Evolution of Schmidt modes in cascaded nonlinear systems"
SFB/TRR 142-Workshop, Bad Sassendorf (Germany), November 2023 (talk)

vii. **D. Scharwald**, T. Meier, and P. Sharapova
"Phase Sensitivity of Compensated High-Gain SU(1,1) Interferometers" [Multimode SU(1,1) interferometers at high gain]
Central European Workshop on Quantum Optics (CEWQO), Milan (Italy), July 2023 (poster)

viii. Lucas Gehse, **Dennis Scharwald**, and Polina Sharapova
"Orbital angular momentum modes generated in the parametric down-conversion process with a non-Gaussian pump"
DPG Spring Meeting (SAMOP), Hanover (Germany), March 2023 (poster)

ix. **Dennis Scharwald** and Polina Sharapova
"Improving the Phase Sensitivity of SU(1,1) Interferometers by Phase Matching Compensation"
DPG Spring Meeting (SAMOP), Hanover (Germany), March 2023 (talk)

x. **D. Scharwald** and P. Sharapova
"Phase Super-Sensitivity in Compensated High-Gain SU(1,1) Interferometers"
SFB/TRR 142-Workshop, Bad Sassendorf (Germany), November 2022 (poster)

xi. **D. Scharwald**, F. Twisden-Peareth, J. Sperling, and P. Sharapova
"Generation and Characterization of Multiphoton States of Light"
SFB/TRR 142-Workshop, Bad Sassendorf (Germany), June 2022 (poster)

xii. **Dennis Scharwald** and Polina Sharapova
"A stepwise approach to the BSV description"
DPG Spring Meeting (SAMOP), Erlangen (Germany, online), March 2022 (talk)

Acknowledgments

We acknowledge financial support of the Deutsche Forschungsgemeinschaft (DFG) via Project SH 1228/3-1 and via the TRR 142/3 (Project No. 231447078, Subproject No. C10) Furthermore, we thank the PC2 (Paderborn Center for Parallel Computing) for providing computation time. Several important tools have been used in the context of this thesis:

- *Python* [G. van Rossum *et al.*, CWI Quarterly **4**, 283 (1991)], as the main programming language.
- *NumPy* [C. R. Harris *et al.*, Nature **585**, 357 (2020)] and *SciPy* [P. Virtanen *et al.*, Nat. Methods **17**, 261 (2020)] as the main numerical packages used for computations.
- *Matplotlib* [The Matplotlib Development Team, "Matplotlib: Visualization with Python" (multiple versions, Zenodo, 2024)] as the main library used for the generation of the data plots. Figures 3.5, 4.2, 5.2, 5.3, 5.5, 5.7 and 5.8 additionally use the *batlow* colormap [F. Crameri, "Scientific colour maps" (version 8.0.0, Zenodo, 2023)].

Danksagung

Zum Abschluss dieser Dissertation möchte ich mich noch ganz herzlich bei einigen Personen bedanken. Zunächst gilt mein Dank **Dr. Polina Sharapova** für die Chance über die vergangenen Jahre in deiner Arbeitsgruppe geforscht haben zu können und für die gute Betreuung und Unterstützung während der Promotion, insbesondere auch in anstrengenden Phasen und bei unlösbar erscheinenden Herausforderungen des Projektes. Im Rahmen des Projektes konnte ich daher mein Wissen zur parametrischen Fluoreszenz und SU(1,1) Interferometern vertiefen und an einigen sehr interessanten und lehrreichen Workshops im In- und Ausland teilnehmen.

Ferner möchte ich mich auch bei den restlichen Mitgliedern der Promotionskommission bedanken, nämlich: **Prof. Dr. Torsten Meier** als Erstgutachter, **Prof. Dr. Jan Sperling** als Zweitgutachter und **Prof. Dr. Thomas Zentgraf** als Vorsitzender der Promotionskommission.

Im Rahmen meiner Forschung konnte ich an einer Kollaboration mit Partnern aus Erlangen teilnehmen, auf deren Basis ich wertvolles Wissen sammeln konnte. Daher möchte ich mich bei **Prof. Dr. Maria Chekhova**, **Dr. Ismail Barakat** und **Mahmoud Kalash** für die produktive Zusammenarbeit und die aufschlussreichen Diskussionen bedanken.

Ebenfalls für die erfolgreiche Zusammenarbeit im Zusammenhang mit PDC mit Laguerre-Gauß'schen Pumpmoden und für das Korrekturlesen möchte ich **Lucas Gehse** danken.

Weiterhin möchte ich mich bei **Prof. Dr. Sina Saravi** bedanken für das Ermöglichen eines nahtlosen Übergangs in eine Anschlussstelle mit einem neuen und interessanten Forschungsthema.

Darüber hinaus möchte ich **Simone Lange** für ihre engagierte Unterstützung bei allerlei organisatorischen Angelegenheiten danken.

Zuletzt möchte ich mich noch bei meiner **Familie**, allen **Kommilitoninnen** und **Kommilitonen**, sowie **Freundinnen** und **Freunden** bedanken, die mir während des Studiums und der Forschung beigestanden und mich immer wieder motiviert haben und ebenso diese Dissertation Korrektur gelesen haben.

Paderborn und Lippstadt,
23. Januar 2026